

ABSTRACT

CAREY, LEIAH MARIE. Probing the Structure-Function Relationship of a Multifunctional Enzyme using Crystallographic Diffraction Methods. (Under the direction of Dr. Reza Ghiladi.)

The marine annelid *Amphitrite ornata* possesses the ability to chemically detoxify deleterious aromatic compounds prevalent in its environment, which is afforded by its coelomic hemoglobin, Dehaloperoxidase (DHP). In addition to its oxygen transport function, DHP also possesses peroxidase, peroxygenase, oxidase and oxygenase enzymatic functions, resulting in 5 activities that coexist at a single heme reactive center. Structurally, DHP possesses the canonical α -helical globin fold associated with oxygen transport, yet lacks the structural homology with archetypical monofunctional examples of which it shares enzymatic reactivity, such as horseradish peroxidase, *Aae*APO, cytochrome *c* oxidase and cytochrome P450 monooxygenase. The structure-function paradigm has been extensively studied and well-defined for monofunctional enzymes, however this understanding is lacking when applied to multifunctional systems. In an effort to discern how DHP accommodates this multifunctional reactivity, a structural approach utilizing crystallographic diffraction is undertaken in the investigations presented here.

DHP is introduced in Chapter 1, presenting discussions on the various reactivities embodied in this multifunctional system, previous crystallographic structural analyses residing in the RCSB PDB, and spectroscopic data correlating ligand binding to their respective functional consequence. Chapter 2 presents mechanistic and structural studies of DHP reactivity with 2,4-dihalophenols, a class of substrate that is structurally intermediate between 4-halophenol inhibition and 2,4,6-trihalophenol peroxidase reactivity. The consequence of the number of halogens on substrate binding orientation is examined via crystallographic studies, and this halogen-directed binding is interpreted through reactivity comparisons between mono- (4-halophenol), di- (2,4-dihalophenol) and trihalophenols (2,4,6-trihalopenol), thus contributing to our knowledge of DHP reactivity with halophenols. Chapter 3 examines the two naturally occurring isoenzymes, DHP A and DHP B, which differ by only 5 of the 137 amino acids, yet exhibit pronounced differences in enzymatic reactivity. Systematic investigations of these substitutions utilizing mutagenesis, spectroscopic analysis, reactivity studies and crystallographic structural analysis identify the I9L substitution to have the greatest

effect on isoenzyme differences in reactivity, yet this isoelectric substitution has no direct contact with the heme active site. In Chapter 4, the knowledge of substrate binding sites of different mechanistic substrates is utilized in rationally designing mutagenesis studies in an effort to direct enzymatic functionality. The plasticity of the heme active center is further elaborated through DHP's ability to preserve peroxidase reactivity, albeit at a lower capability, even when a peroxidase substrate binding site is sterically blocked. Chapter 5 is a collection of crystallographic case studies in an effort to advance the knowledge of DHP's representation of the structure-function paradigm when applied to a multifunctional catalytic globin. The first neutron crystallographic structure of DHP, in addition to being the first multifunctional heme enzyme characterized by this technique, is presented in the ferric resting state. Advances include the unambiguous assignment of hydrogen atom coordinates to protonation states of mechanistically important residues, as well as the discovery of a distal water network previously unobserved in X-ray crystallographic structures. The crystallographic binding site of the first peroxygenase substrate, 4-nitrophenol, is presented which allows a direct correlation between substrate binding and a mechanism for O-atom transfer. The X-ray crystallographic structure of a Mn-protoporphyrin IX variant of DHP B reveals DHP B's ability to regain its native fold after denaturation and substitution of the porphyrin cofactor. Lastly, the assumption that tyrosine ring rotation angles in WT DHP are representative of the phenylalanine ring rotation angles in DHP mutants is confirmed, further supporting the radical migration pathway elucidated via EPR spectral assignment provided by the TRSSA generated simulated EPR spectra.

© Copyright 2017 Leah Marie Carey

All Rights Reserved

Probing the Structure-Function Relationship of a Multifunctional Enzyme using
Crystallographic Diffraction Methods

by
Leiah Marie Carey

A dissertation submitted to the Graduate Faculty of
North Carolina State University
in partial fulfillment of the
requirements for the Degree of
Doctor of Philosophy

Chemistry

Raleigh, North Carolina

2017

APPROVED BY:

Dr. Reza Ghiladi
Chair of Advisory Committee

Dr. Stefan Franzen

Dr. Robert Rose

Dr. Tatyana Smirnova

DEDICATION

To the person who reminds me how to smile, showers me with unwavering love and support, reminds me of my strengths when I have forgotten them and is the purest inspiration I have ever known, I dedicate this dissertation to my daughter, Miss Pearl Ronin Hollingsworth.

BIOGRAPHY

Leiah Marie Carey was born the first child to Tim and Kathy Carey in the evening of February 16th, 1979 in Chapel Hill, NC. She called Saxapahaw, NC home until graduating from Southern Alamance High School in 1997 and went out into the world on her own. In late December 2007, her daughter Pearl was born. She obtained her Bachelor of Science in Chemistry in 2012 from the University of North Carolina at Greensboro and entered the Chemistry Ph. D. program at North Carolina State University that same year. Upon joining the Ghiladi research group, she directed her training toward a physical approach to investigate the chemistry of biological systems, from which she quickly discovered her love for crystallography. She soon realized this was exactly what she had been searching for: a career path that embraces curiosity, is intellectually stimulating and emotionally satisfying.

ACKNOWLEDGMENTS

The support I've received while working toward this personal goal has been instrumental to my success and words cannot fully express my gratitude. I would like to thank my graduate mentor, Dr. Reza Ghiladi, for the opportunity to pursue my graduate studies in your lab. The insight, support and experiences you have provided me are the cornerstones of my success. In particular, thank you for allowing me to grow independently in my research and respecting my responsibility as a parent, both of which have helped me learn to balance the many facets of life while pursuing a goal. For your continuous support and interest in my research, willingness to always provide resources and assistance, and sharing your enthusiasm for scientific discovery and education, I would like to thank Dr. Stefan Franzen. Without your insistence on the need to continue crystallographic work after Junjie left and offering me the use of the different capabilities of your lab, I might not have pursued a research project outside the expertise of my lab nor realized that I truly enjoy crystallographic work. For Dr. Paul Swartz, thank you for opening your lab to me and dealing my insistent questions, which helped me develop a deeper understanding and appreciation for crystallography. For my labmates, both past and present, thank you for many insightful discussions, willingness to help, being able to share the excitement and passion for research and basically just being great people. You guys were a pleasure to work. Thank you to my parents (and Pearl's grandparents) for your support in my decision to pursue this daunting and lengthy endeavor and for taking such great care of Pearl, which allowed me the time needed to get the work done. Thank you Bosque, because I couldn't have returned to school without your help caring for my infant daughter. Finally, for the unwavering support and assistance that has made life manageable, thank you Mr. David.

TABLE OF CONTENTS

LIST OF TABLES.....	ix
LIST OF FIGURES.....	xii
LIST OF SCHEMES.....	xix
LIST OF ABBREVIATIONS.....	xx
Chapter 1: X-ray Crystallographic and Spectroscopic Analysis of Dehaloperoxidase (DHP) on Deposited Structures.....	1
1.1 Introduction.....	1
1.2 Global Structural Analysis.....	2
1.3 The Multiple Functions of Dehaloperoxidase.....	4
1.4 Brief Overview of Deposited Dehaloperoxidase X-ray Crystallographic Structures.....	6
1.5 Unusual Flexibility of the Distal Histidine: Structural and Spectroscopic Correlations.....	11
1.6 Inhibitor Binding Site Characterization.....	13
1.7 Peroxidase Substrate Binding Site(s) Characterization.....	15
1.8 Peroxygenase Substrate Binding Site(s) Analysis.....	19
1.8.1 Haloindoles: 5-bromoindole and 7-bromoindole.....	19
1.8.2 4-nitrophenol.....	21
1.9 Preface of Presented Work in Proceeding Chapters.....	22
1.10 References.....	24
Chapter 2: Bridging the Functional Gap Between Reactivity and Inhibition in Dehaloperoxidase B from <i>Amphitrite ornata</i>: Mechanistic and Structural Studies of 2,4-dihalophenol.....	28
2.1 Abstract.....	28
2.2 Introduction.....	28
2.3 Experimental.....	30
2.3.1 Materials and Methods.....	30
2.3.2 Enzyme Assay Protocol.....	30
2.3.3 LC-MS Studies.....	31
2.3.4 Substrate Binding Studies.....	31
2.3.5 Stopped-flow UV-visible Studies.....	32
2.3.6 Protein Crystallization and X-ray Diffraction Studies.....	32
2.4 Results.....	33
2.4.1 Enzyme Assays.....	33
2.4.2 MS Product Characterization and ¹⁸ O Labeling Studies.....	35
2.4.3 Substrate Binding Study.....	42
2.4.4 Stopped-flow Studies of 2,4-dichlorophenol Reactivity.....	44
2.4.5 Protein Crystallization and X-ray Diffraction Studies.....	49

2.5 Discussion.....	54
2.6 Conclusion.....	60
2.7 Supporting Information.....	61
2.8 References.....	68
Chapter 3: How Nature Tunes isoenzyme Activity in the Multifunctional Catalytic Globin Dehaloperoxidase from <i>Amphitrite ornata</i>	73
3.1 Author Contributions.....	73
3.2 Abstract.....	73
3.3 Introduction.....	74
3.4 Experimental.....	78
3.4.1 Materials.....	78
3.4.2 Construction of Mutant DHP Plasmids.....	78
3.4.3 Molecular Weight Determination.....	79
3.4.4 Peroxidase Studies.....	79
3.4.5 Peroxygenase Studies.....	80
3.4.6 5-Br-indole Binding Studies.....	80
3.4.7 Stopped-flow UV-visible Studies.....	81
3.4.8 EPR Spectroscopy.....	81
3.4.9 Protein Crystallization and X-ray Diffraction Studies.....	81
3.5 Results.....	82
3.5.1 UV-visible Spectroscopic Studies.....	82
3.5.2 EPR Spectroscopic Studies.....	85
3.5.3 Peroxidase Studies.....	87
3.5.4 Peroxygenase Studies.....	88
3.5.5 5-Br-indole Binding Studies.....	90
3.5.6 Non-native I9 Mutants.....	91
3.5.7 Stopped-flow UV-visible Spectroscopic Studies.....	91
3.5.8 X-ray Diffraction Studies.....	92
3.6 Discussion.....	98
3.7 Conclusion.....	102
3.8 Acknowledgements.....	103
3.9 Supporting Information.....	103
3.10 References.....	110
Chapter 4: Selective Tuning of Activity in a Multifunctional Enzyme as Revealed in the F21W Mutant of Dehaloperoxidase B from <i>Amphitrite ornata</i>	117
4.1 Author Contributions.....	117
4.2 Abstract.....	117
4.3 Introduction.....	118
4.4 Experimental.....	121

4.4.1 Materials.....	121
4.4.2 Construction of Mutant DHP Plasmids.....	121
4.4.3 Protein Crystallization and X-ray Diffraction Studies.....	122
4.4.4 Peroxidase Studies.....	122
4.4.5 Peroxygenase Studies.....	123
4.4.6 5-Br-indole Binding Studies.....	123
4.4.7 Stopped-flow UV-visible Studies.....	124
4.5 Results.....	124
4.5.1 Overexpression, Purification and Characterization of DHP B (F21W).....	124
4.5.2 Activity Assays.....	126
4.5.3 Isotopically-labeled Oxygen Studies.....	127
4.5.4 Stopped-flow UV-visible Spectroscopy.....	128
4.5.5 X-ray Crystallographic Studies.....	131
4.6 Discussion.....	134
4.7 Conclusion.....	138
4.8 Acknowledgements.....	138
4.9 Supplementary Material.....	139
4.10 References.....	141

Chapter 5: Further Exploring the Structure-Function Relationship in Dehaloperoxidase Through X-ray and Neutron Crystallography: Four Case Studies.....	146
5.1 Case Study 1 – Neutron Diffraction Structure of Ferric DHP B.....	146
5.1.1 Introduction.....	146
5.1.2 Experimental.....	149
5.1.3 Results and Discussion.....	153
5.1.4 Summary of Case Study 1.....	161
5.2 Case Study 2 – Elucidation of the 4-Nitrophenol (4NP) and 4- Nitrocatechol (4NC) Crystallographic Binding Sites in DHP B...	162
5.2.1 Abstract.....	162
5.2.2 Experimental.....	163
5.2.3 Results and Discussion.....	163
5.2.4 Summary of Case Study 2.....	169
5.3 Structural Analysis of DHP B Reconstituted with Mn Protoporphyrin IX.....	170
5.3.1 Introduction.....	170
5.3.2 Experimental.....	170
5.3.3 Results and Discussion.....	171
5.3.4 Summary of Case Study 3.....	176
5.4 Tyrosine Rotation Angle Validation: X-ray Crystallographic Analysis of DHP B (Y28F) and DHP B (Y38F).....	177

5.4.1 Introduction.....	177
5.4.2 Experimental.....	178
5.4.3 Results and Discussion.....	179
5.4.4 Summary of Case Study 4.....	183
5.5 References.....	184

LIST OF TABLES

Table 1.1	Crystal structures of DHP deposited into the PDB, arranged from most recent to initial structure.....	8
Table 1.2	Distances (Å) given for the heme Fe and the halogen and alcohol moieties of the inhibitors (4XP) and the substrates (TXP).....	18
Table 2.1	Substrate conversion (%), providing 2,4-DCP and 2,4-DBP reactivity with ferric DHP B and oxyferrous DHP B. Substrate conversion in the presence of 500 μM 4-BP inhibitor is given in parenthesis. Reactivity of previously established substrates is provided for comparison.....	34
Table 2.2	K_d Values for Ligand Binding to Ferric DHP B at pH 7	43
Table 2.3	X-ray Data Collection and Refinement Statistics for WT DHP B complexed with 2,4-dichlorophenol (2,4-DCP) (5WN6 and 5WMZ), 2,4-dibromophenol (2,4-DBP) (5WMY), 4-chlorophenol (4-CP) (6AOE) and 4-bromophenol (4-BP) (6AOF).....	51
Table 2.4	Distal pocket atomic distances of substrate (2,4-DCP or 2,4-DBP) and heme environments, given in Å. Values provided are averages of both protomers. Atomic distances for 2,4,6-trihalophenols and 4-halophenols are provided for comparison.....	52
Table 3.1	UV-visible spectroscopic features of ferric DHP variants at pH 7.....	85
Table 3.2	Kinetics data for the oxidation of TCP and conversion percentage of 5-Br-indole as catalyzed by ferric DHP in the presence of H ₂ O ₂ at pH 7....	89
Table 3.3	5-Br-indole dissociation constants (K_d) for WT DHP and selected mutants.....	90
Table 3.4	UV-visible spectroscopic features and rate of formation of Compound ES in WT DHP and selected variants at pH 7.....	92
Table 3.5	X-ray Data Collection and Refinement Statistics for DHP B (L9I) (5V5Q), DHP A (I9L) (5V5R), and WT DHP B (5V5J). All structures were solved in the oxyferrous state.....	95

Table 3.6	Selected Distances and Angles for Protomers A & B (Protomer B in parentheses).....	96
Table S3.7	Mutagenic Primers Used to Construct the DHP A Mutants.....	104
Table S3.8	Calculated and experimentally determined monomeric molecular weights of the dehaloperoxidase mutants.....	104
Table S3.9	Rmsd Values for DHP Protomer C ^α Least Squares Quadratic (LSQ) Alignment.....	106
Table 4.1	Kinetic parameters for the oxidation of TCP, and percent substrate conversion for the oxygenation of 5-Br-indole, 7-Br-indole and 4-NP...	127
Table 4.2	Comparison of UV-visible spectroscopic data for the ferric, Compound ES, and Compound RH species in DHP B (F21W) and WT DHP isoenzymes A and B at pH 7.....	129
Table 4.3	X-ray Data Collection and Refinement Statistics for DHP B (F21W) (5VLX).....	132
Table 4.4	Selected distances (Å) for DHP B (F21W) and WT DHP B (PDB accession 3IXF).....	133
Table 5.1	Comparison of neutron and X-ray scattering characteristics for selected atoms.....	148
Table 5.2	Enfors Minimal Media composition.....	151
Table 5.3	Neutron and data collection and refinement statistics for ferric WT DHP B.....	156
Table 5.4	Selected Distances in the Neutron Structure of Ferric DHP B for Protomer A.....	160
Table 5.5	Data collection and refinement statistics for DHP B co-crystallized in the presence of 4-nitrophenol (4-NP) and 4-nitrocatechol (4-NC).....	164
Table 5.6	Distal pocket distances of ligand (4NP, 4NC, and 4BP ¹⁸) and heme environments, given in Å. Atom nomenclature for 4-NP and 4-NC is shown in Figure 5.7.....	167

Table 5.7	X-ray data collection and refinement statistics for Mn-DHP B	173
Table 5.8	Selected porphyrin-related atomic distances of Mn-DHP B and WT DHP B (pdb accession 3IXF). All distances given in Å.....	176
Table 5.9	Data collection and refinement statistics for DHP B (Y28F) and DHP B (Y38F).....	181
Table 5.10	Rotation angle of the phenol ring in different tyrosine residues in DHP B (Y28F) and DHP B (Y38F), ranked in closeness to the target values...	182

LIST OF FIGURES

Figure 1.1	Image of <i>Amphitrite ornata</i> , from which DHP was discovered.....	1
Figure 1.2	X-ray crystal structures of A) sperm whale myoglobin (SWMb, PDB accession code 1A6G), B) DHP A (PDB accession code 1EW6) and C) cytochrome <i>c</i> peroxidase (CcP, PDB accession code 1ZBY). It is clearly shown that DHP possesses the conserved globin fold as displayed in Mb.....	3
Figure 1.3	Protoporphyrin IX prosthetic group, as found in DHP, Mb and HRP. Pyrrole rings (A-D) and heme edges (α - δ) are labeled in accordance with convention.....	4
Figure 1.4	Xe crystallographic binding sites observed in DHP.....	10
Figure 1.5	Sites of single amino acid mutations of DHP A, utilized previously for mechanistic and reactivity investigations.....	11
Figure 1.6	A) Room temperature resonance Raman spectrum of WT DHP A. Core markers for 6cHS and 5cHS hemes are annotated for ν_3 . B) Room temperature crystal structure (1EW6) emphasizing i) the water that occupies the Fe 6 th coordination site, and ii) distal histidine His55 in an equilibrium between the open (solvent exposed) and closed (internal) conformations.....	13
Figure 1.7	A) Resonance Raman spectra of WT DHP A in the presence of the indicated inhibitor. [DHP A] = 100 μ M; [4IP] = 1 mM; [4BP], [4CP] and [4FP] = 8 mM. B) Superposition of the para-halogenated phenolic inhibitor structures depicting orientation within the distal pocket; 4IP (red, 3LB1), 4BP (green, 6AOF), 4CP (blue, 6AOE) and 4FP (purple, 3LB4).....	14
Figure 1.8	A) Resonance Raman core size marker bands of WT DHP B (100 μ M), and WT DHP B in the presence of TBP (200 μ M), TCP (3 mM) and TFP (4 mM). B) Crystallographic binding site of TBP (4FH6). C) Internal and external binding sites of TCP in the DHP A (Y34N/S91G) mutant (4KN3). Sterically, it is shown that both TCP binding sites cannot be simultaneously occupied.....	16

Figure 1.9	Resonance Raman spectra of DHP B in solution with A) bromine-substituted indoles at different positions and B) 5-haloindoles of different halogens. [DHP] = 50 μ M, [5-haloindole] = 500 μ M.....	20
Figure 1.10	Geometry optimized structure for A) 5-bromoindole and B) 7-bromoindole.....	21
Figure 1.11	The binding of 4NP with DHP B is characterized through A) UV-visible spectral perturbation via titration of 4NP, B) binding isotherm yielding the dissociation constant of 260 μ M, and C) X-ray crystallographic binding site of 4NP in the distal pocket of DHP B.....	22
Figure 2.1	HPLC chromatograms, as observed at $\lambda = 288$ nm, of the 2,4-DCP (A) and 2,4-DBP (B) reactions with 10 μ M ferric DHP B, 500 μ M = [substrate] = [H ₂ O ₂].....	35
Figure 2.2	Kinetic data for the reaction of pre-formed Compound I [DHP B (Y28F/Y38F)] with 2,4-dichlorophenol (2,4-DCP).....	45
Figure 2.3	Kinetic data for the reaction of pre-formed Compound ES with 2,4-dichlorophenol (2,4-DCP).....	47
Figure 2.4	Kinetic data for the reaction of oxyferrous DHP B with 2,4-dichlorophenol (2,4-DCP) and hydrogen peroxide.....	48
Figure 2.5	X-ray crystal structures depicting the halophenol binding sites within the distal pocket of DHP B, as viewed from the heme β edge. A) 2,4-DCP _{α} binding site, named due to its proximity to the heme α edge (5WMZ). B) 2,4-DCP _{β} binding site, again named due to its orientation with respect to the heme β edge (5WN6). C) Superposition of 2,4-DCP _{α} and 2,4-DCP _{β} binding sites, showing they are exclusive of each other and both sites cannot be occupied simultaneously. D) 2,4-DBP binding site, above the heme α edge (5WMY). E) 4-BP distal binding orientation (6AOF). F) 4-CP binding orientation (6AOE). 4-BP and 4-CP have identical binding sites, distal of the heme residing between the Fe and β edge.....	50

Figure 2.6	Superposition of selected halophenol binding sites. A) 2,4-DBP (green) and 2,4-DCP _α (silver); B – D) Comparison of monohalophenol (blue) and trihalophenol (pink) binding sites with the elucidated dihalophenol binding sites. B) Brominated variants; C) Chlorinated variants (α heme edge proximity); D) Chlorinated variants (β heme edge proximity).....	59
Figure S2.7	Optical difference spectra (left) and titration curves (right) of 2,4-dichlorophenol (top) and 2,4-dibromophenol (bottom) binding to 10 μM DHP B (100 mM KP _i , pH 7, 5% MeOH v/v). The calculated dissociation constant is provided in each titration curve.....	62
Figure S2.8	TOP: LC chromatogram of the reaction of 2,4-dichlorophenol (500 μM) with DHP B (10 μM) in the presence of H ₂ O ₂ (500 μM) at 25 °C (5% MeOH in 100 mM KP _i , pH 7). Unlabeled peaks correspond to dimer and trimer products of various levels of oxidation and chlorination. BOTTOM: ESI-MS total ion chromatograms obtained for single ring species.....	63
Figure S2.9	ESI-MS total ion chromatograms obtained from the 1a (left panel) and 1c (right panel) reaction products of the ¹⁸ O isotopic labeled 2,4-DCP oxidation catalyzed by ferric DHP B conducted under the following conditions: A) unlabeled water and hydrogen peroxide B) labeled H ₂ ¹⁸ O ₂ and unlabeled water; C) labeled H ₂ ¹⁸ O and unlabeled hydrogen peroxide; D) ¹⁸ O labels on both H ₂ ¹⁸ O ₂ and H ₂ ¹⁸ O.....	64
Figure S2.10	ESI-MS total ion chromatograms obtained from the 1b (left panel) and 1d (right panel) reaction products of the ¹⁸ O isotopic labeled 2,4-DCP oxidation catalyzed by ferric DHP B conducted under the following conditions: A) unlabeled water and hydrogen peroxide B) labeled H ₂ ¹⁸ O ₂ and unlabeled water; C) labeled H ₂ ¹⁸ O and unlabeled hydrogen peroxide; D) ¹⁸ O labels on both H ₂ ¹⁸ O ₂ and H ₂ ¹⁸ O.....	65
Figure S2.11	TOP: LC chromatogram of the reaction of 2,4-dibromophenol (500 μM) with DHP B (10 μM) in the presence of H ₂ O ₂ (500 μM) at 25 °C (5% MeOH in 100 mM KP _i , pH 7). Unlabeled peaks correspond to dimer and trimer products of various levels of oxidation and bromination. BOTTOM: ESI-MS total ion chromatograms obtained for single ring species.....	66

Figure S2.12	ESI-MS total ion chromatograms obtained from the 2a (left panel), 2b (middle panel) and 2c (right panel) reaction products of the ^{18}O isotopic labeled 2,4-DBP oxidation catalyzed by ferric DHP B conducted under the following conditions: A) unlabeled water and hydrogen peroxide B) labeled $\text{H}_2^{18}\text{O}_2$ and unlabeled water; C) labeled H_2^{18}O and unlabeled hydrogen peroxide; D) ^{18}O labels on both $\text{H}_2^{18}\text{O}_2$ and H_2^{18}O	67
Figure 3.1	C^α superposition of the A protomers of DHP A (PDB accession code 1EW6, teal) and DHP B (PDB accession code 5V5J, purple), highlighting substitution sites between isoenzymes (isoenzyme A residue listed first): proximal side N/S81 and S/G91, distal side R/K32 and Y/N34, with I/L9 located 15 Å from the heme.....	77
Figure 3.2	UV-visible spectra of A) WT DHP A, WT DHP B, DHP A (I9L), DHP B (L9I) and DHP A (I9V), B) single mutants of DHP A, C) I9L containing double mutants of DHP A, D) double mutants of DHP A lacking the I9L substitution, and E) I9L containing triple mutants of DHP A. All spectra were recorded at 10 μM enzyme concentration in 100 mM KPi buffer (pH 7, 25 °C).....	83
Figure 3.3	EPR spectra of ferric WT DHP A (black), DHP A (I9L) (blue), WT DHP B (green), and DHP B (L9I) (red), and the result of their deconvolution into three individual ferric heme EPR signals, rhombic high spin, axial high spin, and mixed spin.....	87
Figure 3.4	Panels A-C: LSQ C^α superposition of DHP A (I9L) (green), DHP B (L9I) (teal), as viewed from the heme β edge. A) Superposition of the A protomers. B) Magnified view from panel A of the Leu9 and Ile9 residues. C) Heme active site from panel A. D) LSQ C^α superposition of DHP B (L9I) and WT DHP B (yellow). E) LSQ C^α superposition of DHP A (I9L) and WT DHP A (yellow; PDB accession code 2QFN).....	97
Figure S3.5	Kinetic data obtained by optical spectroscopy for the reaction of DHP A (I9L) with H_2O_2	105
Figure S3.6	The asymmetric unit of DHP B (L9I) consisting of a homodimer of protomers A and B. The 9 th position lies along the dimer interface, highlighted in teal.....	106

Figure S3.7	LSQ C α superposition of DHP A (I9L) and DHP B (L9I), focusing on the distal side of the heme cavity as well as the region containing the residue at position 9.....	107
Figure 4.1	Superposition of substrate binding sites within the distal pocket of DHP as viewed from the heme γ edge: TBP (yellow, PDB 4FH7), 4-NP (purple, PDB 5CHQ), 4-BP (green, PDB 3LB2), and both internal (TCP _{interior}) and external (TCP _{exterior}) conformations of TCP (cyan, PDB 4KN3).....	120
Figure 4.2	UV-visible spectra of ferric (red) and oxyferrous (black) DHP B (F21W) in 100 mM KP _i (pH 7).....	125
Figure 4.3	ESI-MS total ion chromatograms obtained for the reaction product 5-Br-2-oxindole (A: H ₂ ¹⁸ O, H ₂ ¹⁶ O ₂ ; B: H ₂ ¹⁶ O, H ₂ ¹⁸ O ₂). Reaction conditions: [5-Br-indole] = [H ₂ O ₂] = 500 μ M, [enzyme] = 10 μ M, 100 mM KP _i (pH 7), 25 $^{\circ}$ C.....	128
Figure 4.4	Kinetic data obtained by optical spectroscopy for the reaction of DHP B (F21W) with H ₂ O ₂	130
Figure 4.5	A) DHP B (F21W) (silver) C α superposition with WT DHP B (cyan; PDB 3IXF), highlighting the F21/W21 residues. Only one conformation for F21 is shown for clarity. B) Distal pocket of the DHP B (F21W) mutant, as viewed from the heme β edge. There are two water molecules in the distal pocket, forming a H-bonding network with W21, T56, Y38, and the heme propionate arms. All distances are given in Å	131
Figure 4.6	DHP B (F21W) mutant distal pocket superposition with TCP [TCP _{interior} (PDB 4KMV) and TCP _{exterior} (PDB 4KMW)] and 4-NP (PDB 5CHQ) substrates.....	137
Figure S4.7	Optical difference spectra of 5-Br-indole (10-130 eq.) binding to 10 μ M DHP B (F21W) in 10% MeOH/100 mM KP _i (v/v) at pH 7; <i>inset</i> – corresponding titration curve.....	140
Figure S4.8	Distal pocket of A) WT DHP B (PDB 3IXF ¹⁸), B) DHP B (F21W) (PDB 5VLX ²) and C) superposition of WT DHP B and DHP B (F21W).....	140

Figure 5.1	Representative ferric DHP B crystals of sufficient size for obtaining neutron diffraction data. A) Perdeuterated DHP B, volume $\sim 0.2 \text{ mm}^3$. B) Protiated DHP B crystal, volume $\sim 2.0 \text{ mm}^3$. C) Representative quasi-Laue diffraction pattern of ferric DHP B. The image was obtained from 20 hour neutron exposure.....	154
Figure 5.2	Room temperature X-ray structure of the perdeuterated DHP B protomer A heme cavity, viewed from the heme β side. $F_0 - F_C$ electron density maps are displayed in green and scaled to 3σ . Blue depicts the $2F_0 - F_C$ maps. A) $2F_0 - F_C$ maps scaled to 2σ . B) $2F_0 - F_C$ maps scaled to 1σ	155
Figure 5.3	Residues Ile 6 and Phe 123 from DHP B, shown modeled into blue nuclear and red electron density maps. Panel A) Nuclear density maps of perdeuterated residues, highlighting the visibility of deuterium atoms (shown in red) at a resolution of 2.05 \AA . Panel B) Electron density maps illustrating the absence of hydrogen atoms, even at a higher resolution, 1.81 \AA	157
Figure 5.4	Neutron structure of ferric DHP B, presenting nomenclature and atomic distances. A) Protomer A ribbon structure, with emphasis placed on the distal pocket environment. B) Proximal environment of protomer A. C) Bis-his heme ligation present in protomer B.....	159
Figure 5.5	Superposition (with atomic distances) of 2,4-dichlorophenol (DCP) β binding site and distal waters found in the neutron ferric DHP B structure.....	160
Figure 5.6	As viewed from the β edge, panels A and B provide atomic distances for 4-NP and 4-NC, respectively. Panels C and D present the distal superposition of 4-NP (5CHQ, green), 4-NC (5CHR, silver) and 4BP (3LB2, purple) structures.....	166
Figure 5.7	Fitting of substrates A) 4NP and B) 4NC into their respective $2mF_0 - DF_c$ electron density maps, contoured to 1σ	167
Figure 5.8	Superposition of substrate binding sites within the distal pocket: 4-NP (green), 4-NC (silver), TBP (pink) and both internal and external conformations of TCP (cyan). Panel A is viewed from the heme γ edge while panel B is viewed from the heme β edge.....	169

Figure 5.9	Distal cavity of Mn-DHP B protomer B. As shown, there exists two water molecules at the entrance of the cavity, participating in a hydrogen-bonding network with T56, Y38, and propionate arm A. The presence of distal waters in this orientation has only been observed previously in the DHP B (F21W) mutant.....	174
Figure 5.10	LSQ C α superposition of WT DHP B (3IXF, ¹⁷ silver) and Mn-DHP B (teal) protomer A. Emphasis is placed on the heme cavity, where it is clearly shown that the porphyrins occupy identical orientations.....	175
Figure 5.11	Diagram portraying the dihedral angle that dictates the hyperfine splitting of the tyrosyl radical signal by the two methylene hydrogens, H β ₁ and H β ₂	177
Figure 5.12	The locations of the 4 tyrosine residues (Y16, Y28, Y38, and Y107) in DHP B. The tyrosine \rightarrow phenylalanine mutations at positions 28 and 38 are indicated, with Phe shown in silver.....	180

LIST OF SCHEMES

Scheme 1.1	Reversible oxygen transport as carried out by globins.....	5
Scheme 1.2	Oxidative dehalogenation of trihalophenols yielding their corresponding quinone products as catalyzed by DHP via a peroxidase mechanism.....	5
Scheme 1.3	Oxidation of monohaloindoles to form either 2-oxindole or 3-oxindole products. The oxygen atom inserted in the product is derived from H ₂ O ₂ as necessitated by a peroxygenase pathway.....	6
Scheme 1.4	Oxidation of 2,3-dimethylindole to form either 2,3-dimethyl-3 <i>H</i> -indol-3-ol or <i>N</i> -(2-acetylphenyl)acetamide products. The oxygen atom inserted in the product is derived from O ₂ as necessitated by an oxygenase pathway.....	6
Scheme 1.5	Oxidation of 5-Br-3-oxindole to form 5,5'-Br ₂ -indigo. The product oxidation, characterized by a lack of atom incorporation and dependence on O ₂ , is representative of an oxidase pathway.....	6
Scheme 2.1	Proposed oxidation pathways of 2,4-dichlorophenol in the presence of DHP.....	37
Scheme 2.2	Proposed oxidation pathway of 2,4-dibromophenol in the presence of DHP B.....	40
Scheme 2.3	Proposed 2,4-Dichlorophenol Peroxidase Cycle for Dehaloperoxidase B.....	57

LIST OF ABBREVIATIONS

2,4-DBP	2,4-dibromophenol
2,4-DCP	2,4-dichlorophenol
2,4-DXP	2,4-dihalophenol
4BP	4-bromophenol
4CP	4-chlorophenol
4FP	4-fluorophenol
4IP	4-iodophenol
4XP	4-halophenol
4NC	4-nitrocatechol
4NP	4-nitrophenol
5BI	5-bromoindole
5XI	5-haloindole
7BI	7-bromoindole
CcP	Cytochrome c peroxidase
COOT	Crystallographic object-oriented toolkit
DHP	Dehaloperoxidase
DHP A	Dehaloperoxidase A
DHP B	Dehaloperoxidase B
DMSO	Dimethyl sulfoxide
EPR	Electron paramagnetic resonance
FPLC	Fast protein liquid chromatography
G	Glycine
I	Isoleucine
IPTG	isopropyl- β -D-1-thiogalactopyranoside
ITC	Isothermal calorimetry
K	Lysine
K _d	Dissociation constant
L	Leucine
LB	Lysogeny broth
LSQ	Least squares quadratic
Mb	Myoglobin
ML	Mother liquor
MPEG	Monomethyl polyethylene glycol
MWCO	Molecular weight cut off
N	Asparagine
NMR	Nuclear magnetic resonance
PDB	Protein data bank
PEG	Polyethylene glycol
PHENIX	Python-based hierarchial environment for integrated xtallography
PMSF	phenylmethylsulfonyl fluoride

R	Arginine
r.m.s.d.	Root mean square deviation
RCSB	Research Collaboratory for Structural Bioinformatics
rR	Resonance Raman
Rz	Reinheitzahl
S	Serine
SDS-PAGE	Sodium dodecyl sulfate polyacrylamide gel electrophoresis
SER-CAT	Southeast regional collaborative access team
SP-FF	Sepharose fast flow
STI	soybean trypsin inhibitor
SWMb	Sperm whale myoglobin
TBP	2,4,6-tribromophenol
TCP	2,4,6-trichlorophenol
TFP	2,4,6-trifluorophenol
TIP	2,4,6-triiodophenol
TPCK	N- <i>p</i> -tosyl-L-phenylalanine chloromethyl ketone
TRSSA	Tyrosyl radical spectra simulation algorithm
TXP	2,4,6-halophenol
V _m	Matthew's coefficient
WT	Wild-type
Y	Tyrosine

Chapter 1

X-ray Crystallographic and Spectroscopic Analysis of Dehaloperoxidase (DHP) on Deposited Structures

1.1 Introduction

The terebellid polychaete *Amphitrite ornata* possesses a unique defense mechanism that has surfaced in response to toxins found in benthic ecosystems. Coinhabitants, such as *Notomastus lobatus* and *Saccoglossus kowalevskii*, biosynthesize brominated aromatic compounds, which in turn deters predators and lowers competition for resources. *A. ornata*, as shown in Figure 1.1, obtains its reddish color due to the presence of its hemoglobin, termed dehaloperoxidase (DHP). As a globin, the primary function of DHP is oxygen transport, but interestingly this enzyme is also capable of the chemical detoxification of these halogenated compounds through multiple mechanistic pathways. As such, DHP is the first globin to possess biologically relevant peroxidase and peroxygenase activities, along with recently discovered oxygenase and oxidase capabilities. Understanding how one globin can perform five different activities could lead to insight on enzymatic structure-function relationships.



Figure 1.1. Image of *Amphitrite ornata*, from which DHP was discovered.

DHP was first discovered for its oxygen-transport capability in 1977 by Bonaventura *et al.*¹ Observance of its peroxidase activity led to the rediscovery of DHP in 1996 by Lovell *et al.*² DHP exists as two isoenzymes, DHP A and DHP B, with only 5 amino acids differentiating the two. The structural and reactivity differences between the two isoenzymes will be further elaborated in Chapter 3. It was discovered in 2001 that two unique genes are responsible for DHP A and DHP B, *dhpA* (GenBank accession number AF284381) and *dhpB* (AF285090), respectively.³ Crystallographic studies revealed that the enzyme possessed a traditional globin fold despite exhibiting a very low sequence homology with other globins.⁴ In our lab, peroxygenase, oxygenase and oxidase activities for DHP have been characterized, adding to the scope of this enzyme's functionality.⁵ Given the multiple possible activities within this single protein, the question thus arises as to what parameters dictate which enzymatic function is observed. Could this coexistence of 5 functions residing at a single active site be understood through structural analysis?

1.2 Global Structural Analysis

DHP is classified as a globin due to its canonical globin helical fold. Structurally, DHP has the appearance of a traditional oxygen transport protein. When compared with the prototypical globin, myoglobin (Mb), the overall folds are very similar (Figure 1.2, panels A & B). The largest difference lies in the proximal region. The proximal histidine of DHP occupies position 89, while in Mb the proximal histidine is two residues further toward the C-terminus at position 91. The proximal histidine in Mb is located on helix F, however this perturbation in sequence places DHP's His89 in a loop region between helices F & G. Due to the shifted orientation, the imidazole ring of the distal histidine is rotated 60° in DHP when compared to Mb.⁶

However, structural comparison of DHP to other peroxidases reveals a very low homology (Figure 1.2, B & C). Compared to traditional peroxidases, such as horseradish peroxidase (HRP) or cytochrome *c* peroxidase (CcP), DHP's peroxidase capabilities are diminished. At pH 7.0, DHP B shows a 3 fold decrease in activity while DHP A exhibits activity decrease close to an order of magnitude.^{9,10} However, DHP possesses the highest peroxidase activity of

any known globin.^{2,11} This lower peroxidase activity may be related to the absence of the traditionally conserved distal arginine and proximal aspartate, which are found in many peroxidases to be necessary for optimal catalytic activity.^{12,13} The 60° rotation of the proximal Histidine 89, in comparison with Mb, places the N^ε into a hydrogen-bonding interaction with the carbonyl oxygen on L83. This interaction restores some of the negative charge density on the proximal His in peroxidases, yet absent in globins.¹⁴ For DHP to exhibit a biologically relevant peroxidase activity, yet possess the conserved globin tertiary fold, the structure-function relationship must be examined on a more local view, rather than the global approach.

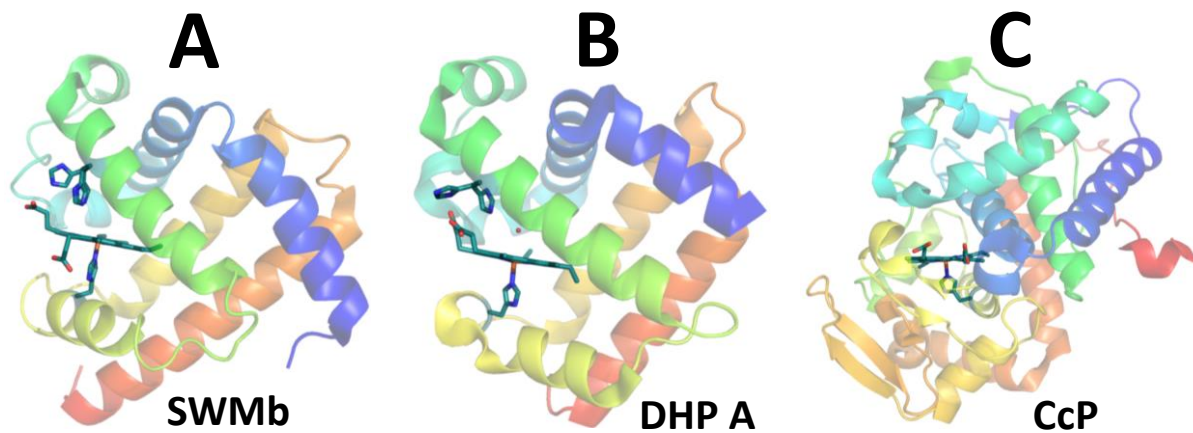


Figure 1.2. X-ray crystal structures of **A**) sperm whale myoglobin (SWMb, PDB accession code 1A6G)⁷, **B**) DHP A (PDB accession code 1EW6)⁴ and **C**) cytochrome *c* peroxidase (CcP, PDB accession code 1ZBY).⁸ It is clearly shown that DHP possesses the conserved globin fold as displayed in Mb.

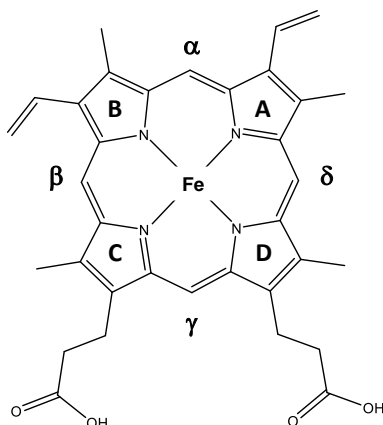


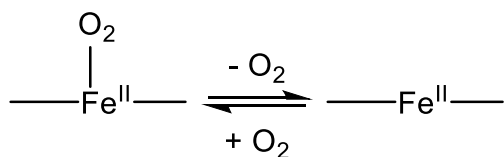
Figure 1.3. Protoporphyrin IX prosthetic group, as found in DHP, Mb and HRP. Pyrrole rings (A-D) and heme edges (α - δ) are labeled in accordance with convention.

The observance of multi-functional enzymes is not a novel concept. However, DHP exhibits functions that traditionally require different iron oxidation states to proceed. Oxygen transport requires a ferrous, Fe^{II} , heme while the peroxidase function requires a ferric, Fe^{III} , heme to initiate the traditional catalytic cycle. DHP has developed a switching mechanism that allows the heme activation for multiple functions to coexist at a single heme center. Protoporphyrin IX, shown in Figure 1.3, is the heme cofactor that is found at DHP's catalytic center, and is a conserved feature in many globins and peroxidases.^{12,15}

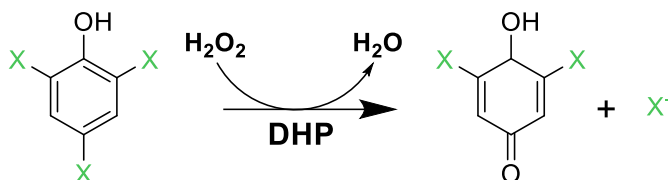
1.3 The Multiple Functions of Dehaloperoxidase

DHP possesses a heme cavity large enough to accommodate halophenols and haloindoles for peroxidase and peroxygenase activity, respectively^{5,16,17}. This expanded heme cavity is unnecessary for performing the globin oxygen transport function. Further insight on the multi-functional nature of DHP may be gained through structural analysis of its heme cavity, especially in regards to the distal histidine at the entrance, internal residue orientation and electronic nature, and in the orientation of the substrate itself. However, to fully understand the structure-function relationships observed and hypothesized, clarification of each function is beneficial.

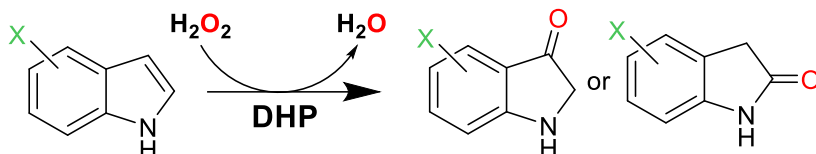
Structurally, the primary function of DHP resides in oxygen transport. Scheme 1.1 illustrates the reversible binding of molecular oxygen with a ferrous heme. Scheme 1.2 provides the overall reaction for the oxidative dehalogenation of 2,4,6-trihalophenols, producing the corresponding 2,4-dihaloquinone product. This reaction proceeds through a peroxidase pathway, resulting with the oxygen atom inserted into the product being derived from water and not from H₂O₂. Scheme 1.3 depicts the oxidation of halogenated indoles to produce either 2-oxindole or 3-oxindole. Peroxygenase activity requires that the oxygen atom inserted must be derived from the hydrogen peroxide co-substrate. Scheme 1.4 illustrates the oxidation of 2,3-dimethylindole. There is no dependence on H₂O₂, as the oxygen atom inserted is derived from molecular oxygen, O₂, as required for oxygenase activity. Oxidase activity is also dependent on O₂, however lacking the atom incorporation into the product, as depicted in the oxidation of 5-Br-3-oxindole to 5,5'-Br₂-indigo in Scheme 1.5. These multiple functions were validated through anaerobic and ¹⁸O isotopic labeling studies.⁵



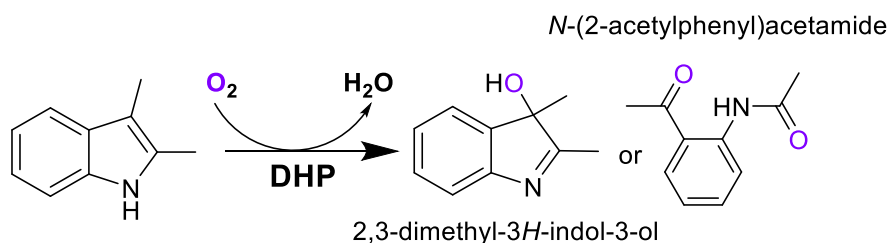
Scheme 1.1. Reversible oxygen transport as carried out by globins.



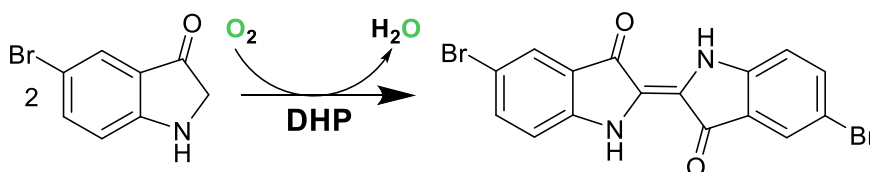
Scheme 1.2. Oxidative dehalogenation of trihalophenols yielding their corresponding quinone products as catalyzed by DHP via a peroxidase mechanism.



Scheme 1.3. Oxidation of monohaloindoles to form either 2-oxindole or 3-oxindole products. The oxygen atom inserted in the product is derived from H_2O_2 as necessitated by a peroxygenase pathway.



Scheme 1.4. Oxidation of 2,3-dimethylindole to form either 2,3-dimethyl-3*H*-indol-3-ol or *N*-(2-acetylphenyl)acetamide products. The oxygen atom inserted in the product is derived from O_2 as necessitated by an oxygenase pathway.



Scheme 1.5. Oxidation of 5-Br-3-oxindole to form 5,5'- Br_2 -indigo. The product oxidation, characterized by a lack of atom incorporation and dependence on O_2 , is representative of an oxidase pathway.

1.4 Brief Overview of Deposited Dehaloperoxidase X-ray Crystallographic Structures

X-ray crystallography has been utilized to obtain structural insight of this multi-functional enzyme in an effort to further probe structure-function relationships. The first crystal structure of DHP (Protein Data Bank accession code 1EW6) was published in 2000 from the Lebioda Lab at the University of South Carolina.⁴ At this time the sequence was unknown, so the closest phylogenetic relative could not be established. Thus, a starting model for molecular replacement

was difficult. DHP was thought to be structurally related to the globin family due to its molecular weight and the presence of the heme. However, myoglobin at first provided a poor model for the experimental electron density.^{4,11} Initial geometric and phase information was obtained by heavy metal derivatization utilizing Hg, complexation with 4-iodophenol, and the anomalous diffraction of the heme Fe. This allowed for the resolution of the heme center and several helical loops adjacent to this area. From this information, the presence of a general globin fold became apparent and a model of myoglobin was utilized to form the molecular envelope of the protein. Although this structure was not determined fully *de novo*, the initial steps were performed without preconceived notions and relied on the experimental data. This initial DHP structure refined to a resolution of 1.78 Å with R_{work} and R_{free} values of 20.7% and 22.5%, respectively. This crystal, and every DHP structure since, belonged to space group $P2_12_12_1$, resulting in all cell angles of 90°. Unit cell lengths were found to be $a=68.50$ Å, $b=68.40$ Å, and $c=61.00$ Å, values which have been similarly determined for all subsequently refined structures of DHP.^{4,11}

Currently, there are 40 crystal structures released in the Protein Data Bank (PDB) for DHP and 12 deposited structures awaiting release upon publication (HPUB), as provided below in Table 1.1.¹⁸ Of the ~50 total structures, 34 are of isoenzyme A and the others are of the B isoenzyme. The initial DHP A structure was deposited in 2000, followed by only 4 additional structure depositions by the year 2010. However, in the past 7 years, 35 more structures were released, with 12 in 2013 alone. Every single structure since 2010 is either a mutant variant of DHP or complexed with a ligand, either as a substrate, inhibitor, or with direct ligation to the heme Fe.¹⁸ Thus, it is clear that recent crystallographic studies have been driven by the desire to explain mechanistic and functional details surrounding DHP's heme center.

There exists a variety of ligands that have been crystallized in complex with DHP, each providing additional insight into the nature of the enzyme and its active site. CO and CN^- are adducts that occupy the 6th coordination site of the heme in the ferrous and ferric oxidation states, respectively.¹⁹ The interaction ofazole pollutants with DHP B were investigated to enhance knowledge of their toxicity on a molecular level.²⁰

Table 1.1. Crystal structures of DHP deposited into the PDB, arranged from most recent to initial structure.¹⁸

PDB Accession No.	Isoenzyme	Ligand	Mutant	Date of Deposition
5VTS	B		Y28F	HPUB
5VTT	B		Y38F	HPUB
5V5Q	B		L9I	HPUB
5V5R	A		I9L	HPUB
5VLX	B		F21W	HPUB
5V5J	B		Oxyferrous form	HPUB
5WMY	B	DBP		HPUB
5WMZ	B	DCP		HPUB
5WN6	B	DCP		HPUB
6AOE	B	4CP		HPUB
6AOF	B	4BP		HPUB
5LKV	B	imidazole		8/17
5LLZ	B	benzotriazole		8/17
5LK9	B	indazole		8/17
5K1L	B	benzimidazole		6/17
5CHQ	B	4NP		4/16
5CHR	B	4NC		4/16
4JYQ	A	CO		4/14
4KJT	A		L100F	2/14
4JAC	A		T56S	11/13
4GZG	A	CO		9/13
4KMV	A	TCP	L100F	9/13
4KMW	A	TCP	Y34N	9/13
4KN3	A	TCP	Y34N/S91G	9/13
4HSW	A		L100F	5/13
4HSX	A	4BP	L100F	5/13
4FH6	A	TBP		3/13
4FH7	A	TBP		3/13
4ILZ	A	TBP		3/13
4DWT	A	CO		2/13
4DWU	A	CO		2/13
3OK5	A	4BP	H55D	9/11
3ORD	A	Xe		9/11
3OJ1	A		H55D	8/11
3O7N	A		V59W	7/11
3MOU	A	Xe		4/11
3MYM	A		M86E	4/11
3LB1	A	4IP		11/10

Table 1.1 continued

3LB2	A	4BP		11/10
3LB3	A	4CP		11/10
3LB4	A	4FP		11/10
3K3U	A		V59W	11/10
3KUN	A	CN		6/10
3KUO	A	CN		6/10
3IXF	B		B isoenzyme	5/10
3DR9	A		Deoxy form	1/09
2QFK	A		Ferric form	7/08
2QFN	A		Oxyferrous form	7/08
1EWA	A	4IP		5/00
1EW6	A			5/00

Ligand abbreviations: DBP, 2,4-dibromophenol; DCP, 2,4-dichlorophenol; TCP, 2,4,6-trichlorophenol; TBP, 2,4,6-tribromophenol; 4IP, 4-iodophenol; 4BP, 4-bromophenol; 4CP, 4-chlorophenol; 4FP, 4-fluorophenol; 4NP, 4-nitrophenol; 4NC, 4-nitrocatechol.

Xe was observed bound to DHP at 2 locations, as shown in Figure 1.4. Xe binding sites are representative of spacious areas in the enzyme, most notably in the heme cavity. These Xe binding sites aid in the discovery of the distal and proximal landscape by noting vacancies in the enzymatic volume.²¹ Surrounded by internal hydrophobic residues (F35, F24, F21, L100, F60 and V59) resides the Xe1 binding site, located 4.8 Å above the heme Fe in the heme distal cavity. The other Xe binding site, Xe2, was observed external to the pocket, located 10 Å from the heme Fe. This external Xe2 binding site is located in the vicinity of residues L62, R69, D79, T82 and L83. Xe occupancies varied between the Xe1 and Xe2 sites as well as amongst subunits of DHP. For subunit A, the Xe1 binding site was characterized by 50% occupancy, while the Xe2 site possessed 10%. However, in subunit B the Xe1 occupancy drops to 20% while the Xe2 presence increases to 30%.

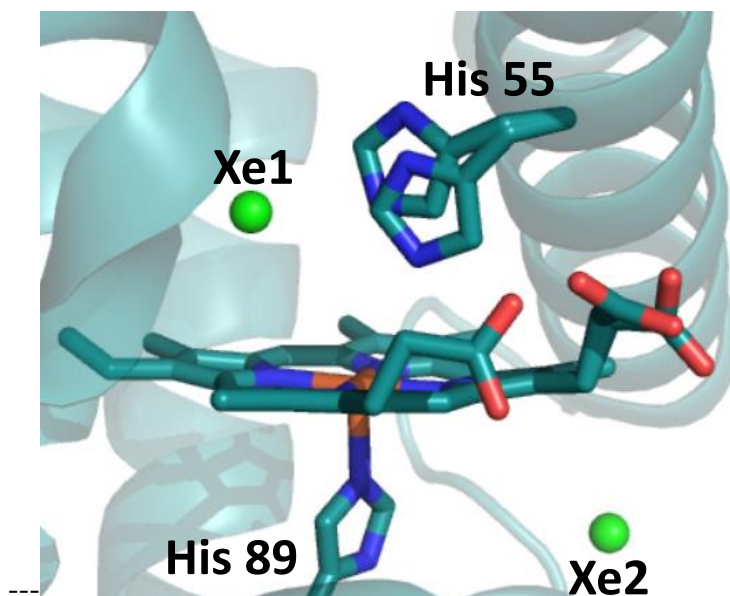


Figure 1.4. Xe crystallographic binding sites observed in DHP.

Single amino acid variants of DHP A have been crystallized to determine the structural differences that correlate to kinetic variations in the peroxidase activity, as shown in Figure 1.5. The H55D mutant examined the role of the distal histidine, His55, in the activation and regulation of peroxidase activity given this residue's role as a general acid-base that facilitates O-O bond cleavage of bound H_2O_2 (*vide infra*). The T56S mutation was utilized to examine neighboring amino acid dependency on the flexibility and function of the distal histidine 55.²² Mutations L100F and V59W investigated the role of residues inside the distal pocket and their effect on substrate and inhibitor binding.²³ Mutations M86E and M86D introduced a proximal charge relay that is conserved in peroxidases but absent in globins. This latter study strove to address the structural difference but functional similarities of DHP to other peroxidases.¹⁴

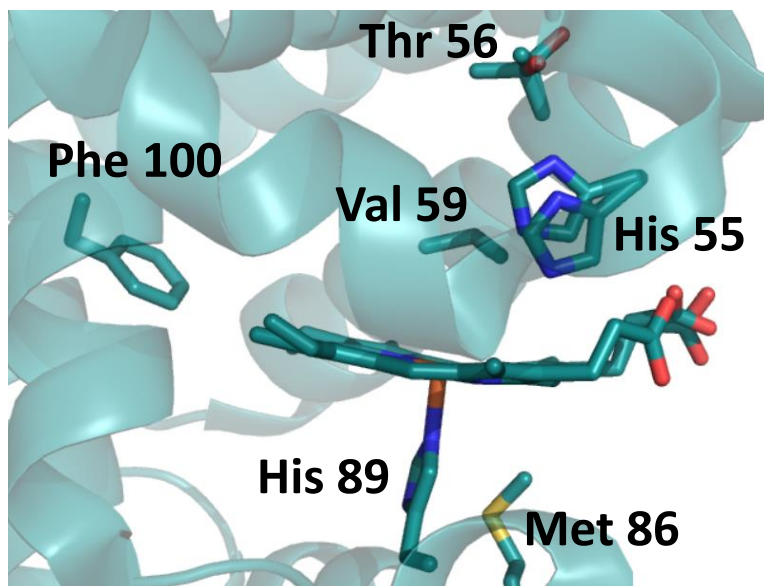


Figure 1.5. Sites of single amino acid mutations of DHP A, utilized previously for mechanistic and reactivity investigations.

1.5 Unusual Flexibility of the Distal Histidine: Structural and Spectroscopic Correlations

X-ray crystallography has provided direct evidence supporting the spectroscopic assignment of enzymatic states, ligand occupation, and geometric orientation. Distal histidines are conserved features throughout both globin and peroxidase families, and are shown to play a crucial role in oxygen stabilization and enzymatic activity, respectively²⁴⁻²⁸. In globins, the distal histidine has been shown to reside in a closed, or internal, orientation when molecular oxygen is bound to the heme Fe, helping stabilize the bound ligand. In the absence of O₂, the distal histidine has been shown to reside in an open, or exposed, orientation. The environmental pH also is a factor in histidine orientation, with the open orientation dominating at lower pH. The protonation of histidine's imidazole ring has been suggested as the key factor regarding this pH-dependent distal histidine orientation.

Regarding peroxidase activity, the distal histidine promotes peroxide activation by serving as an acid and base for the cleavage of the peroxide O-O bond, according to the Poulos-Kraut push-pull peroxidase mechanism.²⁹ The closed position is of adequate distance to promote

peroxide activation, while the open position is incapable of involvement due to the much greater distance. The heme Fe-distal histidine N^δ distance for DHP A is 5.4 Å,³⁰ which lies intermediate between that for globins and peroxidases at 4.1 – 4.6 Å^{7,15,31} and 5.5 – 6.0 Å,^{12,13} respectively. This intermediate distance between two different classes of proteins may help explain the globin and peroxidase functional coexistence in DHP, but is not the sole deciding factor.

The flexibility of the distal histidine has been well documented in globins, however DHP exhibits this flexibility in a manner that is dictated by a number of different factors. The orientation of the distal histidine has been correlated to ligand occupation in the distal pocket. Smaller ligands, such as molecular oxygen and water, are stabilized by the closed orientation of the heme, whereas larger ligands, such as mono-, di- and trihalophenols, sterically push the distal histidine to the open orientation^{17,21,27,32,33}. Through this correlation, the coordination state of the heme Fe can be directly related to the histidine conformation via spectroscopic means. In particular, resonance Raman (rR) spectroscopy possesses the ability to assess the coordination and spin states of the heme Fe. High frequency core marker bands for ν_2 , ν_3 , and ν_{10} denote the presence of the ferric heme iron in 5-coordinated high spin (5cHS) and 6-coordinated high spin (6cHS) populations^{9,14,34}. The presence of ferric 5cHS heme is observed at 1494 cm⁻¹ (ν_3), 1568 cm⁻¹ (ν_2) and 1632 cm⁻¹ (ν_{10}), while ferric 6cHS heme is observed at 1481 cm⁻¹ (ν_3), 1562 cm⁻¹ (ν_2), and 1611 cm⁻¹ (ν_{10}) (Figure 1.6A). Through analysis of these vibrational transitions, the coordination number of the Fe is determined. X-ray crystallographic structures have been obtained which further support the rR assignment of these bands^{14,20,22,34}.

An equilibrium between 5cHS and 6cHS heme species exists in the metaquo state of DHP. Figure 1.6 shows the correlation between ferric DHP X-ray crystal structures and rR spectroscopy, both of which were obtained at room temperature. For each core marker band, ν_2 , ν_3 , and ν_{10} , there are populations represented by both 5cHS and 6cHS assigned frequencies. The existence of this equilibrium is further validated by the multiple distal histidine conformations obtained crystallographically^{11,21,33,35,36}.

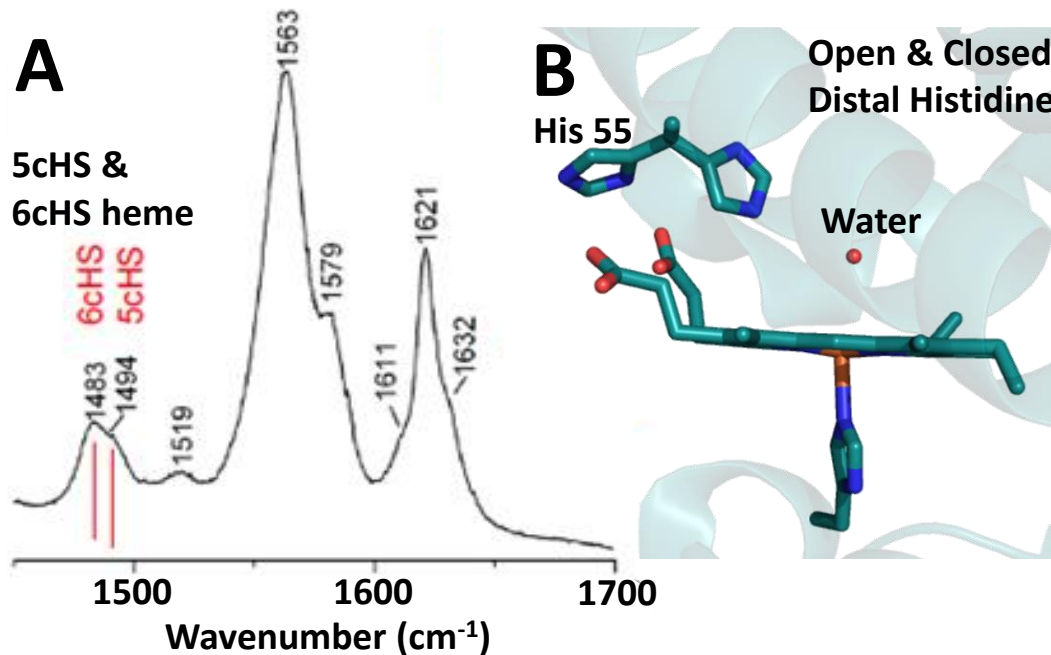


Figure 1.6. A) Room temperature resonance Raman spectrum of WT DHP A. Core markers for 6cHS and 5cHS hemes are annotated for ν_3 .³⁷ B) Room temperature crystal structure (1EW6) emphasizing i) the water that occupies the Fe 6th coordination site, and ii) distal histidine His55 in an equilibrium between the open (solvent exposed) and closed (internal) conformations.⁴

1.6 Inhibitor Binding Site Characterization

The inhibitor binding site has been well characterized within the distal cavity^{11,33,38–40}. Resonance Raman spectroscopy has shown the equilibrium shift toward a more dominant 5-coordinate high spin Fe species in the presence of *para*-halophenol inhibitors. Analysis of the core markers ν_3 , ν_2 , and ν_{10} clearly shows a population shift towards a 5cHS heme upon the introduction of the *para*-halogenated phenol (Figure 1.7A). Inhibitors 4IP, 4BP, 4CP, and 4FP have all been shown crystallographically to be located above the heme Fe at a distance too great for ligation, in an orientation that is nearly perpendicular to the heme plane.^{4,37} The halogen is directed toward the Xe1 binding site, with the phenolic O hydrogen toward the cavity entrance, within hydrogen bonding distance to Tyr38. Histidine 55 resides in the open, or solvent exposed, orientation in each structure. The ligand's orientation inside the heme

cavity sterically prohibits the occupation of a 6th ligand for Fe, which supports the rR spectral analysis.

As the size of the halogen increases, inhibitor binding affinity increases as does the depth of the inhibitor within the distal cavity.³⁷ *Para*-iodophenol possesses the strongest binding affinity and largest 5-coordinated population shift, and also coincides with the deepest penetration in the Xe1 binding site among the halogenated inhibitors analyzed. Panel B of Figure 1.7 provides the superposition of the 4 inhibitor crystallographic binding sites (3LB1), 4BP (6AOF), 4CP (6AO3) and 4FP (3LB4), and clearly shows the orientation and depth trend of the series.^{21,37} The 4IP and 4FP structures are complexed with DHP A with the 4BP and 4CP are in complex with DHP B. No isoenzyme effect is observed for the binding sites of *p*-halophenols.

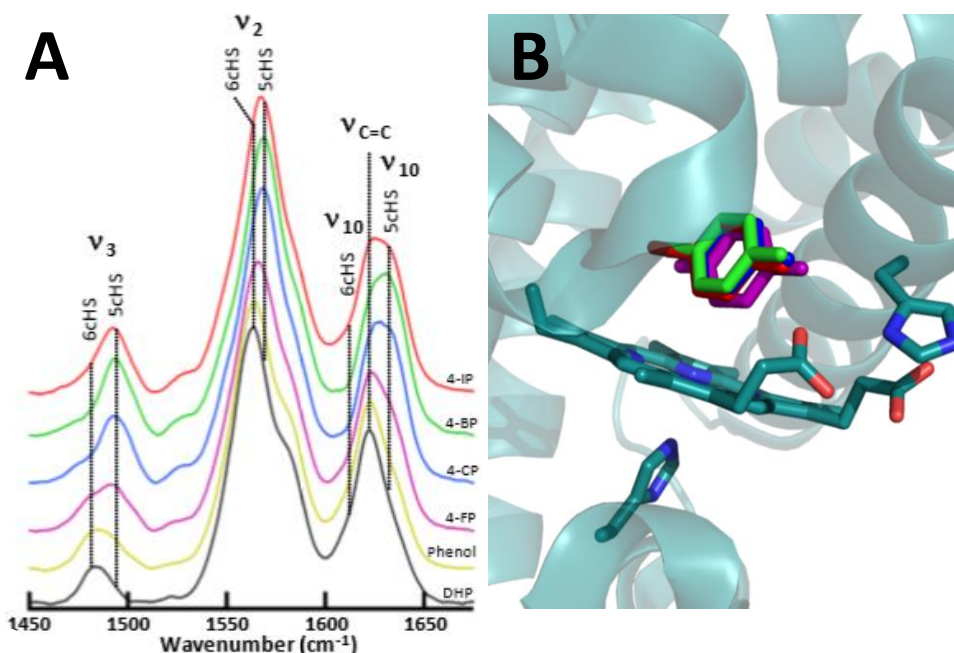


Figure 1.7. A) Resonance Raman spectra of WT DHP A in the presence of the indicated inhibitor. [DHP A] = 100 μ M; [4IP] = 1 mM; [4BP], [4CP] and [4FP] = 8 mM.³⁷ B) Superposition of the *para*-halogenated phenolic inhibitor structures depicting orientation within the distal pocket; 4IP (red, 3LB1), 4BP (green, 6AOF), 4CP (blue, 6AOE) and 4FP (purple, 3LB4).²¹

1.7 Peroxidase Substrate Binding Site(s) Characterization

Substrate binding is a key question that, if solved, could shed tremendous light onto numerous mechanistic questions. Figure 1.8A provides the rR spectra of WT DHP B with the traditional peroxidase substrates, 2,4,6-trihalogenated phenols, TXP (X = I, Br, Cl or F). Analysis of heme core marker bands does show a Fe coordination population shift that is halogen-dependent. However, the population shift is not nearly as pronounced as the monohalophenols, which suggests different binding sites between substrate and inhibitor. The smaller population shift in the substrate spectra suggests the binding site likely exists further from the heme center. When comparing the rR spectra of inhibitors with their corresponding halogenated substrates, in combination with NMR data, an external substrate binding site is realized as a possibility.⁴⁰

The DHP B – TBP rR spectrum closely resembles the WT DHP B trace with a very slight perturbation. The addition of TCP to DHP B increases the 5cHS heme population slightly, whereas the addition of TFP greatly shifts the equilibrium toward the 6cHS heme species, most notably for ν_3 and ν_2 for both substrates. The TFP spectral shifts may be attributed to the smaller size of fluorine that prevents it from binding in the same manner as TBP and TCP. The possibility of an external substrate binding site is again suggested in the TFP spectra. External binding is postulated to enforce an allosteric effect on the enzyme, forcing the distal histidine into the closed position, thus increasing the 6cHS Fe population by stabilizing the distal ligand.^{24, 26} Another consideration is that TFP might ligate to the heme Fe itself, effectively increasing the 6cHS population by becoming the 6th ligand. Crystallographic structural analysis, if and when it is obtained, will help resolve the TFP binding site enigma. The substrate binding affinity shows the same trend as the inhibitors, where the larger halogen results in the stronger binding.²⁵ However, TCP does show a larger 5cHS heme population than TBP, which could suggest different binding modes or provide further corroboration for the external binding site.

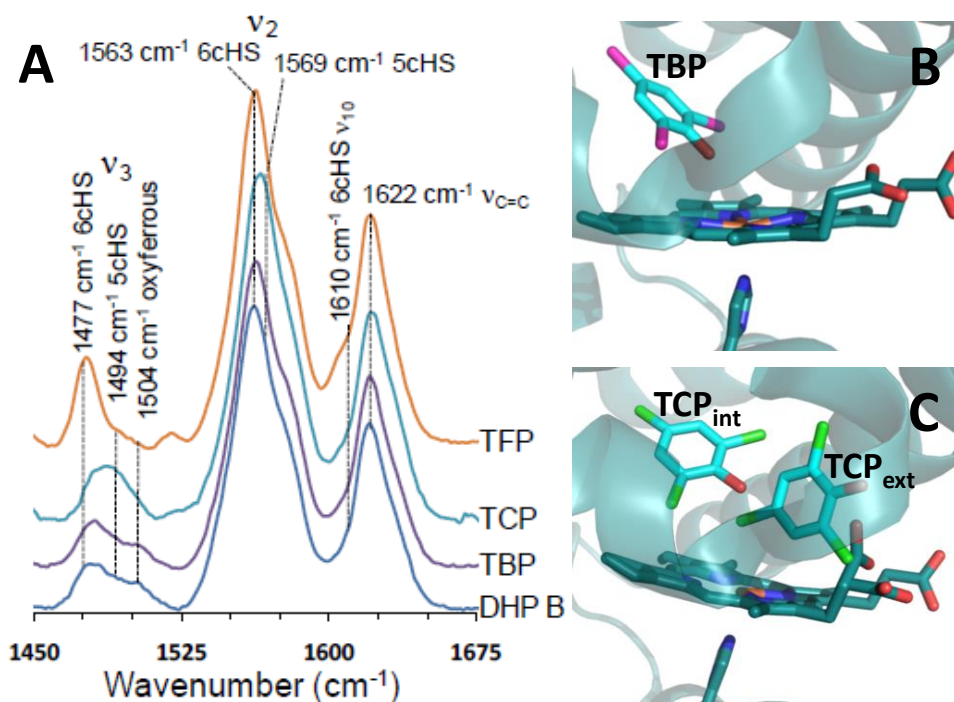


Figure 1.8. A) Resonance Raman core size marker bands of WT DHP B (100 μM), and WT DHP B in the presence of TBP (200 μM), TCP (3 mM) and TFP (4 mM).⁸ B) Crystallographic binding site of TBP (4FH6).¹⁶ C) Internal and external binding sites of TCP in the DHP A (Y34N/S91G) mutant (4KN3).¹⁷ Sterically, it is shown that both TCP binding sites cannot be simultaneously occupied.

The DHP B – TBP rR spectrum closely resembles the WT DHP B trace with a very slight perturbation. The addition of TCP to DHP B increases the 5cHS heme population slightly, whereas the addition of TFP greatly shifts the equilibrium toward the 6cHS heme species, most notably for ν_3 and ν_2 for both substrates. The TFP spectral shifts may be attributed to the smaller size of fluorine that prevents it from binding in the same manner as TBP and TCP. The possibility of an external substrate binding site is again suggested in the TFP spectra. External binding is postulated to enforce an allosteric effect on the enzyme, forcing the distal histidine into the closed position, thus increasing the 6cHS Fe population by stabilizing the distal ligand.^{24, 26} Another consideration is that TFP might ligate to the heme Fe itself, effectively increasing the 6cHS population by becoming the 6th ligand. Crystallographic structural

analysis, if and when it is obtained, will help resolve the TFP binding site enigma. The substrate binding affinity shows the same trend as the inhibitors, where the larger halogen results in the stronger binding.²⁵ However, TCP does show a larger 5cHS heme population than TBP, which could suggest different binding modes or provide further corroboration for the external binding site.

In 2013, binding locations of the traditional DHP peroxidase substrate, 2,4,6-trihalogenated phenols, were crystallographically identified. Notably, thirteen years passed between the first crystal structure of DHP (1EW6, 2000)⁴ and the first peroxidase substrate bound structure (4FH6, 2013).¹⁷ The low aqueous solubility of TXP has been one of the reasons attributed to this difficulty, which also helps explain why the TBP occupancy is only 10% in this structure. The DHP A – TBP structure was obtained from the wild type protein, while the DHP A – TCP structures are all of mutants. Substrate solubility increases with the introduction of organic solvents, and both structures were obtained by soaking crystals in substrate enhanced precipitation solutions. Figure 1.8B provides the binding site of TBP, while Figure 1.8C shows the dual binding sites of TCP (TCP_{int} & TCP_{ext}), all of which were complexed with DHP A variants.

Both TCP and TBP have been resolved in the distal pocket, with slightly different results. Two different binding sites for TCP and one binding site for TBP have been observed. Both TCP_{int} and TBP have been observed in an internal binding site near the α -edge of the heme, although the latter in low occupancy of 10%.^{27, 28} The problem of low occupancy is mainly attributed to the low solubility of TBP. In this internal binding site the substrate's phenolic oxygen is located 3.3 Å and 3.7 Å to the heme Fe, for TCP_{int} and TBP, respectively. There are steric considerations when envisioning substrate binding congruent with successful hydrogen peroxide binding and resultant catalytic activation. For both TCP_{int} and TBP structures, the *para*-halogen is directed towards the Xe1 binding site, while the phenolic oxygen is positioned toward the Fe.

TCP_{ext} was also observed in a unique binding site close to the γ -edge of the heme.²⁸ In this orientation, the *para*-chlorine is directed toward the Fe, while the phenolic oxygen is directed

toward the cavity entrance, within hydrogen bonding distances with Tyr38 and the heme propionate arm D. This second binding site is very similar in orientation and geometry to the inhibitor site, and therefore might perturb the Fe coordination number accordingly. The increased 5cHS heme population in the DHP B – TCP rR spectrum may also be attributed to this TCP_{ext} binding site. Both sites have been speculated as the productive substrate binding site, while also speculated as inhibition sites. The question has yet to be fully resolved, and is still under debate.

Table 1.2. Distances (Å) given for the heme Fe and the halogen and alcohol moieties of the inhibitors (4XP)³³ and the substrates (TXP).^{16,17}

Ligand	PDB accession code	Fe-X dist (Å) (4XP)	Fe-OH dist (Å) (4XP)	Fe-OH dist internal (Å) (TXP)	Fe-4X dist external (Å) (TXP)
4IP	3LB1	5.1	6.4		
4BP	6AOF	5.0	6.7		
4CP	6AOE	4.9	6.7		
4FP	3LB4	4.1	6.6		
TBP	4FH6			3.7	
TCP	4KN3			3.3	4.6

Table 1.2 provides the crystallographic atomic distances between the heme Fe and halogen or phenolic O for the 4XP and TXP structures. It can be seen that the inhibitor distances are too large to be included in Fe's coordination sphere, however their orientation above the Fe could sterically prevent the simultaneous binding of a 6th ligand. The peroxidase substrate distances show a slightly different trend. They are still too large to be coordinated with the Fe yet are closer than the inhibitor distances, and they appear to be close enough to be affected by, or cause, electronic disturbances in the heme environment. In addition to TXP substrates, 2,4-dichlorophenol (DCP) and 2,4-dibromophenol (DBP) have been validated as peroxidase

substrates and their crystallographic binding sites have been determined. This is discussed in detail in Chapter 2.

1.8 Peroxygenase Substrate Binding Site(s) Analysis

1.8.1 - Haloindoles: 5-bromoindole and 7-bromoindole. DHP's peroxidase mechanism has been shown to proceed through a radical pathway, which involves radical migration across several tyrosines.^{9,10,41} In regard to this, the peroxidase substrate need only be accessible to the migratory pathway, not necessarily the heme Fe. However, based on the mechanistic specifics of peroxygenase activity, the inserted oxygen must be derived from hydrogen peroxide. This implies that the substrate must bind in close proximity to the heme Fe in order to obtain the bound oxygen that originated from the heterolytic O-O bond cleavage of bound H₂O₂. The acquisition of peroxygenase substrate distances will provide a more thorough examination of local structure-function relationships, and possibly ligand binding contributions.

Spectral and computational data have been collected on the binding of haloindoles.⁵ The rR spectra of DHP – bromoindole complexes with the bromine atom located at different positions on the molecule is provided in Figure 1.9A. Through analysis of heme core marker bands ν_2 , ν_3 , and ν_{10} , it is observed that the 5cHS/6cHS Fe equilibrium is only perturbed when the bromine is located at the 5-position of the indole ring, while the other brominated positional isomers showed no noticeable difference in the rR data. Interestingly, substrate conversion for 5- and 7-bromoindole are statistically equivalent at 48.1% (± 2.3) and 46.1% (± 1.7), respectively.⁵ The similar percent conversions with respect to the different rR spectra could be indicative of two binding sites for bromoindole, with one specific solely for the 5-substituted substrate. The rR spectra of DHP in the presence of 5-haloindoles, spanning the halogen series, is presented in Figure 1.9B. In line with the binding affinities of the inhibitors (4XP)³³ and peroxidase substrates (TXP),⁹ the binding affinity of 5-haloindoles increases with respect to the size of the halogen. It is shown that 5-iodoindole effects the most pronounced spectral perturbation, yet 5-bromoindole exhibited the greatest substrate conversion.

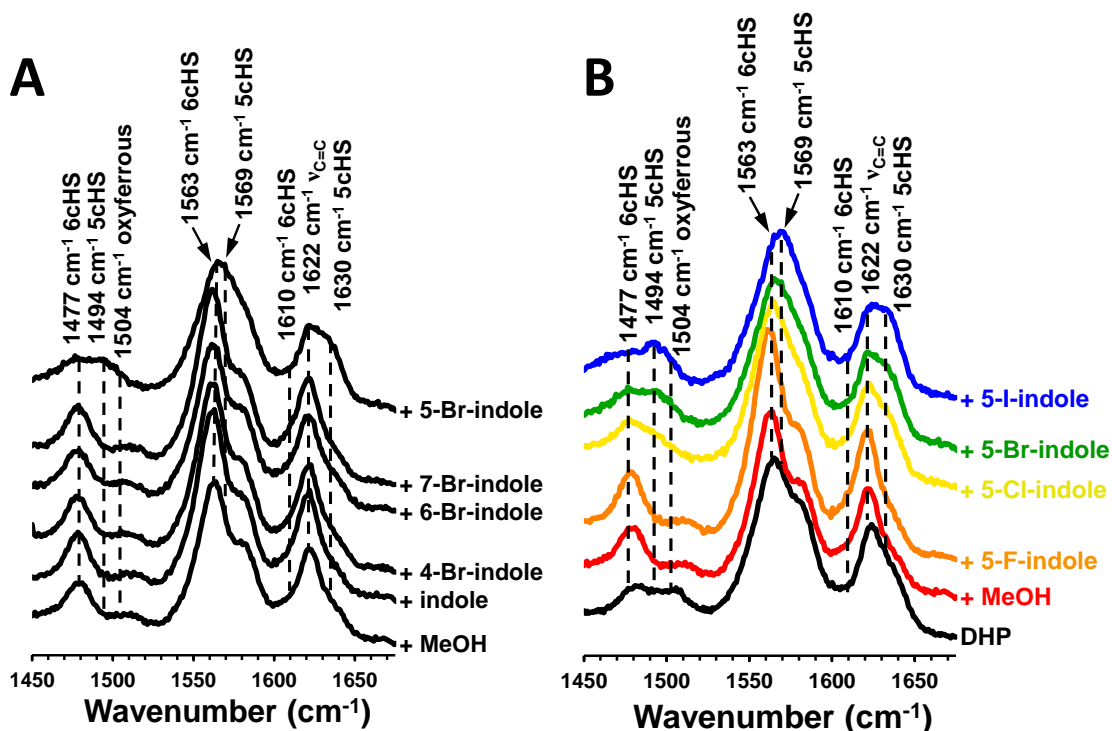


Figure 1.9. Resonance Raman spectra of DHP B in solution with **A)** bromine-substituted indoles at different positions and **B)** 5-haloindoles of different halogens. [DHP] = 50 μ M, [5-haloindole] = 500 μ M.⁵

The geometry optimized calculated models of 5- and 7-bromoindole binding in the distal pocket are provided in Figure 1.10, panels A and B, respectively. Based on the similarities in the rR spectral data, the indoles were placed into crystallographic ligand binding sites to obtain the starting models. Since the presence of neither TBP nor 7BI yields substantial effects on the DHP rR spectral data, TBP from the crystal structure 4FH6¹⁶ was replaced with 7BI to create the starting model for the MD calculations. Likewise, with respect to their similar perturbation of the DHP rR spectra, the 5BI starting model was obtained by replacing 4BP from the crystal structure 3LB2.³³

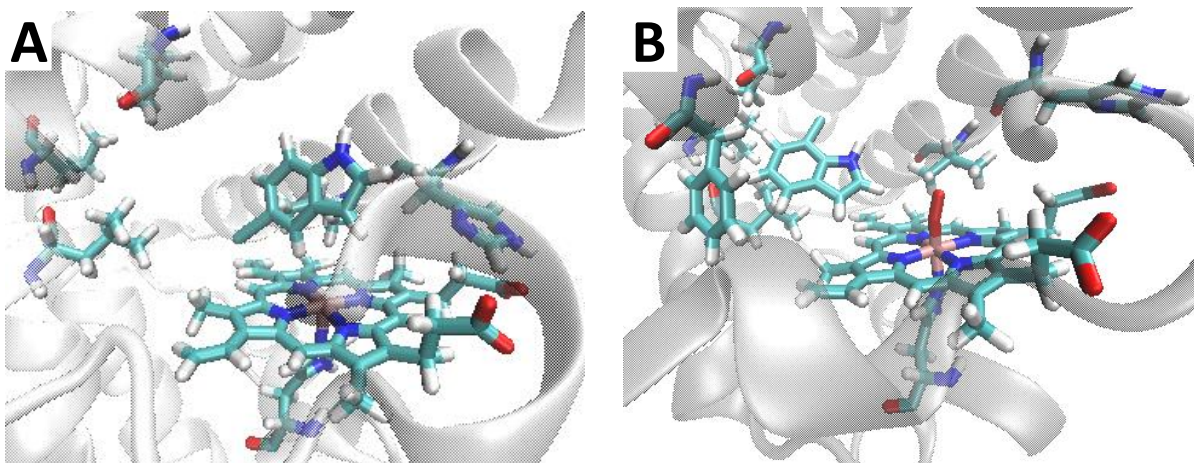


Figure 1.10. Geometry optimized structure for **A)** 5-bromoindole and **B)** 7-bromoindole.⁵

1.8.2 – 4-nitrophenol. The oxidation of 4-nitrophenol (4NP) as catalyzed by DHP has recently been characterized to proceed via a peroxygenase pathway.⁴² Monitoring the perturbation of the heme charge-transfer band at 615 nm showed 4NP to bind in the heme cavity with a dissociation constant (K_d) of 260 μM . The crystallographic binding site of 4NP correlates well with the spectroscopic and mechanistic data, showing the peroxygenase substrate to bind distal to the heme in a position that i) perturbs water ligation to the heme Fe, affecting the heme UV-vis absorption and ii) facilitates oxygen atom transfer due to its close proximity to the heme cofactor. Figure 1.11 provides the UV-vis spectral changes upon titration of 4NP, binding isotherm which provides the K_d value of 260 μM , and crystallographic binding site. The crystallographic analysis of 4NP, in combination with its product 4-nitrocatechol, is presented in detail in Chapter 5.2.

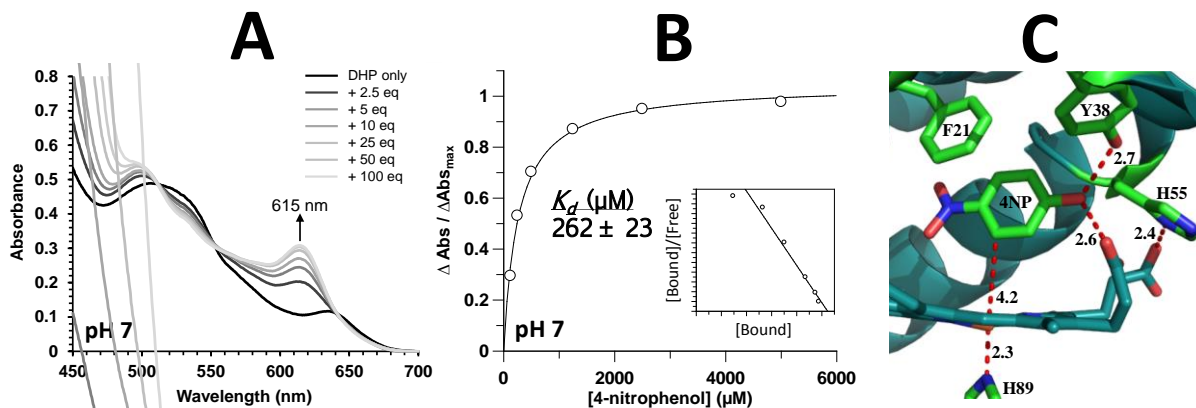


Figure 1.11. The binding of 4NP with DHP B is characterized through **A)** UV-visible spectral perturbation via titration of 4NP, **B)** binding isotherm yielding the dissociation constant of 260 μM , and **C)** X-ray crystallographic binding site of 4NP in the distal pocket of DHP B.

1.9 Preface of Presented Work in Proceeding Chapters

DHP is a heme protein that is capable of 5 different functions accomplished at a single heme center: oxygen transport, peroxidase, peroxygenase, oxygenase and oxidase functions. In particular, DHP is capable of substrate oxidation through both peroxidase and peroxygenase mechanisms, yet it is still unclear what factors dictate which enzymatic function will manifest itself with a particular substrate. Based on the available data, my hypothesis is that the oxygenase and peroxygenase substrates must bind in close proximity to the heme Fe, and that the sites of oxidation of the haloindoles (i.e., the 2- and 3- positions on the indole ring) are unhindered with respect to the ferryl oxygen in contrast to the oxidation site of the tri-halophenols. The steric presence of the halogens on the peroxidase substrate prohibits the direct oxygen insertion in contrast to the peroxygenase substrate, where the halogen is located away from the oxygenation site. Based on structural and steric aspects of the different mechanistic substrates, I surmise that the structure of the substrate dictates the binding mode and orientation, which in turn dictates the mechanistic pathway for oxygen insertion. Structural analysis is utilized to clarify the local structure-function relationship of the substrate binding sites specific for peroxidase and peroxygenase functions.

The proceeding chapters present efforts to enhance the knowledge and understanding of the multifunctional enzyme dehaloperoxidase. Chapter 2 characterizes the structural intermediate between the 4-halophenol inhibitor and the 2,4,6-trihalophenol peroxidase substrate, specifically 2,4-dichlorophenol and 2,4-dibromophenol, as peroxidase substrates whose products in turn are reactive peroxygenase substrates. Their X-ray crystallographic binding sites are elucidated and analysis of halophenol binding with respect to the placement and number of halogens is presented. Chapter 3 addresses the difference between isoenzymes DHP A and DHP B, specifically with the intent of determining how the 5 amino acid substitutions (individually and synergistically) affect reactivity. Chapter 4 presents rational mutagenic design (F21W) with the intent of directing enzymatic reactivity by inhibiting a specific peroxidase substrate binding site, which in turn sheds light on the plasticity of DHP's heme active site and its capability to preserve reactivity. And finally, Chapter 5 presents 4 additional crystallographic case studies detailing neutron diffraction, non-native porphyrin cofactor, substrate binding site determination and assumption validation.

1.10 References

- (1) Weber, R. E.; Mangum, C.; Steinman, H.; Bonaventura, C.; Sullivan, B.; Bonaventura, J. Hemoglobins of Two Terebellid Polychaetes: *Enoplobranchus Sanguineus* and *Amphitrite Ornata*. *Comp. Biochem. Physiol. -- Part A Physiol.* **1977**, *56* (2), 179–187.
- (2) Chen, Y. P.; Woodin, S. A.; Lincoln, D. E.; Lovell, C. R. An Unusual Dehalogenating Peroxidase from the Marine Terebellid Polychaete *Amphitrite Ornata*. *J. Biol. Chem.* **1996**, *271* (9), 4609–4612.
- (3) Han, K.; Woodin, S. A.; Lincoln, D. E.; Fielman, K. T.; Ely, B. *Amphitrite Ornata*, a Marine Worm, Contains Two Dehaloperoxidase Genes. *Mar. Biotechnol.* **2001**, *3* (3), 287–292.
- (4) LaCount, M. W.; Zhang, E.; Chen, Y. P.; Han, K.; Whitton, M. M.; Lincoln, D. E.; Woodin, S. A.; Lebioda, L. The Crystal Structure and Amino Acid Sequence of Dehaloperoxidase from *Amphitrite Ornata* Indicate Common Ancestry with Globins. *J. Biol. Chem.* **2000**, *275* (25), 18712–18716.
- (5) Barrios, D. A.; Antonio, J. D.; Mccombs, N. L.; Zhao, J.; Franzen, S.; Schmidt, A. C.; Sombers, L. A.; Ghiladi, R. A. Peroxygenase and Oxidase Activities of Dehaloperoxidase- Hemoglobin from *Amphitrite Ornata*. *J. Am. Chem. Soc.* **2014**, *136*, 7914–7925.
- (6) Lebioda, L. The Honorary Enzyme Haemoglobin Turns out to Be a Real Enzyme. *Cell. Mol. Life Sci.* **2000**, *57*, 1817–1819.
- (7) Vojtechovsky, J.; Chu, K.; Berendzen, J.; Sweet, R. M.; Schlichting, I. Crystal Structures of Myoglobin-Ligand Complexes at Near-Atomic Resolution. *Biophys. J.* **1999**, *77* (October), 2153–2174.
- (8) Bonagura, C. A.; Bhaskar, B.; Shimizu, H.; Li, H.; Sundaramoorthy, M.; Mcrec, D. E.; Goodin, D. B.; Poulos, T. L. High-Resolution Crystal Structures and Spectroscopy of Native and Compound I Cytochrome c Peroxidase †. *Biochemistry* **2003**, *42*, 5600–5608.
- (9) D’Antonio, J.; D’Antonio, E. L.; Thompson, M. K.; Bowden, E. F.; Franzen, S.; Smirnova, T.; Ghiladi, R. A. Spectroscopic and Mechanistic Investigations of Dehaloperoxidase B from *Amphitrite Ornata*. *Biochemistry* **2010**, *49* (31), 6600–6616.
- (10) Osborne, R. L.; Taylor, L. O.; Han, K. P.; Ely, B.; Dawson, J. H. *Amphitrite Ornata* Dehaloperoxidase: Enhanced Activity for the Catalytically Active Globin Using MCPBA. *Biochem. Biophys. Res. Commun.* **2004**, *324* (4), 1194–1198.

- (11) Zhang, E.; Chen, Y. P.; Roach, M. P.; Lincoln, D. E.; Lovell, C. R.; Woodin, S. A.; Dawson, J. H.; Lebioda, L. Crystallization and Initial Spectroscopic Characterization of the Heme-Containing Dehaloperoxidase from the Marine Polychaete Amphitrite Ornata. *Acta Crystallogr D Biol Crystallogr* **1996**, *52* (Pt 6), 1191–1193.
- (12) Finzelt, B. C.; Poulos, T. L.; Kraut, J. Crystal Structure of Yeast Cytochrome c Peroxidase Refined at 1.7-Å Resolution. *J. Biol. Chem.* **1984**, *259* (21), 13027–13036.
- (13) Gajhede, M.; Schuller, D. J.; Henriksen, A.; Smith, A. T.; Poulos, T. L. Crystal Structure of Horseradish Peroxidase C at 2.15 Å Resolution. *Nat. Struct. Biol.* **1997**, *4* (12), 1032–1038.
- (14) D'Antonio, E. L.; D'Antonio, J.; De Serrano, V.; Gracz, H.; Thompson, M. K.; Ghiladi, R. A.; Bowden, E. F.; Franzen, S. Functional Consequences of the Creation of an Asp-His-Fe Triad in a 3/3 Globin. *Biochemistry* **2011**, *50* (44), 9664–9680.
- (15) Evans, S. V.; Brayert, G. D. High-Resolution Study of the Three-Dimensional Structure of Horse Heart Metmyoglobin. *J. Mol. Biol.* **1990**, *2136*, 885–897.
- (16) Zhao, J.; de Serrano, V.; Zhao, J.; Le, P.; Franzen, S. Structural and Kinetic Study of an Internal Substrate Binding Site in Dehaloperoxidase-Hemoglobin A from Amphitrite Ornata. *Biochemistry* **2013**, *52* (14), 2427–2439.
- (17) Wang, C.; Lovelace, L. L.; Sun, S.; Dawson, J. H.; Lebioda, L. Complexes of Dual-Function Hemoglobin/dehaloperoxidase with Substrate 2,4,6-Trichlorophenol Are Inhibitory and Indicate Binding of Halophenol to Compound I. *Biochemistry* **2013**, *52* (36), 6203–6210.
- (18) Berman, H. M.; Westbrook, J.; Feng, Z.; Gilliland, G.; Bhat, T. N.; Weissig, H.; Shindyalov, I. N.; Bourne, P. E. The Protein Data Bank. *Nucleic Acids Res.* **2000**, *28* (1), 235–242.
- (19) De Serrano, V. S.; Davis, M. F.; Gaff, J. F.; Zhang, Q.; Chen, Z.; Dantonio, E. L.; Bowden, E. F.; Rose, R.; Franzen, S. X-Ray Structure of the Metcyano Form of Dehaloperoxidase from Amphitrite Ornata: Evidence for Photoreductive Dissociation of the Iron-Cyanide Bond. *Acta Crystallogr. Sect. D Biol. Crystallogr.* **2010**, *66* (7), 770–782.
- (20) McCombs, N. L.; Moreno-Chicano, T.; Carey, L. M.; Franzen, S.; Hough, M. A.; Ghiladi, R. A. Interaction of Azole-Based Environmental Pollutants with the Coelomic Hemoglobin from Amphitrite Ornata: A Molecular Basis for Toxicity. *Biochemistry* **2017**, *56* (17), 2294–2303.
- (21) De Serrano, V.; Franzen, S. Structural Evidence for Stabilization of Inhibitor Binding by a Protein Cavity in the Dehaloperoxidase-Hemoglobin from Amphitrite Ornata. *Biopolymers* **2012**, *98* (1), 27–35.

- (22) Jiang, S.; Wright, I.; Swartz, P.; Franzen, S. The Role of T56 in Controlling the Flexibility of the Distal Histidine in Dehaloperoxidase-Hemoglobin from Amphitrite Ornata. *Biochim. Biophys. Acta - Proteins Proteomics* **2013**, *1834* (10), 2020–2029.
- (23) Plummer, A.; Thompson, M. K.; Franzen, S. Role of Polarity of the Distal Pocket in the Control of Inhibitor Binding in Dehaloperoxidase-Hemoglobin. *Biochemistry* **2013**, *52* (13), 2218–2227.
- (24) Poulos, L.; Raag, R. Cytochrome P450cam: Crystallography, Oxygen Activation, and Electron Transfer. *FASEB* **1992**, *6* (2), 674–679.
- (25) Du, J.; Sono, M.; Dawson, J. H. Functional Switching of Amphitrite Ornata Dehaloperoxidase from O₂-Binding Globin to Peroxidase Enzyme Facilitated by Halophenol Substrate and H₂O₂. *Biochemistry* **2010**, *49* (29), 6064–6069.
- (26) de Montallana, P. R. O. *Cytochrome P450: Structure, Mechanism, and Biochemistry*; Kluwer Academic/Plenum Publishers: New York, 2005.
- (27) Chen, Z.; De Serrano, V.; Betts, L.; Franzen, S. Distal Histidine Conformational Flexibility in Dehaloperoxidase from Amphitrite Ornata. *Acta Crystallogr. Sect. D Biol. Crystallogr.* **2009**, *65* (1), 34–40.
- (28) Davydov, R.; Osborne, R. L.; Sun, H. K.; Dawson, J. H.; Hoffman, B. M. EPR and ENDOR Studies of Cryoreduced Compounds II of Peroxidases and Myoglobin. Proton-Coupled Electron Transfer and Protonation Status of Ferryl Hemes. *Biochemistry* **2008**, *47* (18), 5147–5155.
- (29) Poulos, T. L.; Kraut, J. The Stereochemistry of Peroxidase Catalysis. *J. Biol. Chem.* **1980**, *255* (17), 8199–8205.
- (30) De Serrano, V.; Chen, Z.; Davis, M. F.; Franzen, S. X-Ray Crystal Structural Analysis of the Binding Site in the Ferric and Oxyferrous Forms of the Recombinant Heme Dehaloperoxidase Cloned from Amphitrite Ornata. *Acta Crystallogr. Sect. D Biol. Crystallogr.* **2007**, *63* (10), 1094–1101.
- (31) Phillips, G. N.; Arduini, R. M.; Springer, B. A.; Sligar, S. G. Crystal Structure of Myoglobin From a Synthetic Gene. *Proteins Struct. Funct. Genet.* **1990**, *7*, 358–365.
- (32) De Serrano, V.; Chen, Z.; Davis, M. F.; Franzen, S. X-Ray Crystal Structural Analysis of the Binding Site in the Ferric and Oxyferrous Forms of the Recombinant Heme Dehaloperoxidase Cloned from Amphitrite Ornata. *Acta Crystallogr. Sect. D Biol. Crystallogr.* **2007**, *63* (10), 1094–1101.

- (33) Thompson, M. K.; Davis, M. F.; Serrano, V. De; Nicoletti, F. P.; Howes, B. D.; Smulevich, G.; Franzen, S. Internal Binding of Halogenated Phenols in Dehaloperoxidase-Hemoglobin Inhibits Peroxidase Function. *Biophys. J.* **2010**, *99* (5), 1586–1595.
- (34) Belyea, J.; Belyea, C. M.; Lappi, S.; Franzen, S. Resonance Raman Study of Ferric Heme Adducts of Dehaloperoxidase from Amphitrite Ornata. *Biochemistry* **2006**, *45* (48), 14275–14284.
- (35) De Serrano, V.; Dantonio, J.; Franzen, S.; Ghiladi, R. A. Structure of Dehaloperoxidase B at 1.58 Å Resolution and Structural Characterization of the AB Dimer from Amphitrite Ornata. *Acta Crystallogr. Sect. D Biol. Crystallogr.* **2010**, *66* (5), 529–538.
- (36) Zhao, J.; de Serrano, V.; Franzen, S. A Model for the Flexibility of the Distal Histidine in Dehaloperoxidase-Hemoglobin A Based on X-Ray Crystal Structures of the Carbon Monoxide Adduct. *Biochemistry* **2014**, *53* (15), 2474–2482.
- (37) Nicoletti, F. P.; Thompson, M. K.; Howes, B. D.; Franzens, S.; Smulevich, G. New Insights into the Role of Distal Histidine Flexibility in Ligand Stabilization of Dehaloperoxidase-Hemoglobin from Amphitrite Ornata. *Biochemistry* **2010**, *49* (9), 1903–1912.
- (38) Franzen, S.; Ghiladi, R. A.; Lebioda, L.; Dawson, J. H. Multi-Functional Hemoglobin Dehaloperoxidases. In *Heme Peroxidases*; The Royal Society of Chemistry, 2016; pp 218–244.
- (39) Franzen, S.; Thompson, M. K.; Ghiladi, R. A. The Dehaloperoxidase Paradox. *Biochim. Biophys. Acta - Proteins Proteomics* **2012**, *1824* (4), 578–588.
- (40) Davis, M. F.; Bobay, B. G.; Franzen, S. Determination of Separate Inhibitor and Substrate Binding Sites in the Dehaloperoxidase-Hemoglobin from Amphitrite Ornata. *Biochemistry* **2010**, *49* (6), 1199–1206.
- (41) Dumariéh, R.; D'Antonio, J.; Deliz-Liang, A.; Smirnova, T.; Svistunenko, D. A.; Ghiladi, R. A. Tyrosyl Radicals in Dehaloperoxidase: How Nature Deals with Evolving an Oxygen-Binding Globin to a Biologically Relevant Peroxidase. *J. Biol. Chem.* **2013**, *288* (46), 33470–33482.
- (42) McCombs, N. L.; D'Antonio, J.; Barrios, D. A.; Carey, L. M.; Ghiladi, R. A. Nonmicrobial Nitrophenol Degradation via Peroxygenase Activity of Dehaloperoxidase-Hemoglobin from Amphitrite Ornata. *Biochemistry* **2016**, *55* (17), 2465–2478.

Chapter 2

Bridging the Functional Gap Between Reactivity and Inhibition in Dehaloperoxidase B from *Amphitrite ornata*: Mechanistic and Structural Studies of 2,4-dihalophenol

*Leiah M. Carey and Reza A. Ghiladi**

2.1 Abstract

Dehaloperoxidase (DHP), a multifunctional catalytic globin, possesses reactivity with a variety of phenolic compounds, such as nitrophenols, guaiacols and halophenols. There exists a wealth of mechanistic and structural studies regarding 2,4,6-trihalophenol peroxidase reactivity and 4-halophenol inhibition, yet the details are lacking in regard to the structural intermediate of these two, 2,4-dihalophenol. We have identified both 2,4-dichlorophenol (2,4-DCP) and 2,4-dibromophenol (2,4-DBP) to undergo sequential oxidation via DHP through a peroxidase mechanism, followed by subsequent peroxygenase functionality. The X-ray crystallographic binding sites have been elucidated in complex with DHP B, with 2 observed for 2,4-DCP (1.95 Å and 1.49 Å) and 1 for 2,4-DBP (1.91 Å). These two substrates possess the tightest binding affinity with DHP observed, which is rationalized through the multiple stabilizing interactions observed in the crystallographic binding sites of each. The consequence of number of halogens on substrate binding orientation is examined via crystallographic studies and this halogen-directed binding is interpreted through reactivity comparisons between mono- (4-halophenol), di- (2,4-dihalophenol) and trihalophenols (2,4,6-trihalophenol), thus enhancing the knowledge of DHP reactivity with halophenols.

2.2 Introduction

Dehaloperoxidase (DHP), the coelomic globin from the marine annelid *Amphitrite ornata*, is the first oxygen transport protein identified that possesses a biologically relevant peroxidase activity.¹⁻³ In fact, DHP has also been shown to catalyze oxidative chemistry through peroxygenase, oxygenase and oxidase pathways, presenting DHP to be a multi-functional

enzyme with 5 functions coexisting at a single heme active center.^{4,5} Accordingly, DHP can accommodate as substrates a variety of aromatic compounds, such as halopyrroles,⁶ substituted indoles⁴ and substituted phenols.^{1,7-10} In the case of phenolic substrates, a number of outcomes have been observed: peroxygenase oxidation of 4-nitrophenol,⁵ peroxidase oxidation of 2,4,6-trihalophenol,⁷⁻¹⁰ and enzyme inhibition by 4-halophenol.^{2,9,11,12}

Regarded as its native peroxidase substrate, the reaction of DHP with 2,4,6-tribromophenol (and more generally 2,4,6-trihalophenols (TXP)) has been well-studied. Multiple TXP binding sites have been suggested by NMR,^{8,13,14} resonance Raman,^{7,12,15,16} and magnetic circular dichroism¹⁷ spectroscopic studies, and revealed a dependence between halogen identity and the substrate binding strength. Mechanistic investigations show TXP reactivity to occur via two sequential one-electron oxidation steps initiated upon H₂O₂ binding, consistent with the traditional peroxidase mechanism.^{2,7,10,18,19} X-ray crystallographic methods have elucidated binding sites for 2,4,6-tribromophenol²⁰ and 2,4,6-trichlorophenol,²¹ showing the molecules to bind within the distal pocket toward the heme edge, in an orientation which could still facilitate heme activation and subsequent reactivity.

Substrate conversion of 4-halophenols (4XP) has been previously observed,²² yet they function as inhibitors in the presence of other substrates. X-ray crystallographic studies have elucidated 4-halophenol (F, Cl, Br and I)^{11,23} binding sites within the distal pocket directly over the heme cofactor, residing between the Fe and heme β edge. Mutagenic studies^{12,24,25} and molecular dynamic simulations^{26,27} have demonstrated that 4XP binding stabilization depends upon distal pocket polarity, H-bonding contributions of residues, and hydrophobic stabilization of the halide atom. Given its position above the heme-iron, the 4XP binding site has implications toward its mechanistic role – oriented in a position that can hinder catalytic activation by: i) excluding other ligands from entering the pocket, ii) sterically preventing H₂O₂ binding to the Fe, iii) forcing the distal histidine out of the pocket, preventing its participation in H₂O₂ cleavage and subsequent heme activation, and iv) competitive binding amongst substrates.

Given our understanding that trihalophenols are peroxidase substrates, yet monohalophenols as inhibitors, here we explored the reactivity of 2,4-dihalophenols with DHP using both structural and spectroscopic methods, in order to further probe the structure-function paradigm in DHP.

2.3 Experimental

2.3.1 Materials and Methods. Isotopically labeled $\text{H}_2^{18}\text{O}_2$ (90% ^{18}O -enriched) and H_2^{18}O (98% ^{18}O -enriched) were purchased from Icon Isotopes (Summit, NJ). Acetonitrile (MeCN) was HPLC grade and all other chemicals were purchased from VWR, Sigma-Aldrich or Fisher Scientific and used without further purification. UV-visible spectroscopy was performed on a Varian Cary 50 UV-visible spectrophotometer. Ferric samples of enzymes were expressed and purified as previously reported.^{7,28} Oxyferrous DHP was obtained by the aerobic addition of excess ascorbic acid to a solution of ferric DHP, followed by application of the enzyme over a PD-10 desalting column.²⁹ Stock solutions (25 mM) of 2,4-DCP and 2,4-DBP were prepared in MeOH, stored in the dark at $-80\text{ }^\circ\text{C}$ until needed, and periodically screened by HPLC to ensure that they had not degraded. Aliquots were stored on ice during use. Solutions of H_2O_2 were prepared fresh daily and kept on ice until needed. The concentration was determined spectrophotometrically ($\epsilon_{240} = 43.6\text{ M}^{-1}\text{cm}^{-1}$).³⁰

2.3.2 Enzyme Assay Protocol. Reactions were performed in triplicate in 100 mM KP_i (pH 7)/5% MeOH at $25\text{ }^\circ\text{C}$. Buffered solutions (total reaction volume 200 μL) of DHP (10 μM final concentration) and substrate (500 μM final concentration) were pre-mixed, and then the reaction was initiated upon addition of H_2O_2 (500 μM final concentration). After 5 minutes, reactions were quenched with excess catalase. The reaction sample was diluted 10-fold with 1,800 μL of 100 mM KP_i (pH 7). Diluted samples were analyzed using a Waters e2695 Bioseparations Module coupled with a Waters 2998 Photodiode Array Detector, and equipped with a Thermo-Scientific ODS Hypersil (150 mm x 4.6 mm) 5 μm particle size C_{18} column. Separation of observed analytes was performed using a linear gradient of binary solvents (solvent A - H_2O containing 0.1% trifluoroacetic acid: solvent B – MeCN containing 0.1%

trifluoroacetic acid). Elution was performed using the following conditions: 1.5 mL/min of 95:5 (A:B) to 5:95 using a linear gradient over 10 min; 5:95 isocratic for 2 minutes; 5:95 to 95:5 using a linear gradient over 1 min, and then isocratic for 3 min. Data analysis was performed using the Empower 3 software package (Waters Corp.). Control experiments were also performed as above, either in the absence of hydrogen peroxide (non-oxidant control) or the absence of enzyme (non-enzymatic control).-

2.3.3 LC-MS Studies. Experiments were analyzed using a Thermo Fisher Scientific Exactive Plus Orbitrap mass spectrometer with heated-electrospray ionization (HESI) probe (Thermo Scientific, San Jose, CA) equipped with a Thermo Hypersil Gold (50 x 2.1 mm) 1.9 μm particle size C_{18} column. Analyte separation was performed using a linear gradient of binary solvents (solvent A - H_2O containing 0.1% formic acid: solvent B - MeCN), with an elution profile (0.5 mL/min, A:B) of 99:1 to 0:100 over 20 minutes. Samples were analyzed using electrospray ionization in negative mode to provide observation of the $[\text{M}-\text{H}]^-$ species. Spectra were collected each second while scanning in the range from 100 – 1000 m/z. Data analysis was performed using Thermo Xcalibur software. A final reaction volume of 200 μL (100 mM KPi , pH 7, 5% MeOH (v/v)) containing 10 μM enzyme, 50 eq. of substrate, and 50 eq. of peroxide (^{18}O labeled or non-labeled) was allowed to react for 5 min before quenching with excess catalase. For the H_2^{18}O studies, stock solutions of the reactants ($[\text{enzyme}] = 190 \mu\text{M}$; $[\text{H}_2\text{O}_2] = 8.8 \text{ mM}$) in unlabeled buffer were kept at sufficiently high concentrations to allow for the 98% enriched H_2^{18}O to be diluted to ~82% in the final reaction mixture. Labeled water, rather than buffer, brought the reaction to its final volume in the H_2^{18}O studies. Undiluted reaction mixture aliquots of 15 μL were injected for LC-MS analysis.

2.3.4 Substrate Binding Studies. Adapted from previously published protocols,³¹ 25 mM 2,4-dihalophenol stock solutions were prepared in MeOH. The UV-visible spectrophotometer was referenced using a solution of 10 μM ferric wild-type (WT) DHP B in 100 mM KPi , pH 7, containing 5% MeOH. Difference spectra were then acquired in the presence of 0.21 – 64.75 eq. 2,4-dihalophenol while maintaining both constant enzyme and MeOH concentrations.

Analysis by nonlinear regression using the GraFit software package (Erithacus Software Ltd.) of the experiments conducted in triplicate was performed as previously described.^{4,5,32}

2.3.5 Stopped-flow UV-visible Studies. Optical spectra were recorded at room temperature using a Bio-Logic SFM-400 triple-mixing stopped flow instrument coupled to a rapid scanning diode array UV-visible spectrophotometer. Stock 2,4-DCP solutions (25 mM) were prepared in MeOH with all remaining solutions prepared in 100 mM KPi (pH 7). Data were collected (900 scans total) over a three-time domain regime (1.5, 15, and 150 ms; 300 scans each) using the Bio Kinet32 software package (Bio-Logic). All data were evaluated using the Specfit Global Analysis System software package (Spectrum Software Associates) and fit to exponential functions as one-step/two-species or two-step/three-species irreversible mechanisms where applicable. For data that did not properly fit these models, experimentally obtained spectra at selected time points detailed in the figure legends are shown. Data were baseline corrected using the Specfit function.

All experiments using ferric DHP were performed in the double-mixing mode, where enzyme at a final concentration of 10 μM was reacted with 10 equivalents of H_2O_2 using an aging line prior to the second mixing step to observe Compound ES / Compound I reactivity with 2,4-DCP substrate (30 eq.), ($[\text{MeOH}]_f = 1.2\%$). Oxyferrous DHP B experiments were performed as single-mixing mode, where the enzyme solution was pre-incubated with 10 equivalents of 2,4-DCP substrate ($[\text{MeOH}]_f = 1.7\%$).

2.3.6 Protein Crystallization and X-ray Diffraction Studies. Non-His tagged DHP B was overexpressed and purified per literature protocol.⁵ Crystals were obtained through the hanging-drop vapor diffusion method. DHP B was concentrated to 12 mg/mL in 20 mM sodium cacodylate buffer (pH 6.4) and crystals were grown from mother liquor solutions of 28-32% PEG 4000 and 0.2 M ammonium sulfate, equilibrated against identical reservoir solutions. Protein to mother liquor ratios varied between 1:1, 1.33:1, 1.66:1 and 2:1. At 4 °C crystals, grew after 3 days. The crystals were then soaked for 12 hours in substrate enhanced reservoir solutions of 32 or 34 % PEG 4000 and 0.2 M ammonium sulfate. Substrate final concentrations of 26.5 mM 2,4-DCP (5% MeOH v/v), 36 mM 2,4-DCP (5% DMSO v/v), ~40

mM (saturated) 2,4-DBP (5% DMSO v/v), 77.4 mM 4-CP (5% DMSO v/v) and 27 mM 4-BP (5% DMSO v/v) were used to obtain ligand bound structures 2,4-DCP $_{\alpha}$, 2,4-DCP $_{\beta}$, 2,4-DBP, 4-CP and 4-BP, respectively. The crystals were cryo-protected by briefly dipping them in reservoir solution enhanced with 20% glycerol and then flash frozen in liquid N₂. Data were collected at 100 K on the SER-CAT 22-ID beamline (2,4-DCP $_{\alpha}$ and 4-BP) and SER-CAT 22-BM beamline (4-CP, 2,4-DCP $_{\beta}$ and 2,4-DBP) at the APS synchrotron facility, utilizing a wavelength of 1.00 Å. All data were scaled and integrated using HKL2000,³³ molecular replacement was performed with Phaser-MR³⁴ from the PHENIX³⁵ suite of programs using 3IXF³⁶ monomer as the search model, model building and manual placement of waters utilized COOT³⁷ and refinement was carried out using phenix.refine.³⁸

2.4 Results

2.4.1 Enzyme Assays. The hydrogen peroxide-dependent oxidation of 2,4-dichlorophenol (2,4-DCP) and 2,4-dibromophenol (2,4-DBP) as catalyzed by DHP B at pH 7 was monitored by HPLC. Reactions were initiated upon addition of 500 μ M H₂O₂ to a solution containing 10 μ M enzyme and 500 μ M substrate (2,4-DCP or 2,4-DBP), incubated at 25 °C for five minutes, and then quenched with catalase. Reactivity, as characterized by the percentage of substrate conversion, was determined by monitoring the loss of the substrate peak. Representative HPLC chromatograms of ferric DHP B/H₂O₂ reactions with 2,4-DCP and 2,4-DBP are shown in Figure 2.1, panels A and B, respectively. Multiple peaks were observed for both 2,4-DCP and 2,4-DBP reactions, however this HPLC study solely provided analysis of substrate reactivity. Characterization of the multiple product peaks via LC-MS is discussed further in the text.

It was found that both 2,4-DCP and 2,4-DBP are equally reactive in terms of substrate conversion (Table 2.1) with ferric DHP B (2,4-DCP: 58.9 \pm 3.4%; 2,4-DBP: 56.2 \pm 2.9%) and oxyferrous DHP B (2,4-DCP: 58.1 \pm 5.1%; 2,4-DBP: 53.9 \pm 1.5%). Reactivity of 2,4-DCP and 2,4-DBP was found to be identical for oxyferrous DHP B compared to the ferric enzyme, indicating that the reaction can be initiated from either the globin active (Fe^{II}-O₂) or peroxidase-active (Fe^{III}) states, a result that has been observed previously for peroxidase [2,4,6-

trichlorophenol (TCP)] and peroxygenase [(5-bromoindole (5BI) and 4-nitrophenol (4NP)] oxidations.^{21, 26} The observations in this study provided the comparative substrate reactivities, as determined via 5 minute end-point assay, of 2,4-DCP \approx 2,4-DBP > 5BI⁴ > 4NP⁵ > pyrrole⁶ (substrate conversions provided in Table 2.1).

In the presence of 500 μ M 4-bromophenol (4BP), a known inhibitor of TCP and haloindole oxidation,¹¹ reactivity was slightly attenuated for both substrates: i) 2,4-DBP reactivity decreased by 1.2 fold with both ferric and oxyferrous DHP B; ii) 2,4-DCP reactivity decreased by 1.9 fold with oxyferrous DHP B, however with the ferric enzyme, reactivity was attenuated by 2.1 fold. For ferric DHP B reactivity, 4BP inhibition of 2,4-DCP is identical to 5BI, yet is lower than pyrrole (5.5 fold) and 4NP (no reactivity observed). Among substrates analyzed by HPLC, inhibition by 4BP was shown to have the smallest effect on 2,4-DBP reactivity, yet 4BP was shown to essentially shut down 4NP reactivity.

Table 2.1. Substrate conversion (%), providing 2,4-DCP and 2,4-DBP reactivity with ferric DHP B and oxyferrous DHP B. Substrate conversion in the presence of 500 μ M 4-BP inhibitor is given in parenthesis. Reactivity of previously established substrates is provided for comparison.^(a)

<u>Substrate</u>	<u>Ferric DHP B</u>	<u>Oxyferrous DHP B</u>	<u>Ref.</u>
2,4-DCP	58.9 \pm 3.4 (28.3 \pm 0.6)	58.1 \pm 5.1 (30.6 \pm 0.8)	
2,4-DBP	56.2 \pm 2.9 (45.5 \pm 1.2)	53.9 \pm 1.5 (42.9 \pm 0.9)	
Pyrrole	27.9 \pm 3.8 (5.1 \pm 0.6)	17.8 \pm 1.0 (n.a.) ^(d)	6
5BI	48.1 \pm 2.3 (23.2 \pm 5.1)	44.9 \pm 4.8 (n.a.) ^(d)	4
4NP ^(b)	39.4 \pm 0.7 (n.d.) ^(c)	37.6 \pm 1.7 (n.a.) ^(d)	5

^(a) Reaction conditions: [substrate] = [H₂O₂] = 500 μ M, [DHP B] = 10 μ M, 100 mM KP_i buffer at pH 7; ^(b) 4NP reactions were performed at pH 6; ^(c) n.d. = not detected; ^(d) n.a. = not available

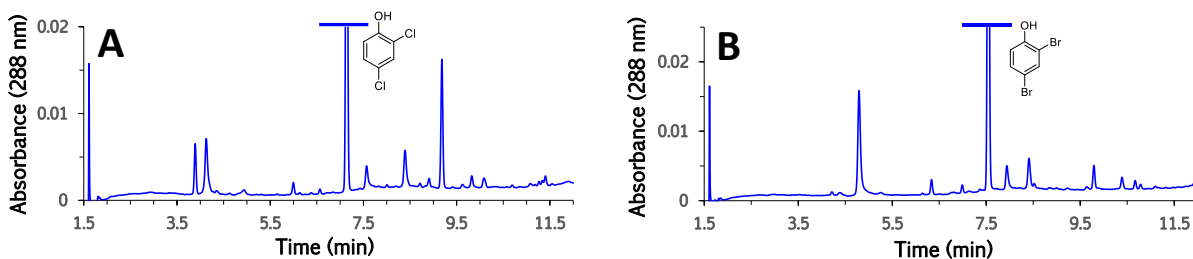


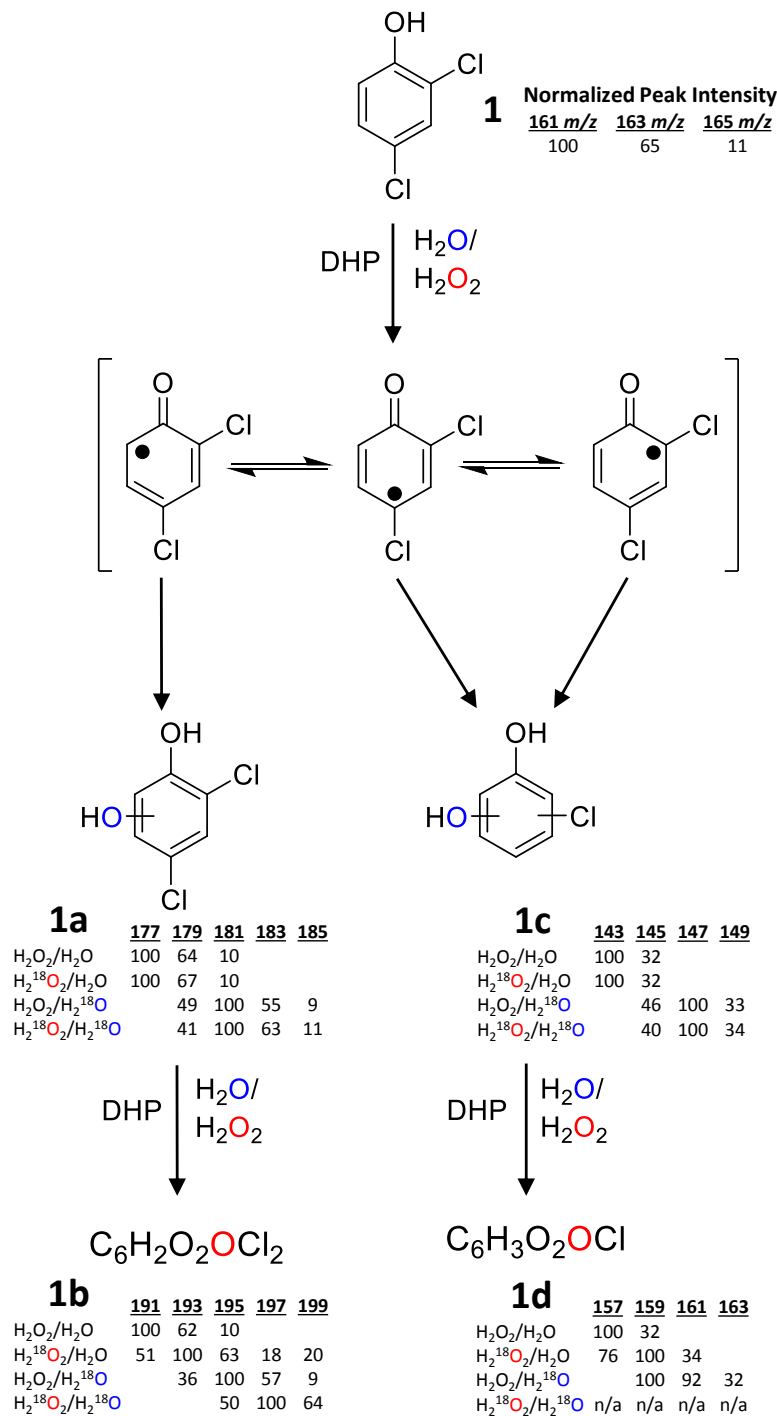
Figure 2.1. HPLC chromatograms, as observed at $\lambda = 288$ nm, of the 2,4-DCP (**A**) and 2,4-DBP (**B**) reactions with 10 μM ferric DHP B, 500 μM = [substrate] = $[\text{H}_2\text{O}_2]$. The peak area at $t_{\text{R}} = 7.16$ min and 7.54 min were used to determine percent substrate conversion for 2,4-DCP (**A**) and 2,4-DBP (**B**), respectively. The chromatograms are zoomed in to better show the product peaks, effectively cutting off the top of the substrate peaks.

2.4.2 MS Product Characterization and ^{18}O Labeling Studies. The hydrogen peroxide-dependent oxidation of 2,4-dichlorophenol (2,4-DCP) and 2,4-dibromophenol (2,4-DBP) as catalyzed by ferric WT DHP B at pH 7 was analyzed by LC-MS. Reactions were initiated upon addition of 500 μM H_2O_2 to a solution containing 10 μM enzyme and 500 μM substrate (2,4-DCP or 2,4-DBP), incubated at 25 $^\circ\text{C}$ for five minutes, and then quenched with catalase. Products were characterized by the respective m/z of the $(\text{M} - \text{H})^-$ ion. Isotopic distributions were normalized with respect to the most intense peak. Studies employing labeled $\text{H}_2^{18}\text{O}_2$ and H_2^{18}O (90% and 98% ^{18}O -atom enriched, respectively) were performed to determine the source of the O-atom incorporation. LC retention times, MS peak distributions and m/z shifts were evaluated under each of the 4 labeling reaction conditions: 1) unlabeled H_2O_2 and H_2O ; 2) labeled $\text{H}_2^{18}\text{O}_2$ and unlabeled H_2O ; 3) unlabeled H_2O_2 and labeled H_2^{18}O and 4) both labeled $\text{H}_2^{18}\text{O}_2$ and H_2^{18}O . From this analysis, reaction schemes for 2,4-DCP and 2,4-DBP oxidation as catalyzed by ferric DHP B are proposed.

2,4-dichlorophenol – As shown in the HPLC studies, the reaction of 2,4-DCP with DHP B resulted in multiple products. The vast majority of the product peaks corresponded to dimers and trimers of various degrees of oxidation and (de)chlorination, however four single ring products were identified and characterized (Figure S2.8). The products are labeled in accordance to their position in the proposed 2,4-DCP reaction (Scheme 2.1). From the ^{18}O

isotopic labeling LC-MS studies, reaction Scheme 2.1 is proposed for the enzymatic oxidation of 2,4-DCP by ferric DHP B. The peak ratios, peak intensities (normalized to the most intense peak) and corresponding m/z values obtained from different reaction conditions are provided adjacent to each product.

The initial oxidation of 2,4-DCP proceeds through a peroxidase mechanism, resulting in the oxygen atom incorporated derived solely from water. The diol product subsequently undergoes secondary oxidation via a peroxygenase mechanism, resulting in oxygen atom incorporation derived from hydrogen peroxide and oxidation to a quinone species. Dechlorinated variants, characterized by the loss of 1 Cl atom, of the diol and hydroxy-benzoquinone species are observed also. As dehalogenation has been observed via a peroxidase mechanism in DHP for 2,4,6-trichlorophenol (TCP) and 2,4,6-tribromophenol (TBP) substrates, it is reasonable to suggest that dehalogenation of 2,4-DCP also occurs during the peroxidase step.^{1,2,8,17} DHP peroxidase chemistry produces a transient, radical-containing product. Resonance structures of phenoxyl radicals place the radical at the *ortho*- or *para*-position from the O position. Dechlorination of TCP has been attributed to the *para*-location of the radical, which yields the observed 2,4-dichloroquinone product. In the case of 2,4-DCP either the *ortho*- or *para*- radical position could direct the dechlorination chemistry. Formation of product **1c** could follow the same mechanism as TCP oxidative-dehalogenation, with selective reactivity at the *para*- position. However, because the Cl atoms of 2,4-DCP (**1**) reside in both *ortho*- and *para*- positions, either one could potentially be reactive. Following this logic, the site of oxygen atom incorporation could also be *ortho*- or *para*-directed into **1c**, resulting in the possibility of multiple isomers. The dechlorinated diol species then can undergo the peroxygenase oxidation step, resulting in the observed mono-chlorinated hydroxy-quinone product **1d**. In the absence of dechlorination, the *ortho*- position is the only option and product **1a** is most likely 3,5-dichlorocatechol. Product **1a** can then undergo the peroxygenase step, resulting in the hydroxy-quinone product **1b**, however it is ambiguous if it is the *ortho*- or *para*-quinone isomer. Further characterization is required to differentiate between possible conformational isomers and identify the molecular structure.



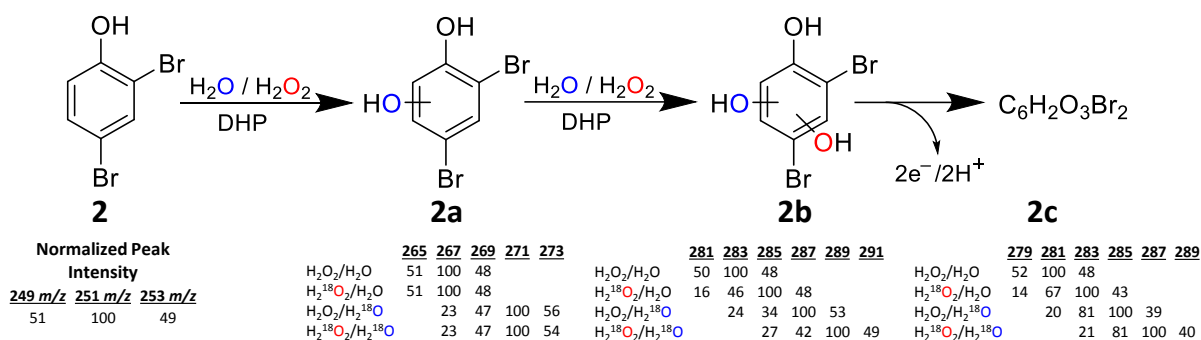
Scheme 2.1. Proposed oxidation pathways of 2,4-dichlorophenol in the presence of DHP.

From the unlabeled reaction the substrate 2,4-DCP was identified at a retention time (t_R) of 8.17 min, (Figure S2.8, **1**), identified by the characteristic 9:6:1 isotopic ratio for 2 chlorine atoms and expected m/z of 161. At $t_R = 7.14$ min (Figure S2.8, **1a**) the same isotopic ratio was observed with an m/z 177 corresponding to a single oxygen atom incorporated into the product. At $t_R = 2.43$ min (Figure S2.8, **1b**) the ratio was again observed, this time with an m/z of 191 which corresponds to the incorporation of 2 oxygen atoms and loss of 2 hydrogen atoms, suggesting a quinone product. Singly dechlorinated products were also observed from the 2,4-DCP reaction: the characteristic ratio of 3:1 for a mono-chlorinated species was observed at $t_R = 5.15$ min (Figure S2.8, **1c**) with an m/z of 143, which corresponds to a loss of Cl and a gain of an oxygen and a hydrogen atom. The second dechlorinated product was observed at $t_R = 3.26$ min (Figure S2.8, **1d**) with the m/z of 157 and peak ratio corresponding to the loss of 1 Cl and 1 H atom, with the addition of 2 O atoms. This species correlates well to a dechlorinated quinone product, however the data are unable to provide an unambiguous assignment as to whether this species was an *ortho*- or *para*- quinone.

In comparison to the unlabeled reactions, products **1a** and **1c** (dichlorinated and monochlorinated, respectively) only exhibited a mass shift in the presence of $H_2^{18}O$. Figure S2.9 provides the ESI-MS total ion chromatograms from each reaction condition for products **1a** and **1c**. The majority of the peaks exhibited a mass increase of 4 Da, yet there is the smaller presence of a 2 Da increase. In the presence of both labeled $H_2^{18}O_2$ and $H_2^{18}O$ the mass increase and peak distributions of **1a** and **1c** closely resembled the results obtained from only labeled $H_2^{18}O$. Employing $H_2^{18}O_2$ and unlabeled H_2O showed no significant increase to a higher mass for **1a** and **1c**, yet the double-labeled experiment with $H_2^{18}O_2$ and $H_2^{18}O$ showed nearly the same mass increase and peak distribution as with $H_2^{18}O$ and unlabeled H_2O_2 . Thus, the data suggest that $H_2^{18}O_2$ does not contribute to O-atom incorporation into **1a** and **1c**, and this lack of influence on the label distribution as a function of hydrogen peroxide is consistent with a peroxidase mechanism. These results also suggested that in addition to the incorporation of a single ^{18}O label from a peroxidase cycle, partial scrambling with the $H_2^{18}O$ solvent also occurred, resulting in the +4 Da species.

Products **1b** (dichlorinated) and **1d** (monochlorinated) showed a mass increase from all reactions run in the presence of an ^{18}O label. Figure S2.10 provides the ESI-MS total ion chromatograms from each reaction condition for products **1b** and **1d**. In the presence of $\text{H}_2^{18}\text{O}_2$ and unlabeled H_2O , **1d** showed a mass increase of 2 Da. For product **1b**, there is also a mass increase of 2 Da for the majority of the peaks, however the presence of the 191 peak corresponds to unlabeled product, which suggests scrambling with the unlabeled solvent. In the presence of H_2^{18}O and unlabeled H_2O_2 , there was a clear increase of 4 Da for **1d** and **1b**, showing a similar ratio of label incorporation as in the single labeled $\text{H}_2^{18}\text{O}_2$ reaction. In the presence of dual labels, $\text{H}_2^{18}\text{O}_2$ and H_2^{18}O , product **1d** was not observed, but **1b** showed mass increases from 2 – 6 Da and the peak distribution not directly correlating neither the $\text{H}_2^{18}\text{O}_2$ and unlabeled H_2O reaction nor the unlabeled H_2O_2 and H_2^{18}O reaction distributions, suggesting **1b** is a secondary metabolite from **1a**. This secondary oxidation most probably proceeds through a peroxygenase mechanism, where the oxygen atom incorporated into the product is derived from hydrogen peroxide, as shown from i) the mass increase in the presence of $\text{H}_2^{18}\text{O}_2$ and unlabeled H_2O reaction and ii) the isotopic distribution of the dual labeled $\text{H}_2^{18}\text{O}_2$ and H_2^{18}O reaction does not correlate well with either single labeled reaction. The sequential oxidation from **1c** to **1d** is likewise suggested for the dechlorinated products.

2,4-dibromophenol – The reaction of 2,4-dibromophenol (2,4-DBP) with DHP B resulted in multiple products, including three single-ring products as well as dimers and trimers possessing various degrees of oxidation (Figure S2.11). Interestingly, the dehalogenation that was observed for 2,4-DCP was not observed here for 2,4-DBP. The product peaks are labeled in accordance to their position in Scheme 2.2. From the ^{18}O isotopic labeling LC-MS studies, Scheme 2.2 is proposed for the enzymatic oxidation of 2,4-DBP by ferric DHP B. The peak ratios, normalized peak intensities and corresponding m/z values obtained from each reaction condition are provided below each product.



Scheme 2.2. Proposed oxidation pathway of 2,4-dibromophenol in the presence of DHP B.

The initial oxidation of 2,4-DBP proceeds through a peroxidase mechanism, resulting in the oxygen atom incorporated into product **2a** derived solely from water. Because 2,4-DBP showed no dehalogenated products, the *ortho*-position is the most likely site of O atom insertion, where product **2a** could possibly be 3,5-dibromocatechol. The diol product subsequently undergoes additional oxidation through a peroxygenase mechanism, resulting in oxygen atom incorporation derived from hydrogen peroxide forming a triol species **2b**. An additional oxidation step is observed without atom incorporation, where the triol species converts to a hydroxy-quinone species **2c**, however it is ambiguous if it is the *ortho*- or *para*-quinone isomer. In the case of an *ortho*-quinone product, O atom incorporation in **2b** most probably occurred between a Br and OH group, resulting in a brominated pyrogallol product. If the identity of **2c** is a *para*-quinone species, O atom incorporation in **2b** most probably occurred between the Br groups, resulting in a 3,5-dibromo-1,2,4-triol product. Again, further characterization is required to differentiate between these possible product identities.

The substrate 2,4-DBP was identified at $t_R = 8.84$ min, (Figure S2.11, **2**) exhibiting the characteristic 1:2:1 isotopic ratio indicative of 2 bromine atoms and the expected m/z of 251. At $t_R = 7.87$ min (Figure S2.11, **2a**) the same isotopic ratio was observed with an m/z of 267, corresponding to a single oxygen atom incorporated into the product. This isotopic ratio again was observed at $t_R = 4.09$ min (Figure S2.11, **2b**) with an m/z 283 that corresponds to the incorporation of 2 oxygen atoms. The third product was observed at $t_R = 3.30$ min (Figure

S2.11, **2c**) with an m/z of 281 which corresponds to the addition of 2 oxygen atoms and the loss of 2 hydrogen atoms. This suggests a further oxidation of product **2b** to its corresponding quinone species, **2c**.

Isotopic ^{18}O labeling studies were conducted in the presence of H_2^{18}O and $\text{H}_2^{18}\text{O}_2$, both separately and together. The ESI-MS total ion chromatograms for products **2a**, **2b** and **2c**, obtained under each reaction condition, are provided in Figure S2.12. For product **2a**, there was no mass shift in the presence of $\text{H}_2^{18}\text{O}_2$ and unlabeled H_2O (Figure S2.12 left panel). In the presence of H_2^{18}O and unlabeled H_2O_2 , there was a clear increase to higher mass where the majority of the peaks exhibit a mass increase of 4 Da, yet there is the presence of a 2 Da increase. The double-labeled experiment with $\text{H}_2^{18}\text{O}_2$ and H_2^{18}O showed nearly the same results as with H_2^{18}O and unlabeled H_2O_2 . Thus, the data suggest that $\text{H}_2^{18}\text{O}_2$ does not play a role in the incorporation of the O-atom into product **2a**, and this lack of influence on the label distribution as a function of hydrogen peroxide is consistent with a peroxidase mechanism. These results also suggested that in addition to the incorporation of a single ^{18}O label from a peroxidase cycle, that partial scrambling with the H_2^{18}O solvent also occurred.

Products **2b** and **2c** exhibited a mass increase from all reactions run in the presence of an ^{18}O label (Figure S2.12 middle and right panels). In the presence of $\text{H}_2^{18}\text{O}_2$ and unlabeled H_2O , both **2b** and **2c** exhibit a mass increase of 2 Da for the majority of the peaks. However, there were also peaks lacking label integration, which again suggests scrambling with the unlabeled solvent. In the presence of H_2^{18}O and unlabeled H_2O_2 , the major peaks showed a mass increase of 4 Da for both **2b** and **2c**, with a similar ratio of label incorporation as in the singly labeled $\text{H}_2^{18}\text{O}_2$ reaction. In the presence of dual labels, $\text{H}_2^{18}\text{O}_2$ and H_2^{18}O , the isotopic distributions for both **2b** and **2c** resembled the labeled H_2^{18}O and unlabeled H_2O_2 reactions, yet the mass of each peak was increased by 2 Da. The data show ^{18}O incorporation into **2b** and **2c** to be dependent on both hydrogen peroxide and water, suggesting **2b** and **2c** are secondary metabolites from **2a**. This secondary oxidation most probably proceeds through a peroxygenase mechanism, where the oxygen atom incorporated is derived from hydrogen peroxide, as shown from: i) the mass increase in the presence of $\text{H}_2^{18}\text{O}_2$ and unlabeled H_2O

reaction and ii) the mass increase in the double-labeled $\text{H}_2^{18}\text{O}_2$ and H_2^{18}O reaction was greater than the H_2^{18}O and unlabeled H_2O_2 reaction. The mass decrease of 2 Da in **2c** compared to **2b** is indicative of further oxidation of **2b** to produce the quinone species that is represented by **2c**.

2.4.3 Substrate Binding Study. Optical spectra were recorded per literature protocol as a function of substrate concentration (0.21 – 64.75 eq; Figure S2.7).³¹ Perturbation of the Soret band was monitored, which in the presence of either 2,4-DCP or 2,4-DBP exhibited hypsochromic and hypochromic shifts. Analysis by nonlinear regression plots provided a calculated A_{max} value, which in turn was used to calculate α for the average ΔA for each [substrate]. A second nonlinear regression plot provided the apparent dissociation constants (K_d) for 2,4-DCP and 2,4-DBP.

As shown in Table 2.2, binding for 2,4-DBP ($K_d = 6.5 \pm 0.6 \mu\text{M}$) was ~4-fold stronger than 2,4-DCP ($K_d = 29 \pm 1 \mu\text{M}$). The low K_d values obtained for 2,4-DBP and 2,4-DCP show that they bind the tightest amongst all substrates and ligands examined, with 2,4-DBP exhibiting the strongest substrate binding observed to date. With respect to the $\text{p}K_a$ values of 7.86 and 8.05 for 2,4-DBP and 2,4-DCP, respectively, the data suggest that binding occurred when the substrates were predominately in their neutral phenol form in pH 7.0 buffer. Structural elements of the DHP active site involving H-bonding, aromatic π stacking and hydrophobic interactions to 2,4-DCP and 2,4-DBP that lead to such strong binding affinities were elucidated by X-ray crystallography (vide infra).

Notably, the K_d values for 2,4-DBP and 2,4-DCP are lower than K_d values for known peroxygenase substrates: the 5-substituted halogens (5-I-indole: $62 \pm 10 \mu\text{M}$; 5-Br-indole: $150 \pm 10 \mu\text{M}$; 5-Cl-indole: $317 \pm 23 \mu\text{M}$) and nitro-containing phenols (4-nitrophenol: $260 \pm 20 \mu\text{M}$; 2,4-dinitrophenol; $100 \pm 20 \mu\text{M}$). With respect to the peroxidase substrate 4-nitrocatechol (4-NC) ($K_d = 40 \pm 1 \mu\text{M}$), the binding of 2,4-DBP was 6 fold stronger, while the binding strength of 2,4-DCP was on par with 4-NC, with only a 1.4 fold increase. The dissociation constants for 2,4-DBP and 2,4-DCP are significantly lower than that for 4-bromophenol ($K_d \sim 1.15 \text{ mM}$),¹¹ a known inhibitor of the enzyme. In comparison withazole³² ligands that bind

directly to the heme-Fe, again 2,4-DCP and 2,4-DBP present higher substrate affinity, with 2,4-DBP possessing roughly an order of magnitude stronger binding.

Table 2.2. K_d Values for Ligand Binding to Ferric DHP B at pH 7.

Substrate	K_d (μM)	$K_d^{\text{F}^-}$ (mM) ⁹
2,4-dichlorophenol	29 ± 1	74.1 ± 4.3 ^(a)
2,4-dibromophenol	6.5 ± 0.6	172.0 ± 9.0 ^(a)
2,4,6-tribromophenol	n. r.	24 ± 1 ^(a)
2,4,6-trichlorophenol	n. r.	14.5 ± 0.8 ^(a)
4-bromophenol ¹¹	1,150	12.3 ± 0.8 ^(a)
4-nitrophenol ⁵	260 ± 20	18 ± 1 (pH 5) ^(b)
4-nitrocatechol ⁵	40 ± 1	31 ± 3 (pH 5) ^(b)
2,4-dinitrophenol ⁵	100 ± 20	90 ± 9 (pH 5) ^(b)
2,4,6-trinitrophenol ⁵	n. d.	30 ± 1 (pH 5) ^(b)
5-chloroindole ⁴	320 ± 20	8.6 ± 0.3 ^(a)
5-bromoindole ⁴	150 ± 10	13.2 ± 0.5 ^(a)
5-iodoindole ⁴	60 ± 10	16.8 ± 0.4 ^(a)
imidazole ³²	52 ± 2	n.d. ^(c)
benzotriazole ³²	82 ± 3	n.d. ^(c)
benzimidazole ³²	110 ± 8	n.d. ^(c)

K_d value of fluoride binding in the presence of ^(a) 1 mM of substrate⁹ or ^(b) 500 μM nitrophenol substrate,⁵ ^(c) n. d. = not determinable due to lack of spectral changes.

No K_d value for 2,4,6-tribromophenol (TBP) has been directly determined as the UV-visible spectra do not exhibit any substrate-dependent shifts (data not shown). We can attributed this outcome to the binding of TBP deep in the hydrophobic cavity of DHP, leaving the distal space directly above the heme vacant, which has been previously observed via X-ray crystallography and is discussed below. However, in order to further probe TBP binding to DHP, a competition assay with the heme-fluoride binding equilibrium was employed (Table 2.2).⁹ In this method, substrates that bind within the DHP active site lead to a decreased binding affinity of fluoride to the heme ($K_d^{\text{F}^-} = 4.5 \pm 0.4$ mM). A comparison of the $K_d^{\text{F}^-}$ values at pH

7 reveals that TBP binding is stronger than the inhibitor 4-BP, yet weaker than the 2,4-DBP substrate, resulting in the substrate binding affinity order: 4-BP < 2,4,6-TBP < 2,4-DBP. Again, 2,4-DBP was determined to possess the highest binding affinity amongst substrates examined, which correlated well to the aforementioned binding study.

2.4.4 Stopped-flow Studies of 2,4-dichlorophenol Reactivity. Single and double-mixing stopped-flow methods were used to investigate the reaction of 2,4-dichlorophenol (2,4-DCP) with H₂O₂-activated DHP, pre-formed either as Compound I, Compound ES, or with the oxyferrous species itself as the starting state.

Compound I Reactivity – Ferric DHP B (Y28F/Y38F) was reacted with 10 molar equivalents of H₂O₂ at pH 7, incubated for 150 ms to allow for the maximum accumulation of Compound I, and its subsequent reaction with 2,4-DCP was monitored (Figure 2.2). No activated enzyme (i.e., pre-formed Compound I [406 (Soret), 528, 645 nm])³⁹ was observed. Rather, a ferric-like DHP B (Y28F/Y38F) species [403 (Soret), 516, 649 nm] that normally forms in the substrate-free DHP B (Y28F/Y38F)/H₂O₂ reaction after 800 ms was the first spectrum recorded (after 2.5 ms), suggesting that Compound I was reduced by the substrate within the mixing time of the stopped-flow apparatus. This initial species then converted ($k_{obs} = 2.622 \pm 0.007 \text{ s}^{-1}$) to another species [410 (Soret), 503, 615 nm] whose spectral features do not match with any previously observed DHP B species. As such, this may be possibly indicative of substrate- and/or product-bound DHP B (Y28F/Y38F), but the identity of this off-pathway reaction product was not further explored.

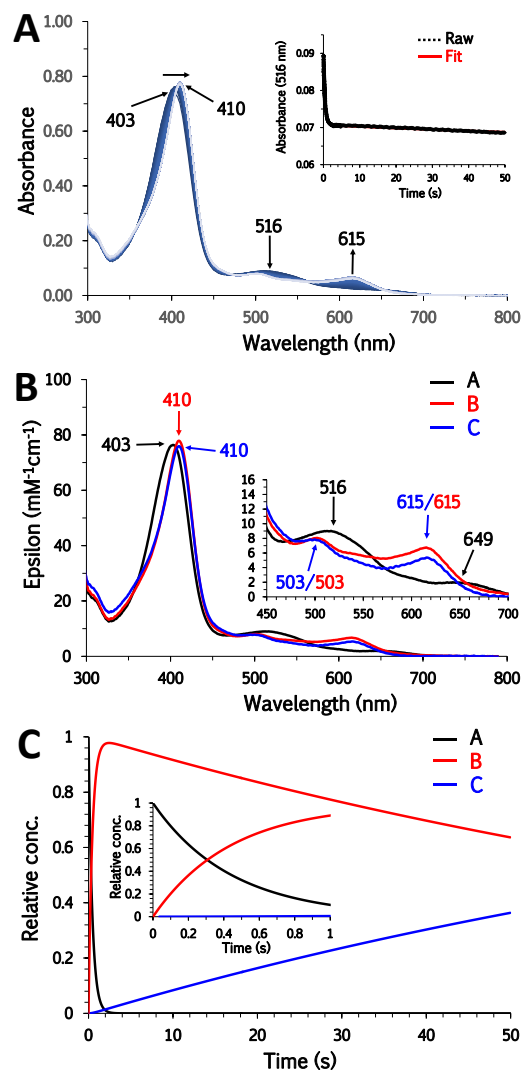


Figure 2.2. Kinetic data for the reaction of pre-formed Compound I [DHP B (Y28F/Y38F)] with 2,4-dichlorophenol (2,4-DCP). **A**) Stopped-flow UV-visible spectra of the double-mixing reaction of preformed DHP B (Y28F/Y38F) Compound I (10 μM), itself formed in an initial mixing step from ferric DHP B (Y28F/Y38F) reacted with a 10-fold excess of H_2O_2 in an aging line for 150 ms, with a 30-fold excess of 2,4-DCP at pH 7 (900 scans over 50 sec); *inset* - the single wavelength (516 nm) dependence on time obtained from the raw spectra and its fit with a superposition of the calculated spectral components. **B**) calculated spectra of the three reaction components derived from the SVD analysis: ferric-like DHP B (Y28F/Y38F) (black), ferric-like DHP B (Y28F/Y38F) in the presence of 2,4-DCP substrate and products (red), and the final ferric-like DHP B (Y28F/Y38F) in the presence of 2,4-DCP substrate and products (blue). **C**) time dependences of the relative concentrations for the three components shown in the middle panel as determined from the fitting of the spectra in the top panel. *Inset* – time dependences of concentrations in the initial second of data collection.

Compound ES Reactivity – Ferric DHP B (10 μM) was reacted with 10 molar equivalents of H_2O_2 at pH 7, incubated for 500 ms to allow for the maximum accumulation of Compound ES,⁷ and subsequently mixed with 30 equivalents of 2,4-DCP (Figure 2.3). The preformed Compound ES [421 (Soret), 547, 580 nm] was rapidly reduced ($k_{\text{obs}} = 20.19 \pm 0.03 \text{ s}^{-1}$) back to ferric-like DHP B [407 (Soret), 504, 628 nm]. This species was converted ($k_{\text{obs}} = 0.048 \pm 0.002 \text{ s}^{-1}$) to ferric DHP B exhibiting bleaching of the Soret [407 (Soret), 504, 628 nm]. Under these conditions, Compound RH, the stable form of DHP that forms from H_2O_2 -activation in the absence of substrate, was not observed and DHP B returns to a ferric resting state following 2,4-DCP reactivity.

Oxyferrous DHP Reactivity (Figure 2.4) – In the absence of substrate, previous studies have shown that a slight bleaching of the Soret band and/or long timescale conversion to Compound RH occurs upon the reaction of oxyferrous DHP with H_2O_2 , and only when TCP^{8,40} or indole¹⁴ substrates were present were fast timescale reactive intermediates observable. This substrate-dependent activation of DHP was investigated here with 2,4-DCP using stopped-flow methods. Upon rapid mixing of a solution of oxyferrous DHP B pre-incubated with 10 eq. of 2,4-DCP with 10 equivalents of H_2O_2 , substantial spectral changes were observed. The initial observation was an oxyferrous species with a slight hypsochromic shift in the Soret, possibly due to the presence of 2,4-DCP [417 (Soret), 543, 578 nm; $t = 50 \text{ ms}$]. The oxyferrous species was found to convert to the substrate or product-bound ferric enzyme [405 (Soret), 503, 582, 636 nm] within 2.25 s. The final species (49.95 s) is represented by a bathochromic and hypochromic shift of the Soret to 407 nm, an increase in absorbance between 300-350 nm, slight hyperchromic shift of the Q-band region, and no noticeable spectral feature at 582 nm.

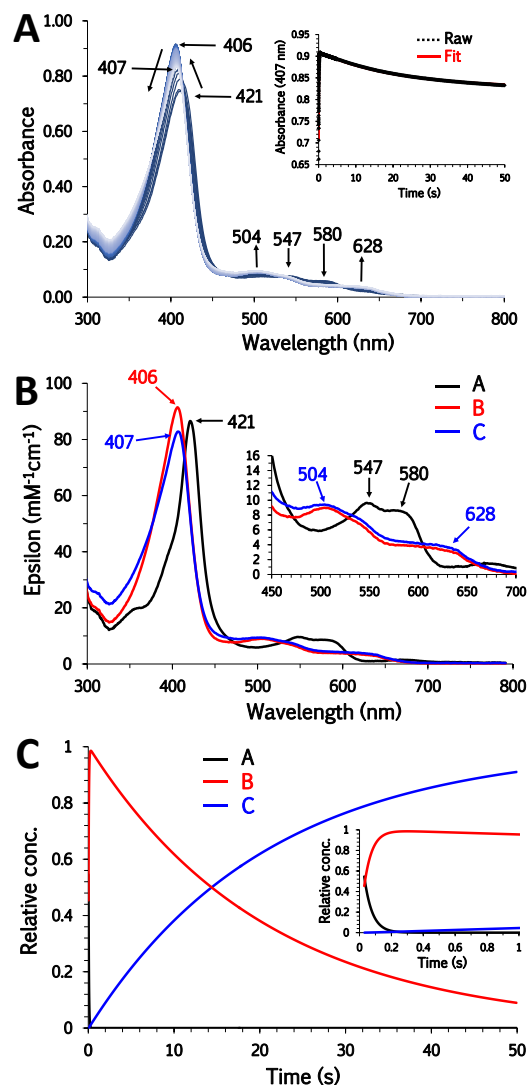


Figure 2.3. Kinetic data for the reaction of pre-formed Compound ES with 2,4-dichlorophenol (2,4-DCP). A) stopped-flow UV-visible spectra of the double-mixing reaction of preformed DHP B Compound ES (10 μM), itself formed in an initial mixing step from ferric DHP reacted with a 10-fold excess of H_2O_2 in an aging line for 500 ms, with a 30-fold excess of 2,4-DCP at pH 7 (900 scans over 50 sec); *inset* - the single wavelength (407 nm) dependence on time obtained from the raw spectra and its fit with a superposition of the calculated spectral components. B) calculated spectra of the three reaction components derived from the SVD analysis: Compound ES (black), ferric DHP B in the presence of excess 2,4-DCP (red), and ferric-like DHP B with excess 2,4-DCP (blue). C) time dependences of the relative concentrations for the three components shown in the middle panel as determined from the fitting of the spectra in the top panel. *inset* – time dependences of concentrations in the initial second of data collection.

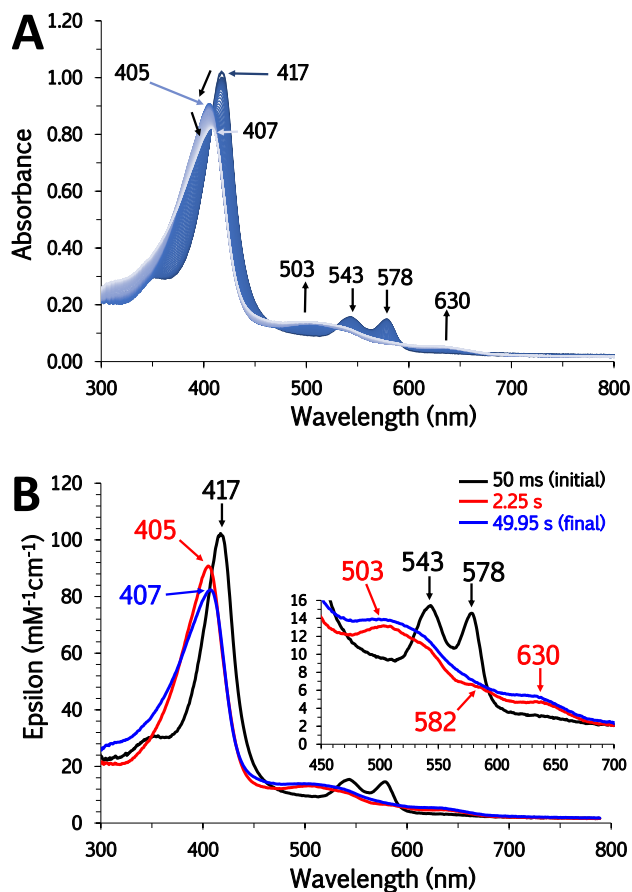


Figure 2.4. Kinetic data for the reaction of oxyferrous DHP B with 2,4-dichlorophenol (2,4-DCP) and hydrogen peroxide. A) stopped-flow UV-visible spectra of the single-mixing reaction between oxyferrous DHP B (10 μM) pre-incubated with 10 equiv. 2,4-DCP and a 10-fold excess of H_2O_2 at pH 7 (900 scans over 50 sec). B) experimentally obtained spectra for oxyferrous DHP B (black, $t = 50$ ms), its reduction to ferric-like DHP B in the presence of excess 2,4-DCP (red, $t = 2.25$ s), and ferric-like DHP B with slight bleaching of the heme ($t = 50$ s).

The main observations from these stopped-flow studies with 2,4-DCP were i) Compound I was rapidly reduced by 2,4-DCP within the mixing time of the instrument to a ferric-like enzyme state; ii) Compound ES and oxyferrous DHP were reduced to a ferric-like enzyme within 200 ms and 2.25 seconds, respectively; iii) 2,4-DCP, in the presence of H_2O_2 , was found

to be capable of oxyferrous DHP B catalytic activation; and iv) no product-driven reduction of the enzyme to the oxyferrous state was observed.

2.4.5 Protein Crystallization and X-ray Diffraction Studies. Non-His tagged DHP B was successfully overexpressed, purified and crystallized. Crystal incubation in the presence of ligand (4-CP, 4-BP, 2,4-DCP or 2,4-DBP) successfully yielded the DHP B – ligand complexes, as determined by X-ray crystallographic diffraction methods. X-ray data collection and refinement statistics are provided in Table 2.3. DHP B crystallized as a homo-dimer in the asymmetric unit of space group $P2_12_12_1$, consistent with each previously deposited crystal structure. The protomer environments were found to be identical within each structure, in particular the orientation of ligand binding site within the DHP B distal cavity. All distances provided are an average between the two promoters. The ligand binding site orientations are shown in Figure 2.5.

The DHP B–2,4-DBP complexed structure (5WMY) possessed R_{merge} , R_{free} and R_{work} values of 15.2%, 20.76%, and 15.88%, respectively (Table 2.3). Refined to a resolution of 1.93 Å, a single binding site in the distal cavity was observed for 2,4-DBP (Figure 2.5 D). Partial occupancy of 2,4-DBP was observed at 90 % in protomer A and 80 % in protomer B, with a distal water bound to the Fe in the absence of substrate. The molecule is bound 4.1 Å above the heme, between the Fe and α edge. The aromatic ring is oriented for π -stacking interactions with F21, the OH group is directed toward the Fe (4.92 Å), the *o*-Br is directed toward the Xe1⁴¹ binding site and the *p*-Br is directed deep in the heme cavity. The distal histidine, H55, was found in the interior, or “closed” conformation within the cavity, with its N^ε at a H-bonding distance of 2.54 Å from the OH group, further stabilizing 2,4-DBP binding.

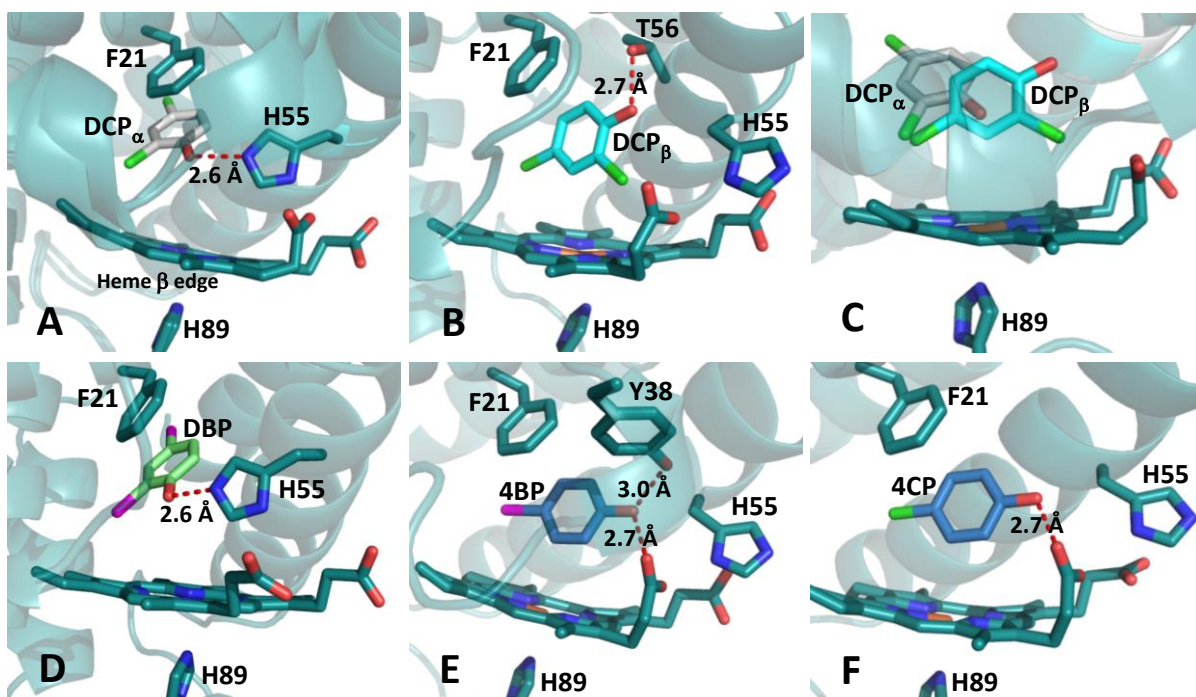


Figure 2.5. X-ray crystal structures depicting the halophenol binding sites within the distal pocket of DHP B, as viewed from the heme β edge. **A)** 2,4- DCP_α binding site, named due to its proximity to the heme α edge (5WMZ). **B)** 2,4- DCP_β binding site, again named due to its orientation with respect to the heme β edge (5WN6). **C)** Superposition of 2,4- DCP_α and 2,4- DCP_β binding sites, showing they are exclusive of each other and both sites cannot be occupied simultaneously. **D)** 2,4-DBP binding site, above the heme α edge (5WMY). **E)** 4-BP distal binding orientation (6AOF). **F)** 4-CP binding orientation (6AOE). 4-BP and 4-CP have identical binding sites, distal of the heme residing between the Fe and β edge.

Table 2.3. X-ray Data Collection and Refinement Statistics for WT DHP B complexed with 2,4-dichlorophenol (2,4-DCP) (5WN6 and 5WMZ), 2,4-dibromophenol (2,4-DBP) (5WMY), 4-chlorophenol (4-CP) (6AOE) and 4-bromophenol (4-BP) (6AOF).

	2,4-DCP _β	2,4-DCP _α	2,4-DBP	4-CP	4-BP
PDB Entry	5WN6	5WMZ	5WMY	6AOE	6AOF
Data Collection					
Wavelength (Å)	1.00	1.00	1.00	1.00	1.00
Temperature (K)	100	100	100	100	100
Space Group	P2 ₁ 2 ₁ 2 ₁				
Unit-cell parameters (Å)					
<i>a</i>	59.60	57.02	56.91	59.58	59.64
<i>b</i>	67.77	66.21	66.25	67.38	67.49
<i>c</i>	67.55	69.97	69.72	67.70	67.75
Unique reflections	20,624 (1,019) ^a	42,731 (2,116) ^a	20,247 (1,016) ^a	21,635 (1,047) ^a	46,357 (2,307) ^a
Completeness (%)	99.6 (99.8) ^a	96.1 (96.7) ^a	98.8 (99.7) ^a	99.6 (99.6) ^a	99.8 (99.8) ^a
R _{merge} (%) ^b	7.1 (48.1)	7.6 (66.7)	15.2 (56.9) ^a	8.1 (56.5) ^a	11.9 (55.0) ^a
I/σ(I)	15.3 (2.2) ^a	19.94 (2.1) ^a	10.9 (2.4) ^a	14.6 (1.9) ^a	20.6 (2.1) ^a
Redundancy	5.6 (5.6) ^a	5.0 (4.9) ^a	4.8 (4.7) ^a	4.8 (4.7) ^a	4.8 (4.3) ^a
Refinement					
Resolution (Å)	1.95	1.49	1.93	1.91	1.48
R _{work} (%) ^c	19.92 (24.40) ^a	14.31 (15.54) ^a	16.23 (18.07) ^a	18.48 (22.51) ^a	17.76 (22.40) ^a
R _{free} (%) ^d	26.13 (28.74) ^a	18.73 (20.78) ^a	20.63 (22.05) ^a	24.47 (28.83) ^a	21.50 (23.89) ^a
No. of protein atoms	2,270	2,390	2,314	2,251	2,397
No. of ligand atoms	18	18	18	16	16
No. of solvent atoms	142	297	245	184	342
R.m.s.d from ideal geometry ^e					
Bond lengths (Å)	0.008	0.005	0.006	0.007	0.006
Bond angles (°)	0.974	0.927	0.884	0.916	0.951
Ramachandran plot (%)					
Most favored region	97.41	97.38	98.15	97.78	98.15
Addl allowed region	2.59	1.87	1.85	2.22	2.59

^aValues in parentheses are for the highest resolution shell. ^bR_{merge} = $\sum_h \sum_i [|I_i(h) - \langle I(h) \rangle| / \sum_h \sum_i I_i(h)] \times 100\%$, where I_i(h) is the ith measurement and ⟨I(h)⟩ is the weighted mean of all measurements of I(h). ^cR_{work} = $\sum |F_o - F_c| / \sum F_o \times 100\%$, where F_o and F_c are the observed and calculated structure factors, respectively. ^dR_{free} is the R factor for the subset (9%) of reflections selected before and not included in the refinement. ^eRoot-mean-square deviation. ^fRamachandran plot created via MolProbity.

Table 2.4. Distal visible spectroscopic features of ferric DHP variants 2,4,6-trihalophenols and 4-halophenols are provided for comparison.

	2,4-DCP_β	2,4-DCP_α	2,4-DBP	4-CP	4-BP	2,4,6-TCP_{ext}	2,4,6-TCP_{int}	2,4,6-TBP
PDB accession code	5WN6	5WMZ	5WMY	6AOE	6AOF	4KMW ²¹	4KMV ²¹	4FH6 ²⁰
H55 N ^ε ...OH (phenol)	7.03	2.59	2.54	5.90	5.99	4.64	2.70	5.22 _{in} /11.69 _{ext}
H55 N ^δ ...OH (phenol)	5.28	4.53	4.51	4.93	4.08	2.52	4.70	6.41 _{in} /10.51 _{ext}
F21 C ^ζ ... C ¹ (phenol)	4.18 (C ²)	3.89	3.80	4.55 (C ²)	4.69 (C ²)	5.63 (C ²)	4.18	5.49
F21 C ^γ ... C ⁴ (phenol)	3.43 (C ⁵)	4.01	4.00	3.63 (C ⁵)	3.66 (C ⁵)	4.73 (C ⁵)	4.16	6.02
Fe...OH (phenol)	7.07	4.88	4.92	6.67	6.73	7.95	4.62	3.89
Fe...X ^{C2} (phenol)	4.93	5.13	5.14	----	----	6.32	5.13	4.45
Fe...X ^{C4} (phenol)	4.65	8.62	8.74	4.95	5.01	3.53	9.11	9.04
Fe...X ^{C6} (phenol)	----	----	----	----	----	8.64	6.88	6.01
Fe-H55 N ^δ	8.57	6.22	6.19	8.45	8.47	8.41	5.99	6.36 _{in} /9.52 _{ex}
Fe-H55 N ^ε	10.44	5.80	5.74	10.37	10.46	9.71	5.40	5.14 _{in} /10.42 _{ex}
Fe-H89 N ^ε	2.35	2.24	2.31	2.34	2.22	2.36	2.14	2.09
Fe to pyrrole N plane	0.09	0.07	0.11	0.055	0.063	0.075	0.045	0.046

Two binding orientations were determined for 2,4-DCP, labeled with respect to their proximity to the heme α and β edges as 2,4-DCP $_{\alpha}$ (Figure 2.5 A) and 2,4-DCP $_{\beta}$ (Figure 2.5 B), respectively. The DHP B–2,4-DCP $_{\alpha}$ complex possesses R_{merge} , R_{free} and R_{work} values of 7.6 %, 18.69 %, and 14.31 %, respectively, and refined to a resolution of 1.49 Å (Table 2.3). Partial occupancy of 2,4-DCP $_{\alpha}$ was observed at 81 % in protomer A and 94 % in protomer B. The DHP B–2,4-DCP $_{\beta}$ complex provided R_{merge} , R_{free} and R_{work} values of 7.1 %, 26.86 %, and 20.16 %, respectively, refining to a resolution of 1.95 Å (Table 2.3). Partial occupancy of 2,4-DCP $_{\beta}$ was observed at 80 % in protomer B with full occupancy in protomer A. The binding orientation of 2,4-DCP $_{\alpha}$ is identical to that observed for 2,4-DBP (Figure 2.6 A). The 2,4-DCP $_{\beta}$ binding site orients the molecule above the heme, between the Fe and β edge. The O γ of T56 is rotated into the distal pocket interacting with the OH group of 2,4-DCP $_{\beta}$ at a hydrogen bonding distance of 2.7 Å. The Cl atoms are facing toward the heme, with the *p*-Cl directed toward the Xe1 binding site and the *o*-Cl oriented toward the cavity entrance at the heme γ edge (Figure 2.5 B). In this orientation, H55 is found in the solvent-exposed, or “open” conformation. The 2,4-DCP $_{\beta}$ binding site is very similar to the orientation of 4-nitrocatechol (4-NC), another peroxidase substrate. Both 2,4-DCP $_{\beta}$ and 4-NC are located in the distal pocket between the heme Fe and β edge, interact with T56 via H-bonding, the substituent on the 4th position resides in the Xe1 binding site, and H55 is observed in the external conformation.

The monohalophenol (4-XP, X = F, Cl, Br, I) binding sites have been previously elucidated by X-ray crystallography in DHP A.¹¹ Given that 2,4-DCP and 2,4-DBP were complexed with DHP B, for comparative purposes the 4-CP and 4-BP complexes of DHP B were structurally characterized here by X-ray crystallography. The DHP B–4-CP complex yielded R_{merge} , R_{free} and R_{work} values of 8.1%, 24.07% and 18.50%, respectively, and refined to a resolution of 1.92 Å (Table 2.3). The binding site orientation is identical within the dimer, with partial occupancies of 78 % and 93 % for protomers A and B, respectively. Similar to the 2,4-DCP $_{\beta}$ binding site, 4-CP was observed distal to the heme between the Fe and β edge, resulting in H55 exclusion from the distal pocket and occupying its external conformation (Figure 2.5 F). The

Cl atom resides in the Xe1 site while the OH group is directed toward the cavity opening, at a H-bonding distance of 2.7 Å from the heme propionate arm D.

The DHP B–4-BP structure refined to a resolution of 1.48 Å, possessing R_{merge} , R_{free} and R_{work} values of 11.9%, 20.97% and 17.80%, respectively (Table 2.3). Although 4-BP occupancy of 82 % in protomer A differs from 73 % in protomer B, the binding environments are identical. The substitution of Cl for the larger halide Br bears no consequence on binding orientation, reflected in the observation of 4-BP residing in the same orientation as 4-CP (Figure 2.5 E). The only noticeable difference in the distal environment is the position of Y38 within H-bonding distance of 3.0 Å with the OH moiety of 4-BP. Analysis of 4-CP and 4-BP binding sites with respect to DHP A¹¹ and DHP B yielded virtually identical orientations, showing the isoenzymes of DHP to have no consequence on distal ligand binding. This is further supported in the DHP A–2,4-DCP complexed structure, showing 2,4-DCP's orientation to be identical to the 2,4-DCP_β binding site. However, for consistency, further analysis of 4-CP and 4-BP binding sites will focus on DHP B structures. Structures of DHP B in complex with either 2,4,6-trichlorophenol (TCP) or 2,4,6-tribromophenol (TBP) were unable to be obtained.

2.5 Discussion

The activity studies presented here demonstrate that DHP is able to catalyze the oxidation of 2,4-dihalophenols in the presence of hydrogen peroxide via sequential peroxidase and peroxygenase steps. Isotope labeling studies demonstrated that the first oxygen atom incorporated into the initial diol product was derived exclusively from water. Such chemistry has previously been reported for the oxidation of 2,4,6-trihalophenols by DHP proceeding via a well-established peroxidase mechanism.¹⁸ Interestingly, the diol product itself proved to be a substrate for DHP, yielding halogenated benzenetriol and hydroxybenzoquinone products in what labeling studies indicate proceeds via a peroxygenase-based mechanism. Thus, the sequential oxidation of both 2,4-DCP and 2,4-DBP is shown to utilize the multi-functional nature of DHP B to perform the chemistry observed. This differs from the well-studied

oxidation of peroxidase substrates, 2,4,6-TCP and 2,4,6-TBP, which results in the formation of a single major product. However, sequential oxidation and multifunctional activation have been observed previously in the oxidation of 4-nitrophenol (4NP). But in contrast to the chemistry observed for 2,4-DCP and 2,4-DBP, 4NP oxidation initially proceeds through a peroxygenase mechanism then subsequent peroxidase reactivity.

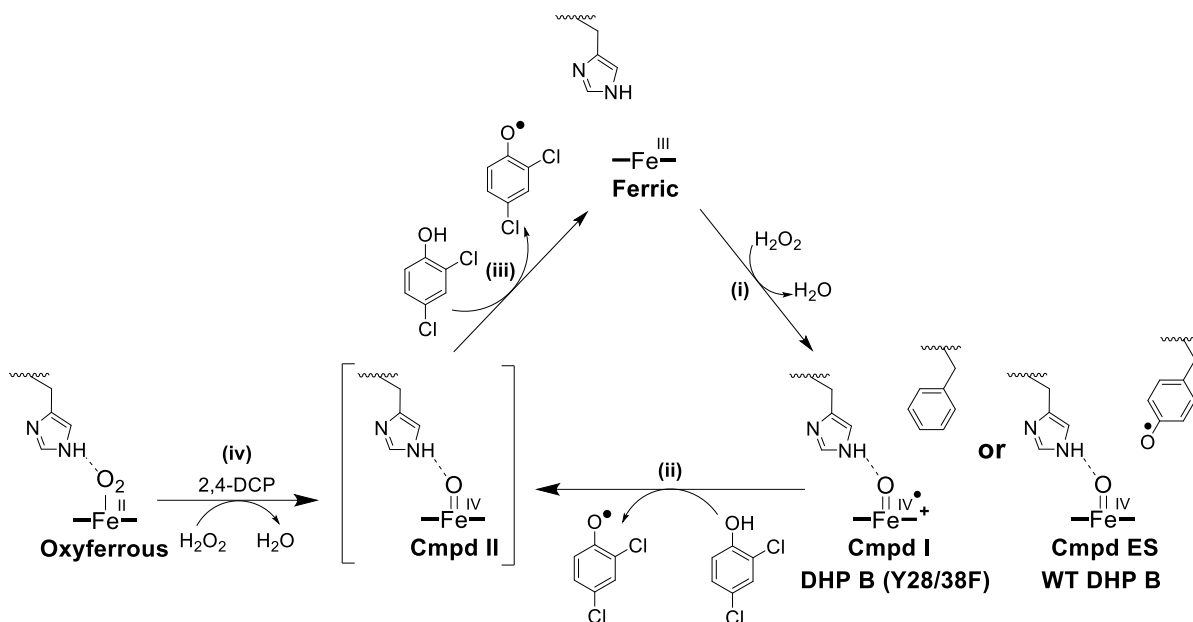
As the principal reactive species in heme peroxidases,⁴² P450s,^{43,44} peroxygenases,⁴⁵ and other hemoproteins,^{46,47} the ferryl-containing Compound I, ES, and II intermediates were explored here for their mechanistic role(s) in the DHP-catalyzed oxidation of 2,4-DCP. Compounds I and ES, either of which is formed from the reaction of the ferric enzyme with hydrogen peroxide, both contain an Fe(IV)-oxo species, yet differ in that Compound I possesses a second oxidizing equivalent as a porphyrin π -cation radical, whereas Compound ES has this radical residing on an amino acid (i.e., a tyrosyl radical in DHP²²) rather than on the porphyrin ring.^{7,28} Compound II also possesses a ferryl center, but no additional oxidizing equivalent. When pre-formed from the DHP B(Y28F/Y38F) mutant owing to the lack of tyrosines near the heme active site,³⁹ the reaction of Compound I with 2,4-DCP yielded ferric DHP within the mixing time (<1.5 ms) of the stopped-flow apparatus. Complete reduction of Compound I back to the ferric enzyme has been consistently observed within the instrument mixing time for the previously studied nitrophenol, haloindole, and pyrrole substrates. By comparison, when pre-formed from the wild-type enzyme, Compound ES was reduced by 2,4-DCP to ferric DHP within 250 ms, with an apparent rate constant (k_{obs}) of $20.19 \pm 0.03 \text{ s}^{-1}$, which is slower than its reduction by 5BI (<2.5 ms, 25 eq.), yet considerably faster than reduction by TCP (18.5 s, 30 eq.), pyrrole (22 s, 50 eq.) or 4NP (~30 s, pH 6.0, 10 eq.) under similar experimental conditions (100 mM KPi , pH 7). The results suggest that both Compounds I and ES are catalytically competent species for the oxidation of 2,4-DCP via a peroxidase mechanism.

When starting in the oxyferrous state, DHP reactivity has been shown previously to be initiated via a Compound II intermediate when in the presence of hydrogen peroxide and 1 equiv substrate (TCP or haloindole). Here, oxyferrous DHP B was activated by 2,4-DCP in the

presence of H₂O₂, however the enzyme was oxidized to the ferric state in 2.25 seconds without an observable Compound II species. Interestingly, oxyferrous DHP B reactivity in the presence of 2,4-DCP (10 eq.) showed conversion within 2.25 s, faster than TCP (10.5 s, pH 8.0, 30 eq.), 5BI (> 30 s, 2.5 eq., 5 eq. H₂O₂), 4NP (8 s, pH 6.0, 10 eq.) and pyrrole (>50 s, 50 eq.).

Despite the broad range exhibited in their pre-steady state kinetics, the results from the 2,4-DCP endpoint assays (Table 2.1) show that virtually identical substrate loss and product formation were observed whether ferric DHP B (Compound ES) or oxyferrous DHP B (Compound II) were employed. One possible interpretation of these kinetic vs. endpoint assay results is that DHP proceeds through a common pathway regardless of the starting conditions. As both reactive intermediates (Compounds I and ES) were reduced by substrate to the ferric enzyme, we suggest that in addition to the 2-electron chemistry associated with Compound I, one-electron processes may play a role in the initial turnover of DHP, for example, to reduce Compound II to the ferric state, and that the subsequent activity (either peroxygenase or peroxidase) proceeds as observed from the ferric enzyme.

On the basis of the results obtained above, we propose the following catalytic cycle for the *in vitro* hydrogen peroxide-dependent oxidation of 2,4-dichlorophenol by ferric DHP (Scheme 2.3): ferric DHP reacts with 1 equiv. H₂O₂ (step i), forming either Compound I (DHP B (Y28F/Y38F)) or Compound ES (WT DHP B). One-electron reduction of either of these two ferryl species by 2,4-DCP leads to formation of Compound II (step ii). Compound II is further reduced in a second one electron step by 2,4-DCP, leading to regeneration of the ferric enzyme (step iii). The ferric enzyme is then available for reactivation by a second equivalent of hydrogen peroxide, thereby leading to additional benzenediol formation when reacting with 2,4-DCP as the substrate (via a second peroxidase cycle), or to hydroxybenzoquinone formation via a peroxygenase cycle.



Scheme 2.3. Proposed 2,4-Dichlorophenol Peroxidase Cycle for Dehaloperoxidase B.

Three additional comments can be made about the 2,4-DCP peroxidase mechanism in DHP: first, although Scheme 2.3 presents a ferric-centric catalytic cycle, it has been demonstrated previously that DHP is able to initiate both peroxidase and peroxygenase catalytic cycles from the globin-active oxyferrous state: oxyferrous DHP reacts with H_2O_2 in the presence of either trihalophenol^{8,19,40} or haloindoles⁴ substrate, thereby forming Compound II. Here, we did not observe Compound II formation when employing 2,4-DCP as substrate when starting from oxyferrous DHP (step iv). However, it is likely that when starting from the oxyferrous form, Compound II is formed initially and the catalytic cycle commences directly from Compound II and proceeds as stated in Scheme 2.3. Second, it is important to note under these conditions that Compound RH, the stable form of DHP that forms from H_2O_2 -activation in the absence of substrate, was not observed. Third, the conversion to oxyferrous DHP that is noted in similar assays which employ other physiological substrates (i.e., trihalophenols and haloindoles) was also not observed. Thus, the product-driven^{4,7} reduction of ferric DHP that

rescues the globin-active oxyferrous form was not observed here, an outcome that was unexpected given that 2,4-DCP is likely a physiological substrate.

Superpositions of 4-BP, 2,4-DBP and 2,4,6-TBP binding sites are provided in Figure 2.6B and 4-CP, 2,4-DCP and 2,4,6-TCP binding sites are superposed in Figure 2.6 C-D, with representative atomic distances provided in Table 2.4. Halophenol binding can be analyzed in relation to the number of halogens:

I) Monohalophenol binding - Both 4-BP and 4-CP bind distal to the heme, between the Fe and heme β edge, with their respective halogen residing in the Xe1 binding site. The OH group is directed toward the cavity entrance, resulting in the H55 residing in the external conformation.

II) Dihalophenol binding - The *p*-halophenol site binding is very similar to that of 2,4-DCP $_{\beta}$, with both located in the same position distal to the heme, the *para*- halogens are located in the Xe1 site, and H55 adopts its external conformation (Figure 2.6 D). With regard to the 2,4-DCP $_{\alpha}$ and 2,4-DBP binding sites, the main similarity to the 4-halophenol binding site is the presence of a halogen in the Xe1 binding site. However, for 2,4-DCP $_{\alpha}$ and 2,4-DBP this halogen is located at the *ortho* rather than the *para* position (Figure 2.6, C and B, respectively). Thus, the presence of the second halogen rotates the molecule to accommodate α -edge binding.

III) Trihalophenol binding - For TXP binding, the addition of the third halogen directs 2,4,6-TBP²⁰ and 2,4,6-TCP $_{\text{int}}$ ²¹ (Figure 2.6, B and C, respectively) both to bind deep in the distal cavity beneath F21 at the α edge of the heme in close proximity to L100, residing in the Xe1 binding site⁴¹ with the hydroxyl group pointed towards the heme Fe, and H55 adopting the internal conformation.^{11,16} This is similar to 2,4-DBP and 2,4-DCP $_{\alpha}$, as all substrates reside at the heme α edge, the OH is directed toward the heme Fe and H55 resides in the distal cavity, however the presence of a third halogen on 2,4,6-TBP and 2,4,6-TCP $_{\text{int}}$ places the entire molecule in the Xe1 binding site instead of one halogen atom. A second binding site is observed for 2,4,6-TCP $_{\text{ext}}$ which slightly resembles the 2,4-DCP $_{\beta}$ binding site from similar distal locations and the external H55 conformation (Figure 2.6 D). However, the *p*-Cl atom of 2,4,6-TCP $_{\text{ext}}$ is positioned toward the heme Fe and the phenolic OH is within hydrogen bonding

distance to Y38, as previously seen with para-substituted phenol substrates. There is no occupancy in the Xe1 binding site, with the 2,4,6-TCP_{ext} molecule situated at the γ edge of the heme between both heme propionate arms. Both 2,4,6-TCP_{ext} and 2,4-DCP _{β} molecules are observed near the cavity entrance with their OH directed toward the exterior. However, 2,4,6-TCP_{ext} resides closer to the cavity entrance, possibly due to the additional steric hindrance induced by the addition of a Cl atom. This is in contrast to 2,4,6-TBP and 2,4,6-TCP_{int} binding, where the presence of the 3rd halogen results in binding deeper in the distal pocket than 2,4-DCP _{α} and 2,4-DBP substrates.

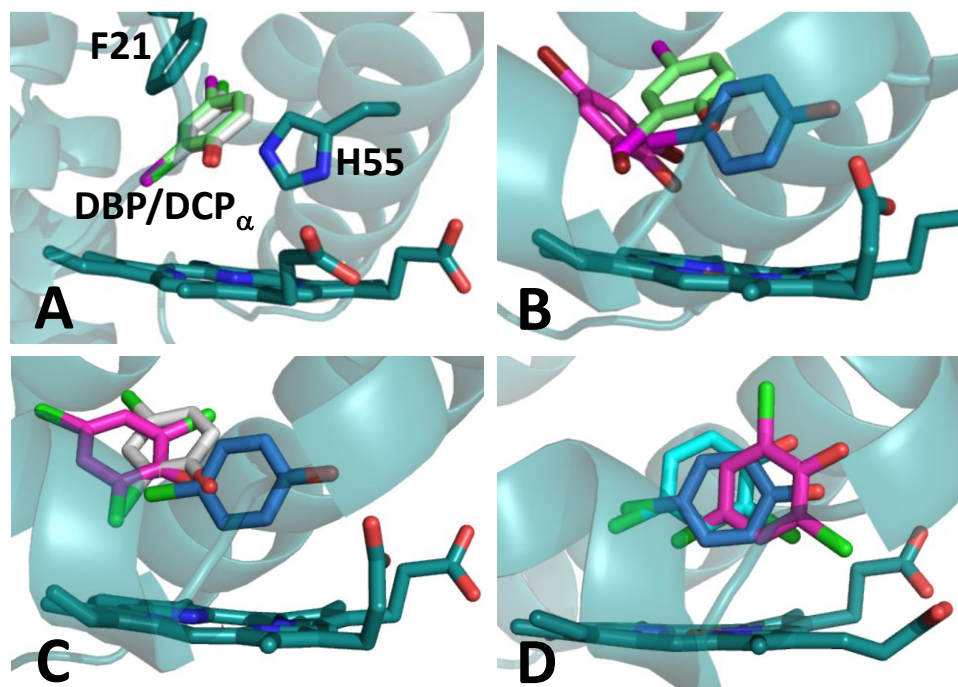


Figure 2.6. Superposition of selected halophenol binding sites. **A)** 2,4-DBP (green) and 2,4-DCP _{α} (silver), showing these two molecules possess identical binding sites. **B – D)** Comparison of monohalophenol (blue) and trihalophenol (pink) binding sites with the elucidated dihalophenol binding sites. **B)** Brominated variants: 4-bromophenol, 2,4-dibromophenol and 2,4,6-tribromophenol. **C)** Chlorinated variants (α heme edge proximity): 4-chlorophenol, 2,4-dichlorophenol _{α} and 2,4,6-trichlorophenol_{int}. **D)** Chlorinated variants (β heme edge proximity): 4-chlorophenol, 2,4-dichlorophenol _{β} and 2,4,6-trichlorophenol_{ext}.

For 2,4-DCP_α and 2,4-DBP, the presence of two halogens places the phenol into an orientation that favors π -stacking interactions with F21, the *ortho*-halogen into the well-established Xe1 site, the *para*-halogen deep into the hydrophobic cavity and stabilization from H55 via H-bonding. For these binding sites, the addition of the third halogen reduces favorable F21 interactions through molecular rotation, deeper binding to accommodate the additional steric bulk and a severance of H55 interactions. On the other hand, reduction down to 1 halogen still shows halogen stabilization in the Xe1 site, but greatly decreases F21 interactions and H55 is not interacting. Thus, by analyzing the stabilization factors surrounding each binding site, it is shown that 2,4-DCP_α and 2,4-DBP have the most favorable interactions and their binding orientations support their extremely tight binding affinity for DHP.

2.6 Conclusion

In summary, analysis of DHP reactivity with 2,4-DCP and 2,4-DBP provides further information on the plasticity of the heme active center, both structurally and mechanistically. Initial oxidation of 2,4-DCP and 2,4-DBP substrates occurs through a peroxidase pathway, with subsequent oxidation proceeding through a peroxygenase mechanism. An alternate dehalogenation pathway is present in 2,4-DCP, but unobserved for 2,4-DBP reactivity. The high reactivity could be related, in part, by the observation that 2,4-DCP and 2,4-DBP have the lowest K_d values of any known substrate. X-ray crystallographic studies revealed the binding sites of 2,4-DBP and 2,4-DCP to reside inside the distal cavity, which provides information on the consequence of substrate structure on binding orientation, specifically for halophenols. In support of the observed peroxidase activity, 2,4-DCP and 2,4-DBP were shown to bind in similar orientations to the trihalophenol peroxidase substrates. Thus, as the structural intermediate between 4-halophenol inhibition and 2,4,6-halophenol peroxidase reactivity, 2,4-dihalophenol was found to bind in the distal cavity, with the highest affinity observed, exhibits the highest substrate reactivity known, and is capable of activating both the peroxidase and peroxygenase mechanisms through sequential oxidation steps.

2.7 Supporting Information

Figure S2.7. Optical difference spectra and titration curves of 2,4-DCP and 2,4-DBP binding to ferric DHP B.

Figure S2.8. LC chromatogram of the reaction of 2,4-dichlorophenol with DHP B and the ESI-MS total ion chromatograms obtained for single ring species.

Figure S2.9. ESI-MS total ion chromatograms for products **1a** (A) and **1c** (B) obtained under each ^{18}O labeling reaction condition.

Figure S2.10. ESI-MS total ion chromatograms for products **1c** (A) and **1d** (B) obtained under each ^{18}O labeling reaction condition.

Figure S2.11. LC chromatogram of the reaction of 2,4-dibromophenol with DHP B and the ESI-MS total ion chromatograms obtained for single ring species.

Figure S2.12. ESI-MS total ion chromatograms for products **2a** (A), **2b** (B) and **2c** (C) obtained under each ^{18}O labeling reaction condition.

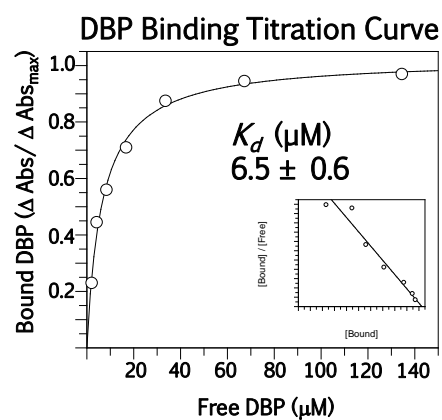
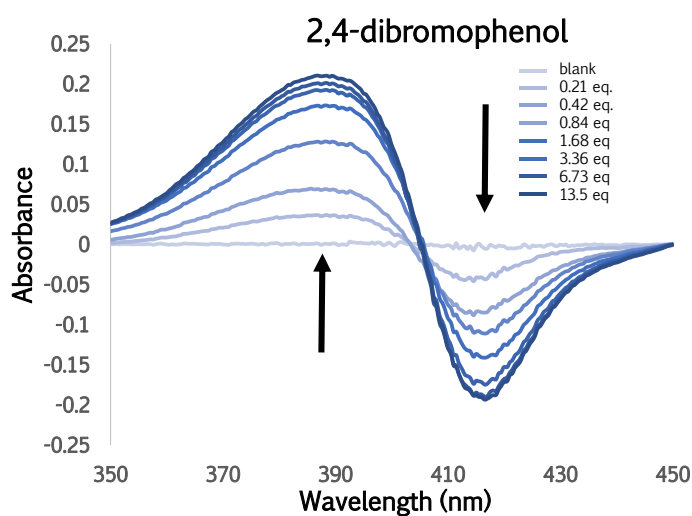
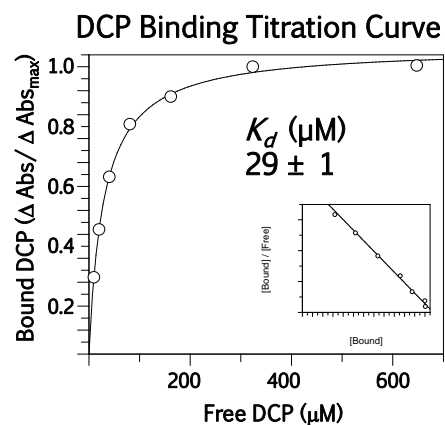
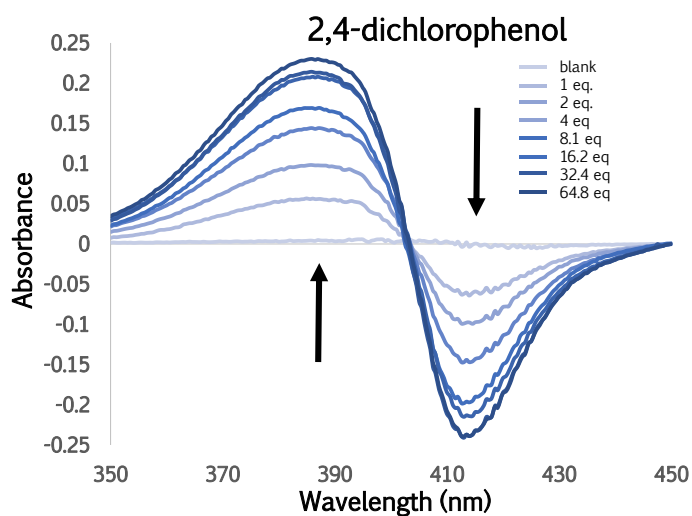


Figure S2.7. Optical difference spectra (left) and titration curves (right) of 2,4-dichlorophenol (top) and 2,4-dibromophenol (bottom) binding to 10 μM DHP B (100 mM KPi , pH 7, 5% MeOH v/v). The calculated dissociation constant is provided in each titration curve.

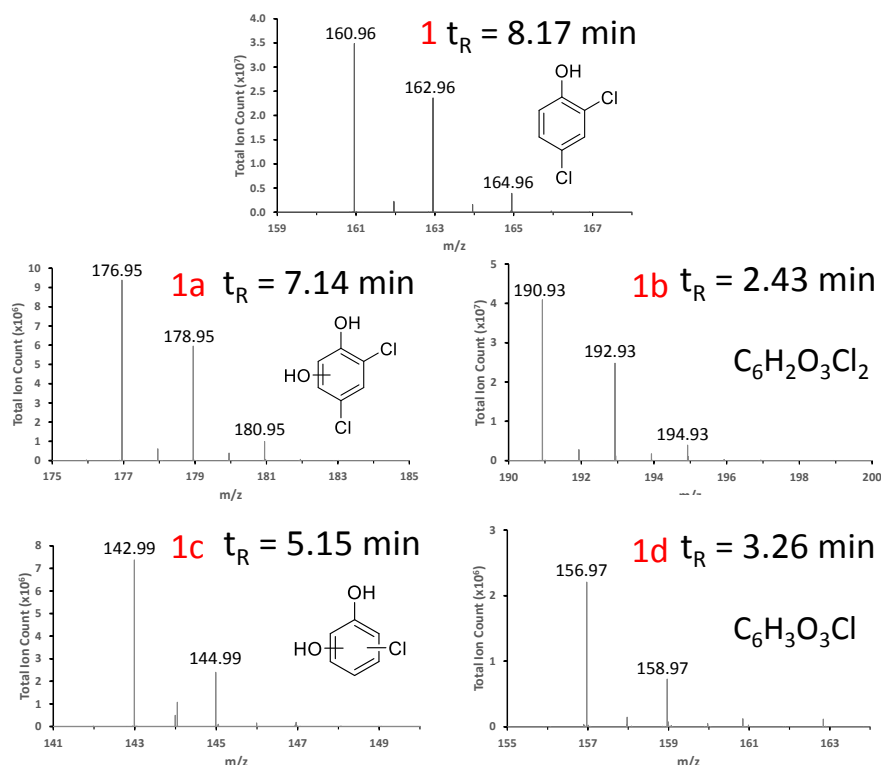
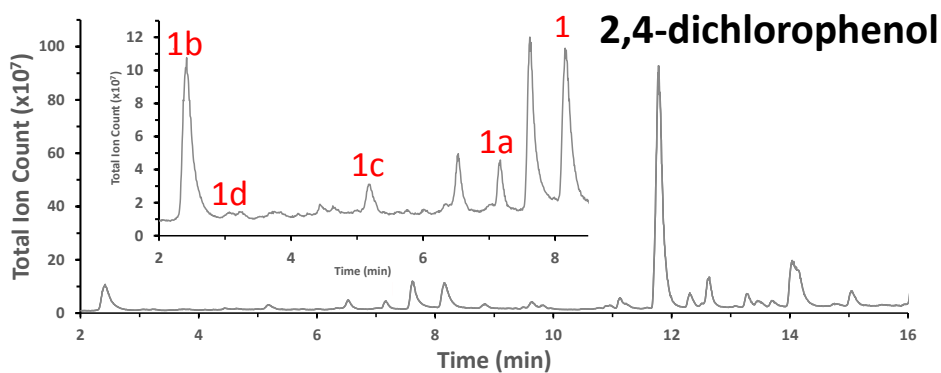


Figure S2.8. TOP: LC chromatogram of the reaction of 2,4-dichlorophenol (500 μM) with DHP B (10 μM) in the presence of H_2O_2 (500 μM) at 25 $^\circ\text{C}$ (5% MeOH in 100 mM KPi , pH 7). Unlabeled peaks correspond to dimer and trimer products of various levels of oxidation and chlorination. **BOTTOM:** ESI-MS total ion chromatograms obtained for single ring species. **1)** 2,4-DCP substrate, **1a)** product with incorporation of 1 O atom, **1b)** product with incorporation of 2 O atoms, **1c)** singly dechlorinated product with incorporation of 1 O atom, **1d)** singly dechlorinated product with incorporation of 2 O atoms.

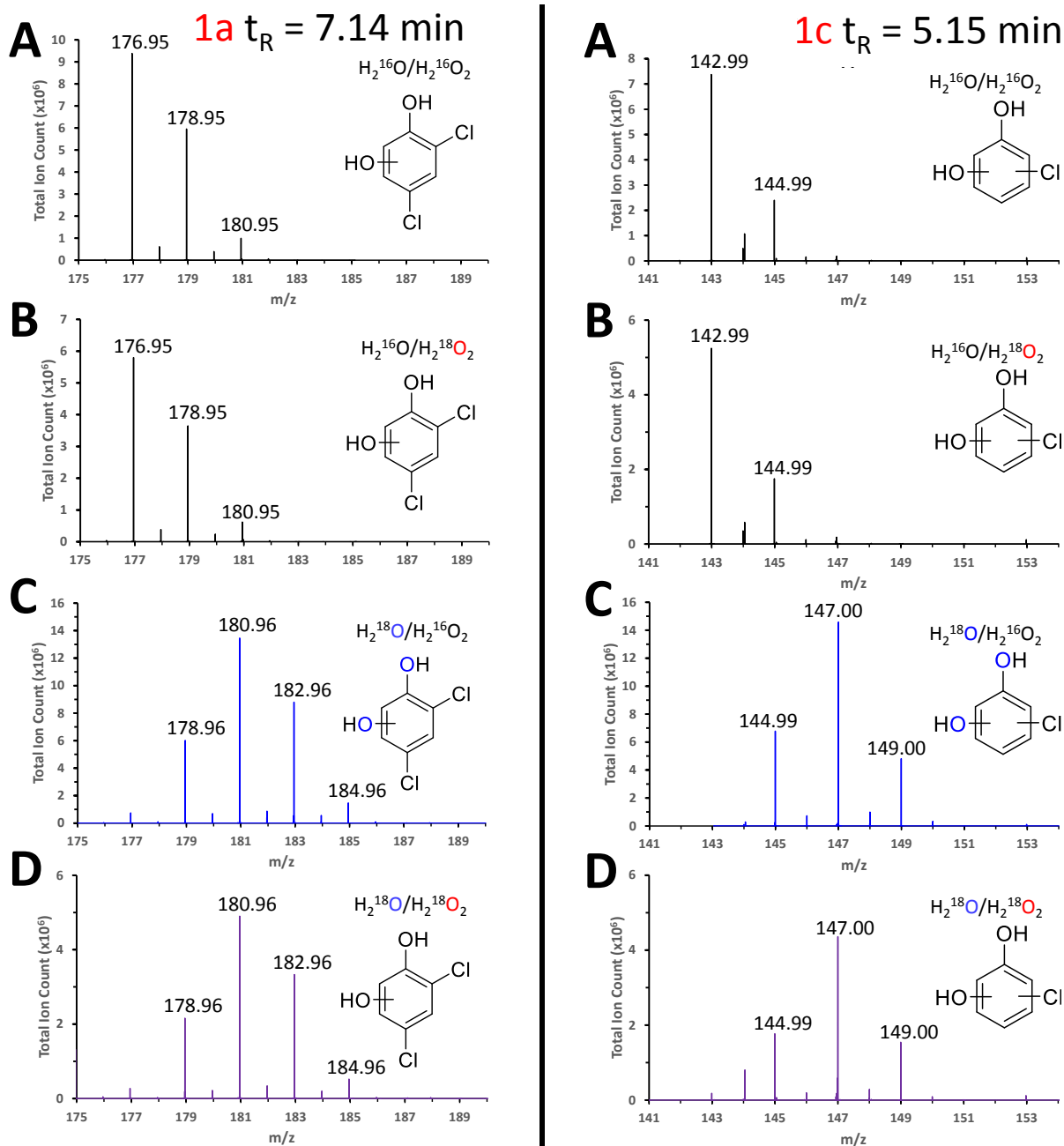


Figure S2.9. ESI-MS total ion chromatograms obtained from the **1a** (left panel) and **1c** (right panel) reaction products of the ^{18}O isotopic labeled 2,4-DCP oxidation catalyzed by ferric DHP B conducted under the following conditions: **A)** unlabeled water and hydrogen peroxide **B)** labeled $\text{H}_2^{18}\text{O}_2$ and unlabeled water; **C)** labeled H_2^{18}O and unlabeled hydrogen peroxide; **D)** ^{18}O labels on both $\text{H}_2^{18}\text{O}_2$ and H_2^{18}O .

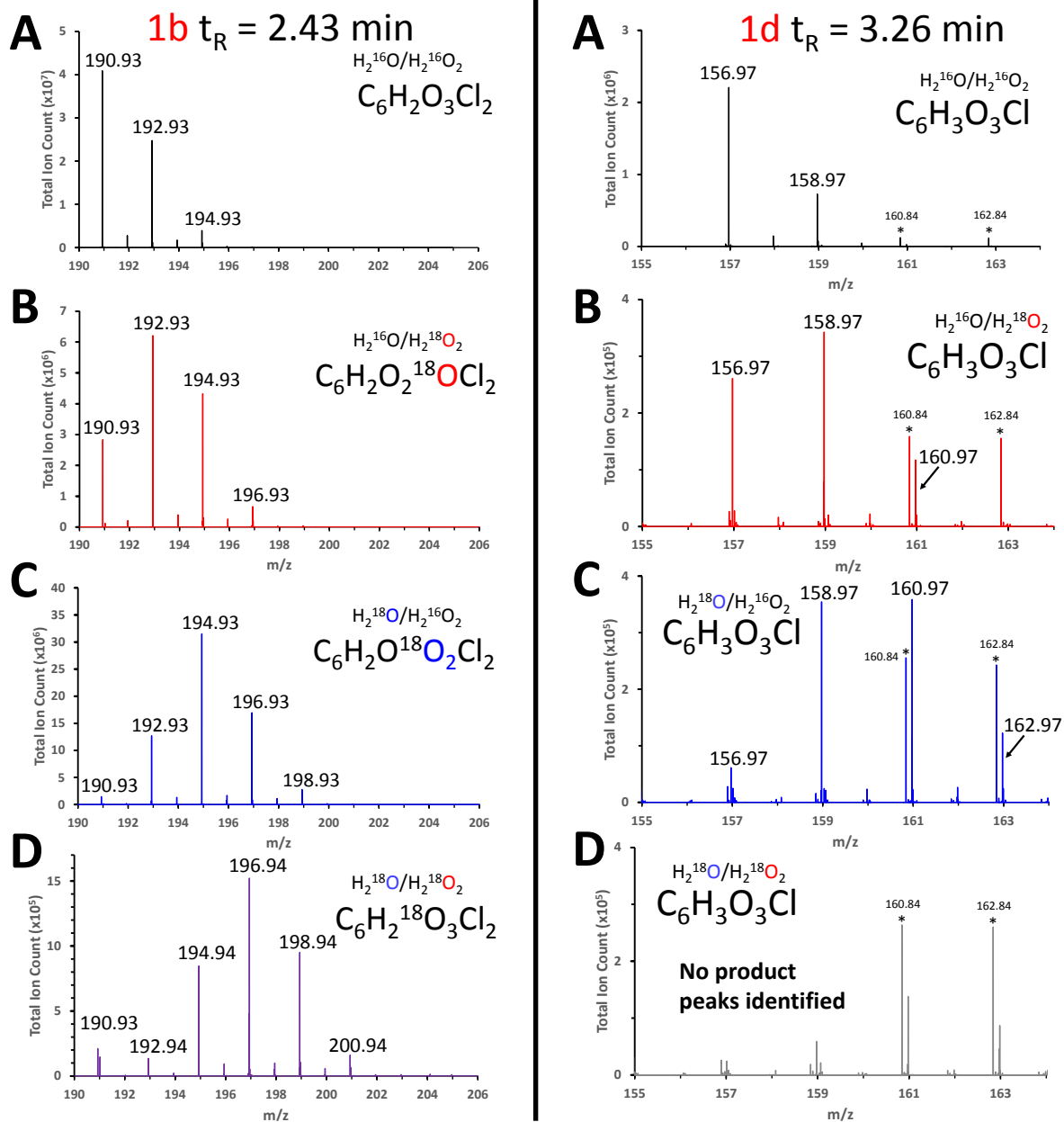


Figure S2.10. ESI-MS total ion chromatograms obtained from the **1b** (left panel) and **1d** (right panel) reaction products of the ^{18}O isotopic labeled 2,4-DCP oxidation catalyzed by ferric DHP B conducted under the following conditions: **A)** unlabeled water and hydrogen peroxide **B)** labeled $H_2^{18}O_2$ and unlabeled water; **C)** labeled $H_2^{18}O$ and unlabeled hydrogen peroxide; **D)** ^{18}O labels on both $H_2^{18}O_2$ and $H_2^{18}O$.

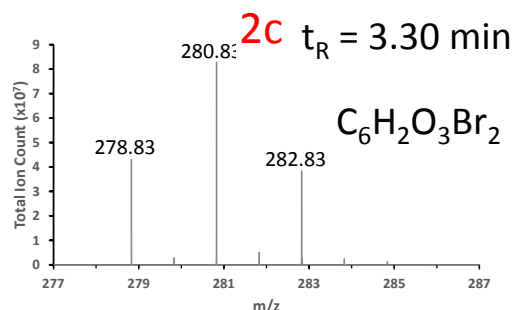
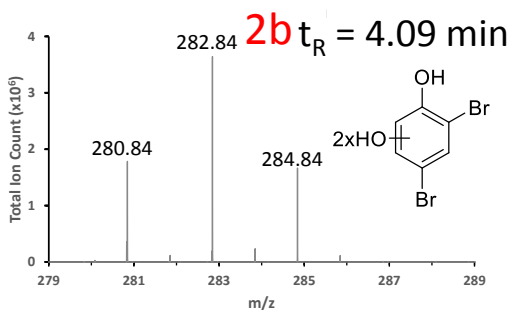
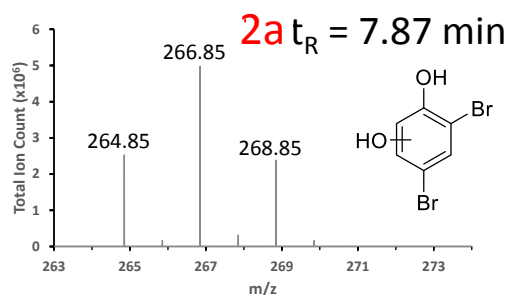
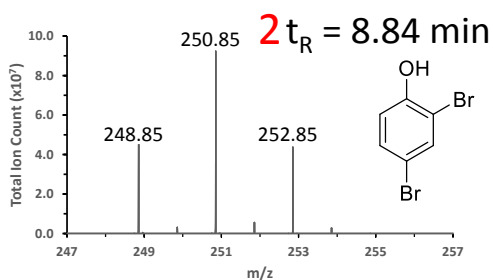
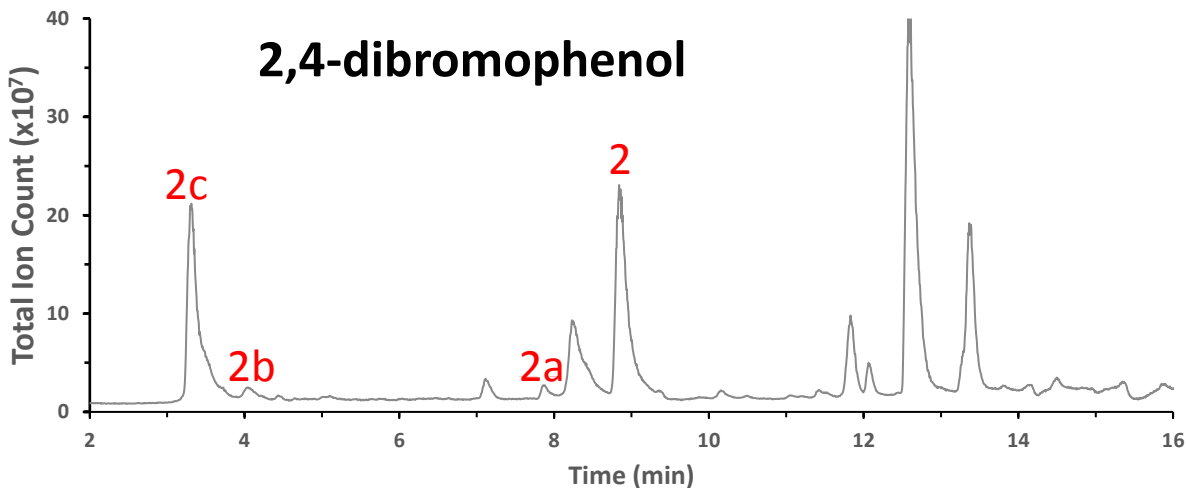


Figure S2.11. TOP: LC chromatogram of the reaction of 2,4-dibromophenol (500 μM) with DHP B (10 μM) in the presence of H_2O_2 (500 μM) at 25 $^\circ\text{C}$ (5% MeOH in 100 mM KPi , pH 7). Unlabeled peaks correspond to dimer and trimer products of various levels of oxidation and bromination. **BOTTOM:** ESI-MS total ion chromatograms obtained for single ring species. **2)** 2,4-DBP substrate **2a)** product with incorporation of 1 O atom **2b)** product with incorporation of 2 O atoms (triol) **2c)** product with incorporation of 2 O atoms (hydroxy-quinone).

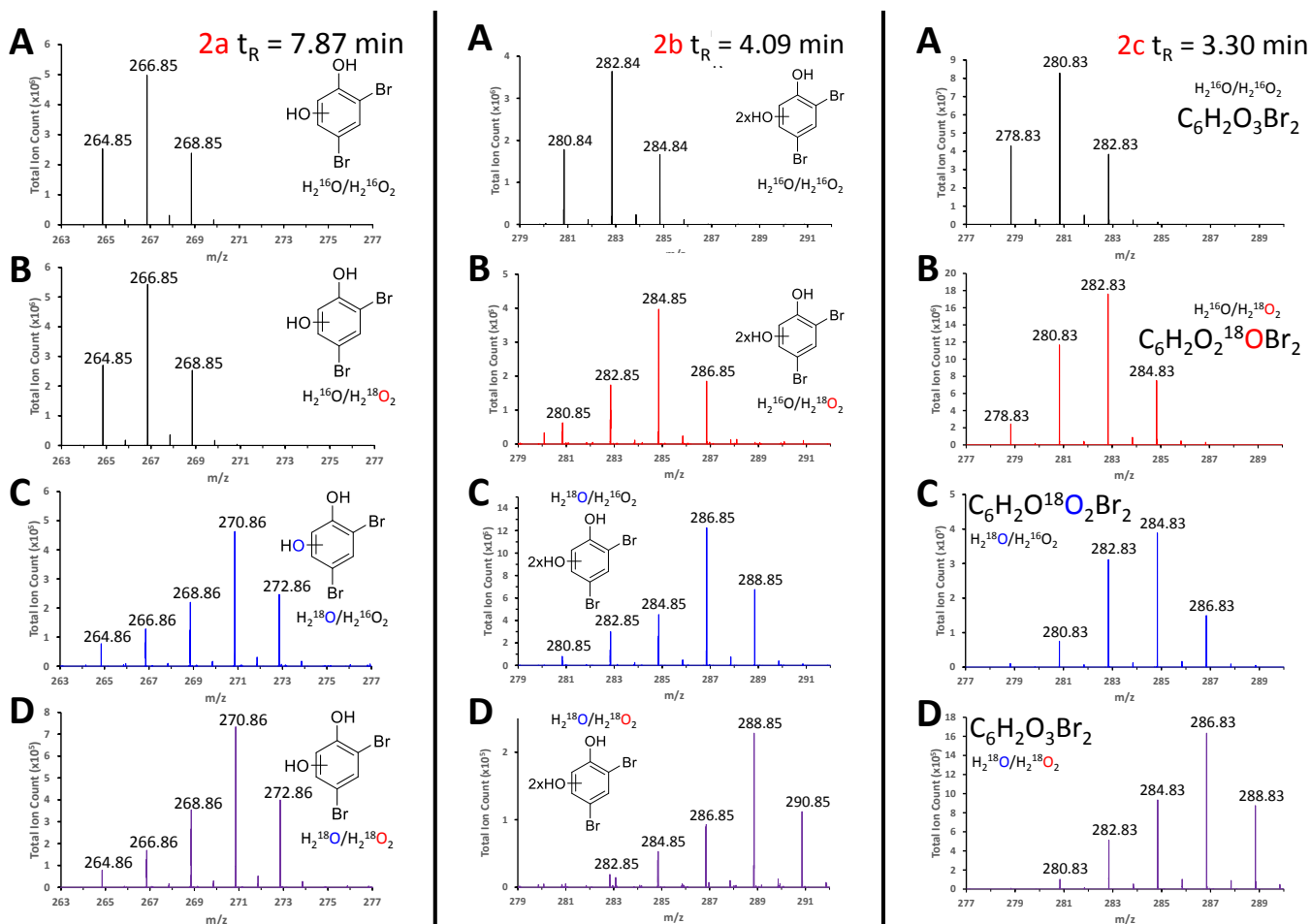


Figure S2.12. ESI-MS total ion chromatograms obtained from the **2a** (left panel), **2b** (middle panel) and **2c** (right panel) reaction products of the ^{18}O isotopic labeled 2,4-DBP oxidation catalyzed by ferric DHP B conducted under the following conditions: **A**) unlabeled water and hydrogen peroxide **B**) labeled $H_2^{18}O_2$ and unlabeled water; **C**) labeled $H_2^{18}O$ and unlabeled hydrogen peroxide; **D**) ^{18}O labels on both $H_2^{18}O_2$ and $H_2^{18}O$.

2.8 References

- (1) Osborne, R. L.; Coggins, M. K.; Raner, G. M.; Walla, M.; Dawson, J. H. The Mechanism of Oxidative Halophenol Dehalogenation by Amphitrite Ornata Dehaloperoxidase Is Initiated by H₂O₂ Binding and Involves Two Consecutive One-Electron Steps: Role of Ferryl Intermediates. *Biochemistry* **2009**, *48* (20), 4231–4238.
- (2) Franzen, S.; Thompson, M. K.; Ghiladi, R. A. The Dehaloperoxidase Paradox. *Biochim. Biophys. Acta - Proteins Proteomics* **2012**, *1824* (4), 578–588.
- (3) Belyea, J.; Gilvey, L. B.; Davis, M. F.; Godek, M.; Sit, T. L.; Lommel, S. A.; Franzen, S. Enzyme Function of the Globin Dehaloperoxidase from Amphitrite Ornata Is Activated by Substrate Binding. *Biochemistry* **2005**, *44* (48), 15637–15644.
- (4) Barrios, D. A.; Antonio, J. D.; McCombs, N. L.; Zhao, J.; Franzen, S.; Schmidt, A. C.; Sombers, L. A.; Ghiladi, R. A. Peroxygenase and Oxidase Activities of Dehaloperoxidase-Hemoglobin from Amphitrite Ornata. *J. Am. Chem. Soc* **2014**, *136*, 7914–7925.
- (5) McCombs, N. L.; D'Antonio, J.; Barrios, D. A.; Carey, L. M.; Ghiladi, R. A. Nonmicrobial Nitrophenol Degradation via Peroxygenase Activity of Dehaloperoxidase-Hemoglobin from Amphitrite Ornata. *Biochemistry* **2016**, *55* (17), 2465–2478.
- (6) McCombs, N. L.; Smirnova, T.; Ghiladi, R. A. Oxidation of Pyrrole by Dehaloperoxidase-Hemoglobin: Chemoenzymatic Synthesis of Pyrrolin-2-Ones. *Catal. Sci. Technol.* **2017**, *7* (14), 3104–3118.
- (7) D'Antonio, J.; D'Antonio, E. L.; Thompson, M. K.; Bowden, E. F.; Franzen, S.; Smirnova, T.; Ghiladi, R. A. Spectroscopic and Mechanistic Investigations of Dehaloperoxidase B from Amphitrite Ornata. *Biochemistry* **2010**, *49* (31), 6600–6616.
- (8) D'Antonio, J.; Ghiladi, R. A. Reactivity of Deoxy- and Oxyferrous Dehaloperoxidase B from Amphitrite Ornata: Identification of Compound II and Its Ferrous-Hydroperoxide Precursor. *Biochemistry* **2011**, *50* (27), 5999–6011.
- (9) Zhao, J.; Moretto, J.; Le, P.; Franzen, S. Measurement of Internal Substrate Binding in Dehaloperoxidase-Hemoglobin by Competition with the Heme-Fluoride Binding Equilibrium. *J. Phys. Chem. B* **2015**, *119* (7), 2827–2838.

- (10) Osborne, R. L.; Taylor, L. O.; Han, K. P.; Ely, B.; Dawson, J. H. Amphitrite Ornata Dehaloperoxidase: Enhanced Activity for the Catalytically Active Globin Using MCPBA. *Biochem. Biophys. Res. Commun.* **2004**, *324* (4), 1194–1198.
- (11) Thompson, M. K.; Davis, M. F.; Serrano, V. De; Nicoletti, F. P.; Howes, B. D.; Smulevich, G.; Franzen, S. Internal Binding of Halogenated Phenols in Dehaloperoxidase-Hemoglobin Inhibits Peroxidase Function. *Biophys. J.* **2010**, *99* (5), 1586–1595.
- (12) Plummer, A.; Thompson, M. K.; Franzen, S. Role of Polarity of the Distal Pocket in the Control of Inhibitor Binding in Dehaloperoxidase-Hemoglobin. *Biochemistry* **2013**, *52* (13), 2218–2227.
- (13) D'Antonio, E. L.; D'Antonio, J.; De Serrano, V.; Gracz, H.; Thompson, M. K.; Ghiladi, R. A.; Bowden, E. F.; Franzen, S. Functional Consequences of the Creation of an Asp-His-Fe Triad in a 3/3 Globin. *Biochemistry* **2011**, *50* (44), 9664–9680.
- (14) Davis, M. F.; Bobay, B. G.; Franzen, S. Determination of Separate Inhibitor and Substrate Binding Sites in the Dehaloperoxidase-Hemoglobin from Amphitrite Ornata. *Biochemistry* **2010**, *49* (6), 1199–1206.
- (15) Belyea, J.; Belyea, C. M.; Lappi, S.; Franzen, S. Resonance Raman Study of Ferric Heme Adducts of Dehaloperoxidase from Amphitrite Ornata. *Biochemistry* **2006**, *45* (48), 14275–14284.
- (16) Nicoletti, F. P.; Thompson, M. K.; Howes, B. D.; Franzens, S.; Smulevich, G. New Insights into the Role of Distal Histidine Flexibility in Ligand Stabilization of Dehaloperoxidase-Hemoglobin from Amphitrite Ornata. *Biochemistry* **2010**, *49* (9), 1903–1912.
- (17) Osborne, R. L.; Sumithran, S.; Coggins, M. K.; Chen, Y.; Lincoln, D. E.; Dawson, J. H. Spectroscopic Characterization of the Ferric States of Amphitrite Ornata Dehaloperoxidase and Notomastus Lobatus Chloroperoxidase: His-Ligated Peroxidases with Globin-like Proximal and Distal Properties. *J. Inorg. Biochem.* **2006**, *100* (5–6), 1100–1108.
- (18) Franzen, S.; Ghiladi, R. A.; Lebioda, L.; Dawson, J. H. Multi-Functional Hemoglobin Dehaloperoxidases. In *Heme Peroxidases*; The Royal Society of Chemistry, 2016; pp 218–244.

- (19) Sun, S.; Sono, M.; Du, J.; Dawson, J. H. Evidence of the Direct Involvement of the Substrate TCP Radical in Functional Switching from Oxyferrous O₂ Carrier to Ferric Peroxidase in the Dual-Function Hemoglobin/Dehaloperoxidase from Amphitrite Ornata. *Biochemistry* **2014**, *53* (30), 4956–4969.
- (20) Zhao, J.; de Serrano, V.; Zhao, J.; Le, P.; Franzen, S. Structural and Kinetic Study of an Internal Substrate Binding Site in Dehaloperoxidase-Hemoglobin A from Amphitrite Ornata. *Biochemistry* **2013**, *52* (14), 2427–2439.
- (21) Wang, C.; Lovelace, L. L.; Sun, S.; Dawson, J. H.; Lebioda, L. Complexes of Dual-Function Hemoglobin/dehaloperoxidase with Substrate 2,4,6-Trichlorophenol Are Inhibitory and Indicate Binding of Halophenol to Compound I. *Biochemistry* **2013**, *52* (36), 6203–6210.
- (22) Chen, Y. P.; Woodin, S. A.; Lincoln, D. E.; Lovell, C. R. An Unusual Dehalogenating Peroxidase from the Marine Terebellid Polychaete Amphitrite Ornata. *J. Biol. Chem.* **1996**, *271* (9), 4609–4612.
- (23) LaCount, M. W.; Zhang, E.; Chen, Y. P.; Han, K.; Whitton, M. M.; Lincoln, D. E.; Woodin, S. A.; Lebioda, L. The Crystal Structure and Amino Acid Sequence of Dehaloperoxidase from Amphitrite Ornata Indicate Common Ancestry with Globins. *J. Biol. Chem.* **2000**, *275* (25), 18712–18716.
- (24) Sun, S.; Sono, M.; Wang, C.; Du, J.; Lebioda, L.; Dawson, J. H. Influence of Heme Environment Structure on Dioxygen Affinity for the Dual Function Amphitrite Ornata Hemoglobin/dehaloperoxidase. Insights into the Evolutional Structure-Function Adaptations. *Arch. Biochem. Biophys.* **2014**, *545*, 108–115.
- (25) Jiang, S.; Wright, I.; Swartz, P.; Franzen, S. The Role of T56 in Controlling the Flexibility of the Distal Histidine in Dehaloperoxidase-Hemoglobin from Amphitrite Ornata. *Biochim. Biophys. Acta - Proteins Proteomics* **2013**, *1834* (10), 2020–2029.
- (26) Padron, A.; Pardillo, A.; D’Cunha, C.; Chatfield, D. C. MD Study of Wildtype and Mutant Dehaloperoxidase: Insight into Halphenol Ligand Stabilization and Allosteric Role of His55. In *ACS National Meeting and Exposition*; Anaheim, CA, 2011.
- (27) Zhang, Z.; Santos, A. P.; Zhou, Q.; Liang, L.; Wang, Q.; Wu, T.; Franzen, S. Steered Molecular Dynamics Study of Inhibitor Binding in the Internal Binding Site in Dehaloperoxidase-Hemoglobin. *Biophys. Chem.* **2016**, *211*, 28–38.

- (28) Feducia, J.; Dumarieh, R.; Gilvey, L. B. G.; Smirnova, T.; Franzen, S.; Ghiladi, R. A. Characterization of Dehaloperoxidase Compound ES and Its Reactivity with Trihalophenols. *Biochemistry* **2009**, *48* (5), 995–1005.
- (29) D'Antonio, J. Mechanistic Investigations of Oxyferrous and Ferric States of Dehaloperoxidase B from Amphitrite Ornata, 2012.
- (30) Beers, R. F. J.; Sizer, I. W. A Spectrophotometric Method for Measuring the Breakdown of Hydrogen Peroxide by Catalase. *J. Biol. Chem.* **1952**, *195* (1), 133–140.
- (31) Chenprakhon, P.; Sucharitakul, J.; Panijpan, B.; Chaiyen, P. Measuring Binding Affinity of Protein-Ligand Interaction Using Spectrophotometry: Binding of Neutral Red to Riboflavin-Binding Protein. *J. Chem. Educ.* **2010**, *87* (8), 829–831.
- (32) McCombs, N. L.; Moreno-Chicano, T.; Carey, L. M.; Franzen, S.; Hough, M. A.; Ghiladi, R. A. Interaction of Azole-Based Environmental Pollutants with the Coelomic Hemoglobin from Amphitrite Ornata : A Molecular Basis for Toxicity. *Biochemistry* **2017**, *56* (17), 2294–2303.
- (33) Otwinowski, Z.; Minor, W. [20] Processing of X-Ray Diffraction Data Collected in Oscillation Mode. In *Methods in Enzymology*; 1997; Vol. 276, pp 307–326.
- (34) McCoy, A. J.; Grosse-Kunstleve, R. W.; Adams, P. D.; Winn, M. D.; Storoni, L. C.; Read, R. J. Phaser Crystallographic Software. *J. Appl. Crystallogr.* **2007**, *40* (4), 658–674.
- (35) Adams, P. D.; Afonine, P. V.; Bunkóczi, G.; Chen, V. B.; Davis, I. W.; Echols, N.; Headd, J. J.; Hung, L. W.; Kapral, G. J.; Grosse-Kunstleve, R. W.; et al. PHENIX: A Comprehensive Python-Based System for Macromolecular Structure Solution. *Acta Crystallogr. Sect. D Biol. Crystallogr.* **2010**, *66* (2), 213–221.
- (36) De Serrano, V.; Dantonio, J.; Franzen, S.; Ghiladi, R. A. Structure of Dehaloperoxidase B at 1.58 Å Resolution and Structural Characterization of the AB Dimer from Amphitrite Ornata. *Acta Crystallogr. Sect. D Biol. Crystallogr.* **2010**, *66* (5), 529–538.
- (37) Emsley, P.; Lohkamp, B.; Scott, W. G.; Cowtan, K. Features and Development of Coot. *Acta Crystallogr. Sect. D Biol. Crystallogr.* **2010**, *66* (4), 486–501.
- (38) Afonine, P. V.; Grosse-Kunstleve, R. W.; Echols, N.; Headd, J. J.; Moriarty, N. W.; Mustyakimov, M.; Terwilliger, T. C.; Urzhumtsev, A.; Zwart, P. H.; Adams, P. D. Towards Automated Crystallographic Structure Refinement with Phenix.refine. *Acta Crystallogr. Sect. D Biol. Crystallogr.* **2012**, *68* (4), 352–367.

- (39) Dumarieh, R.; D'Antonio, J.; Deliz-Liang, A.; Smirnova, T.; Svistunenko, D. A.; Ghiladi, R. A. Tyrosyl Radicals in Dehaloperoxidase: How Nature Deals with Evolving an Oxygen-Binding Globin to a Biologically Relevant Peroxidase. *J. Biol. Chem.* **2013**, *288* (46), 33470–33482.
- (40) Du, J.; Sono, M.; Dawson, J. H. Functional Switching of Amphitrite Ornata Dehaloperoxidase from O₂-Binding Globin to Peroxidase Enzyme Facilitated by Halophenol Substrate and H₂O₂. *Biochemistry* **2010**, *49* (29), 6064–6069.
- (41) De Serrano, V.; Franzen, S. Structural Evidence for Stabilization of Inhibitor Binding by a Protein Cavity in the Dehaloperoxidase-Hemoglobin from Amphitrite Ornata. *Biopolymers* **2012**, *98* (1), 27–35.
- (42) Dunford, H. B. *Heme Peroxidases*; Wiley-VCH: New York, 1999.
- (43) Sono, M.; Roach, M. P.; Coulter, E. D.; Dawson, J. H. Heme-Containing Oxygenases. *Chem. Rev.* **1996**, *96* (7), 2841–2887.
- (44) Meunier, B.; Visser, P. De; Shaik, S. Mechanism of Oxidation Reactions Catalyzed by Cytochrome P450 Enzymes. *Chem. Rev.* **2004**, *104* (9), 3947–3980.
- (45) Wang, X.; Peter, S.; Kinne, M.; Hofrichter, M.; Groves, J. T. Detection and Kinetic Characterization of a Highly Reactive Heme–Thiolate Peroxygenase Compound I. *J. Am. Chem. Soc.* **2012**, *134* (31), 12897–12900.
- (46) Matsui, T.; Ozaki, S.; Watanabe, Y. On the Formation and Reactivity of Compound I of the His-64 Myoglobin Mutants. *J. Biol. Chem.* **1997**, *272* (52), 32735–32739.
- (47) Matsui, T.; Ozaki, S.; Liang, E.; Phillips, G. N.; Watanabe, Y. Effects of the Location of Distal Histidine in the Reaction of Myoglobin with Hydrogen Peroxide. *J. Biol. Chem.* **1999**, *274* (5), 2838–2844.

Chapter 3

How Nature Tunes Isoenzyme Activity in the Multifunctional Catalytic Globin

Dehaloperoxidase from *Amphitrite ornata*

*Leiah M. Carey*¹, *Roman Gavenko*¹, *Dimitri A. Svistunenko*² and *Reza A. Ghiladi*^{1*}

¹ Department of Chemistry, North Carolina State University, Raleigh, North Carolina, 27695-8204, United States

² School of Biological Sciences, University of Essex, Wivenhoe Park, Colchester, Essex CO4 3SQ, United Kingdom

3.1 Author Contributions

- Mutagenesis, expression and purification of mutant variants of DHP, both containing and lacking the 6X His tag
- Peroxidase and peroxygenase enzymatic assays, substrate binding studies
- X-ray crystallographic structure determination and analysis

3.2 Abstract

The coelomic hemoglobin of *Amphitrite ornata*, termed dehaloperoxidase (DHP), is the first known multifunctional catalytic globin to possess biologically-relevant peroxidase and peroxygenase activities. Although the two isoenzymes of DHP, A and B, differ in sequence by only 5 amino acids out of 137 residues, DHP B consistently exhibits a greater activity than isoenzyme A. To delineate the contributions of each amino acid substitution to the activity of either isoenzyme, the substitutions of the five amino acids were systematically investigated, individually and in combination, using 24 mutants. Biochemical assays and mechanistic studies demonstrated that the mutants that only contained the I9L substitution showed increased i) k_{cat} values (peroxidase activity), ii) 5-Br-indole conversion and binding affinity (peroxygenase activity), and iii) rate of Compound ES formation (enzyme activation). Whereas the X-ray structures of the oxyferrous forms of DHP B (L9I) (1.96 Å), DHP A (I9L) (1.20 Å), and WT DHP B (1.81 Å) showed no significant differences, UV-visible spectroscopy (A_{Soret}/A_{380} ratio) revealed that the I9L substitution increased the 5-coordinate high-spin heme

population characterized by the “open” conformation (i.e., distal histidine swung out of the pocket), which likely favors substrate binding. The positioning of the distal histidine closer to the heme cofactor in the solution state also appears to facilitate activation of DHP via the Compound ES intermediate. Taken together, the studies undertaken here shed light on the structure-function relationship in dehaloperoxidase, but also help to establish the foundation for understanding how enzymatic activity can be tuned in isoenzymes of a multifunctional catalytic globin.

3.3 Introduction

Nature employs protein isoforms for the fine-tuning of metabolic function, whether to match the needs of a given tissue (e.g., heart vs. skeletal muscle lactate dehydrogenase¹), developmental stage (e.g., fetal vs. maternal hemoglobin²), or to respond to an environmental stress (e.g., anoxia-responsive SOD³). Such alteration of function is readily seen in the heme protein superfamily, where isoforms exhibit different kinetic parameters (k_{cat} , K_{M}), substrate binding affinities (K_{d}), redox and/or different regulatory properties, examples of which include: i) k_{cat} : among the 7 isoenzymes of HRP (A1, A2, A3, B, C, D, E) reported by Shannon et al.⁴, HRP-C exhibits nearly 2-fold greater catalytic activity for *o*-dianisidine than the next most active isoform, HRP-B, and is 18-fold more active than HRP-A2, ii) K_{M} : human CYP3A4 exhibits substrate K_{M} values ~3 to 4-fold lower than CYP3A5 or CYP3A7,⁵ iii) K_{d} : fetal ($\alpha_2\gamma_2$) hemoglobin exhibits a $p\text{O}_2$ of 19 mm Hg vs. 26.8 mm Hg for adult ($\alpha_2\beta_2$) hemoglobin,⁶ and iv) regulatory: in rodents, the testicular isoform of cyt *c* (T-cyt *c*) is 86% homologous to somatic cyt *c*, yet exhibits a three-fold increased H_2O_2 -reduction activity and a 4-fold increase in apoptotic activity, the combination of which is believed to help prevent ROS damage of sperm as well as to initiate cell death of dysfunctional or damaged sperm.⁷ In each of these aforementioned *monofunctional* systems, the structure-function relationships between the isoforms have been studied in detail to delineate the impact of specific primary amino acid changes on protein reactivity, including tertiary structure modifications, quaternary structure formation, electron transfer pathway perturbation, active site perturbation, and substrate

promiscuity. By way of comparison, however, our understanding of how structural variations tune reactivity in *multifunctional* isoenzymes is lacking.

Our chosen platform for investigating how amino acid substitutions tune reactivity between isoforms is the enzyme dehaloperoxidase (DHP) from the marine annelid *Amphitrite ornata*. In addition to its oxygen-transport function, this coelomic hemoglobin⁸⁻¹⁰ possesses a broad substrate specificity for the oxidation of halophenols^{11, 12} haloindoles,¹³ and pyrroles,¹⁴ and is therefore the first known multifunctional catalytic globin to possess biologically-relevant peroxidase¹¹ and peroxygenase activities^{13, 14}, as well as an oxidase activity that leads to the formation of indigo.¹³ DHP is believed to have acquired these activities from the evolutionary pressure to detoxify haloaromatic compounds that are present in the benthic ecosystem in which *A. ornata* is found.^{15, 16} Moreover, it has been shown that DHP is not limited to naturally occurring substrates: against compounds of anthropogenic origin, DHP catalyzes the H₂O₂-dependent oxidation of nitrophenols via a peroxygenase mechanism,¹⁷ and DHP is also capable of binding azoles, including imidazole, benzotriazole, benzimidazole, and indazole.¹⁸ Mechanistic studies,¹⁹⁻²⁸ including stopped-flow UV-visible and rapid freeze-quench EPR spectroscopies, have shown that ferric DHP reacts with hydrogen peroxide to yield Compound ES, an iron(IV)-oxo heme center with a radical localized on the protein,^{27, 28} and it is this reactive intermediate that is responsible for oxidizing 2,4,6-trichlorophenol (TCP) to 2,6-dichloroquinone (DCQ) in the DHP peroxidase mechanism.^{28, 29} Studies have also shown that O-atom insertion into 5-Br-indole (yielding 5-Br-2-oxindole) and pyrrole (yielding pyrrol-2-one) likely proceed via Compound I in the DHP peroxygenase mechanism.^{13, 14}

Encoded by separate genes,³⁰ the two isoenzymes of DHP, A and B, have both been isolated and characterized in their recombinant forms.^{12, 27} The differences in primary structure between the two are limited to five amino acid substitutions (note – isoenzyme A is listed first): two of them (R/K32 and Y/N34) are found on the distal side of the heme cofactor, two on the proximal side (N/S81 and S/G91), and the fifth (I/L9) is located in a hydrophobic region of the enzyme without a direct contact to the heme cavity (Figure 3.1).^{31, 32} These amino acid substitutions do not perturb the overall structural fold of DHP when comparing the two isoenzymes.³² However,

they have resulted in DHP B consistently exhibiting a greater reactivity than isoenzyme A: for peroxidase activity, 4.3-fold (tribromophenol) and 2.6-fold (trichlorophenol) higher enzyme turnover numbers (k_{cat}) have been observed,²⁷ whereas for peroxygenase activity, 2.4-fold (5-Br-indole¹³), 1.8-fold (4-nitrophenol¹⁷), and 4.0-fold (2,4-dinitrophenol¹⁷) increased substrate conversions have been noted. The amino acid substitutions, particularly Y/N34, also modify the location (and migration pathway) of the protein radical in Compound ES, with Y34 as the primary radical site in DHP A, and Y38 as that site in DHP B.^{25, 33} Another difference between the two isoenzymes is that although both form an inactivated enzymatic state,¹² Compound RH, upon decay of Compound ES in the absence of a substrate, the UV-visible spectroscopic properties of the Compound RH species are different in DHP B²⁷ when compared to DHP A.²⁸ Despite the differences introduced by these five amino acid substitutions, both isoenzymes have identical formal reduction potentials of $202 \pm 6 \text{ mV}$ ³⁴ and $206 \pm 6 \text{ mV}$ ²⁷ for DHP A and DHP B, respectively, and overall appear to have identical reaction mechanisms. Thus, while the impact of the set of five substitutions together are well described, the contributions of each of these mutations on the catalytic activities of DHP, reaction intermediates, and substrate scope remain unaddressed.

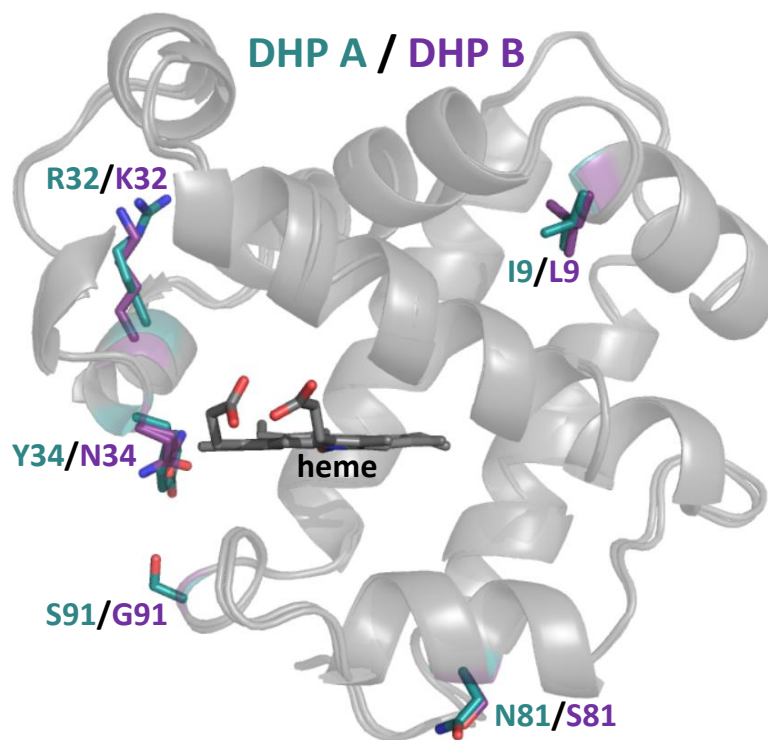


Figure 3.1. C α superposition of the A protomers of DHP A (PDB accession code 1EW6³¹, teal) and DHP B (PDB accession code 5V5J, purple), highlighting substitution sites between isoenzymes (isoenzyme A residue listed first): proximal side N/S81 and S/G91, distal side R/K32 and Y/N34, with I/L9 located 15 Å from the heme.

Given the limited number of amino acid differences (five), the apparent lack of structural difference between the two isoenzymes,³² yet the consistently higher catalytic activity of DHP B over that of A,^{13, 17, 27} DHP represents a unique system by which we can explore in detail how one can tune the structure-function relationship in a multifunctional catalytic globin, and, more specifically, to delineate the contributions of each amino acid substitution to the reactivity of each DHP isoenzyme. To that end, here we present a comparison of DHP A and DHP B along with the systematic investigation of the amino acid differences between the two. Specifically, substitutions of the five amino acids were probed individually and in combination in order to ascertain their effects on the structure-function relationships that discriminate peroxidase and peroxygenase activities between the two isoenzymes. All five single mutants,

all 10 double mutants, six selected triple mutants, and a single quadruple mutant were overexpressed and characterized. Biochemical assays were performed to determine the effect(s) of each mutation on enzyme activity (peroxidase and peroxygenase), stopped-flow UV-visible spectroscopic methods were performed to demonstrate the ability of each variant to generate the catalytically important Compound ES species, and selected crystal structures were obtained to investigate structural effects. Taken together, the studies undertaken here shed light on the structure-function relationship in dehaloperoxidase, but also help to establish the foundation for understanding how enzymatic activity can be tuned in isoenzymes of a multifunctional catalytic globin.

3.4 Experimental

3.4.1 Materials. HPLC grade acetonitrile (MeCN) and reagent-grade chemicals (VWR, Sigma-Aldrich or Fisher Scientific) were used without further purification. Stock solutions (2 mM) of 2,4,6-trichlorophenol (TCP) were prepared in 100 mM potassium phosphate (KPi) buffer (pH 7) and stored at -80 °C. TCP concentration and lack of degradation was monitored by measuring its absorbance at 312 nm ($\epsilon = 3752 \text{ M}^{-1}\text{cm}^{-1}$).²⁸ Stock solutions (10 mM) of 5-bromoindole were prepared in MeOH, stored at -80 °C, and screened by HPLC for degradation prior to use. Aliquots of all reagents were stored on ice during use. Solutions of H₂O₂ were prepared fresh daily and kept on ice until needed. H₂O₂ concentration was determined spectrophotometrically ($\epsilon_{240} = 43.6 \text{ M}^{-1}\text{cm}^{-1}$).³⁵ Ferric samples of DHP A and B were expressed and purified as previously reported.²⁷ Oxyferrous DHP was obtained by the aerobic addition of excess ascorbic acid to a solution of ferric DHP, followed by desalting (PD-10 column).³⁶ Enzyme concentration was determined spectrophotometrically using $\epsilon_{\text{Soret}} = 116,400 \text{ M}^{-1}\text{cm}^{-1}$ for all isoenzymes.²⁷

3.4.2 Construction of Mutant DHP Plasmids. Site-directed mutagenesis was performed using the Quikchange II site-directed mutagenesis kit (Agilent Technologies). Mutagenesis [melt (95 °C, 60 s), anneal (55 °C, 50 s), and extension (68 °C, 360 s)] was performed for 16 cycles. Mutagenic oligonucleotides (Table S3.7) were synthesized by Integrated DNA

Technologies (IDT). The plasmid encoding N-terminal 6x-His-tagged wild-type DHP A was used as a template for single mutations. Double and triple mutants were generated from preceding single and double mutants, respectively. For crystallization, mutants were obtained from vectors lacking the N-terminal poly-His tag.³² The modified plasmids were transformed into BL21-Gold(DE3) competent cells (Agilent Technologies) and selected based on survival on LB-agar-ampicillin (100 $\mu\text{g}/\text{mL}$) plates. The plasmids were extracted using the EZ-10 Spin Column Plasmid DNA Minipreps Kit (Bio Basic). DNA sequencing of the resulting mutated genes in their entirety confirmed the success of the site-directed mutagenesis and the absence of secondary mutations. Recombinant DHP variants were obtained by expression in *E. coli* as previously described.^{25, 27, 28}

3.4.3 Molecular Weight Determination. Experiments were analyzed using a Thermo Scientific Exactive Plus Orbitrap mass spectrometer operated in positive ion mode with a heated-electrospray ionization (HESI) probe (Thermo Scientific, San Jose, CA). The protein samples (5 μL injection volume) were prepared in 100 mM KPi at pH 7. An isocratic mobile phase [90:10 methanol:water containing 0.1% formic acid (v/v)] was employed. The experimentally determined and calculated monomeric molecular weights of the dehaloperoxidase mutants as determined by ESI-mass spectrometry are summarized in Table S3.8.

3.4.4 Peroxidase Studies. The enzymatic activity of DHP was assayed optically from the rate of 2,4,6-trichlorophenol (TCP, 312 nm) conversion to 2,6-dichloro-1,4-benzoquinone (DCQ, 273 nm) as a function of H_2O_2 concentration (10, 25, 50, 75, 100, or 125 μM) in 100 mM KPi (pH 7, 25 $^\circ\text{C}$) using a Cary 50 UV-visible spectrophotometer. Reactions were performed in triplicate. Buffered solutions of DHP and TCP were premixed and the reaction was initiated by the addition of H_2O_2 (1 mL total volume). While the enzyme and the starting TCP concentrations were kept constant in all assays (0.5 and 150 μM , respectively), the dependence of the rate on the H_2O_2 concentration was fit with a classical Michaelis–Menten model using the Grafit 4.0 software package. The kinetics parameters K_m and k_{cat} resulted from

the optimization of the fitting procedure. The TCP concentration was measured using the molar absorptivity coefficient $\epsilon_{312} = 3752 \text{ M}^{-1}\text{cm}^{-1}$.²⁸

3.4.5 Peroxygenase Studies. Reactions were performed in triplicate at pH 7 in 100 mM KP_i containing 5% MeOH (v/v) at 25 °C. Buffered solutions of 5-Br-indole and DHP were premixed, and the peroxygenase reaction was initiated upon the addition of H_2O_2 . Final concentrations were 10 μM DHP, 500 μM 5-Br-indole and 500 μM H_2O_2 in 200 μL total volume. After 5 minutes, reactions were quenched with excess catalase. A 100 μL aliquot of the reaction sample was diluted 10-fold with 900 μL 100 mM KP_i (pH 7). Diluted samples were analyzed using a Waters 2796 Bioseparations Module coupled with a Waters 2996 Photodiode Array Detector, and equipped with a Thermo-Scientific ODS Hypersil C_{18} column (150 x 4.6 mm, 5 μm particle size). Separation of observed analytes was performed using a linear gradient of binary solvents (solvent A - H_2O containing 0.1% trifluoroacetic acid; solvent B – MeCN containing 0.1% trifluoroacetic acid). Elution was performed using the following conditions: (1.5 mL/min A:B) 95:5 to 5:95 linearly over 10 minutes; 5:95 isocratic for 2 minutes; 5:95 to 95:5 linearly over 1 minute, then isocratic for 4 minutes. Data analysis was performed using the Empower software package (Waters Corp.). A calibration curve for 5-Br-indole was performed using serial dilutions of the commercially available analyte to determine the amount of substrate conversion.

3.4.6 5-Br-indole Binding Studies. Adapted from previously published protocols,³⁷ studies were performed in 100 mM KP_i (pH 7) containing 10% MeOH (v/v) at 25 °C using a Cary 50 UV-visible spectrophotometer. Stock solutions of 10 mM 5-Br-indole in MeOH were prepared in glass vials. The spectrophotometer was referenced with 10 μM ferric DHP in 100 mM KP_i (pH 7) containing 10% MeOH (v/v). Difference spectra were then acquired in the presence of 31.25-1000 eq. 5-Br-indole while maintaining both constant enzyme and MeOH concentrations. The total volume of the samples was 200 μL . Analysis by nonlinear regression^{13,17} using the GraFit software package (Erithacus Software Ltd.) of the experiments performed in triplicate provided a calculated A_{max} , which was in turn used to calculate α for

the average ΔA for each substrate concentration. A nonlinear regression plot provided the reported apparent K_d values.^{13, 17}

3.4.7 Stopped-flow UV-visible Studies. Optical spectra were recorded using a Bio-Logic SFM-400 triple-mixing stopped-flow instrument coupled to a rapid scanning diode array UV-visible spectrophotometer. All solutions were prepared in 100 mM KP_i at pH 7, and studies were performed at room temperature. Data were collected (900 scans total) over a three-time domain regime (2.5, 25, and 250 ms; 300 scans each) using the Bio Kinet32 software package (Bio-Logic). Experiments were performed in single-mixing mode where enzyme at a final concentration of 10 μ M was reacted with 2.5-25 equivalents of H_2O_2 to observe spectral features and rate constants of Compound ES and Compound RH formation. All data were evaluated using the Specfit Global Analysis System software package (Spectrum Software Associates) and fit to exponential functions as one-step/two-species or two-step/three species irreversible mechanisms where applicable. Data were baseline corrected using the Specfit autozero function.

3.4.8 EPR Spectroscopy. EPR spectra were recorded in standard 4 mm o.d. quartz EPR tubes using an EMXplus 9.5/2.7 EPR spectrometer system equipped with an In-Cavity Cryo-Free VT system (Bruker Biospin Corporation). Samples (~ 100 μ M) were prepared in 100 mM KP_i buffer (pH 7). The instrumental conditions were as follows: microwave frequency $\nu_{MW} = 9.471$ GHz, microwave power $P = 3.18$ mW, modulation frequency $\nu_m = 100$ kHz, modulation amplitude $A_m = 5$ G, time constant $\tau = 82$ ms, scan rate $V = 22.6$ G s^{-1} , number of scans per spectrum $NS = 1$. The exact resonant frequency of each EPR experiment was measured by an EIP-578 (PhaseMatrix, San Jose, CA) in-line microwave frequency counter.

3.4.9 Protein Crystallization and X-ray Diffraction Studies. Non-His tagged WT DHP B, DHP A (I9L), and DHP B (L9I) were overexpressed and purified per literature protocol.^{17, 18} Crystals were obtained through the hanging-drop vapor diffusion method. DHP A (I9L) was concentrated at 8 mg/mL and its crystals were grown from mother liquor solutions of 28-32% PEG 8000 and 0.2 M ammonium sulfate at pH 6.4, equilibrated against identical reservoir solutions. WT DHP B and DHP B (L9I) were brought to a concentration of 12 mg/mL and

their crystals were grown from mother liquor solutions of 28-32% PEG 4000 and 0.2 M ammonium sulfate at pH 6.4, equilibrated against identical reservoir solutions. Protein to mother liquor ratios varied between 1:1, 1.33:1, 1.66:1 and 2:1. At 4 °C crystals grew from each condition after 3 days. The crystals were cryo-protected by briefly dipping them in reservoir solution enhanced with 20% glycerol and then flash frozen in liquid N₂. Data were collected at 100 K on the SER-CAT 22-ID (DHP A I9L) and 22-BM (WT DHP B, DHP B L9I) beamlines at the APS synchrotron facility, utilizing a wavelength of 1.00 Å. All data were scaled and integrated using HKL2000,³⁸ molecular replacement was performed with Phaser-MR³⁹ from the PHENIX⁴⁰ suite of programs using the 3IXF³² protomer as the search model, model building and manual placement of waters utilized COOT,⁴¹ and refinement was carried out using phenix.refine.⁴² Coordinates and structure factors were deposited in the RCSB Protein Data Bank with the accession codes listed in Table 3.5.

3.5 Results

3.5.1 UV-visible Spectroscopic Studies. The electronic absorption spectra for each of the single, double, and I9L-containing triple mutants of DHP A, as well as for the DHP A (R32K/Y34N/N81S/S91G) quadruple mutant [i.e., DHP B (L9I)], were obtained in 100 mM KP_i (pH 7) and are shown in Figure 3.2. For comparative purposes, the spectra of ferric WT DHP A and B are also presented. The optical characteristics, optical purity ratio (A_{Soret}/A_{280} , R_z), and the ratio of absorbances A_{Soret}/A_{380} and A_{614}/A_{645} of the DHP variants are given in Table 3.1.

As has been previously found for isoenzymes A¹² and B²⁷, the DHP mutants were initially isolated as a mixture of the ferric and oxyferrous oxidation states, but subsequent treatment with an excess of potassium ferricyanide permitted the isolation of their ferric forms. In general, the spectra were typical of high spin ferric heme enzymes ($S = 5/2$); however, despite being freshly prepared in their oxidized state, some variants did exhibit a small (~5%) component of oxyferrous DHP [UV-visible: 417 (Soret), 542, 578 nm³⁶] from a known autoreduction pathway,⁴³ which led to an A_{614}/A_{645} ratio >1.2 for those variants owing to the

absence of the CT1 feature in the 6-coordinate low-spin oxyferrous species. The optical purity ratios (Reinheitzahl or R_z , defined as A_{Soret}/A_{280}) for all mutants were found in the range of ~ 3.8 - 4.9 , in good agreement with the literature values for recombinantly-expressed DHP A¹² and B²⁷, as well as for several mutants previously reported.²⁵ The monomeric molecular weight of each mutant in the ferric oxidation state was determined by electrospray ionization MS, and was found to agree with its corresponding theoretical expected value (Table S3.8).

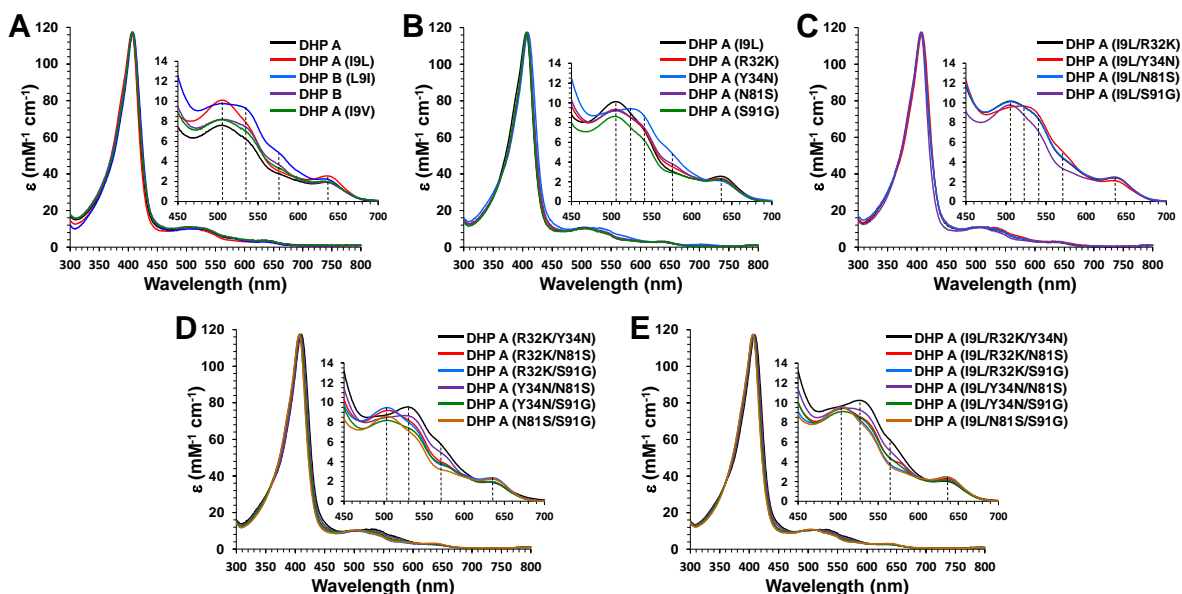


Figure 3.2. UV-visible spectra of A) WT DHP A, WT DHP B, DHP A (I9L), DHP B (L9I) and DHP A (I9V), B) single mutants of DHP A, C) I9L containing double mutants of DHP A, D) double mutants of DHP A lacking the I9L substitution, and E) I9L containing triple mutants of DHP A. All spectra were recorded at 10 μM enzyme concentration in 100 mM KP_i buffer (pH 7, 25 $^\circ\text{C}$).

The shifts in the relative populations of 5-/6-coordinate (5c/6c) high-/low-spin (HS/LS) heme species as a function of the mutations present in each variant can be assessed from the A_{Soret}/A_{380} ratio:^{25, 44, 45} 5cHS hemes exhibit a slightly blue-shifted and lower molar absorptivity coefficient of the Soret band than their 6cHS counterparts, as well as a shoulder at 380 nm,

such that a greater A_{Soret}/A_{380} ratio corresponds to a greater relative population of six-coordinate heme compared to the five-coordinate species. The optical spectra of the two WT DHP isoenzymes and the DHP A single variants are shown in Figures 3.2A and 3.2B, respectively. When compared with the A_{Soret}/A_{380} ratio of DHP A (1.91) and DHP B (1.88), two of the single mutants exhibited markedly different ratios, specifically DHP A (I9L) (1.77) and DHP A (Y34N) (2.05), which correspond to increased and decreased 5cHS heme populations relative to the WT enzyme, respectively.

The optical spectra of the I9L containing DHP A double mutants I9L/R32K, I9L/Y34N, I9L/N81S, and I9L/S91G are shown in Figure 3.2C, and the remaining double mutants are shown in Figure 3.2D. When compared to the single mutants (i.e., R32K, Y34N, N81S or S91G), the following was noted for the corresponding double mutants: i) the addition of the I9L substitution lowered all of the A_{Soret}/A_{380} ratios (higher 5cHS heme population), ii) the addition of the Y34N substitution increased each of the A_{Soret}/A_{380} ratios, and iii) the addition of the S91G substitution lowered the A_{Soret}/A_{380} ratios for the DHP A Y34N/S91G and N81S/S91G variants, but had a negligible effect for I9L/S91G and R32K/S91G. Addition of the I9L substitution to each of the double mutants in Figure 3.2D resulted in the triple mutants I9L/R32K/Y34N, I9L/R32K/N81S, I9L/R32K/S91G, I9L/Y34N/N81S, I9L/Y34N/S91G, and I9L/N81S/S91G (Figure 3.2E), each of which exhibited a shift to a lower A_{Soret}/A_{380} ratio (higher 5cHS heme population) than its corresponding double mutant. Finally, the A_{Soret}/A_{380} ratio for the DHP A (R32K/Y34N/N81S/S91G) quadruple mutant [i.e., DHP B (L9I)] was higher than DHP B, the latter of which contains the I9L substitution. Taken together, the patterns revealed by the analysis of the A_{Soret}/A_{380} ratio suggest that the addition of the Y34N mutation has a stabilizing effect on the six-coordinate ferric heme population, whereas the I9L (primary) and S91G (secondary) mutations shift the equilibrium towards a five-coordinate ferric heme population.

Table 3.1. UV-visible spectroscopic features of ferric DHP variants at pH 7.

Enzyme	λ_{max} (nm)	A_{Soret}/A_{380}	A_{614}/A_{645}	R_z
<i>Wild-type Enzymes</i>				
WT DHP A	407, 506, 535 (sh), 635	1.91	1.06	4.41
WT DHP B	407, 506, 531 (sh), 633	1.88	1.14	4.13
<i>DHP A Single Mutants</i>				
I9L	406, 506, 535 (sh), 636	1.77	0.95	4.28
R32K	407, 506, 535 (sh), 635	1.96	1.08	4.16
Y34N	409, 494 (sh), 524, 556 (sh), 629	2.05	1.39	4.06
N81S	407, 505, 527 (sh), 634	2.00	1.10	4.13
S91G	407, 505, 528 (sh), 634	1.91	1.04	4.48
I9V	407, 507, 530 (sh), 633	2.01	1.15	3.93
<i>DHP A Double Mutants</i>				
I9L/R32K	407, 505, 530 (sh), 635	1.86	1.32	3.92
I9L/Y34N	408, 494 (sh), 523, 559 (sh), 633	1.95	1.19	4.04
I9L/N81S	407, 505, 530 (sh), 635	1.84	1.11	3.79
I9L/S91G	406, 504, 528 (sh), 635	1.80	1.03	4.20
R32K/Y34N	410, 496 (sh), 530, 556 (sh), 629	2.16	1.46	4.02
R32K/N81S	407, 506, 525 (sh), 634	2.00	1.10	4.13
R32K/S91G	407, 505, 524 (sh), 634	1.93	1.11	4.32
Y34N/N81S	408, 495 (sh), 530, 558 (sh), 630	2.12	1.40	4.21
Y34N/S91G	407, 504, 525 (sh), 634	1.95	1.23	4.25
N81S/S91G	407, 503, 527 (sh), 634	1.91	1.10	4.33
<i>DHP A Triple Mutants</i>				
I9L/R32K/Y34N	408, 500 (sh), 527, 557 (sh), 632	2.06	1.21	4.06
I9L/R32K/N81S	407, 505, 525 (sh), 636	1.89	1.00	4.11
I9L/R32K/S91G	406, 504, 525 (sh), 636	1.83	1.06	4.25
I9L/Y34N/N81S	408, 492 (sh), 511, 555 (sh), 634	1.96	1.13	4.21
I9L/Y34N/S91G	407, 507, 525 (sh), 634	1.86	1.11	4.27
I9L/N81S/S91G	406, 505, 526 (sh), 636	1.82	0.92	4.28
<i>DHP A Quadruple Mutant [DHP B (L9I)]</i>				
R32K/Y34N/N81S/S91G	407, 492 (sh), 536 (sh), 570 (sh), 638	1.98	1.36	4.88

R_z , Reinheitszahl value; sh indicates “shoulder”.

3.5.2 EPR Spectroscopic Studies. The EPR spectra of WT DHP A, DHP A (I9L), WT DHP B and DHP B (L9I) in the resting (ferric) state at pH 7 are shown in Figure 3.3. Three line shapes have been identified in these spectra, as follows:

1) *Axial HS* ($g_{\perp} = 5.93$, $g_{\parallel} = 1.999$) – both WT DHP B and DHP A (I9L) can be represented as this line shape only. If we assume that the DHP A (I9L) spectrum is 100% *Axial HS* (1.00

Axial HS), then the WT DHP B spectrum is 0.91 *Axial HS*. The contribution of this line shape to the WT DHP A spectrum is 0.32 *Axial HS*, and to DHP B (L9I) is 0.80 *Axial HS*.

2) *Rhombic HS* ($g_1 = 6.21$, $g_2 = 5.61$, $g_3 = 1.993$) – only present in the WT DHP A spectrum. Its second integral intensity (proportional to concentration), if expressed in the units of integral intensity of the DHP A (I9L) spectrum (which corresponds to 1.00 *Axial HS* units of concentration but is present in the WT DHP A spectrum at the level of 0.32 *Axial HS*) is 0.72 *Axial HS* units of concentration, which in percentage terms gives 69% rhombic and 31% axial forms of the HS ferric heme, consistent with previous results on this protein.³³

3) *Mixed spin* ($g_{\max \text{ low field}} = 6.14$, $g_{\min \text{ high field}} = 1.996$) – present as a low intensity EPR signal in DHP B (L9I) along with the axial HS form (at a level of 0.80 *Axial HS*). This line shape is defined as ‘*Mixed spin*’ owing to its significantly broadened low field feature that can be attributed to a mixed $S=5/2, S=3/2$ spin state of the ferric heme iron.⁴⁶ The integral intensity of this line shape, in common units of *Axial HS*, is 0.36.

The results of the EPR spectroscopic study suggest that the presence of the I9L mutation drives DHP from a mixture of 5c/6c-HS heme in WT DHP A (mixture of rhombic and axial signals) to a 6c HS heme in WT DHP B and DHP A (I9L) (both being purely axial, or nearly so), whereas the L9I mutation reverses this effect with DHP B (L9I) being less axial than WT DHP B. It is important to note that while the low temperature (10 K) EPR data appear to be inconsistent with the room-temperature UV/vis data with regards to *direction* of the shift in the 5c/6c spin-state distribution that is attributable to I9/L9, this spin-state equilibrium is known to be highly temperature-dependent in DHP: previous resonance Raman studies conducted at room temperature have shown the presence of the 5c/6c high-spin equilibrium that shifts toward the 6c form at 12 K.⁴⁷ As such, although the mutation-dependent *direction* of the 5c/6c shift was not expected to be consistent between the two spectroscopic methods owing to this temperature-dependent equilibrium, gratifyingly both the EPR and UV/vis data unequivocally demonstrate that the I9/L9 position does significantly impact the *distribution* of 5c/6c-HS heme in DHP.

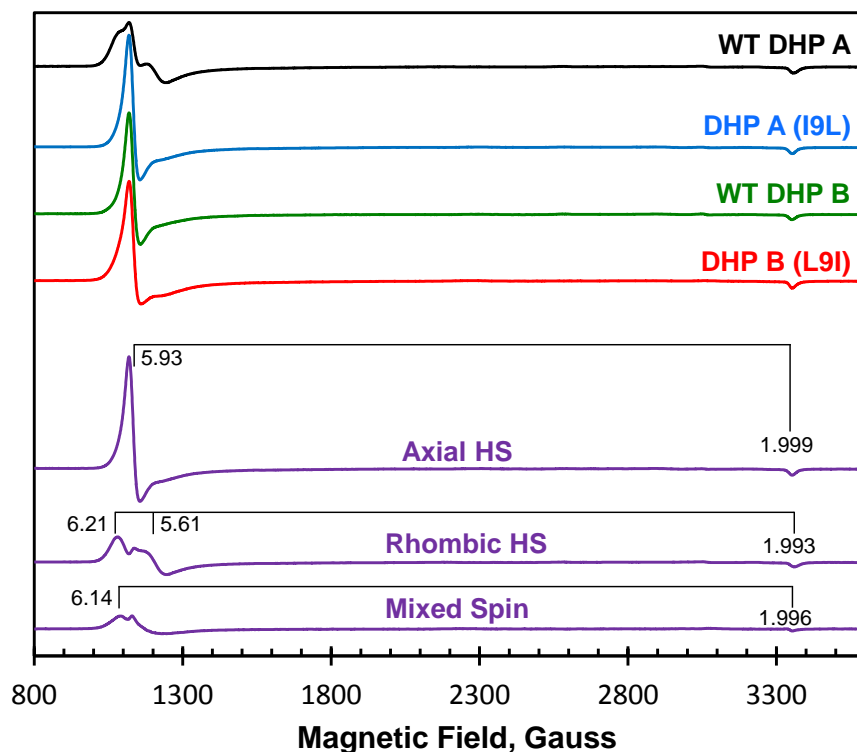


Figure 3.3. EPR spectra of ferric WT DHP A (black), DHP A (I9L) (blue), WT DHP B (green), and DHP B (L9I) (red), and the result of their deconvolution into three individual ferric heme EPR signals, rhombic high spin, axial high spin, and mixed spin. The spectra were obtained at 10 K, and all spectra are plotted at similar amplitudes for comparative viewing. The instrumental conditions were as described in the Experimental section. The principal g -factors of the deconvoluted signals are indicated.

3.5.3 Peroxidase Studies. The H_2O_2 -dependent oxidative dehalogenation of 2,4,6-trichlorophenol (TCP) to the corresponding 2,6-dichloro-1,4-benzoquinone (DCQ) as catalyzed by DHP was monitored by UV-visible spectroscopy. In these studies, the H_2O_2 concentration was varied from 10-125 μM while maintaining fixed concentrations of enzyme (0.5 μM) and TCP (150 μM). The kinetic parameters for each variant are provided in Table 3.2. Compared to DHP A (k_{cat} : $0.90 \pm 0.01 \text{ s}^{-1}$; $k_{\text{cat}}/K_{\text{M}}$: $0.047 \mu\text{M}^{-1}\text{s}^{-1}$), DHP B has a 3-fold higher catalytic turnover (k_{cat} : $2.72 \pm 0.05 \text{ s}^{-1}$), and a 1.8-fold better overall catalytic efficiency ($k_{\text{cat}}/K_{\text{M}}$: $0.083 \mu\text{M}^{-1}\text{s}^{-1}$). Of the five single mutants examined, only DHP A (I9L) showed an

increase in catalytic turnover (2.06 s^{-1}), with the other single mutants ($0.40 - 0.87 \text{ s}^{-1}$) showing a similar or lower catalytic turnover as WT DHP A. The effect of the I9L substitution is further demonstrated by the following: i) each of the four I9L containing double mutants exhibited an increase in catalytic turnover ($1.80 - 4.20 \text{ s}^{-1}$), ii) the five double mutants lacking the I9L substitution possessed similar or lower catalytic turnover numbers ($0.55 - 1.13 \text{ s}^{-1}$) as WT DHP A, iii) addition of the I9L substitution to each of these five double mutants resulted in the triple mutants I9L/R32K/Y34N, I9L/R32K/N81S, I9L/R32K/S91G, I9L/Y34N/N81S, I9L/Y34N/S91G, and I9L/N81S/S91G, all of which exhibited catalytic turnover values ($2.16 - 2.96 \text{ s}^{-1}$) similar to that observed for WT DHP B (2.72 s^{-1}), and iv) reversal of the I9L substitution in DHP B, i.e. DHP B (L9I) [or DHP A (R32K/Y34N/N81S/S91G)] resulted in k_{cat} (0.94 s^{-1}) and K_{m} ($15 \pm 2 \mu\text{M}$) values nearly identical to those for DHP A.

3.5.4 Peroxygenase Studies. The H_2O_2 -dependent oxidation of 5-Br-indole as catalyzed by DHP was monitored by HPLC (Table 3.2). Reactions were initiated upon addition of $500 \mu\text{M}$ H_2O_2 to a solution containing $10 \mu\text{M}$ enzyme and $500 \mu\text{M}$ 5-Br-indole, incubated at $25 \text{ }^\circ\text{C}$ for 5 min, and then quenched with catalase. Previous studies have shown that substrate conversion for WT DHP B ($48.1 \pm 2.3\%$) was 2.4-fold greater than WT DHP A ($20.3 \pm 1.7\%$).¹³ Of the five single mutants examined, both the R32K (10.8%) and N81S (11.0%) variants showed a decrease in substrate conversion, with the other single mutants (19.0-22.2%) exhibiting a similar level as WT DHP A. Although no effect by the I9L substitution was observed in the single mutant, its impact on 5-Br-indole conversion via peroxxygenase activity was demonstrated by the following: i) all four I9L containing double mutants exhibited increases in substrate conversion (21.9 – 38.3%) compared to their corresponding single mutants, ii) the five double mutants lacking the I9L substitution showed no significant variation in the percent conversion of 5-Br-indole (18.0-24.3%) when compared with DHP A, iii) addition of the I9L substitution to each of these five double mutants resulted in ~1.5-2-fold increases for the corresponding triple mutants, and iv) reversal of the I9L substitution in DHP B, i.e. DHP B (L9I) \approx DHP A (R32K/Y34N/N81S/S91G), reduced 5-Br-indole conversion (19.7%) back to a level nearly identical to that observed for DHP A.

Table 3.2. Kinetics data for the oxidation of TCP and conversion percentage of 5-Br-indole as catalyzed by ferric DHP in the presence of H₂O₂ at pH 7.^a

Enzyme	$K_M^{H_2O_2}$ (μ M)	k_{cat} (s ⁻¹)	k_{cat}/K_M (μ M ⁻¹ s ⁻¹)	5-Br-indole conversion (%)
<i>Wild-type enzymes</i>				
WT DHP A	19 ± 2	0.90 ± 0.01	0.047 ± 0.005	20.6 ± 0.3
WT DHP B	33 ± 3	2.72 ± 0.05	0.083 ± 0.008	44.2 ± 0.7
<i>DHP A Single Mutants</i>				
I9L	53 ± 8	2.06 ± 0.06	0.039 ± 0.006	22.2 ± 0.3
R32K	16 ± 1	0.63 ± 0.01	0.039 ± 0.003	10.8 ± 0.5
Y34N	14 ± 1	0.73 ± 0.01	0.052 ± 0.004	19.0 ± 0.5
N81S	83 ± 9	0.87 ± 0.02	0.010 ± 0.001	11.0 ± 0.3
S91G	22 ± 3	0.40 ± 0.01	0.018 ± 0.002	22.9 ± 0.5
I9V	27 ± 3	0.94 ± 0.03	0.034 ± 0.002	17.2 ± 0.2
I9F	69 ± 10	0.47 ± 0.02	0.007 ± 0.001	44 ± 2
<i>DHP A Double Mutants</i>				
I9L/R32K	35 ± 6	1.80 ± 0.05	0.051 ± 0.009	26.7 ± 0.3
I9L/Y34N	112 ± 12	4.2 ± 0.1	0.037 ± 0.004	38.3 ± 0.5
I9L/N81S	39 ± 3	1.93 ± 0.03	0.050 ± 0.004	21.9 ± 0.2
I9L/S91G	43 ± 4	2.05 ± 0.02	0.048 ± 0.004	28.5 ± 0.5
R32K/Y34N	30 ± 1	1.13 ± 0.01	0.038 ± 0.001	21.4 ± 0.5
R32K/N81S	55 ± 4	0.83 ± 0.01	0.015 ± 0.001	18.0 ± 0.7
R32K/S91G	13 ± 2	0.55 ± 0.01	0.042 ± 0.007	23.1 ± 1.0
Y34N/N81S	30 ± 2	0.81 ± 0.01	0.027 ± 0.002	24.3 ± 1.0
Y34N/S91G	19 ± 1	1.11 ± 0.01	0.058 ± 0.003	23.9 ± 0.3
N81S/S91G	32 ± 5	0.96 ± 0.02	0.031 ± 0.005	21.5 ± 0.6
<i>DHP A Triple Mutants</i>				
I9L/R32K/Y34N	33 ± 2	2.76 ± 0.03	0.081 ± 0.005	37.3 ± 0.3
I9L/R32K/N81S	35 ± 4	2.74 ± 0.04	0.078 ± 0.009	33.6 ± 0.7
I9L/R32K/S91G	29 ± 1	2.25 ± 0.01	0.079 ± 0.003	34.5 ± 0.1
I9L/Y34N/N81S	38 ± 2	2.31 ± 0.02	0.061 ± 0.003	37.4 ± 0.4
I9L/Y34N/S91G	51 ± 6	2.96 ± 0.07	0.058 ± 0.007	36.0 ± 0.7
I9L/N81S/S91G	38 ± 4	2.16 ± 0.04	0.057 ± 0.006	29.0 ± 0.1
<i>DHP A Quadruple Mutant [DHP B (L9I)]</i>				
R32K/Y34N/N81S/S91G	15 ± 2	0.94 ± 0.01	0.063 ± 0.008	19.7 ± 0.4

^a All biochemical assays were performed in triplicate. Values reported are the average ± standard deviation.

3.5.5 5-Br-indole Binding Studies. As previously reported,¹³ 5-Br-indole binding to DHP results in hypochromicity and a hypsochromic shift of the Soret band, thereby enabling optical difference spectra to be recorded as a function of substrate concentration (31.25–1000 equiv) for determination of its apparent dissociation constant (K_d). Substrate binding studies were performed on the WT isoenzymes and selected I9 mutants to examine the effect of the I9L substitution on 5-Br-indole binding affinity (Table 3.3). Whereas WT DHP B has a reported K_d value of 150 μM for 5-Br-indole,¹³ no significant changes in the optical difference spectra were observed for WT DHP A, even at the highest concentrations of 5-Br-indole tested, and as such its binding affinity for isoenzyme A is estimated to be $>1400 \mu\text{M}$. Both the single mutant DHP A (I9L) ($K_d = 145 \mu\text{M}$) and the double mutant DHP A (I9L/Y34N) ($K_d = 175 \mu\text{M}$) exhibited 5-Br-indole binding affinities similar to that of DHP B. Reversal of the I9L substitution in DHP B, i.e. DHP B (L9I) \approx DHP A (R32K/Y34N/N81S/S91G), significantly weakened the 5-Br-indole affinity such that no changes in the optical difference spectra were observed, similar to WT DHP A. As such, the 5-Br-indole binding affinity for DHP B (L9I) was estimated to be $>1400 \mu\text{M}$. Decreasing the side chain size with DHP A (I9V) showed no measurable effect on 5-Br-indole binding affinity ($K_d >1400 \mu\text{M}$) when compared with WT DHP A.

Table 3.3. 5-Br-indole dissociation constants (K_d) for WT DHP and selected mutants.

Enzyme	K_d (μM) ^a
WT DHP A	> 1400
WT DHP B	150 ± 10
DHP A (I9L)	145 ± 7
DHP A (I9L/Y34N)	175 ± 6
DHP A (I9V)	> 1400
DHP B (L9I)	> 1400

^a Binding studies were performed in triplicate. Values reported are the average \pm standard deviation.

3.5.6 Non-native I9 Mutants. A variant with a smaller side chain, DHP A (I9V), resulted in no significant changes compared to WT DHP A, neither for peroxidase and peroxygenase activities (Table 3.2), nor for 5-Br-indole binding affinity (Table 3.3). A variant with a larger side chain, DHP A (I9F), exhibited a 2-fold reduction in turnover number for peroxidase activity when compared to DHP A, but yielded a 2-fold increase in 5-Br-indole conversion, putting it on a par with WT DHP B for peroxygenase activity. Both DHP A (I9A) and DHP A (I9G) mutants were successfully obtained through site-directed mutagenesis. However, overexpression of these variants failed in *E. coli*, suggesting that the 9th position may be necessary for protein stability and/or productive folding.

3.5.7 Stopped-flow UV-visible Spectroscopic Studies. To assess the ability of each mutant to form the catalytically active Compound ES species, single-mixing stopped-flow UV-visible spectroscopic methods were employed as previously described.^{27, 28} Using ferric DHP A (I9L) as representative data (Figure S3.5), the following observations were made: an SVD analysis employing a simple three component, irreversible mechanism ($a \rightarrow b \rightarrow c$) revealed that upon rapid mixing (2 ms) of a ferric DHP A (I9L) solution [UV-visible spectrum: 406 (Soret), 506, 535 (sh), 636] with 10 equiv H₂O₂, a new species was observed whose spectral features [UV-visible: 420 (Soret), 546, 587 nm] we attributed to the ferryl-containing intermediate Compound ES based upon our previous assignments of this reaction intermediate in DHP A²⁸ and B²⁷. The experimental value of k_{obs} for Compound ES formation varied linearly with hydrogen peroxide concentration (2.5-25 mol equiv), from which the bimolecular rate constant was determined to be $3.44 \pm 0.08 \times 10^4 \text{ M}^{-1}\text{s}^{-1}$. The DHP A (I9L) Compound ES intermediate further converted to a new species [UV-visible: 412 (Soret), 536, 565 (sh) nm; $k_{\text{obs}} = 0.020 \pm 0.004 \text{ s}^{-1}$], which we have assigned as Compound RH for this variant based upon analogy to the similar, but not identical, species observed in DHP isoenzymes A²⁸ and B²⁷, as well as in various other DHP mutants.²⁵

The UV-visible spectroscopic features and rate of formation of Compound ES in WT DHP and selected variants at pH 7 are provided in Table 3.4. From these data, it was noted that the addition of the I9L substitution to either DHP A or other mutants universally increased the rate

of formation of Compound ES of that new variant: DHP A (I9L) > WT DHP A by 1.6-fold, DHP A (I9L/Y34N) > DHP A (Y34N) by 1.3-fold, DHP A (I9L/S91G) > DHP A (S91G) by 1.4-fold, and DHP A (I9L/Y34N/S91G) > DHP A (Y34N/S91G) by 2.4-fold. Consistent with the observation that the DHP A (I9L) mutant exhibited a rate of formation for Compound ES comparable to that of WT DHP B, the reversal of the I9L substitution in DHP B, i.e. DHP B (L9I) [\approx DHP A (R32K/Y34N/N81S/S91G)], reduced the rate of formation of Compound ES back to a level nearly identical to that observed in DHP A. The Compound ES species in all variants was observed to decay to Compound RH at longer reactions times (data not shown), but this off-pathway reaction was not further explored.

Table 3.4. UV-visible spectroscopic features and rate of formation of Compound ES in WT DHP and selected variants at pH 7. ^a

Enzyme	k_{obs} ($\text{M}^{-1}\text{s}^{-1}$)	λ_{max} (nm)
WT DHP A	$2.22 \pm 0.07 \times 10^4$	420, 545, 585
DHP A (I9L)	$3.44 \pm 0.08 \times 10^4$	420, 546, 587
DHP A (Y34N)	$3.50 \pm 0.02 \times 10^4$	419, 545, 587
DHP A (I9L/Y34N)	$4.62 \pm 0.10 \times 10^4$	419, 544, 585
DHP A (S91G)	$1.73 \pm 0.01 \times 10^4$	417, 544, 585
DHP A (I9L/S91G)	$2.38 \pm 0.03 \times 10^4$	419, 546, 587
DHP A (Y34N/S91G)	$2.43 \pm 0.02 \times 10^4$	419, 546, 586
DHP A (I9L/Y34N/S91G)	$5.92 \pm 0.12 \times 10^4$	419, 546, 587
WT DHP B	$3.50 \pm 0.03 \times 10^4$	419, 545, 585
DHP A (R32K/Y34N/N81S/S91G) [DHP B (L9I)]	$2.26 \pm 0.02 \times 10^4$	417, 543, 587

^a Reactions were performed in triplicate. Values reported are the average \pm standard deviation.

3.5.8 X-ray Diffraction Studies. X-ray diffraction data were collected at the Advanced Photon Source (APS) synchrotron at Argonne National Laboratory on the SER-CAT beamline 22-BM for DHP B (L9I) and WT DHP B, and beamline 22-ID for DHP A (I9L). X-ray data collection and refinement statistics are provided in Table 3.5. DHP B (L9I) refined to a

resolution of 1.96 Å, DHP A (I9L) to a resolution of 1.20 Å, and WT DHP B to a resolution of 1.81 Å. R_{free} values of 24.92 %, 16.92 %, and 19.47 % were calculated for DHP B L9I, DHPA I9L, and WT DHP B, respectively. All DHP crystals underwent rapid reduction in the X-ray beam consistent with previous reports of cryo-radiolytic reduction of heme proteins; as such, the resulting structures were refined in the oxyferrous state.⁴⁸ As shown for DHP B (L9I) (Figure S3.6), each variant crystallized as a homo-dimer in the asymmetric unit, consistent with previous X-ray diffraction studies of DHP,^{16, 17, 21, 31, 32, 43} with all three structures here exhibiting the same conserved dimer interface.

A comparison to each other of the DHP A (I9L) and DHP B (L9I) structures was performed using C^α least squares quadratic (LSQ) alignment (Figure 3.4, panels A-C). The C^α superposition of DHP A (I9L) (green) with that of DHP B (L9I) (teal) (Figure 3.4A) reveals very little variation between the two: i) low rmsd values of 0.5087 Å (A protomers) and 0.4312 Å (B protomers) were found for the homoprotomer superpositions (Table S3.9), ii) the position of the isoleucine (B L9I) and leucine (A I9L) side chains were virtually identical (Figure 3.4B), with differences of 0.12 and 0.01 Å in the Fe – C^α distances for protomers A and B, respectively, iii) the I9 C^α to L9 C^α distance was found to be 0.17 Å for the A protomer comparison, and 0.25 Å for the B protomer comparison (Table S3.9), iv) a slight misalignment in the loop region between helices C and D is observed, however these regions are solvent-accessible and known for higher flexibility than tertiary helical regions, whereas the loop region between helices F and G superpose with very little deviation, v) the hemes align very well despite not being a variable in the C^α LSQ alignment (Figure 3.4C), and vi) DHP B (L9I) has a longer Fe – H89 N ϵ distance by 0.31 Å than DHP A (I9L) (Table 3.6), likely a consequence of the proximal N81S and S91G differences between the parent A and B isoenzymes. Additionally, while the isoleucine (B L9I) and leucine (A I9L) side chains make indirect contacts with the distal pocket through neighboring residues (Figure S3.7), with the exception of Leu13, these neighboring residues remain unperturbed in the hydrophobic area within which they reside. Leu13 shows different conformations between the two mutants, however, this sidechain is not positioned toward the interior and affords no further

consequence on the protein structure. Taken together, as the majority of the differences observed were well below the global rmsd value for each respective alignment, no significant structural differences were observed in the comparison of DHP A (I9L) to DHP B (L9I).

The comparisons of the variants to their respective WT enzymes were also made: the C^α LSQ alignment of DHP B (L9I) with WT DHP B is shown in Figure 3.4D, and that of DHP A (I9L) with WT DHP A is shown in Figure 3.4E. The structure of each mutant was found to superpose to a high level with its respective WT enzyme, as demonstrated by the low rmsd values of 0.5097 Å (protomer A) and 0.5070 Å (protomer B) for WT DHPA/DHP A (I9L), and 0.3361 Å (protomer A) and 0.2454 Å (protomer B) for WT DHP B/DHP B (L9I) (Table S3.9). In both alignments, a slight deviation in the loop region between helices C and D was observed, but the proximal loop between helices F and G were in excellent agreement. *Averaging protomers*, the following observations are made (Table 3.6): i) the Fe – H89 N_ε distance is in line with the wild-type enzyme for DHP A (I9L), and only slightly elongated for DHP B (L9I)/WT B comparison, iii) the Fe – C^α Leu9 distance in DHP A (I9L) is 0.13 Å longer than the Fe – C^α Ile9 distance in WT DHP A, whereas the Fe – C^α Ile9 distance in DHP B (L9I) is 0.08 Å shorter than the Fe – C^α Leu9 distance in WT DHP B, and iv) as shown above, the hemes align very well despite not being a variable in the C^α LSQ alignment. Again, given the minimal differences observed here, it is clear that there are no significant structural differences when comparing either DHP A (I9L) or DHP B (L9I) to their respective wild-type enzymes.

Table 3.5. X-ray Data Collection and Refinement Statistics for DHP B (L9I) (5V5Q), DHP A (I9L) (5V5R), and WT DHP B (5V5J). All structures were solved in the oxyferrous state.

	DHP B (L9I)	DHP A (I9L)	WT DHP B
PDB Entry	5V5Q	5V5R	5V5J
<u>Data Collection</u>			
Wavelength (Å)	1.00	1.00	1.00
Temperature (K)	100	100	100
Space Group	P2 ₁ 2 ₁ 2 ₁	P2 ₁ 2 ₁ 2 ₁	P2 ₁ 2 ₁ 2 ₁
Unit-cell parameters (Å)			
<i>a</i>	58.82	57.67	58.58
<i>b</i>	67.66	67.42	67.02
<i>c</i>	67.55	68.91	68.45
Unique reflections	19,829 (976) ^a	81,222 (3,912)	24,707 (1,176)
Completeness (%)	99.9 (99.9)	96.1 (93.7)	98.9 (96.4)
R _{merge} (%) ^b	5.9 (51.7)	5.3 (47.8)	7.1 (62.3)
I/σ(I)	15.5 (2.3)	25.5 (2.0)	21.5 (2.2)
Redundancy	4.7 (4.8)	4.8 (4.3)	6.8 (6.4)
V _m (Å ³ /Da)	2.26	2.15	2.24
<u>Refinement</u>			
Resolution (Å)	1.96	1.20	1.81
R _{work} (%) ^c	18.58 (25.39)	13.90 (20.87)	16.58 (19.67)
R _{free} (%) ^d	24.92 (34.31)	16.92 (27.39)	19.47 (23.63)
No. of protein atoms	2,275	2,524	2,313
No. of solvent atoms	137	372	193
R.m.s.d from ideal geometry ^e			
Bond lengths (Å)	0.008	0.014	0.006
Bond angles (°)	0.89	1.365	0.85
<u>Ramachandran plot (%)^f</u>			
Most favored region	97.78	97.37	98.15
Addl allowed region	2.22	2.26	1.85
Outliers	0.0	0.38	0.0

^aValues in parentheses are for the highest resolution shell. ^bR_{merge} = $\sum_h \sum_i [|I_i(h) - \langle I(h) \rangle| / \sum_h \sum_i I_i(h)] \times 100\%$, where $I_i(h)$ is the i^{th} measurement and $\langle I(h) \rangle$ is the weighted mean of all measurements of $I(h)$. ^cR_{work} = $\sum |F_o - F_c| / \sum F_o \times 100\%$, where F_o and F_c are the observed and calculated structure factors, respectively. ^dR_{free} is the R factor for the subset (~9%) of reflections selected before and not included in the refinement. ^eRoot-mean-square deviation. ^fRamachandran plot created via MolProbity.

Table 3.6. Selected Distances and Angles for Protomers A & B (Protomer B in parentheses).

	WT DHP A	DHP A (I9L)	DHP B (L9I)	WT DHP B
Fe – H89 N ^ε	2.15 (2.17)	2.18 (2.11)	2.51 (2.40)	2.34 (2.28)
Fe – H55 N ^ε	5.13 (5.08)	5.19 (5.06)	5.10 (5.23)	5.17 (5.29)
Fe-O ₂ O1	2.42 (2.21)	2.52 (2.48)	2.42 (2.42)	2.42 (2.55)
Fe – O ₂ O2	3.64 (3.30)	3.95 (3.89)	3.56 (3.56)	3.60 (3.75)
Fe-O1-O2 bend angle (°)	168 (144)	169 (171)	157 (156)	163 (169)
Fe – Leu9 C ^α	----	17.80 (17.64)	----	17.82 (17.65)
Fe – Leu9 C ^{δ1}	----	15.90 (15.76)	----	16.05 (15.93)
Fe – Leu9 C ^{δ2}	----	16.79 (16.60)	----	16.89 (16.70)
Fe – Ile9 C ^α	17.52 (17.66)	----	17.68 (17.63)	----
Fe – Ile9 C ^δ	15.72 (15.97)	----	16.02 (15.85)	----
Fe – Ile9 C ^{γ2}	14.98 (15.15)	----	15.16 (15.14)	----
H55 N ^ε - O ₂ O1	3.22 (3.14)	3.28 (3.18)	3.07 (3.16)	3.13 (3.29)
H55 N ^ε - O ₂ O2	2.82 (2.84)	2.64 (2.65)	2.74 (2.74)	2.67 (2.85)

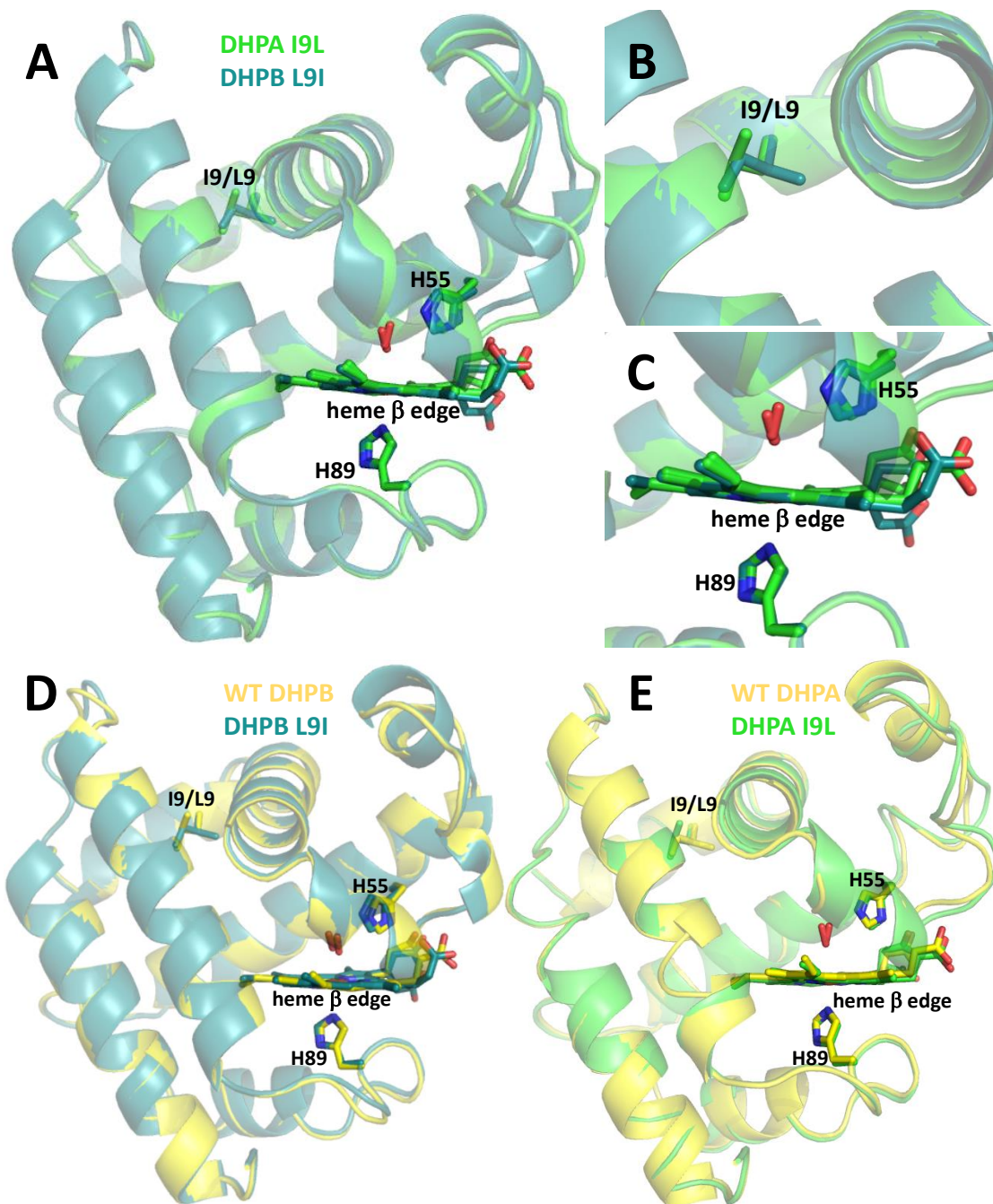


Figure 3.4. Panels A-C: LSQ C α superposition of DHP A (I9L) (green), DHP B (L9I) (teal), as viewed from the heme β edge. A) Superposition of the A protomers. B) Magnified view from panel A of the Leu9 and Ile9 residues. C) Heme active site from panel A. D) LSQ C α superposition of DHP B (L9I) and WT DHP B (yellow). E) LSQ C α superposition of DHP A (I9L) and WT DHP A (yellow; PDB accession code 2QFN⁴⁹).

3.6 Discussion

Our previous work has shown that in the superposition of the backbone traces of isoenzymes A and B, the primary differences between the two structures were limited to areas surrounding the five amino-acid substitutions that distinguish these two isoenzymes.³² These can be clustered into three distinct regions: (i) the distal cavity (R32K and Y34N), (ii) the proximal cavity (N81S and S91G) and (iii) a hydrophobic region enclosed by 9 amino acids located far from the active site (I9L). Although compensatory and/or synergistic mutations that effect catalytic fitness are likely to be present in the isoenzyme structures, thereby making an absolute correlation difficult, the structural changes imparted by these mutations that may possibly affect enzymatic activities of DHP are rationalized *a priori* as follows (note – distances are provided from the oxyferrous structures of DHP A and B from PDB accession codes 2QFN⁴⁹ and 5V5J, respectively, and a full discussion addressing the structural aspects of the proximal and distal cavities can be found in the Supporting Information):

(1) *Distal cavity* – the R32 residue, found in the C helix, is involved in hydrogen bonding interactions with Lys41 (located in the loop region between the C and D helices), Asn26 (located in the B helix) and Pro29 (located in the loop region between the B and C helices). In DHP B, the effect of the R32K mutation results in complete loss of the hydrogen bond to Asn26, elongation of the hydrogen bond to Lys41, and formation of a new hydrogen bond to Tyr38. The shorter lysine also impacts neighboring residues that help define a portion of the hydrophobic distal (substrate binding) pocket. Tyr34, located at the end of the C helix, is the site of the protein radical associated with Compound ES in DHP A at pH 7.³³ As elucidated for the Y34F variant, mutation of this tyrosine to a redox inactive residue shifted the protein radical formed upon H₂O₂-activation to Tyr38,²⁵ and led to an increase in the peroxidase k_{cat} of 1.3-fold compared to the WT enzyme. Interestingly, the Y34N mutation led to the opposite effect on catalytic activity: a reduction in k_{cat} of 1.2-fold in the present study that was virtually identical to the 1.3-fold reduction observed previously by Wang et al.²¹ The structural consequences of the Y34N mutation are both an alteration of the radical migration pathway

that may affect substrate oxidation kinetics, as well as structural perturbations in neighboring residues that may also result in functional differences.

(2) *Proximal cavity* – The effects of the N81S and S91G mutations may be rationalized by their proximity to L83 and the proximal histidine (H89), respectively. First, the Asp-His-Fe charge relay that is typical in peroxidases and whose function is to stabilize the ferryl intermediates through polarization of the proximal histidine is absent in DHP,^{43, 50} replaced with a Leu83-His-Fe relay. As a consequence of the N81S mutation in DHP B, the Leu-His hydrogen bond is shortened, thus positioning Leu83 closer to the proximal histidine. It is important to note that unlike their backbone atoms, both the N81 (DHP A) and S81 (DHP B) side chains are solvent exposed and themselves do not participate in any notable hydrogen bonding interactions.

Located in the loop region between the F and G helices, Ser91 has no significant hydrogen bonding interactions in the DHP A structure, neither through the side chain nor through the backbone. Similarly, Gly91 in DHP B lacks any hydrogen bonding interactions. As such, it is likely that any differences afforded to catalytic activity associated with the S91G mutation are due to the increased flexibility of the protein backbone imparted by the glycine residue that lies just two amino acids from the critically important proximal histidine (H89).

(3) *Hydrophobic region/I9L* – Located in the A loop, Ile9 is found in a hydrophobic region enclosed by Tyr16, Ile20, Phe115, Trp120, Phe60, Met64, Val104, Phe107 and Met108. From the comparison of the isoenzyme A and B structures,³² no significant structural changes are observed for the I9L variant, and therefore it was not expected to affect catalytic activity.

Given the above, the activity studies presented here unexpectedly revealed that the identity of the amino acid at position 9 is a primary factor in tuning the activity of DHP between the two isoenzymes, despite residing over 15 Å from the heme active site. In terms of peroxidase activity, of the 5 amino acids that differentiate isoenzyme A from B, only the DHP A (I9L) variant resulted in an increase in the turnover number compared to DHP A. Further highlighting its importance, the I9L substitution also showed a favorable synergistic effect when paired with other mutations: in every case, the addition of the I9L mutation to the other

single mutants (yielding double mutants) or to non-I9L containing double mutants (yielding triple mutants) led to increased turnover numbers, on a par with that found for isoenzyme B. Moreover, as demonstrated in DHP B (L9I) (but also for non-I9L containing double mutants), the absence of the I9L mutation reduces turnover numbers back to isoenzyme A levels.

The effects of the mutations on 5-Br-indole peroxygenase activity differed slightly from those observed for peroxidase activity noted above, yet still highlight the importance of the I9L substitution. While no single substitution increased the 5-Br-indole conversion compared to DHP A, favorable synergistic effects were observed in the double mutants. Namely, the addition of the I9L mutation to each of the other single mutants (yielding double mutants) led to increased substrate conversion, however several of the non-I9L containing double mutants also exhibited increases (e.g., R32K and N81S single mutants each yielded ~11% substrate conversion, whereas the R32K/N81S double mutant exhibited 18% conversion). The importance of the I9L substitution is best demonstrated by its absence: DHP B (I9L) exhibited a lowered 5-Br-indole conversion that was on a par with DHP A. The increased affinity for 5-Br-indole in variants that contain Leu9 [i.e., WT DHP B, DHP A (I9L) and DHP A (I9L/Y34N); $K_d \sim 145\text{-}175 \mu\text{M}$] compared to those that possess Ile9 [i.e., WT DHP A and DHP B (L9I); $K_d > 1400 \mu\text{M}$] is the likely contributing factor that modulates 5-Br-indole peroxygenase activity in these studies.

Given its distance ($> 15\text{\AA}$) from the heme active site, as well as the fact that it does not directly interact with the substrate binding pocket (despite its effect on 5-Br-indole binding affinity as noted above), the question thus arises as to why the substitution of isoleucine with its constitutional isomer leucine would appear to be the critical residue that accounts for the differences in peroxidase and peroxygenase activities between the two DHP isoenzymes. In order to address this question, the structures of DHP A (I9L) and DHP B (L9I) were determined by X-ray crystallography. However, examination of the structures via C^α LSQ superposition, either in comparison to each other or to their respective wild-type counterparts, revealed no significant differences as a result of the I9L substitution, neither globally nor at the heme active site, that could explain the importance of this position on catalytic activity or substrate binding.

Moreover, the local environment surrounding the 9th position showed negligible deviation in the backbone trace, and while Leu13 does exhibit an altered conformation in the I9L variant, this bears no further effect on adjacent residues or helices. We surmise two possible explanations for the lack of significant structural perturbations caused by the I9L substitution: i) the substitution itself is not remarkable and there are truly no significant observable differences, and/or ii) the location of I9/L9 at the crystallographic dimer interface. In regards to the latter, the additional constraints enforced by crystallographic packing may prevent global or local conformational space (that are accessible in solution as a monomer) from being observed in the crystalline state, thereby appearing to have no structural consequence. It is important to note that DHP is primarily monomeric in solution up to a protein concentration of 3 mM,⁵¹ such that the solution state is the catalytically relevant species for the studies employed here.

Having shown that the structure of DHP in the crystalline state cannot rationalize the impact of the I9L substitution, neither for catalytic activity nor substrate binding, an effect on the solution state structure was considered. Previously it has been hypothesized that H55 is susceptible to the conformation of the protein,^{16, 31, 49, 52-54} and as such this may well be a critical factor in the peroxidase (and by analogy, peroxygenase) activity of DHP in one of two ways: i) the conformational flexibility of the distal histidine may affect substrate/co-substrate binding (i.e., the flexibility of H55 plays a role in maintaining an open distal pocket, which may be necessary for entry/exit of substrate/product molecules, or co-substrate H₂O₂),^{43, 55} and ii) the distance of the distal histidine from the heme cofactor is a critical factor in O-O bond cleavage upon H₂O₂ binding,^{16, 31} particularly as DHP lacks the distal arginine common in most peroxidases that stabilizes the developing negative charge on the oxygen atom of the peroxide molecule during heterolytic cleavage in the “pull effect” of the Poulos-Kraut mechanism.⁵⁶ Here, we explored both of these possibilities in light of the I9L substitution: first, UV-visible spectroscopy was employed to determine the effect a mutation has on the conformational flexibility of the distal histidine by specifically probing the “open” (5cHS) and “closed” (6cHS, water-bound) equilibrium in DHP as demonstrated by the A_{Soret}/A_{380} ratio. It was universally

noted that the presence of the I9L substitution led to an increase in the 5cHS heme population characterized by the “open” conformation (i.e., distal histidine swung out of the pocket), which likely favors substrate binding as reflected by the lower K_d values for 5-Br-indole, and may also favor co-substrate/ H_2O_2 binding since the diffusion of H_2O_2 into the distal pocket has been shown to be facilitated by the greater flexibility of H55 in studies of the T56 mutants of DHP.⁵⁷ Second, stopped-flow UV-visible spectroscopic methods were used to determine the rate constant for the formation of Compound ES, which is proportional to k_{cat} in the peroxidase-modified Michaelis-Menton model proposed for DHP.⁵⁸ The I9L mutants explored here exhibited higher k_{obs} values for Compound ES formation that paralleled with higher peroxidase k_{cat} values. This observation, when coupled with the trend that mutants with the distal histidine closer to the heme Fe also have higher k_{cat} values, together suggest that the I9L substitution likely positions the distal histidine slightly closer to the heme cofactor in the solution state when in the ‘closed’ conformation, thereby facilitating the role of H55 in the Poulos–Kraut mechanism to serve as an acid–base catalyst in the activation of DHP via the Compound ES intermediate.

3.7 Conclusion

The I9L substitution demonstrates the paramount importance of the distal histidine in tuning the activities of DHP. Accomplished not through wholesale changes in the protein architecture, but instead via a subtle change in a single amino acid side chain, the I9L variants show that tuning of enzyme activity by means of altering the conformational flexibility and/or position of the catalytically important distal histidine can be achieved over a great distance. The question thus arises as to whether or not the I9L substitution arose as a compensatory mutation to correct a loss of fitness imparted by the other four substitutions, either individually or synergistically, or if the I9L mutation itself arose primarily out of a need for a more active DHP enzyme. While difficult to address, the studies on the DHP B (L9I) variant revealed virtually identical properties as isoenzyme A, and suggest that the other mutations may play a different role other than tuning the catalytic activity of DHP. Given the multifunctional nature

of DHP, such roles may include discrimination of a substrate that has yet to be identified, improving *in vivo* protein stability (particularly in light of the failure to overexpress other recombinant I9X mutants in *E. coli*), mediating interactions with other proteins or redox cofactors, or other possibilities, and further studies, including X-ray crystallography of the DHP mutants with substrate bound and NMR solution studies to probe protein dynamics, are planned.

3.8 Acknowledgements

This project was supported by NSF CAREER Award CHE-1150709 and NSF CHE-1609446. Mass spectra were obtained at the Mass Spectrometry Facility for Biotechnology at North Carolina State University. Partial funding for the facility was obtained from the North Carolina Biotechnology Center and the National Science Foundation. X-ray diffraction data were collected at Southeast Regional Collaborative Access Team (SER-CAT) 22-BM and 22-ID beamlines at the Advanced Photon Source, Argonne National Laboratory. Supporting institutions may be found at www.ser-cat.org/members.html. Use of the Advanced Photon Source was supported by the U. S. Department of Energy, Office of Science, Office of Basic Energy Sciences, under Contract No. W-31-109-Eng-38.

3.9 Supporting Information.

Table S3.7. Mutagenic Primers Used to Construct the DHP A Mutants.

Table S3.8. Calculated and experimentally determined monomeric molecular weights of the dehaloperoxidase mutants.

Figure S3.5. Kinetic data obtained by optical spectroscopy for the reaction of DHP A (I9L) with H₂O₂.

Figure S3.6. The asymmetric unit of DHP B (L9I) consisting of a homodimer of protomers A and B.

Table S3.9. Rmsd Values for DHP Protomer C[□] Least Squares Quadratic (LSQ) Alignment.

Figure S3.7. LSQ C[□] superposition of DHP A (I9L) and DHP B (L9I), focusing on the distal side of the heme cavity as well as the region containing the residue at position 9.

Discussion of the Structural Features of the Distal and Proximal Cavities in DHP

Table S3.7. Mutagenic Primers Used to Construct the DHP A Mutants.

Mutation	Forward Primer	Reverse Primer
A I9L	CAA GAT ATT GCC ACC <u>CTC</u> CGC GGT GAT CTC CGC	GCG GAG ATC ACC GCG <u>GAG</u> GGT GGC AAT ATC TTG
A R32K	G TAT CCG GAC GAG <u>AAA</u> CGC TAC TTC AAA AAC TAT G	C ATA GTT TTT GAA GTA GCG <u>TTT</u> CTC GTC CGG ATA C
A Y34N	CCG GAC GAG CGC CGC <u>AAC</u> TTC AAA AAC TAT GTC	GAC ATA GTT TTT GAA <u>GTT</u> GCG GCG CTC GTC CGG
A N81S	CTT GCG TCC GAC GCC <u>AGC</u> ACA CTC GTC CAG ATG	CAT CTG GAC GAG TGT <u>GCT</u> GGC GTC GGA CGC AAG
A S91G	G ATG AAA CAG CAT TCC <u>GGC</u> CTG ACG ACT GGA AAC	GTT TCC AGT CGT CAG <u>GCC</u> GGA ATG CTG TTT CAT C
A R32K/Y34N	CCG GAC GAG <u>AAA</u> CGC <u>AAC</u> TTC AAA AAC TAT GTC	GAC ATA GTT TTT GAA <u>GTT</u> GCG <u>TTT</u> CTC GTC CGG
A I9V	CAA GAT ATT GCC ACC <u>GTC</u> CGC GGT GAT CTC CGC	GCG GAG ATC ACC GCG <u>GAC</u> GGT GGC AAT ATC TTG
A I9A	CAA GAT ATT GCC ACC <u>GCC</u> CGC GGT GAT CTC CGC	GCG GAG ATC ACC GCG <u>GCC</u> GGT GGC AAT ATC TTG
A I9G	CAA GAT ATT GCC ACC <u>GGC</u> CGC GGT GAT CTC CGC	GCG GAG ATC ACC GCG <u>GCC</u> GGT GGC AAT ATC TTG
A I9F	GCG GAG ATC ACC GCG <u>TTC</u> GGT GGC AAT ATC TTG	CAA GAT ATT GCC ACC <u>GAA</u> CGC GGT GAT CTC CGC

Table S3.8. Calculated and experimentally determined monomeric molecular weights of the dehaloperoxidase mutants.

Protein	Calculated mass (Da)	Measured Mass (Da)
DHP A WT	16408.51	16408.09
DHP B WT	16274.38	16274.38
I9L	16408.51	16408.03
R32K	16380.50	16380.05
Y34N	16359.44	16359.04
N81S	16381.48	16381.07
S91G	16378.49	16378.03
I9V	16394.49	16394.04
I9L/R32K	16380.50	16380.05
I9L/Y34N	16359.44	16359.04
I9L/N81S	16381.48	16381.01
I9L/S91G	16378.49	16378.03
R32K/Y34N	16331.43	16331.02
R32K/N81S	16353.47	16353.05
R32K/S91G	16350.48	16350.04
Y34N/N81S	16332.41	16332.03
Y34N/S91G	16329.42	16329.03
N81S/S91G	16351.46	16351.04
I9L/R32K/Y34N	16331.43	16331.04
I9L/R32K/N81S	16353.47	16353.02
I9L/R32K/S91G	16350.48	16350.00
I9L/Y34N/N81S	16332.41	16332.02
I9L/Y34N/S91G	16329.42	16329.03
I9L/N81S/S91G	16351.46	16351.03
R32K/Y34N/N81S/S91G (B L9D)	16274.38	16273.99

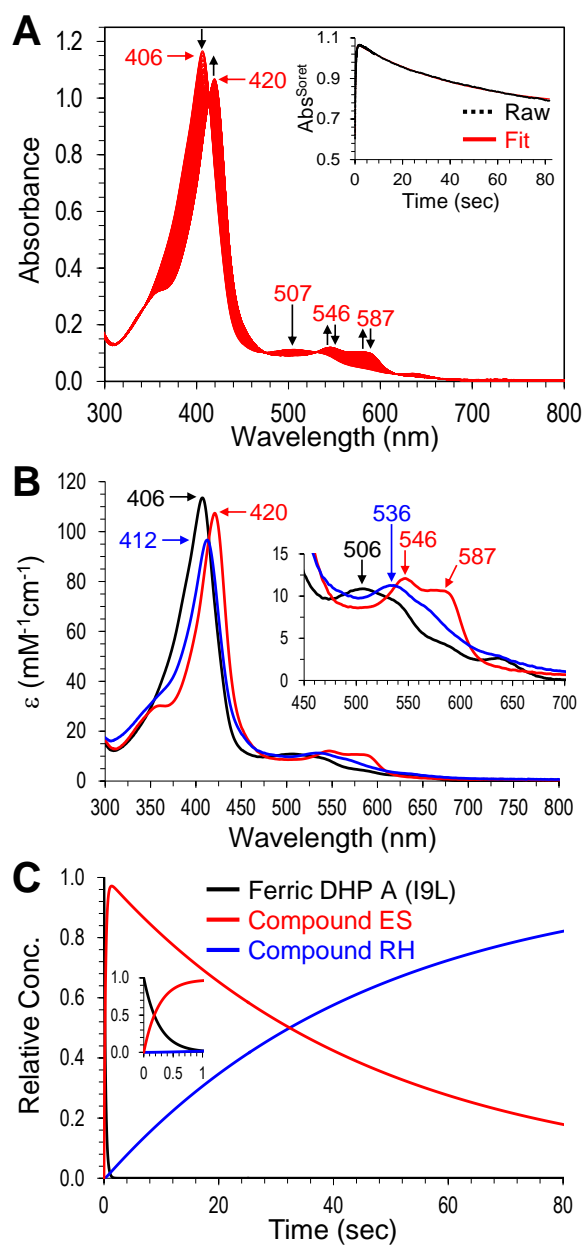


Figure S3.5. Kinetic data obtained by optical spectroscopy for the reaction of DHP A (I9L) with H_2O_2 . A) Stopped-flow UV-visible spectra of DHP A (I9L) ($10 \mu\text{M}$) reacting with a 10-fold excess of H_2O_2 at pH 7.0 (900 scans over 83 sec); *inset* - the single wavelength (420 nm) dependence on time obtained from the raw spectra and its fit with a superposition of the calculated spectra components; B) Calculated spectra of the three reaction components derived from the SVD analysis: ferric heme state (black), Compound ES (red), and Compound RH (blue); C) time dependences of the relative concentrations for the three components shown in panel B as determined by fitting the spectra in panel A.

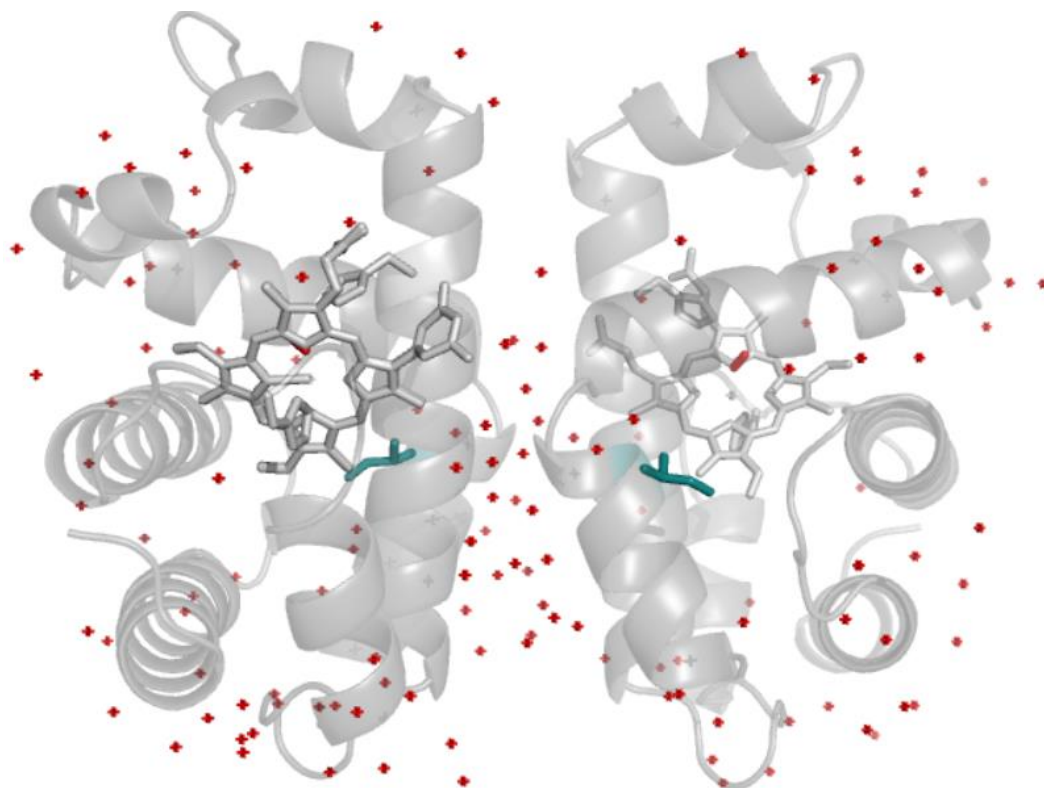


Figure S3.6. The asymmetric unit of DHP B (L9I) consisting of a homodimer of protomers A and B. The 9th position lies along the dimer interface, highlighted in teal.

Table S3.9. Rmsd Values for DHP Protomer C^α Least Squares Quadratic (LSQ) Alignment.^a

Enzymes superposed	Protomer A		Protomer B	
	rmsd (Å)	I/L-9 C _α (Å)	rmsd (Å)	I/L-9 C _α (Å)
DHP A (I9L)/DHP B (L9I)	0.5087	0.17	0.4312	0.25
WT DHPA/DHP A (I9L)	0.5097	0.33	0.5070	0.22
WT DHP B/DHP B (L9I)	0.3361	0.05	0.2454	0.15

^a Within a given variant, superposition of the A and B protomers from the same asymmetric unit (i.e., heteroprotomer superposition) resulted in low rmsd values of 0.3380 Å for DHP B (L9I) and 0.5361 Å for DHP A (I9L), as expected due to the protein chains being of identical composition in the crystallized homo-dimer.

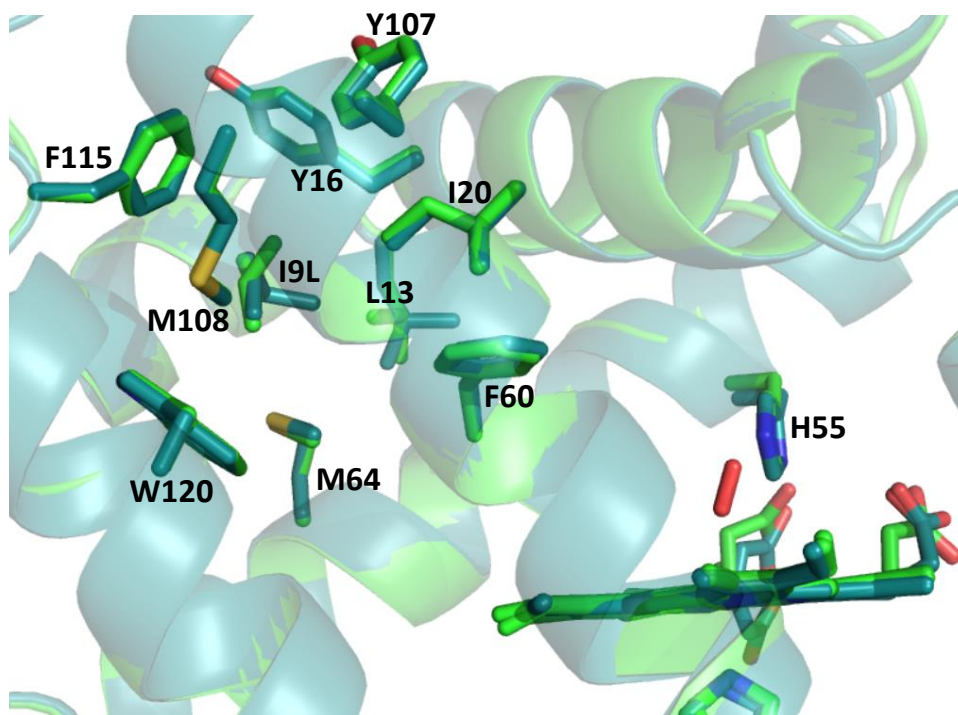


Figure S3.7. LSQ C_{α} superposition of DHP A (I9L) and DHP B (L9I), focusing on the distal side of the heme cavity as well as the region containing the residue at position 9.

Discussion of the Structural Features of the Distal and Proximal Cavities in DHP

Distal cavity – the R32 residue, found in the C helix, is involved in three hydrogen bonding interactions: for the side chain nitrogens, $N^{\eta 1}$ is H-bonded to the backbone carbonyl oxygen of Lys41 (located in the loop region between the C and D helices) at a distance of 3.12 Å and the $N^{\eta 2}$ is H-bonded to the $O^{\delta 1}$ of Asn26 (located in the B helix) at a distance of 3.44 Å, while a 3.10 Å H-bond is found between the R32 backbone amide nitrogen and the backbone carbonyl oxygen of Pro29 (located in the loop region between the B and C helices). In DHP B, the effect of the R32K mutation results in complete loss of the hydrogen bond to Asn26, elongation of the side chain N^{ζ} to Lys41 backbone carbonyl hydrogen bond to 3.59 Å, and formation of a new N^{ζ} to Tyr38 backbone carbonyl hydrogen bond at 2.67 Å, while the Lys32 backbone amide nitrogen to Pro29 backbone carbonyl oxygen hydrogen bond remains intact at 3.18 Å.

The shorter lysine also impacts neighboring residues that help define a portion of the hydrophobic distal (substrate binding) pocket, as seen in the shortening of the Arg33 backbone amide to Asp 30 backbone carbonyl hydrogen bond, from 3.60 Å in DHP A (Arg32) to 3.14 Å in DHP B (Lys32).

Tyr34, located at the end of the C helix, is the site of the protein radical associated with Compound ES in DHP A at pH 7.³³ As elucidated for the Y34F variant, mutation of this tyrosine to a redox inactive residue shifted the protein radical formed upon H₂O₂-activation to Tyr38,²⁵ and led to an increase in the peroxidase k_{cat} of 1.3-fold compared to the WT enzyme. Interestingly, the Y34N mutation led to the opposite effect on catalytic activity: a reduction in k_{cat} of 1.2-fold in the present study that was virtually identical to the 1.3-fold reduction observed previously by Wang et al.²¹ The structural consequences of the Y34N mutation are: in DHP A, Y34 is solvent exposed, its amide N makes a hydrogen bond to the backbone carbonyl of Glu31 at 3.24 Å and the phenolic oxygen is within H-bonding distance (3.59 and 3.02 Å to Nⁿ¹ and Nⁿ², respectively) of Arg33. In DHP B, the Asn34 N^{δ2} makes a hydrogen bond to Glu31 O^{ε2} at 3.65 Å, the Asn34 amide N makes a hydrogen bond to the backbone carbonyl of Glu31 at 3.12 Å, and both Arg33 Nⁿ¹ and its amide nitrogen make hydrogen bonds to the Asp30 backbone carbonyl at 2.78 and 3.14 Å, respectively. Although not directly applicable owing to the presence of a substrate, in the crystal structure of DHP A (Y34N) complexed with TCP,²¹ the Asn34 N^{δ2} makes a 3.41 Å hydrogen bond to the O^{ε2} of Glu31, with no Arg33 side chain H-bonding interactions present. Thus, the consequences of the Y34N mutation are both an alteration of the radical migration pathway that may affect substrate oxidation kinetics, as well as structural perturbations in neighboring residues that may also result in functional differences.

Proximal cavity – The effects of the N81S and S91G mutations may be rationalized by their proximity to L83 and the proximal histidine (H89), respectively. First, the Asp-His-Fe charge relay that is typical in peroxidases and whose function is to stabilize the ferryl intermediates through polarization of the proximal histidine is absent in DHP.^{43, 49} Instead, a hydrogen bond (2.82 Å in DHP A) between the backbone carbonyl of L83 and the N^δ-H of

H89 assumes this charge relay role (i.e., Leu-His-Fe). As a consequence of the N81S mutation in DHP B, this Leu-His hydrogen bond is shortened to 2.62 Å. The effects of the N81S mutation are likely propagated through the neighboring Thr82: in DHP A, the Thr82 backbone carbonyl makes a hydrogen bond (2.98 Å) to the Met86 amide nitrogen, whereas this distance is elongated to 3.19 Å in DHP B, thus positioning Leu83 closer to the proximal histidine. It is important to note that both the N81 (DHP A) and S81 (DHP B) side chains are solvent exposed and themselves do not participate in any notable hydrogen bonding interactions. Rather, backbone hydrogen bonding interactions are important: the residue 81 backbone carbonyl to backbone amide of Glu85 hydrogen bond distances are 2.90 Å for Ser81, and 2.98 Å for Asn81, whereas the residue 81 backbone amide to backbone carbonyl of Ala77 hydrogen bond distances are 2.86 Å for Ser81, and 2.96 Å for Asn81.

Located in the loop region between the F and G helices, Ser91 has no significant hydrogen bonding interactions in the DHP A structure, neither through the side chain nor through the backbone. Similarly, Gly91 in DHP B lacks any hydrogen bonding interactions. As such, it is likely that any differences afforded to catalytic activity associated with the S91G mutation are due to the increased flexibility of the protein backbone imparted by the glycine residue that lies just two amino acids from the critically important proximal histidine (H89).

3.10 References

- (1) Adeva-Andany, M.; López-Ojén, M.; Funcasta-Calderón, R.; Ameneiros-Rodríguez, E.; Donapetry-García, C.; Vila-Altesor, M.; Rodríguez-Seijas, J., Comprehensive review on lactate metabolism in human health. *Mitochondrion* **2014**, *17*, 76-100.
- (2) Sankaran, V. G.; Orkin, S. H., The Switch from Fetal to Adult Hemoglobin. *Cold Spring Harbor Perspectives in Medicine* **2013**, *3*, (1).
- (3) Biemelt, S.; Keetman, U.; Mock, H. P.; Grimm, B., Expression and activity of isoenzymes of superoxide dismutase in wheat roots in response to hypoxia and anoxia. *Plant, Cell & Environment* **2000**, *23*, (2), 135-144.
- (4) Shannon, L. M.; Kay, E.; Lew, J. Y., Peroxidase Isozymes from Horseradish Roots: I. Isolation and Physical Properties. *J. Biol. Chem.* **1966**, *241*, (9), 2166-2172.
- (5) Williams, J. A.; Ring, B. J.; Cantrell, V. E.; Jones, D. R.; Eckstein, J.; Ruterbories, K.; Hamman, M. A.; Hall, S. D.; Wrighton, S. A., Comparative Metabolic Capabilities of CYP3A4, CYP3A5, and CYP3A7. *Drug Metab. Dispos.* **2002**, *30*, (8), 883-891.
- (6) Berg, J. M.; Tymoczko, J. L.; Stryer, L., Section 10.2 Hemoglobin Transports Oxygen Efficiently by Binding Oxygen Cooperatively. In *Biochemistry, Fifth Edition*, W.H. Freeman: 2002.
- (7) Hüttemann, M.; Pecina, P.; Rainbolt, M.; Sanderson, T. H.; Kagan, V. E.; Samavati, L.; Doan, J. W.; Lee, I., The multiple functions of cytochrome c and their regulation in life and death decisions of the mammalian cell: From respiration to apoptosis. *Mitochondrion* **2011**, *11*, (3), 369-381.
- (8) Weber, R. E.; Mangum, C.; Steinman, H.; Bonaventura, C.; Sullivan, B.; Bonaventura, J., Hemoglobins of two terebellid polychaetes: *Enoplobranchus sanguineus* and *Amphitrite ornata*. *Comp. Biochem. Physiol. A Comp. Physiol.* **1977**, *56*, (2), 179-187.
- (9) Chiancone, E.; Ferruzzi, G.; Bonaventura, C.; Bonaventura, J., *Amphitrite ornata* erythrocrucorin. 2. Molecular controls of function. *Biochim. Biophys. Acta* **1981**, *670*, (1), 84-92.
- (10) Chiancone, E.; Brenowitz, M.; Ascoli, F.; Bonaventura, C.; Bonaventura, J., *Amphitrite ornata* erythrocrucorin. 1. Structural properties and characterization of subunit interactions. *Biochim. Biophys. Acta* **1980**, *623*, (1), 146-162.

- (11) Chen, Y. P.; Woodin, S. A.; Lincoln, D. E.; Lovell, C. R., An unusual dehalogenating peroxidase from the marine terebellid polychaete *Amphitrite ornata*. *J. Biol. Chem.* **1996**, *271*, (9), 4609-4612.
- (12) Osborne, R. L.; Taylor, L. O.; Han, K. P.; Ely, B.; Dawson, J. H., *Amphitrite ornata* dehaloperoxidase: enhanced activity for the catalytically active globin using MCPBA. *Biochem. Biophys. Res. Commun.* **2004**, *324*, (4), 1194-1198.
- (13) Barrios, D. A.; D'Antonio, J.; McCombs, N. L.; Zhao, J.; Franzen, S.; Schmidt, A. C.; Sombers, L. A.; Ghiladi, R. A., Peroxygenase and oxidase activities of dehaloperoxidase-hemoglobin from *Amphitrite ornata*. *J. Am. Chem. Soc.* **2014**, *136*, (22), 7914-7925.
- (14) McCombs, N. L.; Smirnova, T.; Ghiladi, R. A., Oxidation of Pyrrole by Dehaloperoxidase-Hemoglobin: Chemoenzymatic Synthesis of Pyrrolin-2-Ones. *Catal. Sci. Technol.* **2017**, *7*, 3104-3118.
- (15) Zhang, E.; Chen, Y. P.; Roach, M. P.; Lincoln, D. E.; Lovell, C. R.; Woodin, S. A.; Dawson, J. H.; Lebioda, L., Crystallization and initial spectroscopic characterization of the heme-containing dehaloperoxidase from the marine polychaete *Amphitrite ornata*. *Acta Crystallogr. D Biol. Crystallogr.* **1996**, *52*, (Pt 6), 1191-1193.
- (16) Lebioda, L.; LaCount, M. W.; Zhang, E.; Chen, Y. P.; Han, K.; Whitton, M. M.; Lincoln, D. E.; Woodin, S. A., An enzymatic globin from a marine worm. *Nature* **1999**, *401*, (6752), 445.
- (17) McCombs, N. L.; D'Antonio, J.; Barrios, D. A.; Carey, L. M.; Ghiladi, R. A., Nonmicrobial Nitrophenol Degradation via Peroxygenase Activity of Dehaloperoxidase-Hemoglobin from *Amphitrite ornata*. *Biochemistry* **2016**, *55*, (17), 2465-2478.
- (18) McCombs, N. L.; Moreno-Chicano, T.; Carey, L. M.; Franzen, S.; Hough, M. A.; Ghiladi, R. A., Interaction of Azole-Based Environmental Pollutants with the Coelomic Hemoglobin from *Amphitrite ornata*: A Molecular Basis for Toxicity. *Biochemistry* **2017**, *56*, (17), 2294-2303.
- (19) Sun, S.; Sono, M.; Wang, C.; Du, J.; Lebioda, L.; Dawson, J. H., Influence of heme environment structure on dioxygen affinity for the dual function *Amphitrite ornata* hemoglobin/dehaloperoxidase. Insights into the evolutional structure–function adaptations. *Arch. Biochem. Biophys.* **2014**, *545*, 108-115.

- (20) Sun, S.; Sono, M.; Du, J.; Dawson, J. H., Evidence of the direct involvement of the substrate TCP radical in functional switching from oxyferrous O₂ carrier to ferric peroxidase in the dual-function hemoglobin/dehaloperoxidase from *Amphitrite ornata*. *Biochemistry* **2014**, *53*, (30), 4956-4969.
- (21) Wang, C.; Lovelace, L. L.; Sun, S.; Dawson, J. H.; Lebioda, L., Complexes of dual-function hemoglobin/dehaloperoxidase with substrate 2,4,6-trichlorophenol are inhibitory and indicate binding of halophenol to compound I. *Biochemistry* **2013**, *52*, 6203–6210.
- (22) Du, J.; Huang, X.; Sun, S.; Wang, C.; Lebioda, L.; Dawson, J. H., *Amphitrite ornata* Dehaloperoxidase (DHP): Investigations of Structural Factors That Influence the Mechanism of Halophenol Dehalogenation Using “Peroxidase-like” Myoglobin Mutants and “Myoglobin-like” DHP Mutants. *Biochemistry* **2011**, *50*, (38), 8172-8180.
- (23) Du, J.; Sono, M.; Dawson, J. H., Functional switching of *Amphitrite ornata* dehaloperoxidase from O₂-binding globin to peroxidase enzyme facilitated by halophenol substrate and H₂O₂. *Biochemistry* **2010**, *49*, 6064-6069.
- (24) Davydov, R.; Osborne, R. L.; Shanmugam, M.; Du, J.; Dawson, J. H.; Hoffman, B. M., Probing the oxyferrous and catalytically active ferryl states of *Amphitrite ornata* dehaloperoxidase by cryoreduction and EPR/ENDOR spectroscopy. Detection of compound I. *J. Am. Chem. Soc.* **2010**, *132*, (42), 14995-15004.
- (25) Dumariéh, R.; D'Antonio, J.; Deliz-Liang, A.; Smirnova, T.; Svistunenko, D. A.; Ghiladi, R. A., Tyrosyl Radicals in Dehaloperoxidase: How nature deals with evolving an oxygen-binding globin to a biologically relevant peroxidase. *J. Biol. Chem.* **2013**, *288*, (46), 33470-33482.
- (26) Franzen, S.; Thompson, M. K.; Ghiladi, R. A., The dehaloperoxidase paradox. *Biochim. Biophys. Acta* **2012**, *1824*, (4), 578-588.
- (27) D'Antonio, J.; D'Antonio, E. L.; Thompson, M. K.; Bowden, E. F.; Franzen, S.; Smirnova, T.; Ghiladi, R. A., Spectroscopic and mechanistic investigations of dehaloperoxidase B from *Amphitrite ornata*. *Biochemistry* **2010**, *49*, (31), 6600-6616.
- (28) Feducia, J.; Dumariéh, R.; Gilvey, L. B.; Smirnova, T.; Franzen, S.; Ghiladi, R. A., Characterization of dehaloperoxidase compound ES and its reactivity with trihalophenols. *Biochemistry* **2009**, *48*, (5), 995-1005.

- (29) Osborne, R. L.; Coggins, M. K.; Raner, G. M.; Walla, M.; Dawson, J. H., The mechanism of oxidative halophenol dehalogenation by *Amphitrite ornata* dehaloperoxidase is initiated by H₂O₂ binding and involves two consecutive one-electron steps: role of ferryl intermediates. *Biochemistry* **2009**, *48*, (20), 4231-4238.
- (30) Han, K.; Woodin, S. A.; Lincoln, D. E.; Fielman, K. T.; Ely, B., *Amphitrite ornata*, a marine worm, contains two dehaloperoxidase genes. *Mar. Biotechnol. (NY)* **2001**, *3*, (3), 287-292.
- (31) LaCount, M. W.; Zhang, E.; Chen, Y. P.; Han, K.; Whitton, M. M.; Lincoln, D. E.; Woodin, S. A.; Lebioda, L., The crystal structure and amino acid sequence of dehaloperoxidase from *Amphitrite ornata* indicate common ancestry with globins. *J. Biol. Chem.* **2000**, *275*, (25), 18712-18716.
- (32) de Serrano, V.; D'Antonio, J.; Franzen, S.; Ghiladi, R. A., Structure of dehaloperoxidase B at 1.58 Å resolution and structural characterization of the AB dimer from *Amphitrite ornata*. *Acta Cryst.* **2010**, *D66*, (Pt 5), 529-538.
- (33) Thompson, M. K.; Franzen, S.; Ghiladi, R. A.; Reeder, B. J.; Svistunenko, D. A., Compound ES of dehaloperoxidase decays via two alternative pathways depending on the conformation of the distal histidine. *J. Am. Chem. Soc.* **2010**, *132*, 17501-17510.
- (34) D'Antonio, E. L.; Bowden, E. F.; Franzen, S., Thin-layer spectroelectrochemistry of the Fe(III)/Fe(II) redox reaction of dehaloperoxidase-hemoglobin. *J. Electroanal. Chem.* **2012**, *668*, 37-43.
- (35) Beers, R. F., Jr.; Sizer, I. W., A spectrophotometric method for measuring the breakdown of hydrogen peroxide by catalase. *J. Biol. Chem.* **1952**, *195*, (1), 133-140.
- (36) D'Antonio, J.; Ghiladi, R. A., Reactivity of deoxy- and oxyferrous dehaloperoxidase B from *Amphitrite ornata*: Identification of compound II and its ferrous-hydroperoxide precursor. *Biochemistry* **2011**, *50*, (27), 5999-6011.
- (37) Chenprakhon, P.; Sucharitakul, J.; Panijpan, B.; Chaiyen, P., Measuring Binding Affinity of Protein-Ligand Interaction Using Spectrophotometry: Binding of Neutral Red to Riboflavin-Binding Protein. *J. Chem. Educ.* **2010**, *87*, (8), 829-831.

- (38) Otwinowski, Z.; Minor, W., Processing of X-ray diffraction data collected in oscillation mode. In *Methods in Enzymology*, Carter Jr., C. W.; Sweet, R. M., Eds. Academic Press: New York, 1997; Vol. 276: Macromolecular Crystallography, part A, pp 307-326.
- (39) McCoy, A. J.; Grosse-Kunstleve, R. W.; Adams, P. D.; Winn, M. D.; Storoni, L. C.; Read, R. J., Phaser crystallographic software. *J. Appl. Crystallogr.* **2007**, *40*, (Pt 4), 658-674.
- (40) Adams, P. D.; Afonine, P. V.; Bunkoczi, G.; Chen, V. B.; Davis, I. W.; Echols, N.; Headd, J. J.; Hung, L. W.; Kapral, G. J.; Grosse-Kunstleve, R. W.; McCoy, A. J.; Moriarty, N. W.; Oeffner, R.; Read, R. J.; Richardson, D. C.; Richardson, J. S.; Terwilliger, T. C.; Zwart, P. H., PHENIX: a comprehensive Python-based system for macromolecular structure solution. *Acta Cryst.* **2010**, *D66*, (Pt 2), 213-221.
- (41) Emsley, P.; Lohkamp, B.; Scott, W. G.; Cowtan, K., Features and development of Coot. *Acta Cryst.* **2010**, *D66*, (Pt 4), 486-501.
- (42) Afonine, P. V.; Grosse-Kunstleve, R. W.; Echols, N.; Headd, J. J.; Moriarty, N. W.; Mustyakimov, M.; Terwilliger, T. C.; Urzhumtsev, A.; Zwart, P. H.; Adams, P. D., Towards automated crystallographic structure refinement with phenix.refine. *Acta Cryst.* **2012**, *D68*, (Pt 4), 352-367.
- (43) Franzen, S.; Ghiladi, R. A.; Lebioda, L.; Dawson, J., Chapter 10 Multi-functional Hemoglobin Dehaloperoxidases. In *Heme Peroxidases*, The Royal Society of Chemistry: 2016; pp 218-244.
- (44) Ghiladi, R. A.; Medzihradzky, K. F.; Rusnak, F. M.; Ortiz de Montellano, P. R., Correlation between isoniazid resistance and superoxide reactivity in *Mycobacterium tuberculosis* KatG. *J. Am. Chem. Soc.* **2005**, *127*, (38), 13428-13442.
- (45) Ghiladi, R. A.; Medzihradzky, K. F.; Ortiz de Montellano, P. R., The role of the Met-Tyr-Trp crosslink in *Mycobacterium tuberculosis* catalase-peroxidase (KatG) as revealed by KatG(M255I). *Biochemistry* **2005**, *44*, 15093-15105.
- (46) Droghetti, E.; Howes, B. D.; Feis, A.; Dominici, P.; Fittipaldi, M.; Smulevich, G., The quantum mechanically mixed-spin state in a non-symbiotic plant hemoglobin: The effect of distal mutation on AHb1 from *Arabidopsis thaliana*. *Journal of Inorganic Biochemistry* **2007**, *101*, (11), 1812-1819.

- (47) Nicoletti, F. P.; Thompson, M. K.; Howes, B. D.; Franzen, S.; Smulevich, G., New insights into the role of distal histidine flexibility in ligand stabilization of dehaloperoxidase-hemoglobin from *Amphitrite ornata*. *Biochemistry* **2010**, *49*, (9), 1903-1912.
- (48) Beitlich, T.; Kuhnel, K.; Schulze-Briese, C.; Shoeman, R. L.; Schlichting, I., Cryoradiolytic reduction of crystalline heme proteins: analysis by UV-Vis spectroscopy and X-ray crystallography. *J. Synchrotron Radiat.* **2007**, *14*, (Pt 1), 11-23.
- (49) de Serrano, V.; Chen, Z.; Davis, M. F.; Franzen, S., X-ray crystal structural analysis of the binding site in the ferric and oxyferrous forms of the recombinant heme dehaloperoxidase cloned from *Amphitrite ornata*. *Acta Cryst.* **2007**, *D63*, (Pt 10), 1094-1101.
- (50) D'Antonio, E. L.; D'Antonio, J.; de Serrano, V.; Gracz, H.; Thompson, M. K.; Ghiladi, R. A.; Bowden, E. F.; Franzen, S., Functional consequences of the creation of an Asp-His-Fe triad in a 3/3 globin. *Biochemistry* **2011**, *50*, (44), 9664-9680.
- (51) Thompson, M. K.; Franzen, S.; Davis, M. F.; Oliver, R. C.; Krueger, J. K., Dehaloperoxidase-Hemoglobin from *Amphitrite ornata* Is Primarily a Monomer in Solution. *J. Phys. Chem. B* **2011**, *115*, (14), 4266-4272.
- (52) Thompson, M. K.; Davis, M. F.; de Serrano, V.; Nicoletti, F. P.; Howes, B. D.; Smulevich, G.; Franzen, S., Internal binding of halogenated phenols in dehaloperoxidase-hemoglobin inhibits peroxidase function. *Biophys. J.* **2010**, *99*, (5), 1586-1595.
- (53) de Serrano, V. S.; Davis, M. F.; Gaff, J. F.; Zhang, Q.; Chen, Z.; D'Antonio, E. L.; Bowden, E. F.; Rose, R.; Franzen, S., X-ray structure of the metcyano form of dehaloperoxidase from *Amphitrite ornata*: evidence for photoreductive dissociation of the iron-cyanide bond. *Acta Cryst.* **2010**, *D66*, (Pt 7), 770-82.
- (54) Chen, Z.; de Serrano, V.; Betts, L.; Franzen, S., Distal histidine conformational flexibility in dehaloperoxidase from *Amphitrite ornata*. *Acta Cryst.* **2009**, *D65*, (Pt 1), 34-40.
- (55) Zhao, J.; de Serrano, V.; Dumarieh, R.; Thompson, M.; Ghiladi, R. A.; Franzen, S., The role of the distal histidine in H₂O₂ activation and heme protection in both peroxidase and globin functions. *J. Phys. Chem. B* **2012**, *116*, (40), 12065-77.

- (56) Poulos, T. L.; Kraut, J., The stereochemistry of peroxidase catalysis. *J. Biol. Chem.* **1980**, *255*, (17), 8199-8205.
- (57) Jiang, S.; Wright, I.; Swartz, P.; Franzen, S., The role of T56 in controlling the flexibility of the distal histidine in dehaloperoxidase-hemoglobin from *Amphitrite ornata*. *Biochimica et Biophysica Acta (BBA) - Proteins and Proteomics* **2013**, *1834*, (10), 2020-2029.
- (58) Ma, H.; Thompson, M. K.; Gaff, J.; Franzen, S., Kinetic analysis of a naturally occurring bioremediation enzyme: dehaloperoxidase-hemoglobin from *Amphitrite ornata*. *J. Phys. Chem. B* **2010**, *114*, (43), 13823-9.

Chapter 4

Selective Tuning of Activity in a Multifunctional Enzyme as Revealed in the F21W Mutant of Dehaloperoxidase B from *Amphitrite ornata*

Leiah M. Carey¹, Kyung Beom Kim^{1, 2}, Nikolette McCombs¹, Paul Swartz³, Cheal Kim², and Reza A. Ghiladi¹✉

¹Department of Chemistry, North Carolina State University, Raleigh, North Carolina, 27695-8204

²Department of Fine Chemistry, Seoul National University of Science and Technology, Seoul, Korea, 139-743

³Department of Structural and Molecular Biochemistry, North Carolina State University, Raleigh, North Carolina, 27695-7622

4.1 Author Contributions

- Mutagenesis, expression and purification of DHP B (F21W), both containing and lacking the 6X His tag
- Peroxidase and peroxygenase enzymatic assays, substrate binding studies
- X-ray crystallographic structure determination and analysis

4.2 Abstract

Possessing both peroxidase and peroxygenase activities with a broad substrate profile that includes phenols, indoles, and pyrroles, the enzyme dehaloperoxidase (DHP) from *Amphitrite ornata* is a multifunctional catalytic hemoglobin that challenges many of the assumptions behind the well-established structure-function paradigm in hemoproteins. While previous studies have demonstrated that the F21W variant leads to attenuated peroxidase activity in DHP, here we have studied the impact of this mutation on peroxygenase activity to determine if it is possible to selectively tune DHP to favor one function over another. Biochemical assays with DHP B (F21W) revealed minimal decreases in peroxygenase activity of 1.2-2.1 fold as measured by 4-nitrophenol or 5-Br-indole substrate conversion, whereas the peroxidase activity catalytic efficiency for 2,4,6-trichlorophenol (TCP) was more than 7-fold decreased.

Binding studies showed a 20-fold weaker affinity for 5-bromoindole ($K_d = 2960 \pm 940 \mu\text{M}$) in DHP B (F21W) compared to WT DHP B. Stopped-flow UV/visible studies and isotope labeling experiments together suggest that the F21W mutation neither significantly changes the nature of the catalytic intermediates, nor alters the mechanisms that have been established for peroxidase and peroxygenase activities in DHP. The X-ray crystal structure (1.96 Å; PDB 5VLX) of DHP B (F21W) revealed that the tryptophan blocks one of the two identified TCP binding sites, specifically TCP_{interior}, suggesting that the other site, TCP_{exterior}, remains viable for binding peroxygenase substrates. Taken together, these studies demonstrate that blocking the TCP_{interior} binding site in DHP selectively favors peroxygenase activity at the expense of its peroxidase activity.

4.3 Introduction

The coelomic hemoglobin of the sediment-dwelling marine worm *Amphitrite ornata* functions as a naturally occurring dehalogenation enzyme that has been termed dehaloperoxidase (DHP)^{1,2}. In addition to being able to oxidize/degrade 7 EPA priority pollutants of phenolic structure (phenol, 2-chlorophenol, 2,4-dichlorophenol, 2,4,6-trichlorophenol, 2-nitrophenol, 4-nitrophenol, and 2,4-dinitrophenol)^{3,4}, DHP more broadly has shown activity against halogenated indoles⁵, pyrroles⁶, and guaiacols. Mechanistic studies⁷⁻¹⁸ have shown that DHP appears to function via a Poulos-Kraut type mechanism¹⁹ in which H₂O₂ reacts with a ferric heme to form DHP Compound I^{13,16}, the iron(IV)-oxo (ferryl) porphyrin π -cation radical species that is common to both the peroxidase²⁰ and P450 cycles²¹. Accordingly, DHP acts on the aforementioned substrates with peroxidase^{2,22}, peroxygenase^{5,6}, and oxidase⁵ mechanisms. Moreover, DHP is known to bind a number of persistent organic pollutants (POPs) belonging to theazole class of compounds²³, including benzotriazole, benzimidazole, indazole, and imidazole that have widespread agricultural and industrial uses. Thus, given the broad substrate scope and multiple catalytic activities exhibited by DHP, one of the outstanding questions is how substrate binding is related to enzyme activity in this

multifunctional and promiscuous catalytic globin, and whether DHP can be tuned to favor one activity over another.

One of the key features of DHP that sets it apart from traditionally studied globins (e.g. myoglobin and hemoglobin), and even many heme peroxidases, is that it possesses a distal small molecule binding site that can accommodate a variety of different substrates (and inhibitors)^{1,2,24,25}, examples of which are shown in Figure 4.1 and include the peroxygenase substrate 4-nitrophenol (4-NP, purple, PDB 5CHQ⁴), inhibitor 4-bromophenol (4-BP, PDB 3LB2²⁶), and the peroxidase substrates 2,4,6-tribromophenol (TBP, yellow, PDB 4FH7²⁷) and 2,4,6-trichlorophenol (TCP, cyan, PDB 4KN3²⁴). Two substrate binding sites were determined for TCP [$\text{TCP}_{\text{interior}}$ (near the heme α edge) and $\text{TCP}_{\text{exterior}}$ (near the heme γ edge and heme cavity)], while TBP was observed to bind in a single site and in a similar orientation as $\text{TCP}_{\text{interior}}$. The observation of multiple binding sites across the entire face of the distal heme cavity is consistent with DHP being a multifunctional catalytic globin. More importantly, one can evaluate the orientation of binding for these substrates in Figure 4.1 against the activities that each is subjected to: the unhindered (at the C2 and C3 positions) nitrophenol substrate is susceptible to DHP peroxygenase activity, possibly via an electrophilic addition by the ferryl intermediate, leading to incorporation of the O-atom from hydrogen peroxide⁴. By contrast, the comparable positions in TBP are sterically hindered by the halogen substituents, precluding O-atom transfer, and leading to substrate oxidation via a peroxidase mechanism²⁷. TCP binds as a peroxidase substrate (i.e., $\text{TCP}_{\text{interior}}$) in a conformation that closely resembles that observed for TBP, but self-inhibition at high concentrations has also been observed²⁴, and has been attributed to the $\text{TCP}_{\text{exterior}}$ site as this conformation orients the para-halogen above the heme iron and to the detriment of H_2O_2 -binding. Although currently there is no indole-bound structure of DHP, both computational studies of haloindole binding⁵ and X-ray structures with bound azoles²³ (as models for indole) strongly suggest that indoles bind in an orientation relative to the ferryl heme that facilitates O-atom transfer via a peroxygenase mechanism.

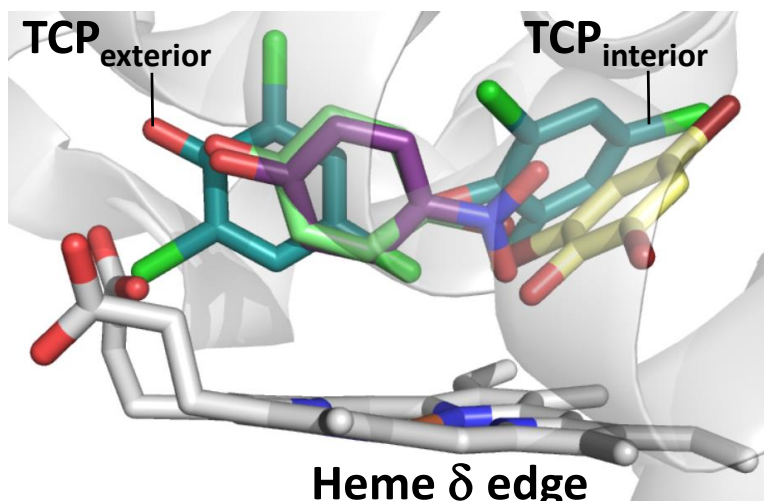


Figure 4.1. Superposition of substrate binding sites within the distal pocket of DHP as viewed from the heme γ edge: TBP (yellow, PDB 4FH7²⁷), 4-NP (purple, PDB 5CHQ⁴), 4-BP (green, PDB 3LB2²⁶), and both internal (TCP_{interior}) and external (TCP_{exterior}) conformations of TCP (cyan, PDB 4KN3²⁴).

Following the identification of the two TCP binding sites in DHP, Dawson and co-workers rationally designed the F21W mutation in DHP A to block one of those sites, TCP_{interior}²⁴. Modeling revealed that the potential W21 rotamers of the mutant either blocked the TCP_{interior} site, or were disallowed because of steric hindrance with the protein. The consequence of the F21W mutation was a 15-fold reduction in catalytic efficiency (k_{cat}/K_M^{TCP}) vs. WT DHP A for peroxidase activity with TCP as the substrate, thus confirming their hypothesis that mutagenesis of F21 to the larger Trp residue would significantly impair peroxidase activity. At that time, however, the peroxygenase⁴⁻⁶ activity of DHP was not known, and the consequence of the F21W mutation on that activity was unexplored. Given the recent identification of the 4-nitrophenol peroxygenase substrate binding site⁴ that does not overlap significantly with TCP_{interior}, and the unknown consequence of the F21W mutation on peroxygenase activity, we were motivated to explore this mutation as a possible means of selectively tuning the activity profile of DHP. To that end, we present here a study of the DHP B (F21W) mutant on peroxygenase activity, including biochemical assays, stopped-flow UV-visible spectroscopic characterization of the activated enzyme, as well as an X-ray crystallographic study of the

mutant. The results demonstrate the ability to favor peroxygenase activity over peroxidase activity in a rationally designed mutant of a multifunctional catalytic globin.

4.4 Experimental

4.4.1 Materials. Unless otherwise specified, all chemicals were of reagent grade, purchased from VWR or Fisher Scientific, and used without further purification. $\text{H}_2^{18}\text{O}_2$ and H_2^{18}O (90% and 98% oxygen atom enriched, respectively) were obtained from ICON Isotopes (Summit, NJ). DHP was expressed, purified and obtained in the ferric oxidation state as previously reported⁹. The enzyme concentration was determined spectrophotometrically using the molar absorptivity coefficient ($\epsilon_{406} = 116,400 \text{ M}^{-1} \text{ cm}^{-1}$)⁹. Stock solutions (2 mM) of trichlorophenol (TCP) were prepared in 100 mM potassium phosphate (KPi) buffer (pH 7) and stored at -80 °C. TCP concentration and lack of degradation was monitored by measuring its absorbance at 312 nm ($\epsilon = 3752 \text{ M}^{-1} \text{ cm}^{-1}$)⁸. Stock solutions (10 mM) of 5-bromoindole and 7-bromoindole were prepared in MeOH, stored at -80 °C in glass vials, and screened by HPLC for degradation prior to use⁵. Aliquots were stored on ice during use. Stock solutions (5 mM) of 4-nitrophenol (4-NP) were prepared fresh in 100 mM KPi (pH 7) when needed. Solutions of H_2O_2 were prepared daily, and stored on ice while protected from light until needed. The concentration of H_2O_2 was determined spectrophotometrically ($\epsilon_{240} = 43.6 \text{ M}^{-1} \text{ cm}^{-1}$)²⁸.

4.4.2 Construction of Mutant DHP Plasmid. Site-directed mutagenesis was performed using the Quikchange II site-directed mutagenesis kit (Agilent Technologies). Mutagenesis [melt (95 °C, 60 s), anneal (55 °C, 50 s), and extension (68 °C, 360 s)] was performed for 16 cycles. Oligonucleotides were synthesized by Integrated DNA Technologies (IDT) (sense 5'-ACC TAT GCA CAG GAC ATT **TGG** CTC GCA TTT TTG AAT AGG-3'; anti-sense 5'-CCT ATT CAA AAA TGC GAG **CCA** AAT GTC CTG TGC ATA GGT-3'). The plasmid encoding an N-terminal poly-His tag wild-type DHP B was used as a template⁹. For crystallization, the mutant was obtained from a plasmid encoding wild-type DHP B lacking the N-terminal poly-His tag¹⁸. The modified plasmids were transformed into *E. coli* BL21-Gold(DE3) competent cells (Agilent Technologies) and selected based on survival on LB-agar-

ampicillin (100 $\mu\text{g}/\text{mL}$) plates. The plasmids were extracted using the spin column plasmid DNA kit (Bio Basic), and the desired mutation and lack of deleterious secondary ones were confirmed by sequencing (Genewiz).

4.4.3 Protein Crystallization and X-ray Diffraction Studies. Non-His tagged DHP B (F21W) was overexpressed and purified following a literature protocol⁴. Crystals were obtained through the hanging-drop vapor diffusion method. DHPB (F21W), in 20 mM Na cacodylate buffer pH 6.4, was concentrated to 12 mg/mL, and the crystals were grown from mother liquor solutions of 28-32 % PEG 4000 and 0.2 M ammonium sulfate at pH 6.4, equilibrated against identical reservoir solutions. Protein-to-mother liquor ratios varied between 1:1, 1.33:1, 1.66:1 and 2:1. At 4 °C crystals grew from each condition after 3 days. The crystals were cryo-protected by briefly dipping them in reservoir solution enhanced with 20% glycerol and then flash frozen in liquid N₂. Data were collected at the Biological X-ray Facility at NCSU on a Rigaku RuH3R with rotating copper anode equipped with a MAR345 CCD image plate detector and Oxford cryojet set at 100 K, utilizing a wavelength of 1.54 Å. All data were scaled and integrated using HKL2000²⁹, molecular replacement was performed with Phaser-MR³⁰ from the PHENIX³¹ suite of programs using the 3IXF¹⁸ monomer as the search model, model building and manual placement of waters utilized COOT³² and refinement was carried out using phenix.refine³³.

4.4.4 Peroxidase Studies. The hydrogen peroxide-dependent oxidative dehalogenation of 2,4,6-trichlorophenol (TCP) to 2,6-dichloro-1,4-benzoquinone (DCQ) as catalyzed by DHP was measured using a Cary 50 UV-vis spectrophotometer. The reactions were performed in triplicate at pH 7 in 100 mM KP_i at 25 °C, with a 1 mL total reaction volume. Buffered solutions of DHP (1.25 μM) and TCP (10 – 800 μM) were premixed and the reaction was initiated by the addition of H₂O₂ (80 μM). The change in absorbance at 272 nm (DCQ, $\epsilon = 14 \text{ mM}^{-1}\text{cm}^{-1}$)⁷ was measured using Cary WinUV Kinetics software over a 30 second time frame with a rate of 1 scan per second. The data were fit to the standard Michaelis-Menten kinetics model using the method of initial rates in the Grafit software package (Erithacus Software).

The apparent kinetics parameters K_M and k_{cat} resulted from the optimization of the fitting procedure.

4.4.5 Peroxygenase Studies. The percent conversions of 5-Br-indole, 7-Br-indole and 4-nitrophenol (4-NP) as catalyzed by DHP in the presence of H_2O_2 were analyzed by HPLC using a Waters 2796 Bioseparations Module coupled with a Waters 2996 Photodiode Array Detector and equipped with an ODS Hypersil C_{18} column (Thermo-Scientific, 150 mm x 4.6 mm, 5 μ m particle size). The reactions were performed in triplicate in 100 mM KP_i (pH 7) at 25 °C. Indole reactions also contained 5% MeOH (v/v). Buffered solutions of substrate and DHP were premixed, and the peroxygenase reaction was initiated with addition of H_2O_2 . Final concentrations were 10 μ M DHP, 500 μ M substrate and 500 μ M H_2O_2 in 200 μ L total volume. After 5 minutes of incubation at 25 °C, the reaction was quenched with excess catalase and then diluted 1:10 with 1800 μ L of 100 mM KP_i (pH 7). Diluted samples were subjected to HPLC analysis (solvent A - H_2O containing 0.1% trifluoroacetic acid: solvent B – HPLC-grade MeCN containing 0.1% trifluoroacetic acid). The elution method was as follows: 1.5 mL/min of 95:5 (A:B) to 5:95 using a linear gradient over 10 min; 5:95 isocratic for 2 minutes; 5:95 to 95:5 using a linear gradient over 1 min, and then isocratic for 4 min. Analysis was performed using the Empower software package (Waters Corp.).

4.4.6 5-Br-indole Binding Studies. As adapted from previously published protocols^{5,34}, the 5-Br-indole dissociation constant (K_d) was determined in triplicate for DHP in 100 mM KP_i (pH 7) containing 10% MeOH at 25 °C using a Cary 50 UV-vis spectrophotometer. A stock solution of 10 mM 5-Br-indole in MeOH was prepared in a glass vial. The UV-vis spectrophotometer was referenced with 10 μ M ferric DHP in 100 mM KP_i (pH 7) containing 10% MeOH (v/v). The total volume of the samples was 200 μ L with final concentrations of 10 μ M ferric DHP and 10-130 equivalents 5-Br-indole while maintaining 10% MeOH (v/v). Perturbations in the absorbance of the Soret band (ΔAbs) were recorded for each 5-Br-indole concentration (Figure S4.7). Analysis by nonlinear regression using the GraFit software package (Erithacus Software Ltd.) provided a calculated A_{max} , which was used to calculate α

($\Delta A/\Delta A_{\max}$) for the average ΔA for each concentration. A nonlinear regression plot provided the reported K_d values.

4.4.7 Stopped-flow UV-visible Studies. Optical spectra were recorded using a Bio-Logic SFM-400 triple-mixing stopped flow instrument coupled to a rapid scanning diode array UV-visible spectrophotometer. The reactions were conducted at room temperature, and all solutions were prepared in 100 mM KP_i (pH 7). Data were collected (900 scans total) over a three-time domain regime (2.5, 25, and 250 ms; 300 scans each) using the Bio Kinet32 software package (Bio-Logic). All data were evaluated using the Specfit Global Analysis System software package (Spectrum Software Associates) and fit to exponential functions as two-step/three species irreversible mechanisms. Experiments were performed in single-mixing mode where DHP B (F21W) at a final concentration of 10 μ M was reacted with 2.5 - 25 equivalents of H_2O_2 .

4.5 Results

4.5.1 Overexpression, Purification and Characterization of DHP B. Recombinant DHP B (F21W) was obtained by expression in *E. coli* and purified as previously described^{4,9,18}. The monomeric molecular weight of DHP B (F21W) was determined by electrospray ionization MS to be 16,313.11 g/mol, in good agreement with the theoretical expected value (16,313.42 g/mol).

DHP B (F21W) was initially isolated as a mixture of the ferric and oxyferrous forms, as were WT isoenzymes A and B^{8,9}, and subsequent treatment with an excess of potassium ferricyanide permitted the isolation of the ferric form. The electronic absorption spectrum of ferric DHP B (F21W) exhibited features typical of a high-spin ferric heme [UV-visible: 407 (Soret), 504, 634 nm; Figure 4.2] that were similar to those observed previously for WT DHP B [UV-visible: 407 (Soret), 508, 633 nm]⁹. The optical purity ratio (Reinheitzahl or R_z , defined as A_{Soret}/A_{280}) for DHP B (F21W) was found to be 3.63, lower than the literature value for WT DHP B of 4.1^{9,13}. This was expected, however, as the F21W mutation increases the calculated A_{280} molar absorptivity coefficient to 16960 $M^{-1}cm^{-1}$ in DHP B (F21W) from 11460 $M^{-1}cm^{-1}$

in WT DHP B. The A_{Soret}/A_{380} (1.87) ratio for DHP B (F21W) was also similar to that for WT DHP B ($A_{\text{Soret}}/A_{380} = 1.88$; $A_{614}/A_{645} = 1.14$)^{9,13}. However, the A_{614}/A_{645} (0.93) ratio was lower in the F21W mutant, suggesting a slightly lower population of 6-coordinate high-spin heme in the mutant when compared to its wild-type analog. Sodium dithionite reduction of the ferric enzyme in the presence of O_2 yielded oxyferrous DHP B (F21W), with spectral features [UV-visible: 418 (Soret), 544, 578 nm] that were again consistent with the 6-coordinate low-spin oxyferrous forms of the wild-type isoenzymes^{8,9}.

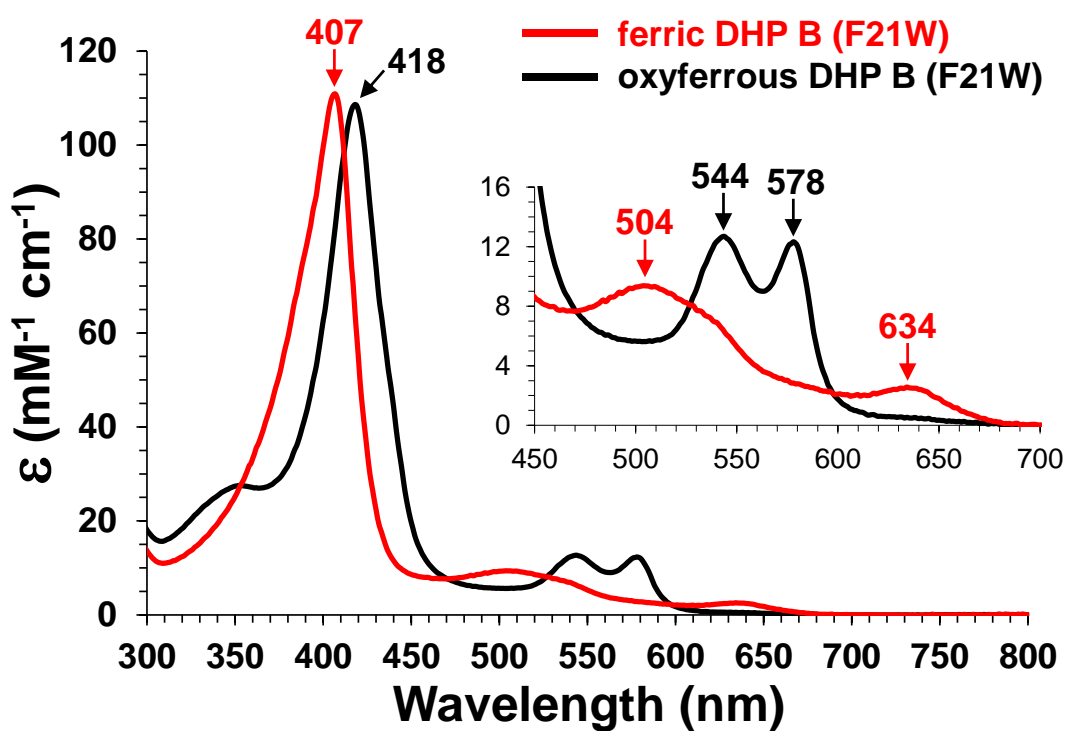


Figure 4.2. UV-visible spectra of ferric (red) and oxyferrous (black) DHP B (F21W) in 100 mM KPi (pH 7).

4.5.2 Activity Assays. The peroxidase activity of DHP for the oxidative dehalogenation of 2,4,6-trichlorophenol (TCP) to 2,6-dichloro-1,4-benzoquinone (DCQ) was monitored spectrophotometrically in a [TCP]-dependent manner at a fixed concentration of H₂O₂. When compared with the kinetic parameters of WT DHP B (Table 4.1; $k_{\text{cat}} = 1.90 \pm 0.20 \text{ s}^{-1}$; $K_{\text{M}} = 90 \pm 20 \text{ }\mu\text{M}$; $k_{\text{cat}}/K_{\text{M}} = 21 \pm 5 \text{ mM}^{-1} \text{ s}^{-1}$), DHP B (F21W) exhibited a 1.5-fold decrease in catalytic turnover ($k_{\text{cat}} = 1.29 \pm 0.07 \text{ s}^{-1}$), a 4.9-fold increase in K_{M} ($440 \pm 50 \text{ }\mu\text{M}$), and a 7.2-fold lower catalytic efficiency ($k_{\text{cat}}/K_{\text{M}} = 2.9 \pm 0.3 \text{ mM}^{-1}\text{s}^{-1}$). These results demonstrate that the F21W mutation significantly affects the peroxidase activity of DHP B, but the effect is less pronounced than that observed for DHP A (F21W) when compared to WT DHP A (3.3-fold lower k_{cat} , 4.6-fold higher K_{M} , and 15-fold lower $k_{\text{cat}}/K_{\text{M}}$)²⁴. When 4-bromophenol ($K_{\text{d}} = 1.15 \text{ mM}$)²⁶, the known inhibitor of DHP peroxidase and peroxygenase activities^{5,9}, was included in the reaction at 500 μM , the rate of TCP oxidation as catalyzed by the F21W mutant was reduced by 45%.

The peroxygenase activity of DHP was monitored by HPLC for the H₂O₂-dependent oxidation of 5-Br-indole, 7-Br-indole, and 4-nitrophenol (4-NP) when initiated from the ferric state at pH 7. Overall, the effect of the F21W mutation on substrate percent conversion was limited: the DHP B (F21W) mutant exhibited a decrease of: i) 1.4-fold for 5-Br-indole ($34.0 \pm 1.6 \text{ \%}$ vs $48.1 \pm 2.3 \text{ \%}$ for WT DHP B [5]), ii) 1.2-fold for 7-Br-indole ($39.4 \pm 1.2 \text{ \%}$ vs $46.1 \pm 1.7 \text{ \%}$ for WT DHP B⁵), and iii) 2.1-fold for 4-NP ($19.1 \pm 0.3 \text{ \%}$ vs $39.4 \pm 0.7 \text{ \%}$ for WT DHP B⁴). As peroxygenase activity was not known at the time when Dawson and co-workers²⁴ first described the effects of the F21W mutation on the catalytic (peroxidase) activity of DHP, no data for DHP A (F21W) are available. However, when compared with WT DHP A, the reactivity of DHP B (F21W) with 5-Br-indole is higher by 1.7 fold ($34.0 \pm 1.6 \text{ \%}$ vs $20.3 \pm 1.7 \text{ \%}$ for WT DHP A⁵), while the 4-NP reactivity is approximately equivalent ($19.1 \pm 0.3 \text{ \%}$ vs $21.6 \pm 0.1 \text{ \%}$ for WT DHP A⁴). As was the case for peroxidase activity, inclusion of 500 μM 4-bromophenol as an inhibitor attenuated 5-Br-indole substrate conversion to $4.6 \pm 1.4 \text{ \%}$.

Table 4.1. Kinetic parameters for the oxidation of TCP, and percent substrate conversion for the oxygenation of 5-Br-indole, 7-Br-indole and 4-NP.

Enzyme	K_M^{TCP} (μM)	Peroxidase ^a		Peroxygenase ^{a,b}			Ref.
		k_{cat} (s^{-1})	k_{cat}/K_M ($\text{mM}^{-1} \text{s}^{-1}$)	5-Br-indole	7-Br-indole	4-nitrophenol	
DHP B (F21W)	440 ± 50	1.29 ± 0.07	2.9 ± 0.3	34.0 ± 1.6	39.4 ± 1.0	19.1 ± 0.3	^c
WT DHP B	90 ± 20	1.90 ± 0.20	21 ± 5	48.1 ± 2.3	46.1 ± 1.7	39.4 ± 0.7	^c
DHP A (F21W)	2,260 ± 512	0.32 ± 0.05	0.14 ± 0.03	n/a	n/a	n/a	[24]
WT DHP A	495 ± 62	1.05 ± 0.07	2.1 ± 0.3	20.3 ± 1.7	n/a	21.6 ± 0.1	[4, 5, 24]

^a reactions were performed with ferric DHP in 100 mM KP_i buffer (pH 7) at 25 °C. ^b values represent percent (%) substrate conversion; n/a = not available. ^c this work.

4.5.3 Isotopically-labeled Oxygen Studies. Studies employing labeled $\text{H}_2^{18}\text{O}_2$ and H_2^{18}O (90% and 98% oxygen atom enriched, respectively) were performed with 5-Br-indole and subsequently analyzed by LC-MS to confirm hydrogen peroxide as the source of the O atom incorporated in the peroxygenase studies. The background-subtracted total ion chromatograms (TICs) are shown in Figure 4.3 for the 5-Br-2-oxindole product. Reactions performed in the presence of H_2^{18}O and unlabeled H_2O_2 show 5-Br-2-oxindole (m/z 212, 214; Figure 4.3A) with product m/z values identical to those obtained from the unlabeled $\text{H}_2\text{O}/\text{H}_2\text{O}_2$ reaction. Gratifyingly, the reactions performed in the presence of $\text{H}_2^{18}\text{O}_2$ in unlabeled H_2O exhibited the characteristic m/z shift of +2 amu (Figure 4.3B) denoting ^{18}O -label incorporation. Similarly, the 5-Br-3-oxindolenine (m/z 210, 212) product only showed a shift of +2 amu in the presence of labeled $\text{H}_2^{18}\text{O}_2$ (data not shown). Taken together, the labeling studies confirmed that the oxygen atom incorporated into the products was derived solely from H_2O_2 , thus demonstrating that the F21W mutation does not alter the reported peroxygenase chemistry.

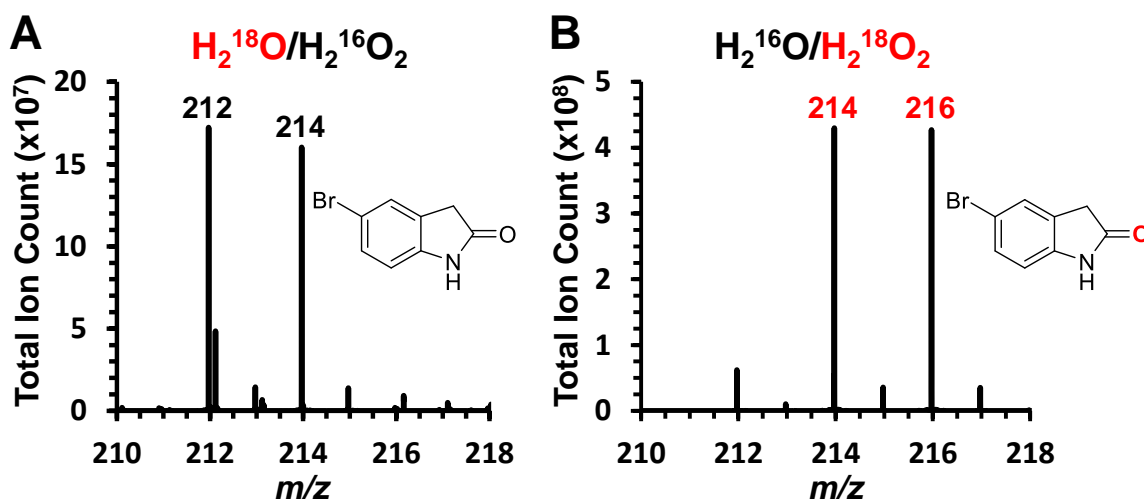


Figure 4.3. ESI-MS total ion chromatograms obtained for the reaction product 5-Br-2-oxindole (A: H₂¹⁸O, H₂¹⁶O₂; B: H₂¹⁶O, H₂¹⁸O₂). Reaction conditions: [5-Br-indole] = [H₂O₂] = 500 μM, [enzyme] = 10 μM, 100 mM KP_i (pH 7), 25 °C.

4.5.4 Stopped-flow UV-visible Spectroscopy. To assess the ability of DHP B (F21W) to form Compound ES, the catalytically active two-electron-oxidized state containing both a ferryl center [Fe^{IV}=O] and a tyrosyl radical, single-mixing stopped-flow UV-visible spectroscopic methods were employed as previously described^{8,9}. Using the 10-eq. H₂O₂ reaction as representative data (Figure 4.4), the following observations were made: an SVD analysis employing a simple three component, irreversible mechanism ($a \rightarrow b \rightarrow c$) revealed that upon rapid mixing (2 ms) of a ferric DHP B (F21W) solution [UV-visible spectrum: 407 (Soret), 505, 535 (sh), 635] with 10 equiv H₂O₂, a new species was observed whose spectral features [UV-visible: 419 (Soret), 545, 587 nm] we attributed to the ferryl-containing intermediate Compound ES based upon our previous assignments of this reaction intermediate in WT DHP A⁸ and B⁹. The experimental value of k_{obs} for Compound ES formation varied linearly with hydrogen peroxide concentration (2.5-25 mol equiv), from which the bimolecular rate constant was determined to be $(6.68 \pm 0.05) \times 10^4 \text{ M}^{-1}\text{s}^{-1}$, in agreement with the values reported for WT isoenzymes [DHP A: $(3.56 \pm 0.02) \times 10^4 \text{ M}^{-1}\text{s}^{-1}$; DHP B: $(1.29 \pm 0.11) \times 10^5 \text{ M}^{-1}\text{s}^{-1}$; Table 4.2]^{8,9}. The DHP B (F21W) Compound ES intermediate further converted to a

new species [UV-visible: 412 (Soret), 535, 565 (sh) nm; $k_{\text{obs}} = 0.012 \pm 0.001 \text{ s}^{-1}$]. We have assigned this as Compound RH, the “reversible heme” state of dehaloperoxidase that forms from the decay of Compound ES in the absence of a co-substrate, for this variant based upon analogy to the similar, but not identical, species observed in DHP isoenzymes A [411 (Soret), 530, 564 (sh) nm; $k_{\text{obs}} = 0.0167 \pm 0.0003 \text{ s}^{-1}$]⁸ and B [411 (Soret), 554, 599 (sh) nm; $k_{\text{obs}} = 0.010 \pm 0.001 \text{ s}^{-1}$]⁹, as well as in various other DHP mutants¹³.

Table 4.2. Comparison of UV-visible spectroscopic data for the ferric, Compound ES, and Compound RH species in DHP B (F21W) and WT DHP isoenzymes A and B at pH 7.

Enzyme	Ferric^a	Compound ES	Compound RH	Reference
DHP B (F21W)	407, 505, 535 (sh) 635	419, 545, 587	412, 535, 565	^b
WT DHP A	407, 504, 538, 635	420, 545, 585	411, 530, 564	[8]
WT DHP B	407, 508, 633	419, 545, 585	411, 554, 599	[9]

^a values reported are in nm; ^b this work.

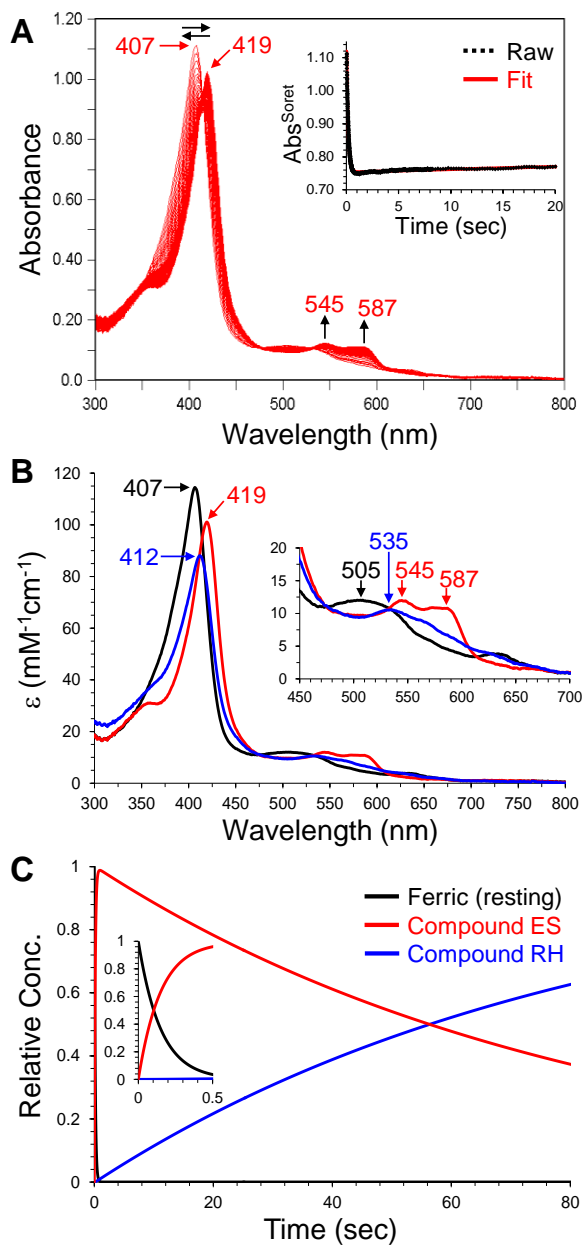


Figure 4.4. Kinetic data obtained by optical spectroscopy for the reaction of DHP B (F21W) with H_2O_2 . A) Stopped-flow UV-visible spectra of the reaction of DHP B (F21W) ($10\ \mu\text{M}$) with a 10-fold excess of H_2O_2 at pH 7 (900 scans over 83 sec); *inset* - the single wavelength (407 nm) dependence on time obtained from the raw spectra and its fit with a superposition of the calculated spectra components; B) Calculated spectra of the three reaction components derived from the SVD analysis: ferric (black), Compound ES (red), and Compound RH (blue); C) time dependences of the relative concentrations for the three components shown in panel B.

4.5.5 X-ray Crystallographic Studies. Non-His tagged DHP B (F21W) was overexpressed, purified, crystallized, and its structure solved by X-ray diffraction methods. X-ray data collection and refinement statistics are provided in Table 4.3. DHP B (F21W) refined to a resolution of 1.96 Å, with R_{merge} , R_{work} and R_{free} values of 8.4%, 16.43% and 20.45%, respectively.

DHP B (F21W) crystallized as a homo-dimer in the asymmetric unit of the $P2_12_12_1$ space group, consistent with all previous DHP crystal structures. The protomer environments were identical, as shown through the global least squared quadratic (LSQ) C^α superpositions: the root mean squared deviation (rmsd) value of 0.3194 Å for the DHP B (F21W) superposition of protomers A and B is consistent with highly homologous structures that possess very little geometric variation over conformational space³⁵⁻³⁷. LSQ C^α superposition of DHP B (F21W) and WT DHP B yielded a rmsd value of 0.3491 Å (average of subunits), which again shows high structural similarity globally. Moreover, the hemes align very well despite not being a variable in the C^α LSQ alignment (Figure 4.5A).

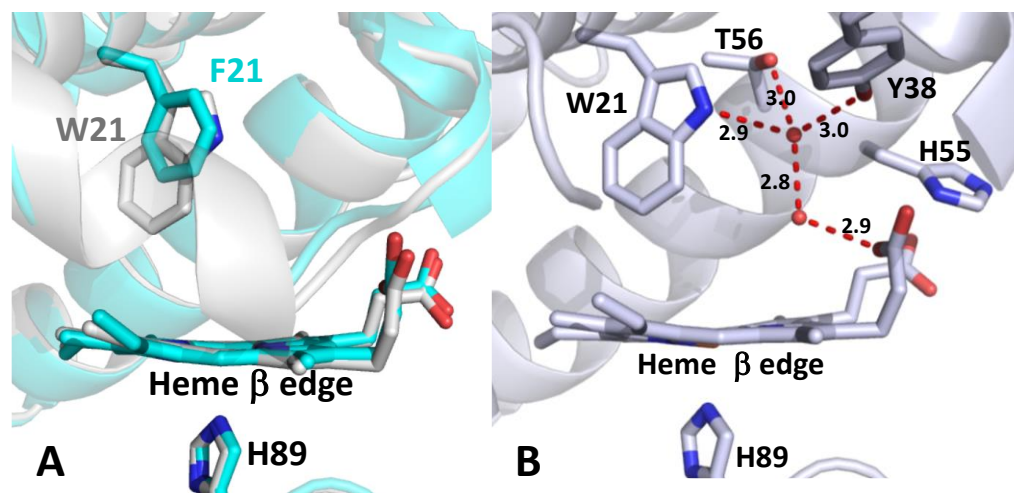


Figure 4.5. A) DHP B (F21W) (silver) C^α superposition with WT DHP B (cyan; PDB 3IXF¹⁸), highlighting the F21/W21 residues. Only one conformation for F21 is shown for clarity. B) Distal pocket of the DHP B (F21W) mutant, as viewed from the heme β edge. There are two water molecules in the distal pocket, forming a H-bonding network with W21, T56, Y38, and the heme propionate arms. All distances are given in Å.

Table 4.3. X-ray Data Collection and Refinement Statistics for DHP B (F21W) (5VLX).

PDB Accession Code	5VLX
<u>Data Collection</u>	
Wavelength (Å)	1.54
Temperature (K)	100
Space Group	P2 ₁ 2 ₁ 2 ₁
Unit-cell parameters (Å)	
<i>a</i>	60.48
<i>b</i>	67.13
<i>c</i>	67.37
Unique reflections	25,631 (1,032) ^a
Completeness (%)	97.8 (80.2) ^a
R _{merge} (%) ^b	8.4 (39.5) ^a
I/σ(I)	25.0 (2.4) ^a
Redundancy	4.5 (3.3) ^a
V _m (Å ³ /Da)	2.21
<u>Refinement</u>	
Resolution (Å)	1.80
R _{work} (%) ^c	16.62 (21.59) ^a
R _{free} (%) ^d	20.44 (29.75) ^a
No. of protein atoms	2,317
No. of solvent atoms	215
R.m.s.d from ideal geometry ^e	
Bond lengths (Å)	0.007
Bond angles (°)	0.926
<u>Ramachandran plot (%)</u>	
Most favored region	98.89
Addl allowed region	1.11

^aValues in parentheses are for the highest resolution shell. ^bR_{merge} = $\frac{\sum_h \sum_i [|I_i(h) - \langle I(h) \rangle|]}{\sum_h \sum_i I_i(h)} \times 100\%$, where $I_i(h)$ is the i^{th} measurement and $\langle I(h) \rangle$ is the weighted mean of all measurements of $I(h)$. ^cR_{work} = $\frac{\sum |F_o - F_c|}{\sum F_o} \times 100\%$, where F_o and F_c are the observed and calculated structure factors, respectively. ^dR_{free} is the R factor for the subset (7.8 %) of reflections selected before and not included in the refinement. ^eRoot-mean-square deviation. ^fRamachandran plot created via MolProbity.

As opposed to the global comparison, a closer inspection of the F21W mutant active site (Figure 4.5B) revealed differences from previous DHP structures (Figure S4.8): the ferric DHP B (F21W) structure shows the absence of the usual water molecule as the heme-Fe sixth ligand.

Rather, unique to this DHP structure is the presence of 2 water molecules in the distal pocket that form a hydrogen-bonding network with W21, T56, Y38, and the heme propionate arms. In WT DHP B, T56 resides in a different conformation, with the O^γ turned away from the pocket, interacting with the E helix. In line with the lack of a water (sixth) ligand in DHP B (F21W), the distal histidine, H55, does not participate in the H-bond network inside the distal pocket, but instead resides in the solvent-open conformation interacting with the heme propionate arms and a sulfate molecule. The heme was observed in a slightly twisted and domed orientation, with the Fe lying 0.06 Å below the heme pyrrole N plane (vs. 0.21 Å for ferric WT DHP B [18]). Comparing subunit-averaged distances (Table 4.4) between DHP B (F21W) and WT DHP B, the Fe – H89 N^ε distance is 0.10 Å longer in the mutant (2.28 Å vs 2.18 Å) while the H89 N^δ – L83 carbonyl O distance is shorter by 0.14 Å (2.73 Å vs 2.87 Å). However, the Fe – H89 C^α distances are comparable (6.15 Å vs 6.13 Å), suggesting that the differences in H89 distances can be ascribed to the side chain itself and not the protein backbone. Additionally, Fe – H55 C^α distances (8.69 Å vs 8.67 Å) and Fe – C^α distances for residue 21 (W21:10.65 Å vs F21:10.75 Å) show very little deviation between mutant and wild-type main chain distances, resulting in similar heme pocket geometries.

Table 4.4. Selected distances (Å) for DHP B (F21W) and WT DHP B (PDB accession 3IXF¹⁸).

	DHP B (F21W)		WT DHP B^a	
	Protomer A	Protomer B	Protomer A	Protomer B
Fe – H89 N ^ε	2.28	2.27	2.18	2.17
H89 N ^δ – L83 O	2.71	2.74	2.92	2.81
Fe – H89 C ^α	6.16	6.14	6.14	6.11
Fe – H55 C ^α	8.61	8.77	8.71	8.63
Fe – F21/W21 C ^α	10.67	10.63	10.76	10.74
Fe – F21/W21	5.06 (C ^η)	5.03 (C ^η)	6.50 (C ^ζ)	6.32 (C ^ζ)
sidechain	5.47 (C ^{ζ2})	5.49 (C ^{ζ2})	6.74 (C ^{ε1})	6.60 (C ^{ε1})

^a for clarity, only distances for the F21 conformer closest to the heme are given for WT DHP B.

4.6 Discussion

Using the previous study of Dawson and co-workers²⁴ as inspiration for the present work, the F21W mutation was rationally designed with the intention of blocking the TCP_{interior} binding site in an effort to increase the selectivity of DHP as a peroxygenase enzyme at the expense of its peroxidase activity. To that end, the DHP B (F21W) mutant exhibited minimal decreases in peroxygenase activity of 1.2-2.1 fold as measured by substrate conversion, whereas the catalytic efficiency of the peroxidase activity was more than 7-fold decreased. Interestingly, Dawson and co-workers showed that the catalytic efficiency for DHP A (F21W) peroxidase reactivity was reduced 15-fold compared to WT DHP A²⁴. Thus, the question arose as to why the effect of the F21W mutation is more muted in DHP B than in DHP A. From a structural standpoint, the differences in primary structure between these two isoenzymes are limited to five amino acid substitutions (note – isoenzyme A is listed first): I/L9, R/K34, Y/N34, N/S81 and S/G91. These amino acid substitutions do not perturb the overall structural fold of DHP when comparing the two isoenzymes,¹⁸ yet they result in DHP B exhibiting a greater reactivity than DHP A for both peroxidase and peroxygenase activities.^{4,5,9} However, why the F21W mutation affects DHP A more than DHP B cannot be addressed by a simple structural comparison (*vide infra*).

To begin to address this question, we performed stopped-flow UV/visible spectroscopic studies to assess whether the formation of the Compound ES intermediate in DHP B (F21W) was altered owing to the introduction of a redox-active tryptophan residue near the active site. However, no significant differences in the rates of formation and decay, nor in its spectral features, were noted for Compound ES, suggesting that the introduction of the F21W mutation does not alter the electronic structure of this reactive intermediate. Similarly, we were concerned if the F21W mutation alters the oxidation pathway of haloindoles (i.e., causes a switch from O-atom transfer to electron transfer), however, isotope labeling studies confirmed the peroxygenase mechanism of DHP remains intact in DHP B (F21W). Taken together, we conclude that the F21W mutation does not significantly change the nature of the catalytic

intermediates, and thus does not alter the mechanisms that have been established in DHP for peroxidase² and peroxygenase⁴⁻⁶ activities.

Having ruled out changes to the catalytic intermediates as being responsible for the differences in activity between DHP A (F21W) and DHP B (F21W), we considered structural (and potentially dynamic) effects of the catalytically relevant proximal and distal histidine residues. Our rationale for such a consideration is that it has been previously shown that tuning of DHP activity may be accomplished by altering i) the proximal cavity charge relay^{11,38} that includes histidine (H89), whose role is to facilitate dioxygen binding to the ferrous heme or to support the Fe(IV) oxidation state in Compounds I, ES and II, and ii) the conformational flexibility and/or position of the catalytically important distal histidine (H55)^{39,40}, which is critical for enzyme activation (i.e., cleavage of Compound 0 to the activated ferryl species). In the context of the structure-function relationship ascribed to these two residues, we propose the following five factors that may individually, or in combination, account for the differential effect of the F21W mutation in DHP A and B when compared to the WT isoenzymes: 1) DHP possesses a Leu-His-Fe charge relay (as opposed to the typical peroxidase Asp-His-Fe one) whose function is to stabilize the ferryl intermediates through polarization of the proximal histidine^{2,11}. In DHP B (F21W), the H89 N^δ – L83 carbonyl O distance of 2.72 Å is shorter by 0.14 Å than that found in WT DHP B (2.87 Å), and would better support a ferryl intermediate. 2) The distal histidine is unusually flexible in DHP, being normally found in equilibrium between the “open” (5cHS) and “closed” (6cHS, water-bound) states in the WT isoenzymes. It has been hypothesized^{1,25,26,41-43} that altering this conformational flexibility may affect substrate/co-substrate binding by gating the accessibility of the active site pocket for entry/exit of substrate/product molecules or co-substrate H₂O₂^{2,40}. In DHP B (F21W), the distal histidine was only found in the ‘open’ (5cHS) solvent-accessible conformation, stabilized by H-bonding interactions with the heme propionate arms and an exogenous sulfate ion. This ‘open’ conformation of H55 enables the presence of active site waters by excluding the H55 from the distal pocket. 3) Although no water ligand was found to bind the heme-Fe in both protomers (a feature that has commonly been observed in ferric DHP structures^{18,43}), two water molecules

were found in the distal pocket. The introduction of a nitrogen-containing indole ring from the tryptophan side chain likely increases the polarity of the distal pocket, creating a more attractive environment for accommodating water molecules in the active site. The presence of these distal waters also involves a H-bonding network that includes the O γ of the T56 sidechain (now unable for stabilization of Helix E), Y38 (site of radical formation in DHP B), a heme propionate arm, and W21. 4) In studies of the T56 mutants of DHP³⁹, a greater conformational flexibility of the distal histidine was noted. In DHP B (F21W), it was noted that the O γ of the T56 sidechain was positioned into the distal pocket instead of its normal role of stabilization of helix E, which could lead to altered H55 flexibility. 5) Although no crystal structure of DHP A (F21W) is available, calculations showed that the orientation of the W21 side chain was directed away from the heme iron and toward the δ heme edge²⁴. In the DHP B (F21W) crystal structure, however, W21 was observed positioned directly toward the heme-Fe, which would likely alter the reactivity in comparison to that of isoenzyme A mutant.

On the whole, the introduction of the F21W mutation causes very little structural perturbation relative to the wild type structure. As shown by the C α superposition, the heme retains the same position and orientation, which was unexpected given the increased size of the tryptophan side chain compared to that of phenylalanine. The most notable difference between the F21W mutant and WT structure was observed in the sidechain distances for the mutated residue. Remarkably, however, the protein backbone and remaining parts of the structure were virtually identical in spite of the steric differences imposed by the larger indole ring. As expected for the F21W mutation, the tryptophan side chain is in closer proximity to the heme cofactor. Averaging subunits, in WT DHP B the closest atom of the phenyl ring to the heme Fe is C ζ at a distance of 6.41 Å, with C ϵ^1 as the next closest atom at 6.67 Å. In the F21W mutant, the C η atom resides 5.05 Å from the heme Fe with the next closest atom, C ζ^2 located 5.48 Å from the Fe. Thus, when compared to F21 in WT DHP B, W21 has a contact \sim 1.3 Å closer to the heme Fe. As a consequence, W21 effectively resides in the TCP_{interior} binding site²⁴ (Figure 4.6A), which can be directly related to the attenuation of peroxidase reactivity. However, peroxidase activity is still observed, which may be explained by the

presence of a second TCP binding site ($\text{TCP}_{\text{exterior}}$). This shows that while the $\text{TCP}_{\text{interior}}$ binding site has a significant role in TCP oxidation, it is not solely responsible for TCP reactivity, and the $\text{TCP}_{\text{exterior}}$ binding site may play a functional role as well through long-range electron transfer.

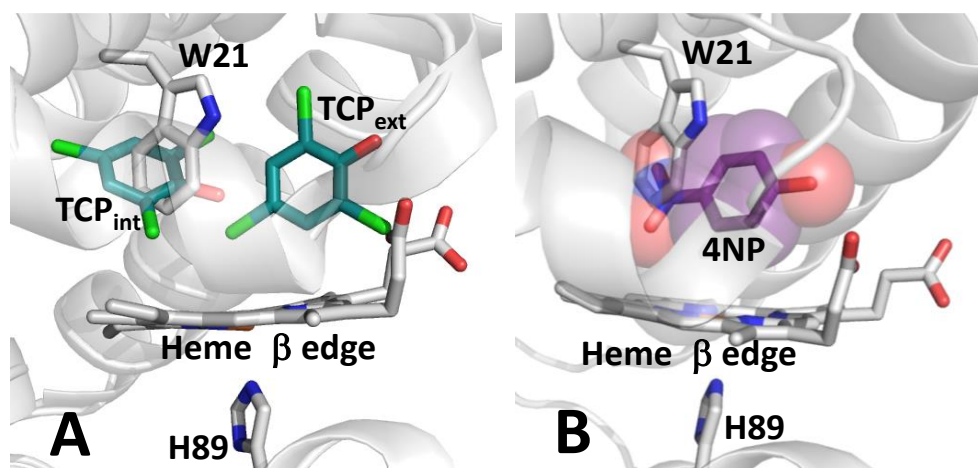


Figure 4.6. DHP B (F21W) mutant distal pocket superposition with TCP [$\text{TCP}_{\text{interior}}$ (PDB 4KMV) and $\text{TCP}_{\text{exterior}}$ (PDB 4KMW)²⁴] and 4-NP (PDB 5CHQ⁴) substrates.

As has been established for DHP, the presence of peroxidase substrates within the heme pocket does not follow the normally observed peroxidase substrate binding motif at the heme γ or δ edge². DHP thus presents an unconventional example of observed internal binding of substrates that undergo oxidation through a mechanism that is generally characterized by substrate binding external of the heme cavity⁴⁴. Internal peroxidase substrate binding is an obvious consequence of the unusually large distal cavity presented in DHP (even though the tertiary structure possesses a traditional globin fold), which is spacious enough to accommodate internal binding of phenolic peroxidase substrates. Thus, the peroxidase mechanism of DHP may in fact exclude the generally observed requirement of external substrate binding, with the two sequential one-electron oxidation steps¹⁵ possibly occurring within the distal cavity.

Peroxygenase reactivity, on the other hand, is characterized by atom transfer, and in order to facilitate this transfer the substrate binding sites have greater constraints on their possible orientations and distances from the activated ferryl intermediate. W21 only partially overlaps with the 4-NP binding site⁴ (Figure 4.6B), specifically with the nitro group of 4-NP, but not with the bulk of the 4-NP substrate. The limited steric clash with the nitro group of 4-NP likely still permits it to bind in an orientation that is in close proximity to the activated heme Fe, which in turn would appear to permit oxygen atom transfer as required for the peroxygenase mechanism. Crystallographic substrate binding sites of 5-Br-indole and 7-Br-indole have yet to be obtained, however computationally⁵ derived binding sites are in good agreement with spectroscopic data: i) 5-Br-indole has been computed to bind in the distal pocket above the heme Fe, which correlates to the substrate's perturbation of the 5cHS/6cHS heme equilibrium to favor the 5cHS species; ii) the 7-Br-indole computed binding site resides deeper in the distal pocket, and consequently the binding of 7-Br-indole has little or no effect on the 5cHS/6cHS heme equilibrium, indicating this substrate binds in an orientation that does not inhibit water ligation to the heme Fe. In DHP B (F21W), the additional steric bulk of the W21 sidechain is in a position to hinder 5-Br-indole binding while not fully blocking the binding site. This was reflected in the dissociation constant for 5-Br-indole in DHP B (F21W) ($K_d = 2960 \pm 940 \mu\text{M}$; Figure S4.7) being 20-fold higher than in WT DHP B ($K_d = 150 \pm 10 \mu\text{M}$), which likely results from either weaker binding in the same site as the WT enzyme, or possibly that binding occurs at a different site. In agreement with the computed binding of 7-Br-indole showing that this substrate resides deeper in the distal pocket, the additional steric bulk of W21 appears have a very small effect on 7-Br-indole reactivity, with a decrease of only 1.2-fold.

4.7 Conclusion

The DHP B (F21W) mutant was rationally designed in an effort to decrease peroxidase reactivity through perturbation of the peroxidase substrate binding site, with a minimal (albeit non-zero) consequence on peroxygenase activity. As such, the F21W mutation enables the selective tuning of activity in this multifunctional hemoprotein. The results provide further

evidence that confirm the plasticity of the DHP heme distal cavity: namely, the distal cavity of DHP can accommodate large substrates (i.e., haloindoles) and increases in side chain volume (i.e., Phe→Trp) while maintaining a nearly identical backbone structure. The dominant change in the side chains appears restricted to the position of the distal histidine in that it is forced into the solvent-exposed conformation. This change does have functional consequences, although it does not itself constitute an off switch – surprisingly, the activation of bound H₂O₂ is robust and appears to be possible even in a structure where H55 is forced into the external position through the combination of binding a large substrate and a large side chain. The F21W mutant further confirms this observation that has been suggested based on observations of X-ray crystal structures of DHP B with large substrates, and suggests that it may be possible to further tune DHP activity through simultaneous mutagenesis of multiple active site residues.

4.8 Acknowledgements

This project was supported by NSF CAREER Award CHE-1150709 and NSF CHE-1609446. Mass spectra were obtained at the Mass Spectrometry Facility for Biotechnology at North Carolina State University. Partial funding for the facility was obtained from the North Carolina Biotechnology Center and the National Science Foundation.

4.9 Supplementary Material

Figure S4.7. Optical difference spectra of 5-Br-indole (10-130 eq.) binding to 10 μM DHP B (F21W) in 10% MeOH/100 mM KP_i (v/v) at pH 7; *inset* – corresponding titration curve.

Figure S4.8. Distal pocket of A) WT DHP B (PDB 3IXF¹), B) DHP B (F21W) (PDB 5VLX²) and C) superposition of WT DHP B and DHP B (F21W). As can be seen in panel C, marked differences between the two structures were observed for F35, T56 and H55, a slight difference was noted for Y38, and no significant differences were seen for L100, V59, and F25.

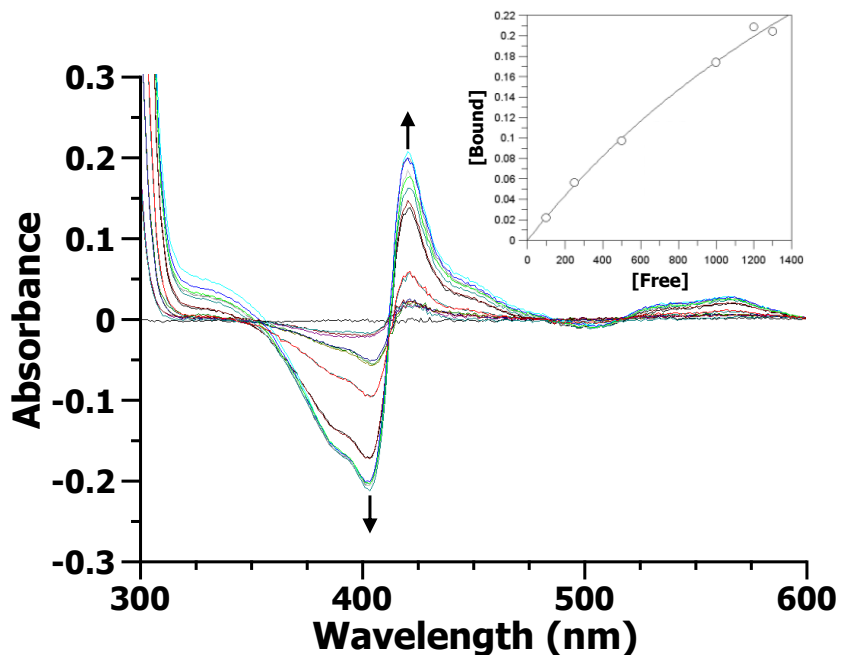


Figure S4.7. Optical difference spectra of 5-Br-indole (10-130 eq.) binding to 10 μ M DHP B (F21W) in 10% MeOH/100 mM KPi (v/v) at pH 7; *inset* – corresponding titration curve.

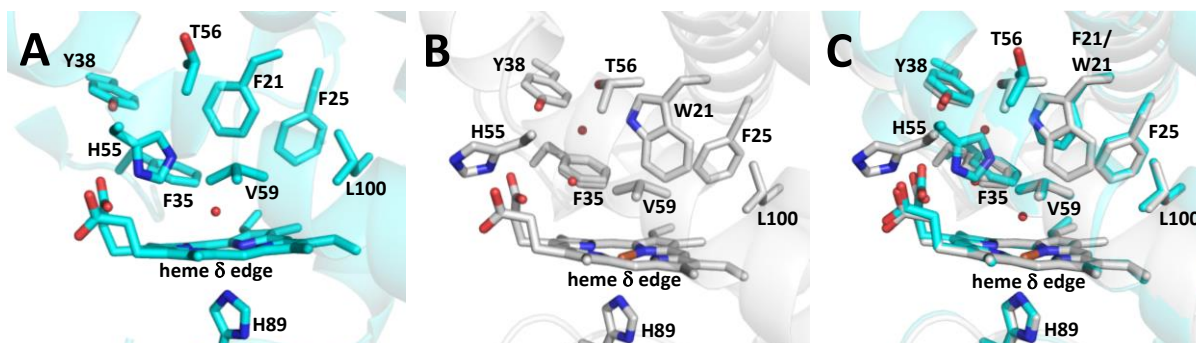


Figure S4.8. Distal pocket of A) WT DHP B (PDB 3IXF¹⁸), B) DHP B (F21W) (PDB 5VLX²) and C) superposition of WT DHP B and DHP B (F21W). As can be seen in panel C, marked differences between the two structures were observed for F35, T56 and H55, a slight difference was noted for Y38, and no significant differences were seen for L100, V59, and F25.

4.10 References

- (1) Lebioda, L.; LaCount, M. W.; Zhang, E.; Chen, Y. P.; Han, K.; Whitton, M. M.; Lincoln, D. E.; Woodin, S. A., An enzymatic globin from a marine worm. *Nature* **1999**, *401*, (6752), 445.
- (2) Franzen, S.; Ghiladi, R. A.; Lebioda, L.; Dawson, J., Chapter 10 Multi-functional Hemoglobin Dehaloperoxidases. In *Heme Peroxidases*, The Royal Society of Chemistry: 2016; pp 218-244.
- (3) Chen, Y. P.; Woodin, S. A.; Lincoln, D. E.; Lovell, C. R., An unusual dehalogenating peroxidase from the marine terebellid polychaete *Amphitrite ornata*. *J. Biol. Chem.* **1996**, *271*, (9), 4609-4612.
- (4) McCombs, N. L.; D'Antonio, J.; Barrios, D. A.; Carey, L. M.; Ghiladi, R. A., Nonmicrobial Nitrophenol Degradation via Peroxygenase Activity of Dehaloperoxidase-Hemoglobin from *Amphitrite ornata*. *Biochemistry* **2016**, *55*, (17), 2465-2478.
- (5) Barrios, D. A.; D'Antonio, J.; McCombs, N. L.; Zhao, J.; Franzen, S.; Schmidt, A. C.; Sombers, L. A.; Ghiladi, R. A., Peroxygenase and oxidase activities of dehaloperoxidase-hemoglobin from *Amphitrite ornata*. *J. Am. Chem. Soc.* **2014**, *136*, (22), 7914-7925.
- (6) McCombs, N. L.; Smirnova, T.; Ghiladi, R. A., Oxidation of Pyrrole by Dehaloperoxidase-Hemoglobin: Chemoenzymatic Synthesis of Pyrrolin-2-Ones. *Catal. Sci. Technol.* **2017**, *7*, 3104-3118.
- (7) Osborne, R. L.; Taylor, L. O.; Han, K. P.; Ely, B.; Dawson, J. H., *Amphitrite ornata* dehaloperoxidase: enhanced activity for the catalytically active globin using MCPBA. *Biochem. Biophys. Res. Commun.* **2004**, *324*, (4), 1194-1198.
- (8) Feducia, J.; Dumariéh, R.; Gilvey, L. B.; Smirnova, T.; Franzen, S.; Ghiladi, R. A., Characterization of dehaloperoxidase compound ES and its reactivity with trihalophenols. *Biochemistry* **2009**, *48*, (5), 995-1005.
- (9) D'Antonio, J.; D'Antonio, E. L.; Thompson, M. K.; Bowden, E. F.; Franzen, S.; Smirnova, T.; Ghiladi, R. A., Spectroscopic and mechanistic investigations of dehaloperoxidase B from *Amphitrite ornata*. *Biochemistry* **2010**, *49*, (31), 6600-6616.
- (10) Thompson, M. K.; Franzen, S.; Ghiladi, R. A.; Reeder, B. J.; Svistunenko, D. A., Compound ES of dehaloperoxidase decays via two alternative pathways depending on the conformation of the distal histidine. *J. Am. Chem. Soc.* **2010**, *132*, 17501-17510.

- (11) D'Antonio, E. L.; D'Antonio, J.; de Serrano, V.; Gracz, H.; Thompson, M. K.; Ghiladi, R. A.; Bowden, E. F.; Franzen, S., Functional consequences of the creation of an Asp-His-Fe triad in a 3/3 globin. *Biochemistry* **2011**, *50*, (44), 9664-9680.
- (12) D'Antonio, J.; Ghiladi, R. A., Reactivity of deoxy- and oxyferrous dehaloperoxidase B from *Amphitrite ornata*: Identification of compound II and its ferrous-hydroperoxide precursor. *Biochemistry* **2011**, *50*, (27), 5999-6011.
- (13) Dumarieh, R.; D'Antonio, J.; Deliz-Liang, A.; Smirnova, T.; Svistunenko, D. A.; Ghiladi, R. A., Tyrosyl Radicals in Dehaloperoxidase: How nature deals with evolving an oxygen-binding globin to a biologically relevant peroxidase. *J. Biol. Chem.* **2013**, *288*, (46), 33470-33482.
- (14) R. L. Osborne, S. Sumithran, M. K. Coggins, Y. P. Chen, D. E. Lincoln and J. H. Dawson, Spectroscopic characterization of the ferric states of *Amphitrite ornata* dehaloperoxidase and *Notomastus lobatus* chloroperoxidase: His-ligated peroxidases with globin-like proximal and distal properties. *J Inorg Biochem* 2006, *100*, 1100-1108.
- (15) Osborne, R. L.; Coggins, M. K.; Raner, G. M.; Walla, M.; Dawson, J. H., The mechanism of oxidative halophenol dehalogenation by *Amphitrite ornata* dehaloperoxidase is initiated by H₂O₂ binding and involves two consecutive one-electron steps: role of ferryl intermediates. *Biochemistry* **2009**, *48*, (20), 4231-4238.
- (16) Davydov, R.; Osborne, R. L.; Shanmugam, M.; Du, J.; Dawson, J. H.; Hoffman, B. M., Probing the oxyferrous and catalytically active ferryl states of *Amphitrite ornata* dehaloperoxidase by cryoreduction and EPR/ENDOR spectroscopy. Detection of compound I. *J. Am. Chem. Soc.* **2010**, *132*, (42), 14995-1500.
- (17) Du, J.; Sono, M.; Dawson, J. H. Functional switching of *Amphitrite ornata* dehaloperoxidase from O₂-binding globin to peroxidase enzyme facilitated by halophenol substrate and H₂O₂. *Biochemistry* **2010**, *49*, 6064-6069.
- (18) de Serrano, V.; D'Antonio, J.; Franzen, S.; Ghiladi, R. A. Structure of dehaloperoxidase B at 1.58 Å resolution and structural characterization of the AB dimer from *Amphitrite ornata*. *Acta Cryst.* **2010**, *D66*, 529-538.
- (19) Poulos, T. L.; Kraut, J. The stereochemistry of peroxidase catalysis. *J. Biol. Chem.* **1980**, *255*, 8199-8205.
- (20) Dunford, H. B. In *Heme Peroxidases*; The Royal Society of Chemistry: 2016, p 99-112.

- (21) *Cytochrome P450: Structure, Mechanism, and Biochemistry*; 4th ed.; Ortiz de Montellano, P. R., Ed.; Springer International Publishing, 2015.
- (22) Franzen, S.; Thompson, M. K.; Ghiladi, R. A. The dehaloperoxidase paradox. *Biochim. Biophys. Acta* **2012**, *1824*, 578-588.
- (23) McCombs, N. L.; Moreno-Chicano, T.; Carey, L. M.; Franzen, S.; Hough, M. A.; Ghiladi, R. A. Interaction of Azole-Based Environmental Pollutants with the Coelomic Hemoglobin from *Amphitrite ornata*: A Molecular Basis for Toxicity. *Biochemistry* **2017**, *56*, 2294-2303.
- (24) Wang, C.; Lovelace, L. L.; Sun, S.; Dawson, J. H.; Lebioda, L. Complexes of dual-function hemoglobin/dehaloperoxidase with substrate 2,4,6-trichlorophenol are inhibitory and indicate binding of halophenol to compound I. *Biochemistry* **2013**, *52*, 6203-6210.
- (25) LaCount, M. W.; Zhang, E.; Chen, Y. P.; Han, K.; Whitton, M. M.; Lincoln, D. E.; Woodin, S. A.; Lebioda, L. The crystal structure and amino acid sequence of dehaloperoxidase from *Amphitrite ornata* indicate common ancestry with globins. *J. Biol. Chem.* **2000**, *275*, 18712-18716.
- (26) Thompson, M. K.; Davis, M. F.; de Serrano, V.; Nicoletti, F. P.; Howes, B. D.; Smulevich, G.; Franzen, S., Internal binding of halogenated phenols in dehaloperoxidase-hemoglobin inhibits peroxidase function. *Biophys. J.* **2010**, *99*, (5), 1586-1595.
- (27) Zhao, J.; de Serrano, V.; Le, P.; Franzen, S. Structural and kinetic study of an internal substrate binding site in dehaloperoxidase-hemoglobin A from *Amphitrite ornata*. *Biochemistry* **2013**, *52*, 2427-2439.
- (28) Beers, R. F., Jr.; Sizer, I. W. A spectrophotometric method for measuring the breakdown of hydrogen peroxide by catalase. *J. Biol. Chem.* **1952**, *195*, 133-140.
- (29) Otwinowski, Z.; Minor, W. In *Methods in Enzymology*; Carter Jr., C. W., Sweet, R. M., Eds.; Academic Press: New York, 1997; Vol. 276: Macromolecular Crystallography, part A, p 307-326.
- (30) McCoy, A. J.; Grosse-Kunstleve, R. W.; Adams, P. D.; Winn, M. D.; Storoni, L. C.; Read, R. J. Phaser crystallographic software. *J. Appl. Crystallogr.* **2007**, *40*, 658-674.

- (31) Adams, P. D.; Afonine, P. V.; Bunkoczi, G.; Chen, V. B.; Davis, I. W.; Echols, N.; Headd, J. J.; Hung, L. W.; Kapral, G. J.; Grosse-Kunstleve, R. W.; McCoy, A. J.; Moriarty, N. W.; Oeffner, R.; Read, R. J.; Richardson, D. C.; Richardson, J. S.; Terwilliger, T. C.; Zwart, P. H. PHENIX: a comprehensive Python-based system for macromolecular structure solution. *Acta Cryst.* **2010**, *D66*, 213-221.
- (32) Emsley, P.; Lohkamp, B.; Scott, W. G.; Cowtan, K. Features and development of Coot. *Acta Cryst.* **2010**, *D66*, 486-501.
- (33) Afonine, P. V.; Grosse-Kunstleve, R. W.; Echols, N.; Headd, J. J.; Moriarty, N. W.; Mustyakimov, M.; Terwilliger, T. C.; Urzhumtsev, A.; Zwart, P. H.; Adams, P. D. Towards automated crystallographic structure refinement with phenix.refine. *Acta Cryst.* **2012**, *D68*, 352-367.
- (34) Chenprakhon, P.; Sucharitakul, J.; Panijpan, B.; Chaiyen, P. Measuring Binding Affinity of Protein-Ligand Interaction Using Spectrophotometry: Binding of Neutral Red to Riboflavin-Binding Protein. *J. Chem. Educ.* **2010**, *87*, 829-831.
- (35) Carugo, O.; Pongor, S. A normalized root-mean-square distance for comparing protein three-dimensional structures. *Protein Science* **2001**, *10*, 1470-1473.
- (36) Cohen, F. E.; Sternberg, M. J. On the prediction of protein structure: The significance of the root-mean-square deviation. *Journal of Molecular Biology* **1980**, *138*, 321-333.
- (37) Chothia, C.; Lesk, A. M. The relation between the divergence of sequence and structure in proteins. *Embo J* **1986**, *5*, 823-826.
- (38) Sun, S.; Sono, M.; Wang, C.; Du, J.; Lebioda, L.; Dawson, J. H. Influence of heme environment structure on dioxygen affinity for the dual function *Amphitrite ornata* hemoglobin/dehaloperoxidase. Insights into the evolutionary structure–function adaptations. *Arch. Biochem. Biophys.* **2014**, *545*, 108-115.
- (39) Jiang, S.; Wright, I.; Swartz, P.; Franzen, S. The role of T56 in controlling the flexibility of the distal histidine in dehaloperoxidase-hemoglobin from *Amphitrite ornata*. *Biochimica et Biophysica Acta (BBA) - Proteins and Proteomics* **2013**, *1834*, 2020-2029.
- (40) Zhao, J.; de Serrano, V.; Dumarieh, R.; Thompson, M.; Ghiladi, R. A.; Franzen, S. The role of the distal histidine in H₂O₂ activation and heme protection in both peroxidase and globin functions. *J. Phys. Chem. B* **2012**, *116*, 12065-77.

- (41) de Serrano, V. S.; Davis, M. F.; Gaff, J. F.; Zhang, Q.; Chen, Z.; D'Antonio, E. L.; Bowden, E. F.; Rose, R.; Franzen, S. X-ray structure of the metcyano form of dehaloperoxidase from *Amphitrite ornata*: evidence for photoreductive dissociation of the iron-cyanide bond. *Acta Cryst.* **2010**, *D66*, 770-82.
- (42) Chen, Z.; de Serrano, V.; Betts, L.; Franzen, S. Distal histidine conformational flexibility in dehaloperoxidase from *Amphitrite ornata*. *Acta Cryst.* **2009**, *D65*, 34-40.
- (43) de Serrano, V.; Chen, Z.; Davis, M. F.; Franzen, S. X-ray crystal structural analysis of the binding site in the ferric and oxyferrous forms of the recombinant heme dehaloperoxidase cloned from *Amphitrite ornata*. *Acta Cryst.* **2007**, *D63*, 1094-1101.
- (44) Kwon, H.; Moody, P. C. E.; Raven, E. L. In *Heme Peroxidases*; The Royal Society of Chemistry: 2016, p 47-60.

Chapter 5

Further Exploring the Structure-Function Relationship in Dehaloperoxidase Through X-ray and Neutron Crystallography: Four Case Studies

Presented in this chapter is a collection of four crystallographic studies designed to investigate the structure-function relationship and properties of DHP. In Section 5.1, the unambiguous assignment of protonation states, water orientations and hydrogen-bonding networks was achieved from analysis of the neutron crystallographic structure of ferric DHP, the first neutron structure of a multifunctional catalytic globin. Section 5.2 explores the relationship between substrate binding loci and enzymatic function with the elucidation of the first peroxygenase substrate binding site, 4-nitrophenol. In Section 5.3, the structural and functional plasticity of the DHP active site is investigated by substituting the native Fe-containing heme cofactor with Mn-PPIX. Finally, in Section 5.4 we obtained the structures of selected mutants of DHP B in order to validate an assumption when assigning EPR radical spectra to specific tyrosine residues, which was used in turn to identify the pathway of radical migration in DHP.

5.1. Case Study 1 – Neutron Diffraction Structure of Ferric DHP B

5.1.1 Introduction

A longstanding question in catalysis is how structure plays a role in influencing chemical reactivity. This is readily apparent in heme proteins where O₂-binding, oxygenase, oxidase, peroxygenase, and electron-transfer reactions all occur at active sites that often contain a surprising number of similarities, both structural and, by consequence, mechanistic. For example, the reactive heme species known as Compound I contains an Fe(IV)-oxo (ferryl) and porphyrin π -cation radical and has been implicated in the mechanisms of cytochrome *c* oxidase,¹ cytochrome P450 monooxygenase, human indoleamine 2,3-dioxygenase, the fungal peroxygenase *Aae*APO, horseradish peroxidase, prostaglandin endoperoxidase synthase

(cyclooxygenase), and has even been shown to form in myoglobin. Despite the common intermediate, the chemical reactivity of each of the aforementioned systems remains exquisitely controlled by the protein structure and its associated H-bonding network to ensure maximum intended function with a minimum of unintended cross reactivity. How Nature achieves this control for the selectivity of function continues to be of interest, yet remains a significant challenge to fully understand.

Our chosen platform for the elaboration of the structural features and other determinants that impart specific discrete functions to heme proteins (and more generally to all proteins) is the enzyme dehaloperoxidase (DHP), the coelomic hemoglobin from the marine worm *Amphitrite ornata*. DHP is a multifunctional enzyme that undergoes oxygenase, oxidase, peroxygenase, and peroxidase reactions at the same heme center that is responsible for reversible O₂-binding. For a number of years the research groups investigating DHP have made the case that it is the first globin identified to possess biologically relevant i) peroxidase activity for trihalophenols and ii) peroxygenase and oxidase activities directly attributable to haloindoles, all of which are known toxins found in shallow mud flats in coastal estuaries. How a simple hemoprotein manages such a broad range of activities inspires this current study of the hydrogen bonding network and consequence of residue protonation states in DHP using neutron diffraction.

The structural information, resolved to atomic clarity, provided from X-ray crystallography is an invaluable asset for investigating the correlation between protein structure and function. The X-ray atomic scattering factors (f) of each atom are directly related its electron density, resulting in more data for the heavier atoms in the sample (Table 5.1). Due to this requirement, hydrogen and deuterium atoms are virtually invisible in X-ray crystallographic structures, yet tend to represent ~50% of the protein atoms. Neutrons are diffracted by atomic nuclei, removing the atomic number dependence on diffractive capability. The atomic scattering lengths of deuterium, oxygen, carbon and nitrogen are similar, providing neutron diffraction

the capability to identify and visualize deuterated water, hydrogen-bonding networks, and protonation states of catalytic intermediates and protein residues, even at moderate resolutions of 2.5 Å.

Table 5.1 Comparison of neutron and X-ray scattering characteristics for selected atoms.

Element	Neutron Scattering length (fm)		Neutron Cross section (barn)		X-ray Atomic Scattering Factor (f)
	Coherent	Incoherent	Coherent	Incoherent	
Hydrogen	-3.741	25.27	1.758	80.27	1
Deuterium	6.671	4.04	5.592	2.05	1
Carbon	6.646	----	5.559	0	6
Oxygen	5.803	----	4.232	0.0008	8
Nitrogen	9.36	----	11.01	0.5	7
Sulfur	2.847	----	1.019	0.007	16
Iron	9.45	----	11.22	0.4	26
Manganese	-3.73	1.79	1.75	0.4	25

The neutron data is representative of thermal neutrons only. X-ray atomic scattering factors provided are calculated at $(\sin \theta)/\lambda=0$. Unit definitions are as follow: 1) fm = 1×10^{-15} m 2) Barn = 1×10^{-24} cm² 3) $f = e^-$

There exists a pronounced isotopic difference between hydrogen and deuterium atoms with regard to both coherent and incoherent neutron scattering. Hydrogen coherent scattering results in a phase shift of 180°, resulting in negative scattering lengths (-3.74 fm) that can give rise to density cancelation in Fourier neutron density maps. Deuterium, on the other hand, possesses a positive scattering length (6.671 fm) and does not promote cancelation in nuclear density maps. Hydrogen also possess an extremely large incoherent scattering cross section when compared to other biological atoms. Table 5.1 provides neutron coherent and incoherent scattering cross sections for selected atoms. Incoherent scattering results in background signal for crystallographic diffraction experiments: hydrogen has an incoherent cross section of 80.27 barn (10^{-24} cm²) while deuterium's incoherent cross section is 2.05 barn. Thus, analysis of biological molecules via neutron diffraction is complicated by the presence of high background

(incoherent) and scattering signal cancelation (coherent) due to the high level of hydrogen atoms. Perdeuteration, or replacement of non-labile hydrogens with deuterium, of biological molecules has proved to be an advantageous technique to combat these caveats of neutron diffraction from biological molecules.² An additional benefit lies in that neutrons are non-ionizing and do not cause observable radiation damage or photoreduction of metal centers in metalloproteins.

From these technical benefits, neutron diffraction has been advantageous in investigating: i) pKa effects resultant from protein environments, as shown in the substrate GTP γ -phosphate protonation states in RAS GTPase³ and darunavir protonation states complexed with HIV-1 protease;⁴ ii) mechanistic investigations into protonation states of residues directly related to catalytic function, as with β -lactamase,⁵ human carbonic anhydrase II (HCAII)⁶ and D-xylose isomerase;⁷ iii) assignment of water molecules as neutral or hydroxide molecules (HCAII);⁶ iv) identification of hydrogen bonding networks;⁸⁻¹² and v) identification of protonation states of reactive intermediates, as shown in the identification of the cytochrome *c* peroxidase (CcP) Compound I as a nonprotonated state.¹ Thus, neutron diffraction is uniquely positioned to investigate if residue protonation states and H-bonding networks are critical determinants for understanding how an enzyme such as DHP is able to perform all five of its associated activities. Presented here is the first crystallographic structure of a multifunctional catalytic globin obtained by neutron diffraction. The DHP B structure was solved in the ferric resting state, deuterated water orientations and hydrogen bonding networks are unambiguously assigned, residue protonation states are determined, and the unexpected presence of water molecules in the distal pocket was observed.

5.1.2 Experimental

Cloning. For the purpose of obtaining kanamycin resistance, the *dhpB* gene was cloned from the pET16b plasmid that confers ampicillin resistance into a pET28a plasmid containing kanamycin selectivity. *E. coli* cells containing the pET28a plasmid were supplied by the Williams Group, NCSU Chemistry Dept. Both the pET28a plasmid and the *dhpB* gene

containing pET-16b plasmid were separately extracted from BL21(DE3) cells using the BioBasic Plasmid Extraction Mini-prep Kit. Each plasmid (750 ng) was doubly-digested with both NcoI-HF and BamHI-HF (New England BioLabs) at 37 °C for 5 hours followed by overnight at 4 °C. The doubly-digested pET28a plasmid and excised *dhpB* gene were obtained from their respective reaction mixtures through separation by electrophoresis on 1% agarose gel and recovered using the BioBasic Gel Extraction Kit. The *dhpB* gene was inserted into the pET28a plasmid via their co-incubation in the presence of ligase at 16 °C overnight. The pET28a plasmid containing the *dhpB* gene was thus transformed into BL21(DE3) competent cells (Novagen) as follows: 2 µL of the plasmid and 25 µL of cells were incubated together on ice for 30 minutes, subjected to heat shock at 42 °C for 40 seconds, returned to ice for 2 minutes, and were then used to inoculate 500 µL of Recovery Media (Sigma). The cells were incubated at 37 °C with orbital shaking (250 rpm) for 30 minutes, and subsequently plated on LB/agar plates containing kanamycin (50 µg/mL). Following overnight incubation at 37 °C, surviving colonies were selected, cultured as above, their plasmids extracted, and the gene incorporation was verified via sequence analysis from GeneWiz.

Perdeuterated Cell Culturing. All media contained the antibiotic kanamycin (50 µg/mL) prepared in either H₂O (DHP B) or 99.8% D₂O (perdeuterated DHP B). Enfors Minimal Media was used (protiated or deuterated), the composition of which is provided in Table 5.2. In the case of 99.8% deuterated minimal media, all hydrated salts were dissolved in D₂O and then dried *in vacuo* via rotary evaporation. This was performed twice in an effort to replace the exchangeable protons with deuterons.

Cell culture in perdeuterated media was achieved from a starting protiated culture using a stepwise approach, as follows: single colonies from the previous transformation were selected and used to inoculate 7 mL LB media, which was incubated at 37 °C with orbital shaking (250 rpm) overnight. Upon reaching OD₆₀₀ of 1.0, 200 µL was used to inoculate 2 mL of protiated minimal media, and was incubated under the previous conditions. At an OD₆₀₀ of 1, the culture was diluted 1:20 (150 µL into 3 mL) into 50% D₂O minimal media, and incubated overnight. The following morning, with an OD₆₀₀ of 1.1, a 1:20 dilution was performed into 75% D₂O

minimal media, followed by 37 °C incubation. Later, at an OD₆₀₀ of 0.5, a 1:20 dilution was again performed, now into 99.8% D₂O minimal media. The temperature was reduced to 28 °C, and the culture was incubated overnight. Upon reaching an OD₆₀₀ of 1.0 the following morning, a 1:30 dilution was performed into 99.8% D₂O minimal media, followed by incubation overnight. The next morning, at an OD₆₀₀ of 1.5, a 1:60 dilution (50 µL into 3 mL) was performed into 99.8% D₂O and was incubated overnight until an OD₆₀₀ of 1.5 was achieved. In an effort to scale-up the growth culture, 2.2 mL was then used to inoculate 22 mL of 99.8% D₂O minimal media and the temperature was increased to 37 °C. When the OD₆₀₀ reached 1.0, 14 mL was used to inoculate 140 mL of 99.8% deuterated minimal media, the temperature was decreased to 30 °C, and was incubation proceeded overnight. Upon reaching an OD₆₀₀ of 2.0, the entire culture was used to inoculate 99.8% deuterated minimal media in a fermentor to a final volume of 1.4 L.

Table 5.2. Enfors Minimal Media composition.¹³

<u>Reagent</u>	<u>Final Conc.</u>	<u>Trace Metals Reagent</u>	<u>Final Conc.</u>
(NH ₄) ₂ SO ₄	53.0 mM	CaCl ₂ •2H ₂ O	3.4 µM
Na ₂ HPO ₄	37.0 mM	CoCl ₂	0.75 µM
KH ₂ PO ₄	11.8 mM	CuSO ₄ •5H ₂ O	0.64 µM
(NH ₄) ₂ -H-Citrate	2.21 mM	FeCl ₃ •6H ₂ O	62 µM
Glycerol- <i>d</i> ₈	54.3 mM	MnSO ₄ •H ₂ O	0.67 µM
MgSO ₄ •7H ₂ O	0.02 %	Na ₂ EDTA•H ₂ O	60 µM
1000X Trace Metals	1X	ZnSO ₄ •7H ₂ O	0.63 µM

Bioreactor Fermentation. Stock solutions of kanamycin (50 mg/mL), IPTG (750 mM), 10% NaOD, and 10% glycerol-*d*₈ feed solution were prepared using 99.8% D₂O. A hemin stock solution (10 mg/mL) was prepared in 200 mM NaOD. A BioFlo 310 Fermentation System (New Brunswick Scientific) enabled monitoring and control of pD, dissolved O₂, temperature, agitation and carbon source availability. The growth and expression were kept at

a constant temperature of 32 °C. Upon inoculation of the fermentor vessel (OD_{600} 0.21), 10 mL of hemin stock solution (10 mg/mL in 0.2 M NaOD) were added to the media. Upon reaching an OD_{600} of 9.8, overexpression of DHP B was induced upon the addition of 1.5 mL of 750 mM isopropyl β -D-1-thiogalactopyranoside (IPTG). Overexpression continued for 20 hours and the cells, at an OD_{600} of 12.6, were collected via centrifugation.

Crystal Growth and Manipulation. Perdeuterated DHP B was purified per literature precedent with only two modifications: introduction of a linear gradient over 20 mL was used to initiate elution on the CM Sepharose FF column rather than direct buffer change, and gentler concentration of the samples by lower rpm during centrifugation was necessary to prevent precipitation of the perdeuterated protein. Homogenous ferric enzyme was obtained by incubation with excess potassium ferricyanide, which was subsequently removed using a Sephadex G-25 desalting column into 20 mM sodium cacodylate buffer (pH 6.4). Perdeuterated DHP B was then brought to a crystallization concentration of 12 mg/mL (740 μ M), which was determined spectroscopically utilizing the Soret (407 nm) absorbance and the molar absorptivity coefficient, ϵ , of 116,400 $M^{-1}cm^{-1}$. MALDI analysis showed replacement of 97% of the non-labile hydrogens with deuteriums, confirming successful perdeuteration of DHP B. Crystals of sufficient neutron diffraction quality were grown via sitting drop vapor-diffusion in 9-well siliconized glass plates in a sandwich box set-up. Mother liquor (ML) was comprised of 32% MPEG 2000, 175 mM ammonium sulfate at pH 6.4, and drop ratios of protein to ML were 1.5:1, 2:1, 2.5:1 and 3:1. Drops reached a total volume of 100 μ L and were equilibrated against 25 mL reservoir solution. Crystals appeared after 6 weeks at 4 °C. The crystals were D_2O exchanged by direct contact with deuterated mother liquor equivalent. Briefly, small aliquots of mother liquor were replaced with deuterated reservoir, the drop was allowed to equilibrate for 10 minutes, and this process was repeated ~25 times. Upon exhaustive D_2O exchange of the drop, crystals were mounted in a thin-walled, 2 mm diameter quartz capillary (Hampton Research) with a plug of deuterated reservoir, and sealed with wax.

Data Collection and Reduction. Room temperature neutron diffraction data were collected on the IMAGINE diffractometer at the High Flux Isotope Reactor (HFIR) at Oak Ridge

National Laboratory. On a 0.3 mm³ ferric perdeuterated DHP B crystal, 20 frames of quasi-Laue data were collected utilizing a bandpass of 2.8 – 4.6 Å, with 20 hours exposure per frame. Each image was indexed and integrated using LAUEGEN, wavelength normalization was performed with LSCALE, then scaled and merged with SCALA. Room temperature X-ray diffraction data were subsequently collected on the same crystal using an in-house rotating-anode Rigaku MicroMax-007 HF equipped with an R-AXIS IV⁺⁺ detector, consisting of 120 frames of 30 seconds exposure each. The frames were indexed and scaled using HKL-3000,¹⁴ molecular replacement was performed with Phaser-MR¹⁵ from the PHENIX¹⁶ suite of programs using 3IXF¹⁷ as the search model, model building and manual placement of waters utilized COOT¹⁸ and refinement was carried out using phenix.refine.¹⁹ Upon removal of waters and ligands, this room temperature X-ray structure served as the starting model for initial rigid-body refinement of the neutron data. Deuterium atoms were added to the starting model, with joint occupancy of hydrogen and deuterium at the exchangeable sites. Model building, manual placement of waters, and refinement of the neutron structure were accomplished using the same method and programs utilized for the X-ray structure. The X-ray and neutron data refined to resolution of 1.76 Å and 2.05 Å, respectively.

5.1.3 Results and Discussion

Large DHP B crystals suitable for neutron diffraction exhibited different morphologies when compared with smaller sized crystals that have been typically employed for X-ray diffraction (Figure 5.1). Specifically, they were of pyramidal or slightly cubic geometries and did not resemble the tri-fold shape that is common in smaller DHP B crystals. The perdeuterated crystals (Figure 5.1A) did not grow as large as the protiated ones (Figure 5.1B), yet were still able to obtain a volume (>0.1 mm³) sufficient for neutron diffraction. Neutron diffraction data were collected on a perdeuterated ferric DHP B crystal of ~0.3 mm³ in volume, and a representative quasi-Laue diffraction pattern of DHP B collected on IMAGINE at the HFIR is shown in Figure 5.1C. The data were scaled, integrated and merged to 1.95 Å, however during refinement the resolution was dropped to 2.05 Å in an effort to obtain reasonable

refinement statistics. Neutron data collection and refinement statistics are provided in Table 5.3.

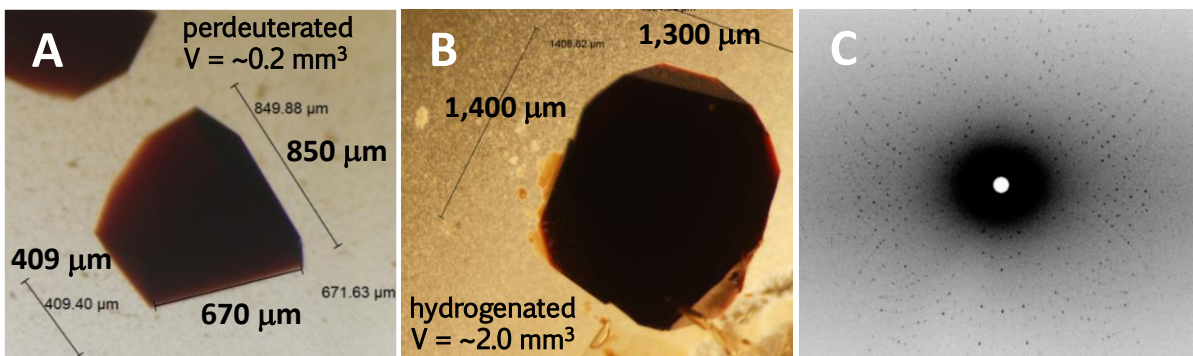


Figure 5.1. Representative ferric DHP B crystals of sufficient size for obtaining neutron diffraction data. **A)** Perdeuterated DHP B crystal grown in MPEG 2000, crystal volume ~ 0.2 mm³. **B)** Protiated DHP B crystal grown in PEG 4000, crystal volume ~ 2.0 mm³. **C)** Representative quasi-Laue diffraction pattern of ferric DHP B. The image was obtained from 20 hour neutron exposure.

Following neutron data collection, room temperature X-ray diffraction data were collected on the same crystal. The X-ray perdeuterated DHP B structure yielded a homo-dimer in the asymmetric unit, belonging to space group $P2_12_12_1$. In addition to the proximal His89 ligand, protomer B was solved to show a partial occupancy of the distal His55 that was coordinated directly to the Fe, yielding a bis-His ligation of the heme cofactor. When in this bis-His ligated state, the heme is positioned slightly out from the cavity. During crystallization trials, several different PEG polymers were screened to produce DHP B crystals, and X-ray data were collected on each successful trial. Every structure solved from a crystal grown in MPEG 2000 possessed one protomer with a bis-His ligated heme, whereas no trials employing other precipitating agents resulted in a bis-His ligated heme. It is reasonable to suspect that MPEG 2000 induces this effect on DHP structure, but only for protomer B; protomer A showed a typical DHP active site structure with only the proximal H89 coordinated to the heme Fe. During room temperature data collection, the ferric heme center of protomer A was quickly

reduced due to the ionizing properties of the X-ray beam. The heme Fe was found to coordinate a distal ligand, consisting of mixed occupancy between molecular oxygen and dimeric MPEG molecules, each one exclusive of the other, as shown in Figure 5.2. Since the neutron diffraction data were collected on a ferric DHP B crystal, the X-ray data were not able to be used for joint-refinement of the neutron structure due to the Fe oxidation state, considering the heme active site is one of the main areas of interest from the neutron data. However, the structure was used as a starting model for the rigid-body refinement of the neutron data once all waters and exogenous (O_2 , MPEG 2000) ligands were removed.

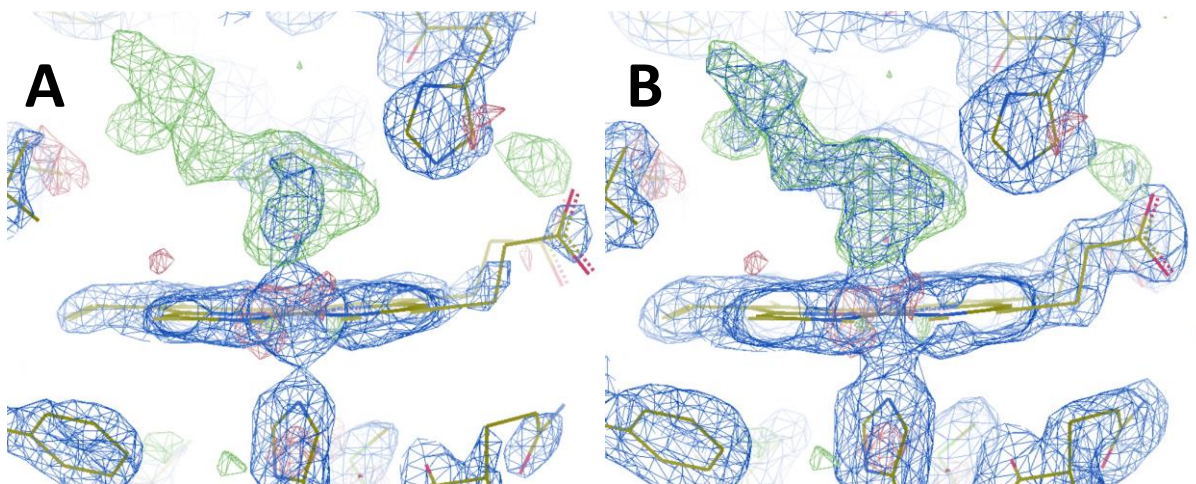


Figure 5.2. Room temperature X-ray structure of the perdeuterated DHP B protomer A heme cavity, viewed from the heme β side. $F_0 - F_C$ electron density maps are displayed in green and scaled to 3σ . Blue depicts the $2F_0 - F_C$ maps. A) $2F_0 - F_C$ maps scaled to 2σ . The blue density coordinated to the Fe is representative of O_2 . B) $2F_0 - F_C$ maps scaled to 1σ . A dimeric MPEG 2000 molecule fits this density. There is a mixed occupancy between O_2 and MPEG 2000 dimer molecules as the distal Fe ligand, each one exclusive of the other.

Table 5.3. Neutron data collection and refinement statistics for ferric WT DHP B.

<u>Data Collection</u>	
Wavelength (Å)	2.8 – 4.6
Temperature (K)	298
Space Group	P2 ₁ 2 ₁ 2 ₁
Unit-cell parameters (Å)	
<i>a</i>	60.44
<i>b</i>	66.12
<i>c</i>	68.38
Number of reflections	85,565 (7,084)
Unique reflections	15,930 (1,900)
Completeness (%)	79.2 (66.3)
R _{pim} (%) ^b	11.8 (20.3)
I/σ(I)	4.8 (2.0)
Redundancy	5.4 (3.7)
<u>Refinement</u>	
Resolution range (Å)	17.23 - 2.05 (2.12 – 2.05)
R _{work} (%) ^c	24.68 (28.38)
R _{free} (%) ^d	28.87 (31.62)
No. of protein atoms	5,087
No. of solvent atoms	49
R.m.s.d from ideal geometry ^e	
Bond lengths (Å)	0.193
Bond angles (°)	1.745
<u>Ramachandran plot (%)</u>	
Most favored region	95.65
Addl allowed region	2.9
Outliers	1.45

^aValues in parentheses are for the highest resolution shell. ^bR_{pim} = $\sum_h \sqrt{1/(n-1)} \sum_i [|I_i(h) - \langle I(h) \rangle| / \sum_h \sum_i I(h)] \times 100\%$, where I_i(h) is the ith measurement and ⟨I(h)⟩ is the weighted mean of all measurements of I(h). ^cR_{work} = $\sum |F_o - F_c| / \sum F_o \times 100\%$, where F_o and F_c are the observed and calculated structure factors, respectively. ^dR_{free} is the R factor for the subset (9.98%) of reflections selected before and not included in the refinement. ^eRoot-mean-square deviation. ^fRamachandran plot created via MolProbity.

Perdeuteration of DHP B resulted in complete nuclear density maps lacking the holes that can result from the hydrogen scattering of neutrons. There was obvious density for the location of deuterium atoms, with Met the only residue that appeared to have mostly hydrogen instead of deuterium on its terminal carbon. Figure 5.3 shows I6 and F123 modeled into their respective nuclear and electron map densities, highlighting the ability to visualize the deuterium atoms in the nuclear density maps. An absence of deuteration on the sidechain oxygen was noted for some Thr, Ser and Tyr residues. However, the vast majority of exchangeable hydrogen atoms were replaced with deuterium, in particular the His residues at the active site.

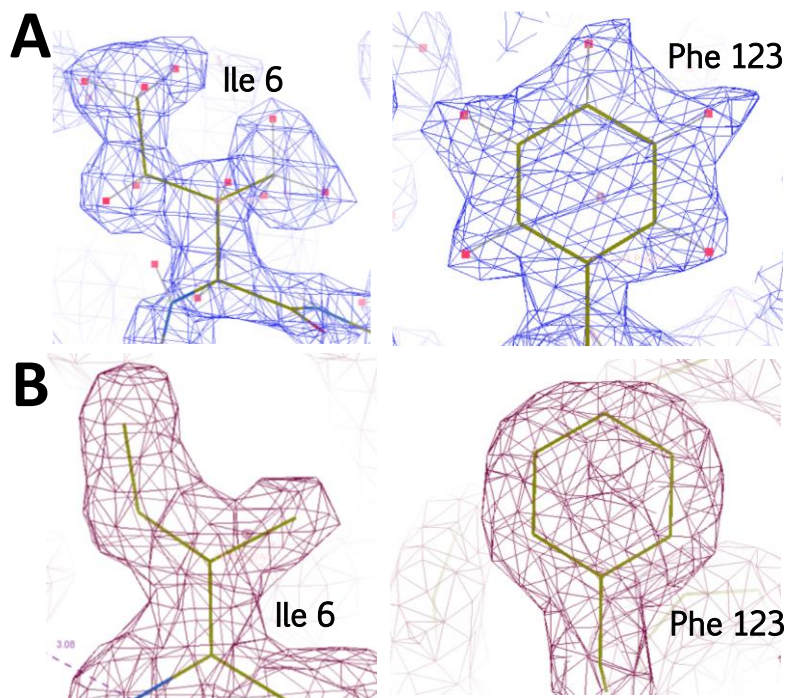


Figure 5.3. Residues Ile 6 and Phe 123 from DHP B, shown modeled into blue nuclear and red electron density maps. Panel A) Nuclear density maps of perdeuterated residues, highlighting the visibility of deuterium atoms (shown in red) at a resolution of 2.05 Å. Panel B) Electron density maps illustrating the absence of hydrogen atoms, even at a higher resolution, 1.81 Å.

Figure 5.4 shows the neutron structure ribbon backbone, with emphasis on the protomer A distal pocket (panel A), the distal pocket (panel B), and the protomer B bis-His ligation (panel C). Atomic distances, residue orientations and distal water nomenclature are also shown. The heme in protomer B of the asymmetric unit dimer was found to be coordinated by both the proximal (H89) and distal (H55) histidines, which are equidistant to the heme Fe at 2.5 Å. The heme is slightly extruded from the distal pocket, as previously described in the X-ray structure. Since the bis-His ligation of the heme is observed in the neutron diffraction data, this further suggests that the bis-His ligation resulted from MPEG 2000 interactions with DHP B and that the X-ray exposure bore no consequence on this protomer's orientation.

Protomer A, on the other hand, shows a water (D₂O-1) coordinated to the heme Fe, as has been seen in previous structures of ferric DHP (Figure 5.4A). H55 is neutral and positioned interior to the distal cavity, stabilized as both a hydrogen bond acceptor from the Fe-coordinated water (D₂O-1) and a hydrogen bond donor to the heme propionate arm A, with a distance of 2.7 Å between both deuterium and heteroatom. In addition to the expected water coordinated to the Fe, there is the presence of two additional water molecules (D₂O-2 and H₂O) in the distal cavity, a finding which has not been observed in previous X-ray structures. These waters exist in a hydrogen-bonding network amongst themselves and the Fe-coordinated water, extending into the distal pocket past the heme $\alpha - \delta$ edge. They are positioned at equal distances of 1.9 Å from D (donor) and O (acceptor) atoms. There was no density for deuterium atoms for the water deepest in the distal pocket, so it was modeled as H₂O. In the proximal region, H89 N^ε is positioned 2.41 Å from the heme Fe. As previously assigned via X-ray diffraction, hydrogen bonding between the D of H89 N^δ and the carbonyl O of L83 was verified in the neutron structure at a distance of 1.6 Å (Figure 5.4B). This interaction provides DHP with the proximal charge relay traditionally required for heme activation, considering DHP lacks the canonical Asp-His-Fe proximal catalytic triad found in most peroxidases. A more extensive collection of selected atomic distances of protomer A are provided in Table 5.4.

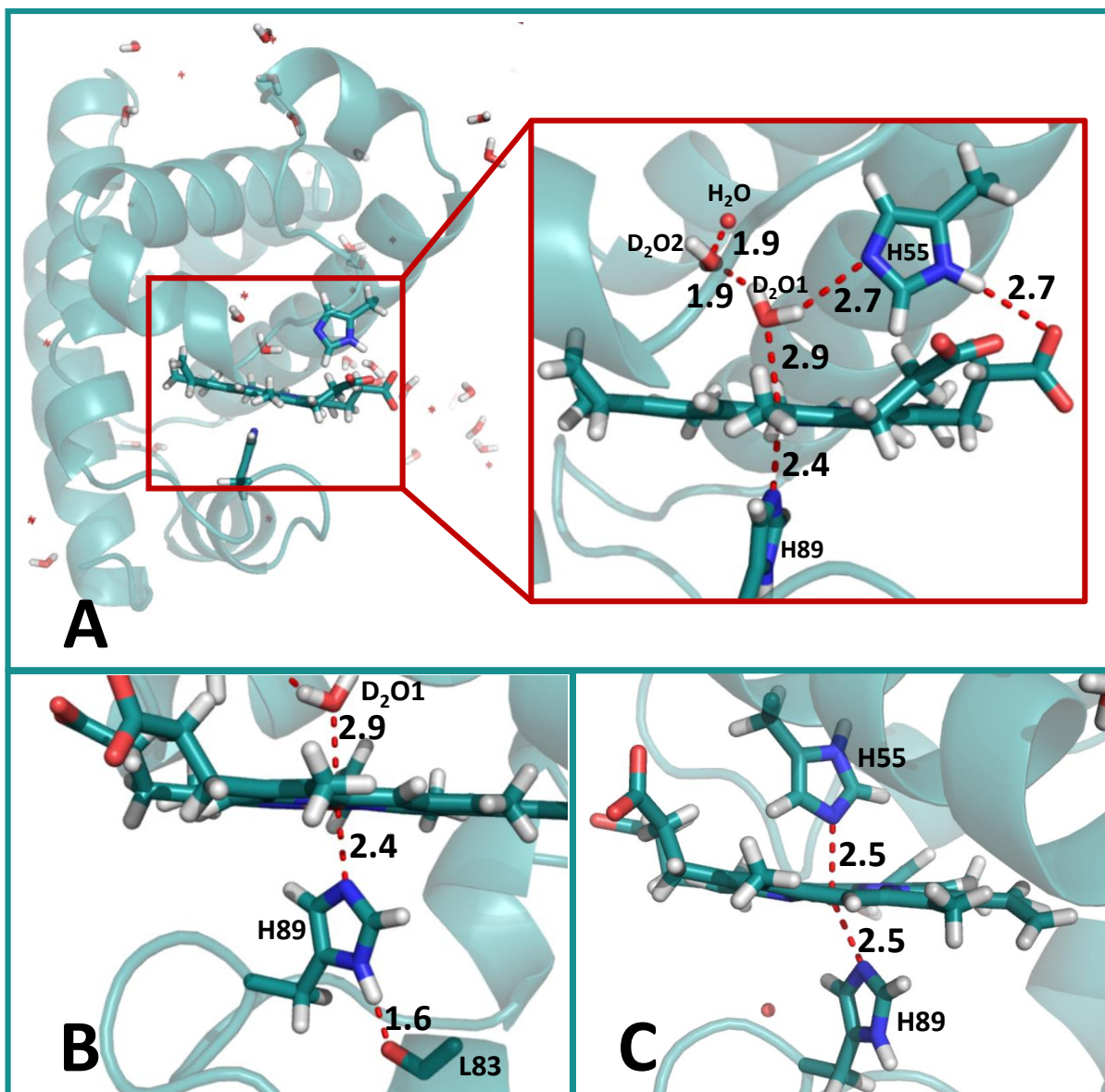


Figure 5.4. Neutron structure of ferric DHP B, presenting nomenclature and atomic distances. **A)** Protomer A ribbon structure, with emphasis placed on the distal pocket environment. **B)** Proximal environment of protomer A. **C)** Bis-his heme ligation present in protomer B.

Table 5.4. Selected Distances in the Neutron Structure of Ferric DHP B for Protomer A.

	Distance (Å)
Fe – O (D ₂ O-1)	2.87
H55 N ^ε – D ¹ (D ₂ O-1)	2.73
H55 N ^ε – O (D ₂ O-1)	3.62
H55 D ^{Nδ} – heme propionate A	2.66
H89 N ^ε – Fe	2.41
H89 N ^δ – O L83	2.56
H89 D ^{Nδ} – O L83	1.56
D ₂ O-1 D ² – O D ₂ O-2	1.90
D ₂ O-1 O – O D ₂ O-2	2.74
D ₂ O-2 O – O H ₂ O	2.59
D ₂ O-2 D ¹ – O H ₂ O	1.95

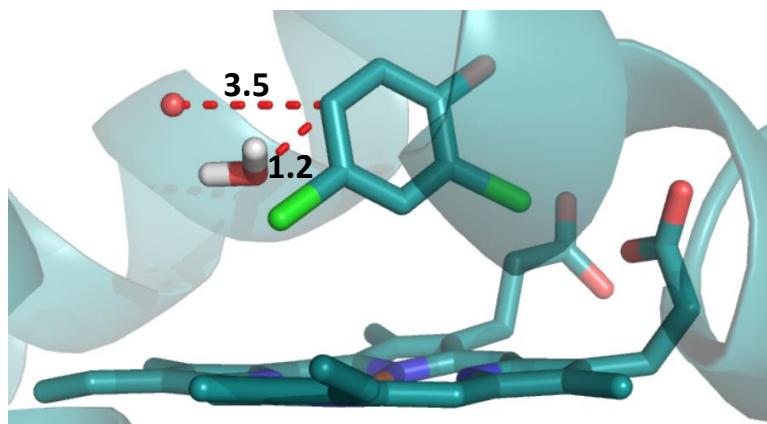


Figure 5.5. Superposition (with atomic distances) of 2,4-dichlorophenol (DCP) β binding site and distal waters found in the neutron ferric DHP B structure. The distal water bound to the heme Fe has been removed for clarification. DCP is a peroxidase substrate, with its product is characterized by the insertion of an oxygen atom, derived from water. The location of the distal waters present a possible mechanistic role.

The presence of waters extending into the distal cavity was unexpected. A distal water network has been observed previously in the X-ray crystallographic structures of DHP B (Chapter 4 DHP B (F21W)) and in the Mn-protoporphyrin IX variant of DHP B (Section 5.3), but has yet to be observed in WT DHP B. Waters have been observed at the entrance of the

heme cavity in high resolution X-ray structures, but never extending to the α - δ edge of the heme. Their presence could have resulted from the crystallization conditions, however the X-ray structures of DHP B crystals grown from identical conditions did not contain the distal waters. Another factor is the temperature of data collection. The neutron data were collected at room temperature, which prevents the conformational trapping that has been noticed before in cryogenic data collection.^{20,21} The room temperature collection could possibly represent a more natural water distribution for DHP B. As shown in Figure 5.5, the presence of distal water molecules may have a mechanistic consequence. The distal waters, minus the Fe coordinated water, are superposed with the 2,4-dicholophenol (DCP) β binding site, showing the H₂O positioned for incorporation into the substrate. DCP is a peroxidase substrate, which signifies that the O atom inserted into the product is derived from water. It is still unclear if the peroxidase substrate leaves the pocket before the water molecule attacks, or if the oxygen atom transfer occurs in the distal pocket. Further studies are required to probe the mechanistic implications of deep-cavity distal waters.

5.1.4 Summary of Case Study 1

In summary, the first neutron crystallographic structure of DHP has been obtained on a ferric perdeuterated protein. One protomer is characterized with a bis-His ligated heme, which is most probably due to the crystallization conditions used. The other protomer exhibits the expected ferric heme environment, with the heme-Fe's 6th coordination site occupied by a water molecule. Unambiguous assignment of residue protonation states, water orientations, donor and acceptors in H-bonding networks, and the unexpected presence of waters deep in the distal cavity, together provide a more complete structural assessment of DHP's multifunctional heme active site. With this enhanced structural understating of the ferric resting state, questions naturally arose about the substrate complexed form of DHP. Presented next is an investigation into the structural consequence of substrate binding in the distal cavity and its relationship to functional pathway: 4-nitrophenol and 4-nitrocatechol binding sites.

5.2 Case Study 2 – Elucidation of 4-Nitrophenol (4NP) and 4-Nitrocatechol (4NC) Crystallographic Binding Sites in DHP B

The following Case Study is adapted from: Nikolette L. McCombs, Jennifer D'Antonio, David A. Barrios, Leah M. Carey and Reza A. Ghiladi “Nonmicrobial nitrophenol degradation via peroxygenase activity of dehaloperoxidase-hemoglobin from *Amphitrite ornata*” *Biochemistry*, **2016**, *55*, 2465-2478. LMC contributed to this work by performing the non-His tagged DHP B expression, purification and crystallization, and determining the structures of DHP B by X-ray crystallography when complexed with the substrate 4-nitrophenol (4NP) and the substrate/product 4-nitrocatechol (4NC).

5.2.1 Abstract

The marine hemoglobin dehaloperoxidase (DHP) from *Amphitrite ornata* was found to catalyze the H₂O₂-dependent oxidation of nitrophenols, an unprecedented non-microbial degradation pathway for nitrophenols by a hemoglobin. Using 4-nitrophenol (4-NP) as a representative substrate, the major monooxygenated product was 4-nitrocatechol (4-NC). Isotope labeling studies confirmed that the O-atom incorporated was derived exclusively from H₂O₂, indicative of a peroxygenase mechanism for 4-NP oxidation. Accordingly, X-ray crystal structures of 4-NP (1.87 Å) and 4-NC (1.98 Å) bound to DHP revealed a binding site in close proximity to the heme cofactor. Peroxygenase activity could be initiated from either the ferric or oxyferrous states with equivalent substrate conversion and product distribution. The 4-NC product was itself a peroxidase substrate for DHP, leading to the secondary products 5-nitrobenzene-triol and hydroxy-5-nitro-1,2-benzoquinone. DHP was able to react with 2,4-dinitrophenol (2,4-DNP), but was unreactive against 2,4,6-trinitrophenol (2,4,6-TNP). pH dependence studies demonstrated increased reactivity at lower pH for both 4-NP and 2,4-DNP, suggestive of a pH effect that precludes the reaction with 2,4,6-TNP at or near physiological conditions. Stopped-flow UV-visible spectroscopic studies strongly implicate a role for Compound I in the mechanism of 4-NP oxidation. The results demonstrate that there may be a much larger number of non-microbial enzymes that are underrepresented when it comes to understanding the degradation of persistent organic pollutants such as nitrophenols in the environment.

5.2.2 Experimental

Protein Crystallization and X-ray Diffraction Studies. Non-His tagged DHP B was overexpressed and purified per literature protocol,¹⁷ with minor modifications. DHP B crystals were obtained through the hanging-drop vapor diffusion method. Prior to hanging drops, DHP B was incubated for 1 hour at 4 °C with the desired substrate. Final incubated concentrations of DHP B, 4NP and 4NC were 12 mg/mL, 8 mM and 4 mM respectively. The crystals were grown from mother liquor solutions of 30% PEG 4000 and 0.2 M ammonium sulfate at pH 6.4, and were equilibrated against identical reservoir solutions. Protein to mother liquor ratios varied between 1:1, 1.33:1, 1.66:1 and 2:1. At 4 °C crystals grew from each condition after 3 days. The crystals were cryo-protected by briefly dipping them in reservoir solution enhanced with 20% glycerol and then flash frozen in liquid N₂. Data were collected at 100 K on the SER-CAT 22-ID beamline at the APS synchrotron facility, utilizing a wavelength of 1.00 Å. All data were scaled and integrated using HKL2000,²² molecular replacement was performed with Phaser-MR¹⁵ from the PHENIX¹⁶ suite of programs using 3IXF¹⁷ as the search model, model building and manual placement of waters utilized COOT¹⁸ and refinement was carried out using phenix.refine.¹⁹ The DHPB-4NP complex data set refined to a resolution of 1.87 Å and the DHPB-4NC complex refined to the 1.98 Å resolution.

5.2.3 Results and Discussion

Data collection and refinement statistics for WT DHP B co-crystallized in complex with 4-nitrophenol and 4-nitrocatechol are found in Table 5.5, and selected substrate-protein and heme-protein distances can be found in Table 5.6. DHP B crystallized as a homo-dimer in the asymmetric unit, consistent with each previously deposited crystal structure. There is full occupancy of 4-NP in both protomers, while 4-NC fully occupies subunit B however exhibits partial occupancy of 0.5 in subunit A, with O₂ present in the absence of 4-NC. The orientation of each substrate is identical in both of its corresponding subunits. The subsequent structural analysis will focus solely on subunit B.

Table 5.5. Data collection and refinement statistics for DHP B co-crystallized in the presence of 4-nitrophenol (4-NP) and 4-nitrocatechol (4-NC).

	4-nitrophenol	4-nitrocatechol
PDB Entry	5CHQ	5CHR
<u>Data Collection</u>		
Wavelength (Å)	1.00	1.00
Temperature (K)	100	100
Space Group	P2 ₁ 2 ₁ 2 ₁	P2 ₁ 2 ₁ 2 ₁
Unit-cell parameters (Å)		
<i>a</i>	59.77	59.88
<i>b</i>	67.62	67.19
<i>c</i>	67.20	67.44
Unique reflections	23,022 (1,119) ^a	19,721 (966) ^a
Completeness (%)	99.2 (100.0) ^a	100.0 (99.7) ^a
R _{merge} (%) ^b	21.0	13.0
I/σ(I)	9.2 (2.1) ^a	9.9 (2.0) ^a
Redundancy	4.8 (4.5) ^a	4.8 (4.6) ^a
V _m (Å ³ /Da)	2.24	2.26
<u>Refinement</u>		
Resolution (Å)	1.87	1.98
R _{work} (%) ^c	16.41 (19.59) ^a	16.33 (18.91) ^a
R _{free} (%) ^d	23.24 (26.19) ^a	22.05 (29.51) ^a
No. of protein atoms	2309	2264
No. of ligand atoms	20	24
No. of solvent atoms	238	206
R.m.s.d from ideal geometry ^e		
Bond lengths (Å)	0.007	0.007
Bond angles (°)	1.084	1.012
<u>Ramachandran plot (%)</u>		
Most favored region	97.56	97.8
Addl allowed region	2.44	2.20

^aValues in parentheses are for the highest resolution shell. ^bR_{merge} = $\frac{\sum_h \sum_i [|I_i(h) - \langle I(h) \rangle|]}{\sum_h \sum_i I_i(h)} \times 100\%$, where $I_i(h)$ is the i^{th} measurement and $\langle I(h) \rangle$ is the weighted mean of all measurements of $I(h)$. ^cR_{work} = $\frac{\sum |F_o - F_c|}{\sum F_o} \times 100\%$, where F_o and F_c are the observed and calculated structure factors, respectively. ^dR_{free} is the R factor for the subset (9%) of reflections selected before and not included in the refinement. ^eRoot-mean-square deviation. ^fRamachandran plot created via COOT.

Both substrates were found to bind in the distal pocket, oriented between the heme β edge and Fe (Figures 5.6 and 5.8). Both molecules are bound 4.2 Å above the heme with a tilt angle

of 25° (in reference to the heme normal) away from the β edge. The aromatic rings are oriented for π -stacking interactions with F21. The nitro groups are positioned internally, residing in the Xe1 binding site, with the OH groups situated near the pocket entrance, stabilized by H-bonding interactions: the heme propionate D and Y38 form a H-bonding network with 4-NP, with distances of 2.6 and 2.7 Å, respectively, to the OH1 of 4-NP. As a tighter binder exhibited by the lower K_d , 4-NC forms H-bonds with both of its OH groups: the heme propionate D and Y38 form H-bonds with OH1, exhibiting distances of 2.7 and 2.8 Å respectively. The OH2 interacts with T56 at a distance of 2.6 Å, and also has a weaker H-bond with Y38 at 3.2 Å. The hydrogen bonding interactions between OH1 of 4-NP or 4-NC and the protein/heme propionates aligns well with the observation from the mechanistic studies that DHP prefers protonated nitrophenolic substrates. This binding mode has been observed previously for the *p*-halogenated phenols (Figure 5.6, C and D). LSQ superposition of the subunit B distal pockets resulted in a 0.114 Å r.m.s.d, with the two substrates occupying identical orientations.

In support of the observed peroxygenase activity, the crystal structure of DHP B complexed with 4-NP showed the substrate in close proximity to the heme Fe from which the inserted O atom is derived. As there is no ferryl structure of DHP B, analysis of a superposition of the 4-NP structure with a surrogate oxyferrous DHP A structure (2QFN²³) approximates the reactive C3 carbon of 4-NP at ~2.9 Å from the O bound to the heme Fe, sufficiently positioned for O-atom transfer to yield the 4-nitrocatechol product. Interestingly, with the OH2 group located 7.9 Å from the heme Fe, 4-NC resides in an orientation that suggests rearrangement following initial 4-NP oxygenation. The possibilities of molecular rotation inside the distal pocket or product removal followed by rebinding as a substrate are logical explanations for the crystallographic 4-NC binding site.

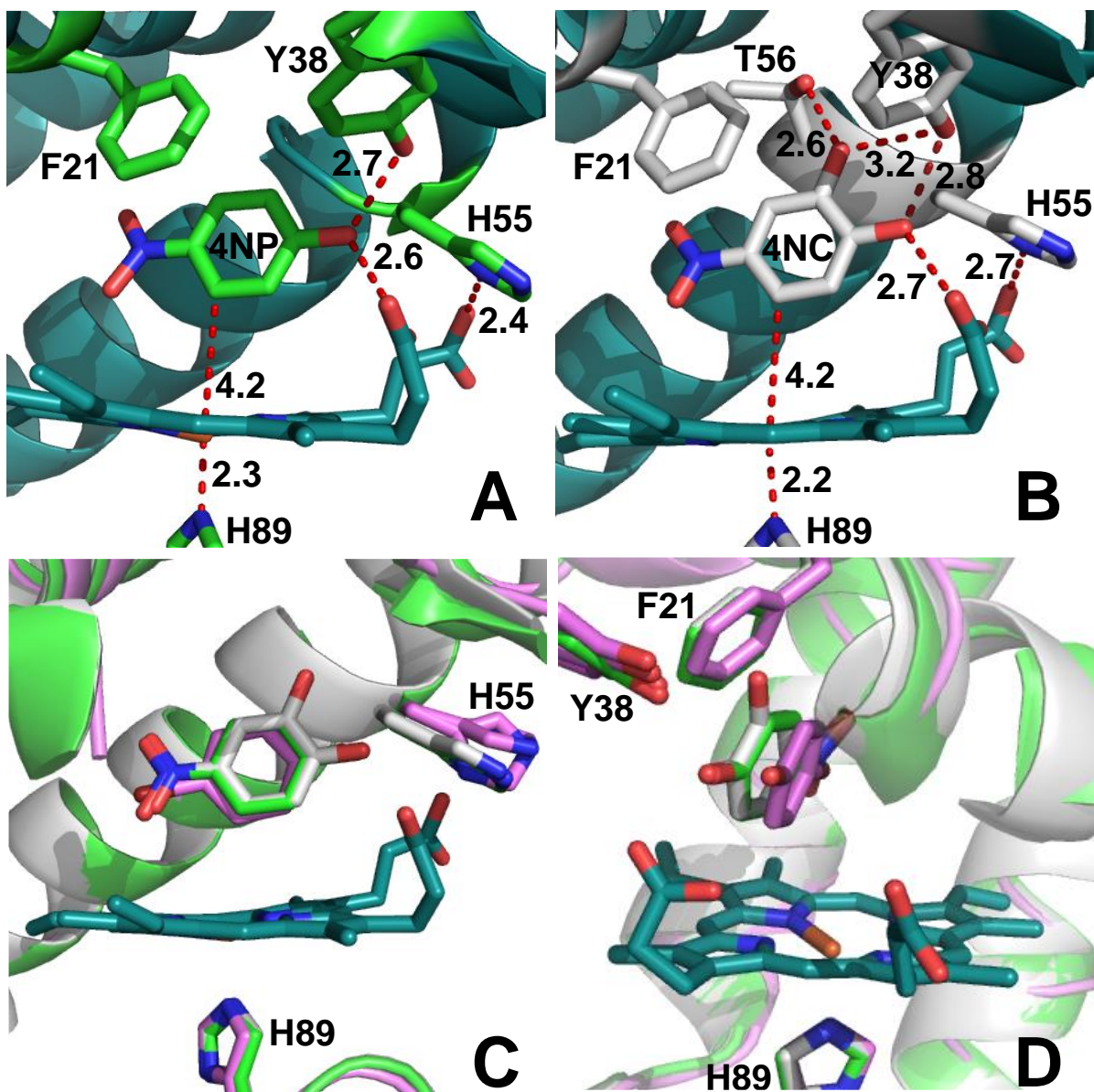


Figure 5.6. As viewed from the β edge, panels A and B provide atomic distances for 4-NP and 4-NC, respectively. Panels C and D present the distal superposition of 4-NP (5CHQ, green), 4-NC (5CHR, silver) and 4BP (3LB2,²⁵ purple) structures. As shown, the 4-NP and 4-NC molecules superpose with little deviation, while 4BP is slightly displaced with regard to the OH at the distal entrance. Panel C is viewed from the β edge, and panel D presents the view from the distal entrance, the γ edge.

Table 5.6. Distal pocket distances of ligand (4NP, 4NC, and 4BP¹⁸) and heme environments, given in Å. Atom nomenclature for 4-NP and 4-NC is shown in Figure 5.7.

	Substrate related distances		
	4-NP (5CHQ)	4-NC (5CHR)	4-BP (3LB2)
H55-N ^δ ...OH (phenol)	4.85 (3.54)	4.51 (3.87)	4.15 (4.34)
Propionate O1D...OH (phenol)	2.63	2.75	2.85
Y38(OH) ... OH (phenol)	2.75	2.81	3.11
T56(OH) ... OH (phenol)	5.06	2.59 (OH2)	
Fe... OH (phenol)	6.82	6.91	6.48
Fe...N/X	5.19	5.12	4.94
Fe...O1-NO ₂	4.66	4.60	
Fe...phenol (C3/C5)	4.2 C3	4.23 C5	
	Heme related distances		
Propionate O1D –H55 N ^δ	2.44 (4.54)	2.64 (4.69)	2.35 (2.98)
Propionate O2D –H55 N ^δ	3.89 (2.99)	3.76 (2.94)	3.55 (3.62)
Fe-H55 N ^δ	8.71 (8.76)	8.66	2.35 (2.98)
Fe-H55 (N ^ε)	9.3 (9.26)	9.22	10.09 (10.40)
Fe-H89 (N ^ε)	2.25	2.25	2.12
Fe to pyrrole N plane ^a	0.06	0.12	0.28
Fe...ligand bend angle (°) ^b	143.87	156.65	166.99
Fe...ligand tilt angle (°) ^c	8.44	9.04	42.8

^a averages of both subunits. ^b the bend angle is defined as Fe-C5-C2. ^c the tilt angle is defined as the angle between the heme perpendicular and the Fe-ligand bond.

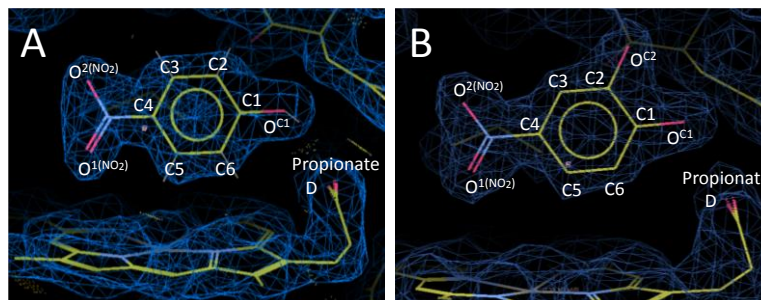


Figure 5.7. Fitting of substrates A) 4NP and B) 4NC into their respective 2mFo-DFc electron density maps, contoured to 1 σ . The nitro group of each substrate is situated in the internal Xe1 binding site²⁹ while the hydroxyl groups form H-bonding interactions with the heme propionate arms, Y38 and T56. Substrate atomic labels are provided for clarification.

The orientation and proximity of both 4-NP and 4-NC resemble that of the putative 5-haloindole binding site that was determined by computational methods and supported by resonance Raman studies,²⁴ and suggest a common peroxygenase binding site for O-atom transfer. By contrast, this peroxygenase substrate site differs from the previously determined peroxidase substrate binding sites: TBP²⁶ and TCP²⁷ both bind deep in the distal cavity beneath F21 in close proximity to L100 at the α edge of the heme, residing in the Xe1 binding site²⁶ with the hydroxyl group pointed towards the heme Fe, and with H55 found in the ‘closed’ (internal) conformation (Figure 5.8).^{25,28} This is in contrast to the nitrophenol structures where only the nitro group resides in the Xe1 binding site. Moreover, the peroxidase substrates not only reside near a heme edge, they are both positioned such that a halogen substituent is facing the heme iron, thus sterically hindering O-atom transfer from an activated ferryl intermediate to a nearby carbon atom on the substrate. By way of comparison, 4-nitrophenol, and haloindoles by extension, reside near the reactive heme center well-positioned for O-atom transfer directly from the ferryl intermediate, with no such steric hindrance. Distal superposition of peroxidase and peroxygenase substrate binding sites is provided in the Figure 5.8. Interestingly, TCP also possesses a second binding site that closer resembles nitrophenol binding: the Cl substituent of the C4 carbon is directed toward the heme-Fe, H55 is found in the ‘open’ (external) conformation and the phenolic OH is within hydrogen bonding distance to Y38, as seen with the nitrophenol substrates. This alternate TCP binding site is situated at the γ edge of the heme, with the molecule residing between both heme propionate arms. Thus, when one considers all possible substrates (halophenols, haloindoles, nitrophenols) for DHP, there is ample evidence to suggest a common binding motif necessary for peroxygenase activity, but such binding alone is not sufficient as to determine peroxygenase vs. peroxidase activity.

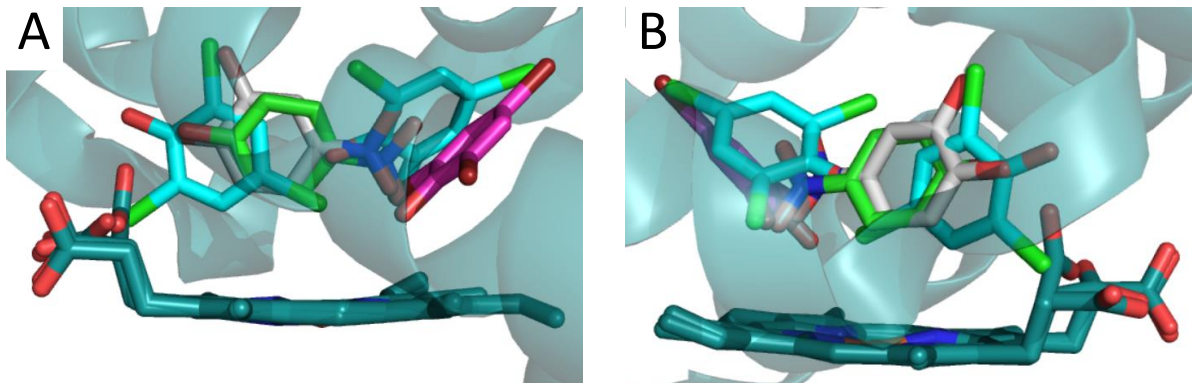


Figure 5.8. Superposition of substrate binding sites within the distal pocket: 4-NP (green), 4-NC (silver), TBP²⁶ (pink) and both internal and external conformations of TCP²⁷ (cyan). Panel A is viewed from the heme γ edge while panel B is viewed from the heme β edge.

5.2.4 Summary of Case Study 2

In summary, the nitrophenol and nitrocatechol substrate binding studies presented here in Case Study 2 enhances our understanding of the plasticity of DHP's heme reactive center, not only in regard to multifunctional coexistence but also in its ability to accommodate multiple substrate binding modes. In an effort to further probe functional and structural plasticity of DHP, the heme Fe was replaced with a Mn atom in the following study.

5.3 Structural Analysis of DHP B Reconstituted with Mn Protoporphyrin IX

5.3.1 Introduction

Manganese-substituted derivatives of heme proteins are well represented in literature, spanning at least the past 50 years. Investigations into the catalytic and spectral differences been reported for the Mn variants of hemoglobin (Hb),^{30,31} myoglobin (Mb),^{32,33} cytochrome P450,³⁴ prostaglandin H2 synthase (PGHS-1),³⁵ nitric oxide synthase (NOS),³⁶ cytochrome *c*,³⁷ cytochrome *b*₅,³⁸ cytochrome *c* peroxidase (CcP),^{33,39} heme-nitric oxide/oxygen proteins (H-NOX)⁴⁰ and horseradish peroxidase (HRP).^{31,33} While there is a wealth of studies involving Mn PPIX variants of hemoproteins, the crystallographic structural characterization of these variants is scarce by comparison, consisting of only 4 proteins: PGHS-1,³⁵ H-NOX,^{40,41} cytochrome P450_{cam}⁴² and Mb.⁴³ Presented here is an X-ray crystallographic structural analysis of Mn-PPIX reconstituted DHP B (Mn-DHP B). In addition to further exploring the established functional plasticity of DHP, Mn-DHP B provides the opportunity to address questions related to whether or not there are structural changes in the protein scaffold upon uptake of a non-native metal PPIX cofactor, whether or not the Mn-PPIX cofactor binds in the same orientation/geometry as the native heme cofactor, and can the observed differences in reactivity between the native and non-native cofactor-containing DHP systems be related to their structural differences.

5.3.2 Experimental

Preparation of Mn-PPIX Reconstituted DHP B. Non-His tagged DHP B was overexpressed and purified per literature protocol.⁴⁴ DHP B, in 100 mM potassium phosphate buffer (KP_i), was adjusted at 0 °C to pH 2.3-2.5 by dropwise additions of 0.1 M HCl, followed by immediate mixing with an equal volume of ice-cold 2-butanone. The mixture was vigorously shaken for 30 s and allowed to stand at 0 °C for 1 min until the deeply colored upper 2-butanone layer containing the extracted native heme cofactor was well separated from the colorless lower aqueous phase layer containing the apoenzyme. The 2-butanone phase was removed, and the remaining aqueous phase was extracted twice more with 2-butanone, and

then dialyzed against distilled water to remove any remaining 2-butanone. The dialyzed solution was centrifuged to remove insoluble material and kept at 4 °C. Apoprotein, in 10 mM KPi at pH 7.0, was mixed with Mn-PPIX solution (2 mg Mn-PPIX dissolved in minimal 0.1 M NaOH) and allowed to stand at 0 °C for 10 min. The mixture was then adjusted to pH 5.5 and passed through a carboxymethyl cellulose (CM) column equilibrated with 10 mM KPi, pH 5.5. The reconstituted Mn-DHP B was absorbed on the column, whereas the unbound Mn-PPIX passed through the column. The column was washed with 5 column volumes of 10 mM KPi buffer, pH 5.5. The absorbed complex was slowly recovered with elution buffer (10 mM KPi, pH 7.2) and stored at 0 °C. The reconstituted enzyme concentration was determined spectrophotometrically by measuring one peak of the split Soret (λ_{max} 374 nm) and respective molar absorptivity, $\epsilon_{(377)} = 75,000 \text{ M}^{-1}\text{cm}^{-1}$.^{33,39,45}

Protein Crystallization and X-ray Diffraction Studies. Crystals were obtained through the hanging-drop vapor diffusion method. At an enzyme concentration of 12 mg/mL in 20 mM Na cacodylate buffer (pH 6.4), crystals were obtained from the 2:1 ratio of enzyme to a 32% PEG 8000, 0.2 M ammonium sulfate mother liquor, equilibrated against an identical reservoir solution. At 4 °C, crystals grew after 3 days. The crystals were cryo-protected by briefly dipping them in reservoir solution enhanced with 20% glycerol and then flash frozen in liquid N₂. Data were collected at 100 K on the SER-CAT 22-ID beamline at the APS synchrotron facility, utilizing a wavelength of 1.00 Å. All data were scaled and integrated using HKL2000,²² molecular replacement was performed with Phaser-MR¹⁵ from the PHENIX¹⁶ suite of programs using 3IXF¹⁷ as the search model, model building and manual placement of waters utilized COOT¹⁸ and refinement was carried out using phenix.refine.¹⁹ The DHP B Mn-protoporphyrin IX data set refined to a resolution of 1.40 Å.

5.3.3 Results and Discussion

Apo-DHP B was successfully reconstituted with Mn-PPIX, yielding Mn-DHP B. In regard to reactivity, enzymatic assays showed that Mn-DHP B retained peroxidase and peroxygenase reactivity for 2,4,6-trichlorophenol (TCP) and 5-bromoindole (5BI), respectively, albeit

diminished with respect to WT DHP B. Catalytic activation of Mn-DHP B could not be achieved using H₂O₂, however the use of organic peroxides, such as *meta*-chloroperoxybenzoic acid (*m*CPBA) and peracetic acid (PAA), were found to be successful. In an effort to expand DHP's substrate scope, styrene and 1,4-cyclohexadiene were investigated as potential substrates for Mn-DHP B and WT DHP B. Reactivity was observed in both enzymes and in these examples the Mn-DHP B variant exhibited greater substrate conversion than WT. Full details of the reactivity observed with Mn-DHP B will be reported elsewhere, with the remainder of this discussion focusing on the structural details.

Mn-DHP B was successfully purified, crystallized and the structure solved to atomic resolution. Data collection and refinement statistics are provided in Table 5.7. Crystals of Mn-DHP B were of the same reddish color as WT DHP B crystals. They possessed a trifold appearance, growing much smaller than WT DHP B. The space group, P2₁2₁2₁, remains conserved among DHP crystals, along with unit cell size and the presence of a dimer in the asymmetric unit. Lacking a distal ligand in both protomers, the Mn was found to be 5-coordinated and domed toward the proximal histidine, H89. The distal cavity in protomer A contained no solvent or ligands, and the distal histidine, H55, was observed in both the “closed”, or internal, conformation and the “open”, or external, conformation. This dual conformation of H55 has been previously observed, and is attributed to the flexibility of the distal histidine to access the structural equilibrium between the two conformers.^{26,46,47}

For protomer B, the proximal environment is identical to protomer A. However, H55 is observed only in the external conformation, with its N^δ positioned toward the porphyrin propionate arm A at the hydrogen-bonding distance of 2.62 Å. There were 2 water molecules present in the distal pocket, forming a hydrogen-bonding network at the cavity entrance with T56, Y38, and the porphyrin propionate arm A, as shown in Figure 5.9. This distal water network has only been observed once before in the crystal structure of DHP B (F21W). The locations of the waters are virtually identical, with the H₂O-2 – Y38 and H₂O-1 – propionate distances shortened by 0.2 Å in this Mn-DHP B structure.

Table 5.7. X-ray data collection and refinement statistics for Mn-DHP B .

Mn-DHP B	
PDB Entry	6BBY
<u>Data Collection</u>	
Wavelength (Å)	1.00
Temperature (K)	100
Space Group	P2 ₁ 2 ₁ 2 ₁
Unit-cell parameters (Å)	
<i>a</i>	56.70
<i>b</i>	66.01
<i>c</i>	69.15
Unique reflections	51,939 (2,571) ^a
Completeness (%)	99.9 (100.0) ^a
R _{merge} (%) ^b	5.7 (67.6) ^a
I/σ(I)	24.6 (2.2) ^a
Redundancy	4.8 (4.7) ^a
V _m (Å ³ /Da)	2.15
<u>Refinement</u>	
Resolution (Å)	1.40
R _{work} (%) ^c	14.26 (16.99) ^a
R _{free} (%) ^d	18.89 (23.29) ^a
No. of protein atoms	2,481
No. of ligand atoms	---
No. of solvent atoms	326
R.m.s.d from ideal geometry ^e	
Bond lengths (Å)	0.009
Bond angles (°)	1.648
<u>Ramachandran plot (%)</u>	
Most favored region	98.66
Addl allowed region	1.00

^aValues in parentheses are for the highest resolution shell. ^bR_{merge} = $\frac{\sum_h \sum_i |I_i(h) - \langle I(h) \rangle|}{\sum_h \sum_i I_i(h)} \times 100\%$, where $I_i(h)$ is the i^{th} measurement and $\langle I(h) \rangle$ is the weighted mean of all measurements of $I(h)$. ^cR_{work} = $\frac{\sum |F_o - F_c|}{\sum F_o} \times 100\%$, where F_o and F_c are the observed and calculated structure factors, respectively. ^dR_{free} is the R factor for the subset (9%) of reflections selected before and not included in the refinement. ^eRoot-mean-square deviation. ^fRamachandran plot created via COOT.

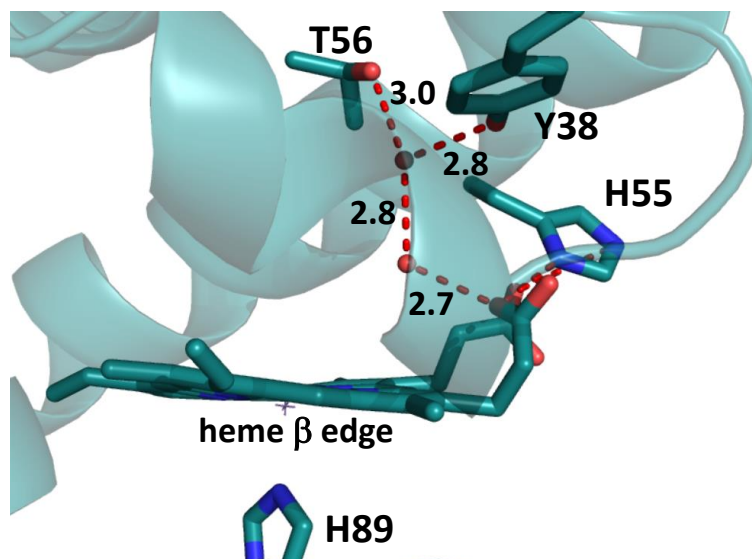


Figure 5.9. Distal cavity of Mn-DHP B protomer B. As shown, there exists two water molecules at the entrance of the cavity, participating in a hydrogen-bonding network with T56, Y38, and propionate arm A. The presence of distal waters in this orientation has only been observed previously in the DHP B (F21W) mutant.

Comparison with the WT DHP B structure (3IXF)¹⁷ yields globally identical structures, as validated in the LSQ C α superposition r.m.s.d values of 0.4602 Å and 0.2956 Å for protomers A and B, respectively. This shows that DHP's structural plasticity can accommodate apo-protein denaturation and reinsertion of the Mn-PPIX cofactor, yet still return to its native tertiary structure. The porphyrin orientations were in agreement with each other, even though they were not taken into account in the superposition calculation. Provided in Figure 5.10 is the C α superposition of protomer A, with Mn-DHP B shown in teal and WT DHP B portrayed in silver. The distal cavities showed identical geometries in relation to the distal residue orientations and distance to the metal, and selected atomic distances are provided in Table 5.8. A slight elongation of the metal – H89 N ϵ bond by 0.11 Å was observed in Mn-DHP B, accompanied by a slight decrease in the H89 N δ – L83 O distance by 0.13 Å, however this most likely due to the apical distortion of the Mn downward toward the H89. It is shown that there are no global structural changes to the protein scaffold nor localized changes to the active

site environment. The Mn-PPIX was found to reside in the exact orientation as the native heme, and DHP retained its native structure in spite of the structural rearrangement necessary for incorporation of the non-native cofactor, Mn-PPIX.

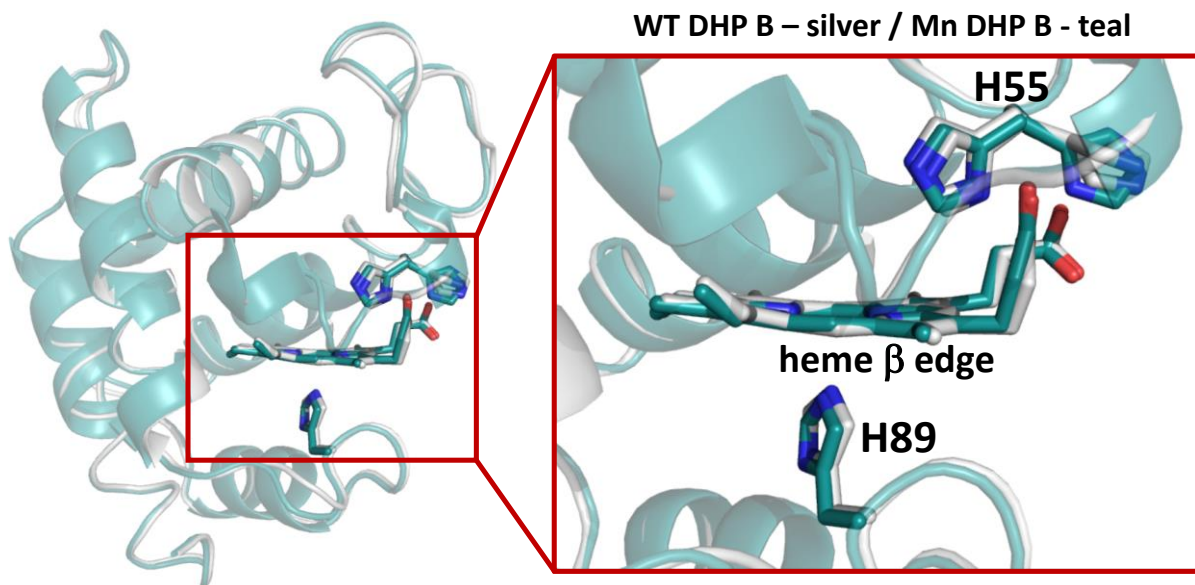


Figure 5.10. LSQ C α superposition of WT DHP B (3IXF,¹⁷ silver) and Mn-DHP B (teal) protomer A. Emphasis is placed on the heme cavity, where it is clearly shown that the porphyrins occupy identical orientations, even though they were not considered in the superposition calculation. Mn-DHP B possesses the native fold of WT DHP B, showing that the insertion of Mn-PPIX yielded no structural consequence on the protein.

Table 5.8. Selected porphyrin-related atomic distances of Mn-DHP B and WT DHP B (pdb accession 3IXF). All distances given in Å. (^a value for conformation B)

	Mn-DHP B		WT DHP B	
	Subunit A	Subunit B	Subunit A	Subunit B
Metal – H89 N ^ε	2.28	2.30	2.18	2.17
H89 N ^δ – L83 O	2.74	2.74	2.92	2.81
Metal – H89 C ^α	6.19	6.18	6.14	6.11
Metal – H55 C ^α	8.90 (8.97) ^a	8.64	8.71	8.63
Metal – 21 st C ^α	10.68	10.75	10.76	10.74
Metal – 59 th C ^α	5.88	5.79	5.81	5.76
Metal – 35 th C ^α	10.12	9.85	10.08	10.29
Metal – 100 th C ^α	10.22	10.27	10.27	10.26 (10.30) ^a

5.3.4 Summary of Case Study 3

In summary, replacement of the native heme cofactor with Mn-PPIX yielded no structural consequence on the structure of DHP B. The lack of a 6th ligand coordinated to the Mn-PPIX is typical for Mn, and a notable difference from the native heme cofactor. The presence of a distal water network was unexpected, but not a novel find for variants of DHP B. Further studies are required to assess their consequence, if any at all, in Mn-DHP B. Thus, the reactivity differences observed between Mn-DHP B and WT DHP B are most likely derived from the electronic nature of the metal itself and not due to changes in the protein structure that affect function.

5.4 Tyrosine Rotation Angle Validation: X-ray Crystallographic Analysis of DHP B (Y28F) and DHP B (Y38F)

5.4.1 Introduction

The tyrosyl radical spectra simulation algorithm (TRSSA) can calculate EPR spectral parameters utilizing the dependency of C_1 electron density and the phenoxy ring rotational angle.⁴⁸ As the ring rotates along the $C_\beta - C_1$ bond, the methylene hydrogens have periodic changes in their hyperfine splitting of the radical signal. As a result, calculated spectra that mirror experimental spectra can provide optimal rotational angles. Figure 5.11 depicts how the ring rotation alters the interaction of the methylene hydrogens, $H_{\beta 1}$ and $H_{\beta 2}$, with the phenolic ring.

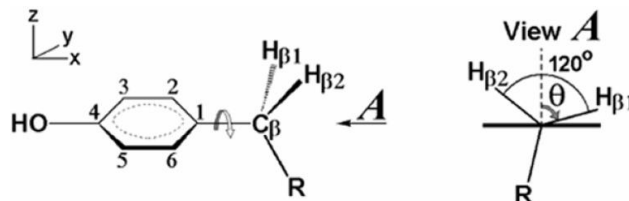


Figure 5.11. Diagram portraying the dihedral angle that dictates the hyperfine splitting of the tyrosyl radical signal by the two methylene hydrogens, $H_{\beta 1}$ and $H_{\beta 2}$.⁴⁸

With the help of the TRSSA, the free radical EPR signal reported for DHP A Compound ES (obtained using rapid-freeze-quench methods) was shown to be a pH-dependent superposition of two different free radical EPR signals assigned to different tyrosine residues, Tyr-34 and Tyr-38. Assignment of the initial rapid-freeze-quench EPR spectra utilized TRSSA to reproduce experimental spectra and provide tyrosyl rotation angles.⁴⁹ Crystallographic tyrosyl rotation angles were extracted from PDB accession number 1EW6, the original DHP crystal structure, and compared with the target angles derived from TRSSA. Through this angular comparison, the EPR spectra were assigned to their corresponding tyrosyl radical

signals. To further confirm the original EPR spectral assignments, a series of Tyr→Phe mutants were then systematically explored by rapid-freeze-quench EPR methods. TRSSA was utilized again to simulate EPR spectra, however this time the angles were obtained from 3IXF and were used as parameters to model the spectra, instead of using the spectra to predict the angle rotations.⁵⁰

The tyrosyl angles from the wild type enzyme were utilized in modeling the spectra for the various phenylalanine mutants. Underlying the analysis that led to the spectral assignment of various tyrosyl radicals was the assumption of consistent tyrosyl angles between the WT and mutant enzymes. However, this is still an assumption that has yet to be validated. If the angles in mutants vary by $\sim 20^\circ$, reassignment of the EPR spectra may be required, in particular the reassignment of Y28 in favor of Y107. In an attempt to definitively validate the mutant spectral assignments, the DHP B (Y28F) and DHP B (Y38F) mutants were obtained and crystallized. From their structural analysis, accurate tyrosyl ring rotation angles were obtained which, in turn, were able to validate the assumption used in the TRSSA assignment of the EPR spectra of DHP Compound ES.

5.4.2 Experimental

Construction of Mutant DHP Plasmids. Site-directed mutagenesis was performed using the Quikchange II site-directed mutagenesis method (Agilent Technologies). Mutagenesis [melt (95 °C, 60 s), anneal (55 °C, 50 s), and extension (68 °C, 360 s)] was performed for 18 cycles. Oligonucleotides were synthesized by Integrated DNA Technologies (IDT) [DHP B (Y28F) 5'-GCG TTT CTC GTC CGG AAA CTT ATT CAA AAA TGC-3' (sense) and 5'-GCA TTT TTG AAT AAG TTT CCG GAC GAG AAA CGC-3' (anti-sense); DHP B (Y38F) 5'-G GTC AGA TTT GCC AAA GTT TTT GAA GTT GCG-3' (sense) and 5'-CGC AAC TTC AAA AAC TTT GTC GGC AAA TCT C-3'(anti-sense)]. The plasmid encoding wild-type DHP B lacking the N-terminal poly-His tag was used as a template. The modified plasmids were transformed into BL21(DE3) competent cells (Agilent Technologies) and selected based on survival on LB-agar-ampicillin (100 $\mu\text{g}/\text{mL}$) plates. The plasmids were

extracted using the spin column plasmid DNA kit (Bio Basic), and the desired mutation was confirmed by sequencing (Genewiz).

Protein Crystallization and X-ray Diffraction Studies. Non-His tagged DHP B (Y28F) and DHP B (Y38F) were overexpressed and purified per literature protocol.⁴⁴ Crystals were obtained through the hanging-drop vapor diffusion method. The enzyme was concentrated to 12 mg/mL in 20 mM sodium cacodylate buffer (pH 6.4) and the crystals were grown from mother liquor solutions of 28-34 % PEG 4000 and 0.2 M ammonium sulfate at pH 6.4, equilibrated against identical reservoir solutions. Protein to mother liquor ratios varied between 1:1, 1.33:1, 1.66:1 and 2:1. At 4 °C crystals grew after 3 days. The crystals were cryo-protected by briefly dipping them in reservoir solution enhanced with 20% glycerol and then flash frozen in liquid N₂. Data were collected at 100 K on the SER-CAT 22-BM beamline at the APS synchrotron facility, utilizing a wavelength of 1.00 Å. All data were scaled and integrated using HKL2000,²² molecular replacement was performed with Phaser-MR¹⁵ from the PHENIX¹⁶ suite of programs using 3IXF¹⁷ as the search model, model building and manual placement of waters utilized COOT¹⁸ and refinement was carried out using phenix.refine.¹⁹ The DHPB (Y28F) data set refined to a resolution of 1.57 Å and the DHPB (Y38F) data set refined to the resolution of 1.90 Å.

5.4.3 Results and Discussion

DHP B (Y28F) and DHP B (Y38F) were both successfully purified, crystallized and the molecular structures solved. Data collection and refinement statistics are provided in Table 5.9. As expected, the mutant structures deviated very little with respect to the WT DHP B structure (3XIF), both globally and locally at the mutation site. LSQ C_α superposition of WT DHP B and the two mutants resulted in rmsd values of 0.4125 Å and 0.4182 Å (subunit average) for DHP B (Y28F) and DHP B (Y38F), respectively. At the mutation sites (Y28F and Y38F), the side chains reside in the same orientation, showing these mutations have no consequence on the local environment, as shown in Figure 5.12.

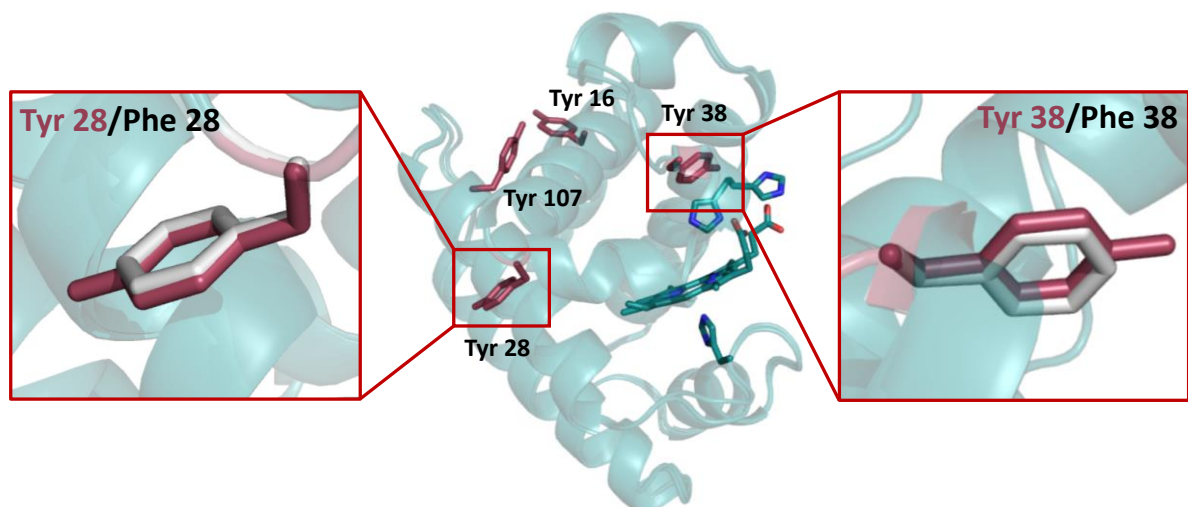


Figure 5.12. The locations of the 4 tyrosine residues (Y16, Y28, Y38, and Y107) in DHP B. The tyrosine → phenylalanine mutations at positions 28 and 38 are indicated, with Phe shown in silver.

The structural analysis of these mutants confirms the previous TRSSA-deduced assignment of the tyrosyl radical spectra obtained for Compound ES. The DHP B (Y28F) mutant's EPR spectrum closely resembled the "pH 5 radical" in DHP A, which has previously been assigned to Y38. This spectral assignment arose from TRSSA input parameters for construction of the simulated spectrum. The phenoxy ring rotation angles (θ°) of -8° and -52° were utilized in the TRSSA calculation, and the DHP A (pdb accession 1EW6) crystal structure was analyzed via the Phenol Ring Rotation Angle Database to identify the tyrosine residue. By assigning the DHP B (Y28F) spectra to be representative of the Y38 radical, the assumption was made that the ring rotation angles in this mutant were identical to wild type DHP A. Analysis of DHP B (Y28F) via the database has shown this assumption to be valid. There are slight differences when related to the deviation from the target angle in DHP A, however tyrosine assignment in relation to their closeness to the target values still results in the spectral assignment of Y38 as the responsible radical species. Table 5.9 provides the rotation angles, closeness to target values, and deviation from previously obtained wild type DHP rotation angles.

Table 5.9. Data collection and refinement statistics for DHP B (Y28F) and DHP B (Y38F).

	DHP B (Y28F)	DHP B (Y38F)
PDB Entry	5VTS	5VTT
<u>Data Collection</u>		
Wavelength (Å)	1.00	1.00
Temperature (K)	100	100
Space Group	P2 ₁ 2 ₁ 2 ₁	P2 ₁ 2 ₁ 2 ₁
Unit-cell parameters (Å)		
<i>a</i>	58.74	58.66
<i>b</i>	68.22	67.69
<i>c</i>	67.57	67.87
	38,130 (1,889) ^a	21,743
Unique reflections		(1,079) ^a
Completeness (%)	98.8 (99.1) ^a	99.9 (99.9) ^a
R _{merge} (%) ^b	5.3 (49.1) ^a	4.6 (39.4) ^a
I/σ(I)	27.7 (2.2) ^a	20.1 (3.1) ^a
Redundancy	5.6 (4.7) ^a	4.7 (4.6) ^a
V _m (Å ³ /Da)	2.18	2.26
<u>Refinement</u>		
Resolution (Å)	1.57	1.90
R _{work} (%) ^c	14.74 (17.32) ^a	16.63 (18.09) ^a
R _{free} (%) ^d	18.80 (25.11) ^a	21.85 (24.42) ^a
No. of protein atoms	2,282	2,294
No. of solvent atoms	233	179
R.m.s.d from ideal geometry ^e		
Bond lengths (Å)	0.006	0.007
Bond angles (°)	0.742	0.809
<u>Ramachandran plot (%)</u>		
Most favored region	98.52	98.15
Addl allowed region	1.48	1.85

^aValues in parentheses are for the highest resolution shell. ^bR_{merge} = $\frac{\sum_h \sum_i [|I_i(h) - \langle I(h) \rangle|]}{\sum_h \sum_i I_i(h)} \times 100\%$, where $I_i(h)$ is the i^{th} measurement and $\langle I(h) \rangle$ is the weighted mean of all measurements of $I(h)$. ^cR_{work} = $\frac{\sum |F_o - F_c|}{\sum F_o} \times 100\%$, where F_o and F_c are the observed and calculated structure factors, respectively. ^dR_{free} is the R factor for the subset (> 5 %) of reflections selected before and not included in the refinement. ^eRoot-mean-square deviation. ^fRamachandran plot created via COOT.

Table 5.10. Rotation angle of the phenol ring in different tyrosine residues in DHP B (Y28F) and DHP B (Y38F), ranked in closeness to the target values.⁴⁸

DHP B (Y28F)		$\theta_{\text{target}} = -8^\circ$	
		Dev. from DHP A (1EW6)	
Tyrosine	θ°	$ \theta - \theta_{\text{target}} ^\circ$	$ \theta - \theta_{\text{target}} ^\circ$
B Tyr 38	-5.973	2	6.9
A Tyr 38	2.274	10.3	1.8
A Tyr 16	27.688	35.7	8.5
B Tyr 16	32.920	40.9	4.5
A Tyr 107	53.282	61.3	8.9
B Tyr 107	56.974	65	8.7
		$\theta_{\text{target}} = -52^\circ$	
		Dev. from DHP A (1EW6)	
Tyrosine	θ°	$ \theta - \theta_{\text{target}} ^\circ$	$ \theta - \theta_{\text{target}} ^\circ$
B Tyr 38	-5.973	46	10.9
A Tyr 38	2.274	54.3	18.8
A Tyr 16	27.688	79.7	8.5
B Tyr 16	32.920	84.9	4.5
A Tyr 107	53.282	105.3	8.9
B Tyr 107	56.974	109	8.7
DHP B (Y38F)		$\theta_{\text{target}} = 46^\circ$	
		Dev. from DHP B (3IXF)	
Tyrosine	θ°	$ \theta - \theta_{\text{target}} ^\circ$	$ \theta - \theta_{\text{target}} ^\circ$
A Tyr 28	45.785	0.2	2.1
B Tyr 28	47.176	1.2	1.5
A Tyr 107	54.082	8.1	1.8
B Tyr 107	56.69	10.7	1.4
B Tyr 16	35.01	11	6.7
A Tyr 16	28.29	17.7	8.6
		$\theta_{\text{target}} = 74^\circ$	
		Dev. from DHP B (3IXF)	
Tyrosine	θ°	$ \theta - \theta_{\text{target}} ^\circ$	$ \theta - \theta_{\text{target}} ^\circ$
B Tyr 107	56.69	17.3	1.4
A Tyr 107	54.082	19.9	1.8
B Tyr 28	47.176	26.8	1.5
A Tyr 28	45.785	28.2	2.1
B Tyr 16	35.011	39	6.7
A Tyr 16	28.286	45.7	8.6

The DHP B (Y38F) mutant was utilized to help identify the Y28 radical EPR spectral assignment. The simulated EPR spectrum was generated by TRSSA, utilizing parameters including θ ° target values of 46° and 74°. The Phenol Ring Rotation Angle Database previously used tyrosyl rotation angles from wild type DHP B (pdb accession 3IXF) to assign the spectral characteristics to Y28, making the assumption that the rotation angles between wild type and mutant DHP B were conserved. Using the database to assess the DHP B (Y38F) ring rotation angles again confirmed the validity of the assumption. The target angle of 46° provided the closest match with ring rotations, exactly as had been shown in WT DHP B. Again, there are slight deviations between closeness to target values for the Y38F mutant and the WT enzyme, however the spectral assignment remains consistent.

5.4.4 Summary of Case Study 4

In summary, the assumption of conserved tyrosyl ring rotation angles between the Y28F and Y38F mutants and the WT DHP B enzyme has been validated. Utilizing the Phenol Ring Rotation Angle Database to analyze the mutant tyrosyl and phenyl rotation angles, obtained here via the newly obtained crystallographic structures, the same tyrosine residues that were previously assigned as the site(s) of radical formation in Compound ES were confirmed here. The new experimental data support the previous assumption, and therefore fully validate the spectral assignment provided by the TRSSA generated simulated EPR spectra.

5.5 References

- (1) Casadei, C. M.; Gumiero, a.; Metcalfe, C. L.; Murphy, E. J.; Basran, J.; Concilio, M. G.; Teixeira, S. C. M.; Schrader, T. E.; Fielding, a. J.; Ostermann, a.; et al. Neutron Cryo-Crystallography Captures the Protonation State of Ferryl Heme in a Peroxidase. *Science*. **2014**, *345* (6193), 193–197.
- (2) Meilleur, F.; Weiss, K.; Myles, D. A. A. *Micro and Nano Technology in Bioanalysis*; Lee, J., Foote, R., Eds.; Humana Press: Totowa, NJ, 2009; Vol. 531.
- (3) Knihtila, R.; Holzapfel, G.; Weiss, K.; Meilleur, F.; Mattos, C. Neutron Crystal Structure of RAS GTPase Puts in Question the Protonation State of the GTP γ -Phosphate. *J. Biol. Chem.* **2015**, *290* (52), 31025–31036.
- (4) Gerlits, O.; Wymore, T.; Das, A.; Shen, C. H.; Parks, J. M.; Smith, J. C.; Weiss, K. L.; Keen, D. A.; Blakeley, M. P.; Louis, J. M.; et al. Long-Range Electrostatics-Induced Two-Proton Transfer Captured by Neutron Crystallography in an Enzyme Catalytic Site. *Angew. Chemie - Int. Ed.* **2016**, *55* (16), 4924–4927.
- (5) Vandavasi, V. G.; Weiss, K. L.; Cooper, J. B.; Erskine, P. T.; Tomanicek, S. J.; Ostermann, A.; Schrader, T. E.; Ginell, S. L.; Coates, L. Exploring the Mechanism of β -Lactam Ring Protonation in the Class A β -Lactamase Acylation Mechanism Using Neutron and X-Ray Crystallography. *J. Med. Chem.* **2016**, *59* (1), 474–479.
- (6) Fisher, S. Z.; Kovalevsky, A. Y.; Domsic, J.; Mustyakimov, M.; Silverman, D. N.; McKenna, R.; Langan, P. Enzymes for Carbon Sequestration: Neutron Crystallographic Studies of Carbonic Anhydrase. *Acta Crystallogr. Sect. D Biol. Crystallogr.* **2010**, *66* (11), 1178–1183.
- (7) Glusker, J. P.; Carrell, H. L.; Kovalevsky, A. Y.; Hanson, L.; Fisher, S. Z.; Mustyakimov, M.; Mason, S.; Forsyth, T.; Langan, P. Using Neutron Protein Crystallography to Understand Enzyme Mechanisms. *Acta Crystallogr. Sect. D Biol. Crystallogr.* **2010**, *66* (11), 1257–1261.
- (8) Bodenheimer, A. M.; O'Dell, W. B.; Stanley, C. B.; Meilleur, F. Structural Studies of *Neurospora Crassa* LPMO9D and Redox Partner CDHIIA Using Neutron Crystallography and Small-Angle Scattering. *Carbohydr. Res.* **2017**, 5–9.

- (9) Wan, Q.; Parks, J. M.; Hanson, B. L.; Fisher, S. Z.; Ostermann, A.; Schrader, T. E.; Graham, D. E.; Coates, L.; Langan, P.; Kovalevsky, A. Direct Determination of Protonation States and Visualization of Hydrogen Bonding in a Glycoside Hydrolase with Neutron Crystallography. *Proc. Natl. Acad. Sci.* **2015**, *112* (40), 12384–12389.
- (10) Shu, F.; Ramakrishnan, V.; Schoenborn, B. P. Enhanced Visibility of Hydrogen Atoms by Neutron Crystallography on Fully Deuterated Myoglobin. *Proc. Natl. Acad. Sci. USA* **2000**, *97* (8), 3872–3877.
- (11) O'Dell, W. B.; Swartz, P. D.; Weiss, K. L.; Meilleur, F. Crystallization of a Fungal Lytic Polysaccharide Monooxygenase Expressed from Glycoengineered *Pichia Pastoris* for X-Ray and Neutron Diffraction. *Acta Crystallogr. Sect. Struct. Biol. Commun.* **2017**, *73* (2), 70–78.
- (12) Gardberg, A. S.; Del Castillo, A. R.; Weiss, K. L.; Meilleur, F.; Blakeley, M. P.; Myles, D. A. A. Unambiguous Determination of H-Atom Positions: Comparing Results from Neutron and High-Resolution X-Ray Crystallography. *Acta Crystallogr. Sect. D Biol. Crystallogr.* **2010**, *66* (5), 558–567.
- (13) Enfors, S. O.; Haggstrom, L. .; Hogskoletryckeriet, Royal institute of Technology: Stockholm, 2000.
- (14) Minor, W.; Cymborowski, M.; Otwinowski, Z.; Chruszcz, M. HKL-3000: The Integration of Data Reduction and Structure Solution - From Diffraction Images to an Initial Model in Minutes. *Acta Crystallogr. Sect. D Biol. Crystallogr.* **2006**, *62* (8), 859–866.
- (15) McCoy, A. J.; Grosse-Kunstleve, R. W.; Adams, P. D.; Winn, M. D.; Storoni, L. C.; Read, R. J. Phaser Crystallographic Software. *J. Appl. Crystallogr.* **2007**, *40* (4), 658–674.
- (16) Adams, P. D.; Afonine, P. V.; Bunkóczi, G.; Chen, V. B.; Davis, I. W.; Echols, N.; Headd, J. J.; Hung, L. W.; Kapral, G. J.; Grosse-Kunstleve, R. W.; et al. PHENIX: A Comprehensive Python-Based System for Macromolecular Structure Solution. *Acta Crystallogr. Sect. D Biol. Crystallogr.* **2010**, *66* (2), 213–221.
- (17) De Serrano, V.; Dantonio, J.; Franzen, S.; Ghiladi, R. A. Structure of Dehaloperoxidase B at 1.58 Å Resolution and Structural Characterization of the AB Dimer from *Amphitrite ornata*. *Acta Crystallogr. Sect. D Biol. Crystallogr.* **2010**, *66* (5), 529–538.
- (18) Emsley, P.; Lohkamp, B.; Scott, W. G.; Cowtan, K. Features and Development of Coot. *Acta Crystallogr. Sect. D Biol. Crystallogr.* **2010**, *66* (4), 486–501.

- (19) Afonine, P. V.; Grosse-Kunstleve, R. W.; Echols, N.; Headd, J. J.; Moriarty, N. W.; Mustyakimov, M.; Terwilliger, T. C.; Urzhumtsev, A.; Zwart, P. H.; Adams, P. D. Towards Automated Crystallographic Structure Refinement with Phenix.refine. *Acta Crystallogr. Sect. D Biol. Crystallogr.* **2012**, *68* (4), 352–367.
- (20) Xu, Q.; Gunner, M. R. Trapping Conformational Intermediate States in the Reaction Center Protein from Photosynthetic Bacteria. *Biochemistry* **2001**, *40* (10), 3232–3241.
- (21) Rader, S. D.; Agard, D. A. Conformational Substates in Enzyme Mechanism: The 120 K Structure of α -Lytic Protease at 1.5 Å Resolution. *Protein Sci.* **1997**, *6* (7), 1375–1386.
- (22) Otwinowski, Z.; Minor, W. Processing of X-Ray Diffraction Data Collected in Oscillation Mode. *Methods Enzymol.* **1997**, *276*, 307–326.
- (23) De Serrano, V.; Chen, Z.; Davis, M. F.; Franzen, S. X-Ray Crystal Structural Analysis of the Binding Site in the Ferric and Oxyferrous Forms of the Recombinant Heme Dehaloperoxidase Cloned from Amphitrite Ornata. *Acta Crystallogr. Sect. D Biol. Crystallogr.* **2007**, *63* (10), 1094–1101.
- (24) Barrios, D. A.; Antonio, J. D.; McCombs, N. L.; Zhao, J.; Franzen, S.; Schmidt, A. C.; Sombers, L. A.; Ghiladi, R. A. Peroxygenase and Oxidase Activities of Dehaloperoxidase-Hemoglobin from Amphitrite Ornata. *J. Am. Chem. Soc.* **2014**, *136*, 7914–7925.
- (25) Thompson, M. K.; Davis, M. F.; Serrano, V. De; Nicoletti, F. P.; Howes, B. D.; Smulevich, G.; Franzen, S. Internal Binding of Halogenated Phenols in Dehaloperoxidase-Hemoglobin Inhibits Peroxidase Function. *Biophys. J.* **2010**, *99* (5), 1586–1595.
- (26) Zhao, J.; de Serrano, V.; Zhao, J.; Le, P.; Franzen, S. Structural and Kinetic Study of an Internal Substrate Binding Site in Dehaloperoxidase-Hemoglobin A from Amphitrite Ornata. *Biochemistry* **2013**, *52* (14), 2427–2439.
- (27) Wang, C.; Lovelace, L. L.; Sun, S.; Dawson, J. H.; Lebioda, L. Complexes of Dual-Function Hemoglobin/dehaloperoxidase with Substrate 2,4,6-Trichlorophenol Are Inhibitory and Indicate Binding of Halophenol to Compound I. *Biochemistry* **2013**, *52* (36), 6203–6210.

- (28) Nicoletti, F. P.; Thompson, M. K.; Howes, B. D.; Franzens, S.; Smulevich, G. New Insights into the Role of Distal Histidine Flexibility in Ligand Stabilization of Dehaloperoxidase-Hemoglobin from Amphitrite Ornata. *Biochemistry* **2010**, *49* (9), 1903–1912.
- (29) De Serrano, V.; Franzen, S. Structural Evidence for Stabilization of Inhibitor Binding by a Protein Cavity in the Dehaloperoxidase-Hemoglobin from Amphitrite Ornata. *Biopolymers* **2012**, *98* (1), 27–35.
- (30) Fabry, T. L.; Simo, C.; Javaherian, K. Preparation of Mesoporphyrin IX and Copper and Manganese Mesoporphyrin Complexes of Apohemoglobin. *Biochim. Biophys. Acta - Protein Struct.* **1968**, *160* (1), 118–122.
- (31) Yonetani, T.; Drott, H. R.; Leigh, J. S. J.; Reed, G. H.; Waterman, M. R.; Asakura, T. Electromagnetic Properties of Hemoproteins. III. Electron Paramagnetic Resonance Characteristics of iron(III) and manganese(II) Protoporphyrins IX and Their Apohemoprotein Complexes in High Spin States. *J. Biol. Chem.* **1970**, *245* (11), 2998–3003.
- (32) Atassi, M. Z. Immunochemistry of Sperm-whale Myoglobins Prepared with Various Modified Porphyrins and Metalloporphyrins. *Biochem. J.* **1967**, *103* (7), 29–35.
- (33) Yonetani, T.; Asakura, T. Studies on Cytochrome c Peroxidase XV. Comparison of Manganese Porphyrin-Containing Cytochrome c Peroxidase, Horseradish Peroxidase, and Myoglobin. *J. Biol. Chem.* **1969**, *244* (17), 4580–4588.
- (34) Gelb, M. H.; Toscano, W. A. J.; Sligar, S. G. Chemical Mechanisms for Cytochrome P-450 Oxidation: Spectral and Catalytic Properties of a Manganese-substituted Protein. *Proc. Natl. Acad. Sci. U. S. A.* **1982**, *79* (19), 5758–5762.
- (35) Gupta, K.; Selinsky, B. S.; Loll, P. J. 2.0 Å Structure of Prostaglandin H₂ Synthase-1 Reconstituted with a Manganese Porphyrin Cofactor. *Acta Crystallogr. Sect. D Biol. Crystallogr.* **2006**, *62* (2), 151–156.
- (36) Hemmens, B.; Gorren, A. C. F.; Schmidt, K.; Werner, E. R.; Mayer, B. Heme Insertion, Dimerization and Reactivation of Heme-free Rat Neuronal Nitric Oxide Synthase. *Biochem. J.* **1998**, *332* (2), 337–342.
- (37) Dickinson, L. C.; Chien, J. C. W. Manganese Cytochrome C. Structure and Properties. *J. Biol. Chem.* **1977**, *252* (17), 6156–6162.

- (38) Ozols, J.; Strittmatter, P. Interaction of Porphyrins and Metalloporphyrins with Apocytochrome b5. *J. Biol. Chem.* **1964**, *239* (4), 1018–1023.
- (39) Yonetani, T.; Asakura, T. Studies on Cytochrome c Peroxidase XI. A Crystalline Enzyme Reconstituted from Apoenzyme and Manganese Protoporphyrin IX. *J. Biol. Chem.* **1968**, *243* (14), 3996–3998.
- (40) Herzik, M. A.; Jonnalagadda, R.; Kuriyan, J.; Marletta, M. A. Structural Insights into the Role of Iron–histidine Bond Cleavage in Nitric Oxide-Induced Activation of H-NOX Gas Sensor Proteins. *Proc. Natl. Acad. Sci.* **2014**, *111* (40), E4156–E4164.
- (41) Winter, M. B.; Klemm, P. J.; Phillips-Piro, C. M.; Raymond, K. N.; Marletta, M. A. Porphyrin-Substituted H-NOX Proteins as High-Relaxivity MRI Contrast Agents. *Inorg. Chem.* **2013**, *52*, 2277–2279.
- (42) Makris, T. M.; Koenig, K. von; Schlichting, I.; Sligar, S. G. The Status of High-Valent Metal Oxo Complexes in the P450 Cytochromes. *J. Inorg. Biochem.* **2006**, *100* (4), 507–518.
- (43) Zahran, Z. N.; Chooback, L.; Copeland, D. M.; West, A. H.; Richter-Addo, G. B. Crystal Structures of Manganese- and Cobalt-Substituted Myoglobin in Complex with NO and Nitrite Reveal Unusual Ligand Conformations. *J. Inorg. Biochem.* **2008**, *102* (2), 216–233.
- (44) McCombs, N. L.; D’Antonio, J.; Barrios, D. A.; Carey, L. M.; Ghiladi, R. A. Nonmicrobial Nitrophenol Degradation via Peroxygenase Activity of Dehaloperoxidase-Hemoglobin from Amphitrite Ornata. *Biochemistry* **2016**, *55* (17), 2465–2478.
- (45) Yonetani, T. Studies on Cytochrome c Peroxidase X. Crystalline Apo- and Reconstituted Holoenzymes. *J. Biol. Chem.* **1967**, *242* (21), 5008–5013.
- (46) Franzen, S.; Thompson, M. K.; Ghiladi, R. A. The Dehaloperoxidase Paradox. *Biochim. Biophys. Acta - Proteins Proteomics* **2012**, *1824* (4), 578–588.
- (47) Zhao, J.; de Serrano, V.; Franzen, S. A Model for the Flexibility of the Distal Histidine in Dehaloperoxidase-Hemoglobin A Based on X-Ray Crystal Structures of the Carbon Monoxide Adduct. *Biochemistry* **2014**, *53* (15), 2474–2482.
- (48) Svistunenko, D. A. Tyrosine Residues in Different Proteins : Phenol Ring Rotation Angle Database. 2004.

- (49) Thompson, M. K.; Franzen, S.; Ghiladi, R. A.; Reeder, B. J.; Svistunenko, D. A. Compound ES of Dehaloperoxidase Decays via Two Alternative Pathways Depending on the Conformation of the Distal Histidine. *J. Am. Chem. Soc.* **2010**, *132* (49), 17501–17510.
- (50) Dumarieh, R.; D'Antonio, J.; Deliz-Liang, A.; Smirnova, T.; Svistunenko, D. A.; Ghiladi, R. A. Tyrosyl Radicals in Dehaloperoxidase: How Nature Deals with Evolving an Oxygen-Binding Globin to a Biologically Relevant Peroxidase. *J. Biol. Chem.* **2013**, *288* (46), 33470–33482.